



ALMA MATER STUDIORUM
UNIVERSITÀ DI BOLOGNA

**DOTTORATO DI RICERCA IN
FISICA**

Ciclo 36°

Settore Concorsuale: 02/A1 - Fisica Sperimentale delle Interazioni Fondamentali

Settore Scientifico Disciplinare: FIS/01 - Fisica Sperimentale

**The interplay of multiplicity and effective energy
for (multi) strange hadron production in pp
collisions at the LHC**

Presentata da: Francesca Ercolessi

Coordinatore Dottorato

Alessandro Gabrielli

Supervisore

Luisa Cifarelli

Co-supervisore

Francesco Noferini

Esame finale anno 2024



Acknowledgements

I am deeply grateful to my supervisors, Professor Luisa Cifarelli and Dr. Francesco Noferini, for their guidance, patience and support throughout this journey. Their mentorship has impacted not only my academic growth but has also touched me on a personal level. A special thank goes to Nicolò Jacazio, who has been a mentor and a friend, offering unwavering support every step of the way. His kindness and dedication have been a constant source of inspiration. I would like to thank Chiara De Martin, Alberto Calivà, Livio Bianchi, Chiara Oppedisano, Rosario Nania, Giulia Clai, for their insights, feedback, and collaborative spirit which were invaluable in shaping my research. Thanks to my fellow travellers Marco, Nicola, Riccardo, Sofia, Giovanni, Gleb, for sharing this journey with me, making many great memories. My thanks go also to all my colleagues in the group at University of Bologna, for the stimulating discussions and the friendly time spent together.

I am deeply grateful to my parents for their unconditional love, belief in my abilities, and constant encouragement. This achievement is a reflection of their sacrifices and unwavering support. I would like to thank Giacomo, for his constant presence, patience and understanding. Last but not least, I am truly grateful for the love and encouragement of my friends.

Abstract

The enhanced production of strange hadrons in heavy-ion collisions relative to that in minimum-bias pp collisions is historically considered one of the first signatures of the formation of a deconfined quark-gluon plasma. At the LHC, the ALICE experiment observed that the ratio of strange to non-strange hadron yields increases with the charged-particle multiplicity at midrapidity, starting from pp collisions and evolving smoothly across interaction systems and energies, ultimately reaching Pb–Pb collisions. The understanding of the origin of this effect in small systems remains an open question. This thesis presents a comprehensive study of the production of K_S^0 strange mesons, Λ ($\bar{\Lambda}$) strange baryons and Ξ^- ($\bar{\Xi}^+$) multi-strange baryons in pp collisions at $\sqrt{s} = 13$ TeV collected in LHC Run 2 with the ALICE detector. A novel approach is exploited, introducing, for the first time, the concept of effective energy in the study of strangeness production in hadronic collisions at the LHC. In this work, the ALICE Zero Degree Calorimeters are used to measure the energy carried by forward emitted baryons in pp collisions, which reduces the effective energy available for particle production with respect to the nominal centre-of-mass energy. The results presented in this thesis provide new insights into the interplay, for strangeness production, between the initial stages of the collision and the produced final hadronic state. Finally, the first Run 3 results on the production of Ω^- ($\bar{\Omega}^+$) multi-strange baryons are presented, measured in pp collisions at $\sqrt{s} = 13.6$ TeV and $\sqrt{s} = 900$ GeV, the highest and lowest collision energies reached so far at the LHC. This thesis also presents the development and validation of the ALICE Time-Of-Flight (TOF) data quality monitoring system for LHC Run 3. This work was fundamental to assess the performance of the TOF detector during the commissioning phase, in the Long Shutdown 2, and during the data taking period.

Table of contents

Abstract	v
List of figures	xi
List of tables	xxvii
Introduction	1
1 High energy nuclear physics	5
1.1 An introduction to QCD	5
1.1.1 The running coupling α_s	6
1.1.2 The QCD phase transition	8
1.1.3 Chiral symmetry in QCD	10
1.2 Heavy-ion collisions	11
1.2.1 Geometry of a heavy-ion collision	12
1.2.2 Space-time evolution of the collision	13
1.2.3 QGP experimental probes	15
1.3 Small hadronic collision systems	26
1.3.1 Collectivity in small systems	27
1.3.2 Dynamics and hadrochemistry of particle production	29
2 Strangeness production in high energy hadronic collisions	33
2.1 Strangeness as a signature of QGP	34
2.1.1 Strangeness enhancement in heavy-ion collisions	38
2.2 Strange hadron production in small collision systems	40
2.2.1 Recent results in small systems	40
2.2.2 Model description of strange hadron production	45

3	Effective energy and multiplicity	53
3.1	Multiplicity studies in different collision systems	53
3.1.1	Results from previous experiments	54
3.2	The effective energy	56
3.2.1	Experimental results on the leading energy	57
3.2.2	Leading effect in heavy-ion collisions	60
3.2.3	Studying the leading effect at the LHC	62
4	ALICE: A Large Ion Collider Experiment	65
4.1	The Large Hadron Collider	65
4.2	ALICE 1 (Run 1 and 2)	67
4.2.1	ALICE sub-detectors	67
4.2.2	The Zero Degree Calorimeters (ZDC)	73
4.2.3	Data acquisition and offline framework	80
4.2.4	Tracking and vertex reconstruction	81
4.2.5	Particle Identification with ALICE	82
4.3	Run 3 upgrade: ALICE 2	84
4.3.1	Detectors upgrade	86
4.3.2	Upgrade of data taking, processing and reconstruction	88
5	TOF data quality assurance and performance in Run 3	91
5.1	The Time-Of-Flight detector	92
5.1.1	The Multigap Resistive Plate Chamber technology	92
5.1.2	Detector readout	95
5.2	Monitoring the TOF data quality in Run 3	98
5.2.1	TOF quality control during the data-taking	99
5.3	TOF performance in Run 3	105
5.3.1	Time calibration	105
5.3.2	Event time measurement	106
5.3.3	TOF-tracks matching efficiency	109
5.3.4	TOF PID	113
5.3.5	Commissioning and Pilot Run 2021	115
5.3.6	Performance in Run 3	117
6	Strangeness enhancement with multiplicity and effective energy	119
6.1	Analysis Strategy	120
6.2	Data and Monte Carlo samples	121

6.3	Event selection and classification	121
6.4	Multiplicity and forward energy measurement	123
6.4.1	ZDC energy calibration	124
6.5	Definition of multi-differential classes	127
6.5.1	Estimators selectivity: VZEROM and SPDClusters	128
6.5.2	Cross-check for auto-correlation biases	135
6.6	Strange hadron reconstruction	137
6.6.1	Signal extraction	140
6.6.2	Contamination from secondary particles	147
6.6.3	Efficiency \times acceptance correction	150
6.6.4	Influence of Monte Carlo p_T shape on the efficiency	153
6.6.5	Normalisation corrections	156
6.7	Systematic uncertainties	158
6.7.1	Uncertainties on strange hadron spectra	159
6.7.2	Systematics on p_T integrated yields	162
6.7.3	Multiplicity and energy uncorrelated uncertainties	164
6.7.4	Systematic uncertainty on the very forward energy measurement	167
7	Results and discussion	169
7.1	Transverse momentum spectra of strange hadrons	169
7.2	Self-normalised hadron yield ratios	172
7.2.1	Standalone analysis	174
7.2.2	Strangeness production at fixed leading energy	175
7.2.3	Strangeness production at fixed midrapidity multiplicity	177
7.3	Phenomenological models	179
7.3.1	Multiplicity and leading energy correlation in the models	180
7.3.2	Correlation with the number of Multi-Parton Interactions (MPI)	181
7.3.3	Comparison of the strange self-normalised yield ratios to model predictions	184
8	First results on Ω production with Run 3 data	191
8.1	Analysis details	191
8.1.1	Data and Monte Carlo samples	192
8.1.2	Event selection and multiplicity percentile	193
8.1.3	Signal extraction	193
8.1.4	Efficiency and normalisation corrections	197
8.1.5	Systematic uncertainties	201

8.2	Results	205
8.3	Perspectives	209
Conclusions		213
References		217
Appendix A Details on the analysis strategy		227
A.1	ZDC energy as an event-by-event estimator	227
A.2	Raw p_T spectra in all event classes	230
A.3	MC p_T shape correction in all event classes	235
A.4	Signal loss corrections in all event classes	243
A.5	Uncorrelated systematics in all event classes	246
Appendix B Transverse momentum spectra of strange hadrons		249

List of figures

1.1	Feynman diagrams of the strong interaction with quark loops (“charge screening”) and gluon loops (“charge anti-screening”).	7
1.2	Summary of α_s measurements as a function of the energy scale Q . Different colours indicate different measurements used to extract the α_s values. The QCD perturbation theory order used to extract α_s is indicated in parentheses. Figure from [13].	8
1.3	QCD phase diagram.	9
1.4	Variation of T_{ch} with μ_B , fitted with the Grand Canonical approach in the THERMUS Model using all available particle ratios. Figure from [17]. . . .	10
1.5	Representation of an ultra-relativistic heavy ions collision.	12
1.6	A Glauber Monte Carlo simulation of an Au–Au collision event at $\sqrt{s_{\text{NN}}} = 200$ GeV with impact parameter $b = 6$ fm. (a) shows the transverse plane visualisation, while (b) the visualisation along the beam axis. Darker circles represent participating nucleons [23].	13
1.7	Distribution of the sum of the signal amplitudes measured in the VZERO detectors in Pb–Pb collisions at $\sqrt{s_{\text{NN}}} = 2.76$ TeV. Figure from [25].	14
1.8	The evolution of a heavy-ion collision at LHC energies [22].	15
1.9	Collision energy dependence of the charged-particle pseudorapidity density at midrapidity ($ \eta < 0.5$) normalised to the average number of participants, $\frac{2}{\langle N_{\text{part}} \rangle} \langle dN_{\text{ch}}/d\eta \rangle$. Data from central AA collisions are compared to measurements in non-single diffractive p(d)A collisions and inelastic (INEL) pp and p \bar{p} collisions. The lines are power-law fits to the data, and the bands represent the uncertainties on the extracted dependencies [22].	17

1.10	Measured multiplicity per unit of rapidity of different hadron species and light nuclei compared to SHM fits from THERMUS, SHARE, Thermal-FIST, and GSI-Heidelberg (see text for references). Differences between the model calculations and the measured yields are shown in the bottom panels. Figure from [22].	19
1.11	Transverse momentum distributions of π^+ , K^+ , p, K_S^0 , and Λ , and the ϕ meson for 0-50% and 80-90% centrality intervals in Pb–Pb collisions at $\sqrt{s_{NN}} = 2.76$ TeV. The data points are scaled for better visibility. Statistical and systematic uncertainties are shown as bars and boxes, respectively. Figure from [22].	20
1.12	Elliptic flow coefficient v_2 of charged pions, charged and neutral kaons, protons, ϕ mesons, and hyperons as a function of p_T for several centrality classes in Pb–Pb collisions at $\sqrt{s_{NN}} = 5.02$ TeV measured by the ALICE Collaboration. Figure from [44].	21
1.13	p_T -differential baryon-to-meson ratios in Pb–Pb divided by the pp ones at the same colliding energy for $(p+p)/(\pi^++\pi^-)$ at $\sqrt{s_{NN}} = 5.02$ TeV and $(\Lambda+\bar{\Lambda})/(2K_S^0)$ at $\sqrt{s_{NN}} = 2.76$ TeV. Figure from [22].	22
1.14	(a) Nuclear modification factor R_{AA} for charged hadrons in central and peripheral Pb–Pb collisions and NSD p–Pb collisions [22]. (b) ATLAS event display of a Pb–Pb collision at $\sqrt{s_{NN}} = 2.76$ TeV showing jet quenching. . .	24
1.15	(a) J/ψ R_{AA} as a function of the charged particle multiplicity. The results of NA50 (SPS), STAR (RHIC) and ALICE (LHC) are compared. Figure from [22]. (b) Elliptic flow of pions, prompt D mesons, inclusive J/ψ , electrons from beauty hadron decays and $\Upsilon(1S)$ in semicentral (30–50%) Pb–Pb collisions at $\sqrt{s_{NN}} = 5.02$ TeV.	25
1.16	Integrated particle-to-pion ratios as a function of the charged particle multiplicity for pp, p–Pb, and Pb–Pb collisions. Figure from [46].	27
1.17	2D two-particle correlation functions for (a) 2.76 TeV Pb–Pb and (b) 5.02 TeV p–Pb collisions for pairs of charged particles with $1 < p_T^{\text{trig}} < 3$ GeV/c and $1 < p_T^{\text{assoc}} < 3$ GeV/c within the $220 < N_{\text{trk}}^{\text{offline}} < 260$ multiplicity bin. Figures from [47].	28
1.18	2D two-particle correlation functions for 7 TeV pp (a) minimum bias events with $1 < p_T < 3$ GeV/c and (b) high multiplicity ($N_{\text{trk}}^{\text{offline}} \geq 110$) events with $1 < p_T < 3$ GeV/c. Figures from [48].	29

1.19	Multiplicity dependence of v_2 , v_3 and v_4 measured using the two-particle cumulant method in small (pp and p–Pb) and large (Xe–Xe and Pb–Pb) collision systems [49].	29
1.20	Average transverse momentum $\langle p_T \rangle$ as a function of the charged particle multiplicity at midrapidity $\langle dN_{ch}/d\eta \rangle$ in pp (left panel), p–Pb (central panel) and Pb–Pb and Xe–Xe (right panel) collisions. Different colours refer to different particle species, as indicated in the legend.	30
1.21	Transverse momentum dependence of p/π and Λ/K_S^0 ratio in pp (left), p–Pb (centre) and Pb–Pb (right) collisions. The red markers refer to events characterised by larger charged particle multiplicity with respect to the blue ones. Figure adapted from [46].	31
2.1	Quarks in the Standard Model.	34
2.2	Lowest-order production of $s\bar{s}$ by gluons and light quarks.	35
2.3	Rates A of $s\bar{s}$ production as function of temperature T . The curves are for $\alpha_S = 0.6$ and $m_s = 150$ MeV [50].	35
2.4	Time evolution of the relative strangeness to baryon density in the plasma for various temperatures T . The curves are for $\alpha_S = 0.6$ and $m_s = 150$ MeV. The vertical line corresponds to a time of ≈ 6 fm/c [50].	36
2.5	(a) Quark flow diagram for indirect strangeness production reaction: annihilation of a $q\bar{q}$ pair and production of a $s\bar{s}$ pair. (b) Quark flow diagram for strangeness exchange reaction: exchange of the s quark from the initial K meson to the final baryon. Quark spectator lines are also indicated [50]. . .	37
2.6	Hyperon-to-pion ratios as a function of $\langle N_{part} \rangle$ in AA collisions and pp collisions at LHC and RHIC energies. The lines are predictions from statistical hadronisation models. Figure from [61].	38
2.7	Strangeness enhancement factors for Ξ and Ω hyperons as a function of the average number of participants measured in different centre-of-mass energies by NA57, STAR and ALICE experiments. ALICE data points are shown with full markers. Figure from [61].	39
2.8	(Left) Ratios of different hadron yields to pions as a function of the charged particle multiplicity measured at midrapidity in pp collisions at $\sqrt{s} = 7$ TeV and 13 TeV, p–Pb collisions at $\sqrt{s_{NN}} = 5.02$ TeV and at $\sqrt{s_{NN}} = 8.16$ TeV, Xe–Xe collisions at $\sqrt{s_{NN}} = 5.44$ TeV and Pb–Pb collisions at $\sqrt{s_{NN}} = 2.76$ TeV and at $\sqrt{s_{NN}} = 5.02$ TeV. (Right) Ratios involving ρ mesons, K^* , $\Sigma^{*\pm}$, $\Lambda(1520)$ and Ξ^* . All yields are obtained at midrapidity. Figure from [22]. .	41

2.9	K_S^0 density spectra (a) and $(\Lambda + \bar{\Lambda})/K_S^0$ (b) as a function of the transverse momentum p_T in pp collisions at $\sqrt{s} = 7$ TeV. The results are shown for inclusive K_S^0 and Λ produced in minimum bias events (black markers), in the underlying event (empty markers), in the jet cone (green markers) and in jets after the subtraction of the contribution from the underlying event (red markers). Figures from [62].	42
2.10	(a) K_S^0 yields per trigger particle and per unit of $\Delta\eta\Delta\phi$ in the full, toward- and transverse-to-leading azimuthal regions. The yields are reported as a function of the midrapidity multiplicity. (b) Ratio between Ξ and K_S^0 full, toward- and transverse-to-leading yields as a function of charged particle multiplicity at midrapidity [63].	44
2.11	Jetty and isotropic events in the transverse plane. Figure from [64].	45
2.12	p_T -differential Ξ to π ratio in the jetty, isotropic and sphericity-integrated events in the multiplicity class [0-10]%. The multiplicity estimation is based on the number of SPD tracklets within $ \eta < 0.8$	46
2.13	Ratios of several particle species measured by the ALICE collaboration as a function of the midrapidity pion yields for pp, p-Pb and Pb-Pb colliding systems compared to the THERMUS strangeness canonical suppression model prediction (black line), in which only the system size is varied. The upper axis shows the radius R of the correlation volume $V = R^3$, which corresponds to the predicted particle ratios. Figure from [72].	47
2.14	Ratios of (multi-)strange hadron yields to pions as a function of the charged particle multiplicity measured at midrapidity. The open (shaded) boxes represent full (multiplicity uncorrelated) systematic uncertainties. Different lines represent predictions of different MC generators for pp collisions at $\sqrt{s} = 13$ TeV. Figure from [75].	49

2.15	Particle yield ratios of (a) Ω (Ω^\pm), (b) Ξ (Ξ^\pm), (c) Λ ($\Lambda + \bar{\Lambda}$), (d) protons ($p+\bar{p}$) and (e) ϕ to charged pions (π^\pm) as functions of charged particle multiplicity at midrapidity in pp and Pb–Pb collisions. Results from full simulations of DCC12 in pp collisions at $\sqrt{s} = 7$ TeV (full red triangles) and Pb–Pb collisions at $\sqrt{s_{NN}} = 2.76$ TeV (full red diamonds) collisions are compared with the ALICE experimental data in pp (black pluses) and Pb–Pb (black crosses) collisions. Results from Pythia8 in pp collisions (grey pluses) and from Pythia8 Angantyr in Pb–Pb (grey crosses) collisions are plotted as references. Results without hadronic rescatterings are also plotted for pp (open orange circles) and PbPb (open orange squared) collisions. Figure from [70].	51
3.1	Average multiplicity of charged particles measured in e^+e^- collisions by various experiments at LEP and and DESY. Figure from Ref. [77].	55
3.2	Average charged particle multiplicity measured in e^+e^- (full black symbols) and pp ($p\bar{p}$) (open symbols) collisions. The full grey symbols indicate the pp ($p\bar{p}$) data after the centre-of-mass energies have been scaled by a factor $\frac{1}{2}$. Figure from Ref. [78].	55
3.3	(a) Scatter plot of the quantities x_1^{leading} and x_2^{leading} , representing the Feynman- x of leading protons in the two hemispheres. Each point in the scatter plot represents one collision event. (b) Average value of x_2^{leading} as a function of x_1^{leading} . Figures from Ref. [79].	58
3.4	Average charged multiplicity as a function of the effective energy $E_{\text{effective}}$, here indicated as $\sqrt{(q_{\text{tot}}^{\text{had}})^2}$, for e^+e^- and pp collisions. The pp data were collected by the SFM experiment at the CERN ISR (full circles). The results from e^+e^- collisions from different experiments are also shown (open circles and triangles). Figure from Ref. [82].	59
3.5	In the abscissa the effective hadronic energy $2E_{\text{had}} \equiv E_{\text{effective}}$ (GeV) available for particle production. In the vertical axis on the left the beam energy, E_{inc} , on the right the total nominal energy of the ISR, $\sqrt{s} = 2E_{\text{inc}}$. Figure from Ref. [80].	59
3.6	Inclusive momentum distributions in pp collisions for $4 \leq E_{\text{effective}} \leq 6$ GeV (a) and $28 \leq E_{\text{effective}} \leq 32$ GeV (b), produced at three ISR nominal energies: $\sqrt{s} = 30, 44, 64$ GeV. TASSO and SPEAR e^+e^- data are shown at \sqrt{s} compatible with pp effective energies. Figures from Ref. [80].	61

3.7	Inclusive transverse momentum distribution measured in pp collisions at the ISR nominal energy $\sqrt{s} = 30$ GeV, for $11 \leq E_{\text{effective}} \leq 13$ GeV. The results are compared with e^+e^- data at $\sqrt{s} = 12$ GeV measured by TASSO at the PETRA electron-positron collider. Figure from Ref. [4].	62
3.8	(a) Charged multiplicity $\langle N_{\text{ch}} \rangle$ in pp, p \bar{p} , e^+e^- , Au–Au and Pb–Pb events as a function of centre-of-mass energy per binary collision. The heavy-ion data are normalised by $\langle N_{\text{part}}/2 \rangle$. (b) The data in (a) are divided by a perturbative QCD fit to the e^+e^- data (dotted line). Figure from Ref. [83].	63
3.9	Effective energy range (here indicated as E_{had}) covered at ISR and LHC as a function of \sqrt{s} . Figure from Ref. [86, 87].	64
4.1	The CERN accelerator complex. Figure from [90].	66
4.2	Schematic view of the ALICE detector.	68
4.3	Schematic view of ALICE 6 layers Inner Tracking System. Figure from [98].	71
4.4	3D view of the TPC field cage [102].	72
4.5	Segmentation of the VZERO-A/VZERO-C arrays [103].	73
4.6	Schematic view of the beamline and the ZDC location.	75
4.7	View of the ZDC location.	75
4.8	(a) Schematic connections of the fibres to the PMTs for the neutron calorimeter. (b) Picture of one Zero Degree Calorimeter for neutrons.	76
4.9	Schematic connections of the fibres to the PMTs for the proton calorimeter.	77
4.10	Spectator energy deposited in the ZDC calorimeters in Pb–Pb collisions as a function of ZEM signal amplitude. The correlation is used to define centrality classes [108].	78
4.11	ZNA energy spectrum requiring signal over the threshold in ZNA but not in ZNC, rejecting thus neutron emission on the opposite side. The dashed lines represent the single fits of the different peaks (1n, 2n, 3n, 4n), while the continuous line is the sum of all the contributions [109].	79
4.12	Correlation between the average charged multiplicity and the average effective energy in PYTHIA pp events, using the leading energy measurement in the ZDC calorimeters (squares), and at the generator-level (circles). Figure from [78].	80
4.13	PID performance of ITS (a), TPC(b), TOF (c), and HMPID (d) detectors. .	83
4.14	ALICE particle identification and reconstruction capabilities, with the p_T coverage corresponding to the published measurements based on pp or Pb–Pb data samples [22].	85

4.15	Impact parameter resolution in $r\phi$ vs p_T in pp collisions at $\sqrt{s} = 13.6$ TeV extracted from Run 3 data compared with Run 2 collisions at $\sqrt{s} = 13$ TeV. .	86
4.16	FIT detector layout [121].	87
4.17	FT0 time resolution in pp 13.6 TeV collected in Run 3.	88
5.1	Layout of the TOF detector in the ALICE space-frame. One of the 18 Super Modules inserted is highlighted, divided into five modules.	93
5.2	Longitudinal cross-section of the intermediate module. The strips are slightly rotated with respect to the horizontal position, oriented inside a module to be perpendicular to the interaction point.	93
5.3	Representation of the design of the ALICE TOF MRPC. The charge deposited by the ionising particle is shown with the corresponding signals on the pickup electrodes.	94
5.4	Sketch of the TOF front-end and readout electronics.	95
5.5	TOF readout scheme in Run 1 and 2.	97
5.6	TOF readout scheme in Run 3.	97
5.7	The Data Quality Control and Assessment (QC) architecture.	99
5.8	Hit map from a pp run at $\sqrt{s} = 13.6$ TeV collected in 2022. Each bin groups hits from the 24 channels read by one FEA. To reduce the material budget in the PHOS acceptance region, the central modules of SM 13, 14 and 15 are not installed, here displayed with a box.	100
5.9	Hit rate in TOF channels, which are flagged as noisy if their rate is above a specific threshold, configurable run-by-run. The x-axis displays the electronics index of the channel. The run displayed is a COSMIC run, i.e. without collisions.	101
5.10	(a) TOF hit time distribution within one LHC orbit (88.92 μ s). (b) TOF hit multiplicity as a function of the Bunch Crossing ID within one LHC orbit. .	102
5.11	Hit multiplicity on the TOF detector integrated in one readout window. . . .	103
5.12	Summary of the TRM slots and crates where readout errors detected during the run. Further details on the nature of the errors are provided by complementary QC plots.	103
5.13	(a) Hit multiplicity on the TOF detector in one of the first Pb–Pb collision runs at $\sqrt{s_{NN}} = 5.36$ TeV at 50 kHz interaction rate. (b) TOF hit multiplicity as a function of the Bunch Crossing ID within one LHC orbit.	104

5.14	(a) Correlation between the event time measured by the TOF detector and the event time measured by the FT0 detector for Pb–Pb collisions at $\sqrt{s_{NN}} = 5.36$ TeV collected in Run 3. (b) Difference between the TOF event time and the FT0 event time.	108
5.15	Section of one MRPC, displaying the readout pads, after the hit of a particle. Δx and Δz are the residuals with respect to the centre of the triggered (green) pad, and R is the matching window.	109
5.16	TOF residuals along the x (a) and z (b) directions as function of ϕ and η , respectively, for ITS constrained tracks (ITS-TPC and ITS-TPC-TRD) in Pb–Pb collisions at $\sqrt{s_{NN}} = 5.36$ TeV. The average value of the residuals is indicated with black points.	110
5.17	Matching efficiency for ITS constrained tracks (ITS-TPC and ITS-TPC-TRD) with $ \eta < 0.8$ as function of the particle transverse momentum Pb–Pb collisions at $\sqrt{s_{NN}} = 5.36$ TeV. A comparison between the efficiency obtained in the data and in the anchored MC simulation is shown.	112
5.18	Matching efficiency for ITS constrained tracks (ITS-TPC and ITS-TPC-TRD) with $ \eta < 0.8$ as function of the Run ID in Pb–Pb collisions at $\sqrt{s_{NN}} = 5.36$ TeV. A comparison between the normalised efficiency, i.e. corrected for readout inefficiencies and dead channels, is shown.	112
5.19	$(t - t_{\text{exp}})$ for pions (a), kaons (b) and protons (c) mass hypotheses in Pb–Pb collisions at $\sqrt{s_{NN}} = 5.36$ TeV.	114
5.20	Particle mass extracted from the time-of-flight measurement in Pb–Pb collisions at $\sqrt{s_{NN}} = 5.36$ TeV.	115
5.21	(a) Particle β as a function of the momentum and (b) particle mass extracted from the time-of-flight measurement in the first Pilot Run pp collisions at $\sqrt{s} = 900$ GeV during November 2021.	116
5.22	Difference between the TOF and expected time-of-flight ($t - t_0^{\text{FT0}} - t_{\text{exp},\pi}$) for tracks with $p_T \sim 1.5$ GeV/c in $\sqrt{s} = 13.6$ TeV collected in Run 3. The event time is measured using the FT0 detector.	117
6.1	Distribution of the VZERO amplitude (left) and SPD clusters (right) in a subset of pp collisions at $\sqrt{s} = 13$ TeV considered for this analysis. VZERO and SPDClusters percentile classes are defined starting from these distributions.	123
6.2	A- vs. C-side signal in ZN (left) and ZP (right).	124
6.3	Run-by-run ZDC calibrations aligned to LHC17j A-side neutron calorimeters.	125
6.4	Signal in the neutron and proton calorimeters for the three data-taking periods after calibrations were applied.	125

- 6.5 (a) Leading energy correlation with ZN energy in VZEROM and SPClusters classes using full GEANT3 simulations with four MC generators: Pythia8, EPOS-LHC, Pythia6 and Phojet. Self-normalised quantities are shown in (b). The leading energy is defined as the energy of primary particles with $|\eta| > 8$. 126
- 6.6 Self-normalised ZN signal as a function of the self-normalised charged-particle multiplicity measured at midrapidity ($|\eta| < 0.5$) in pp collisions at $\sqrt{s} = 13$ TeV. 127
- 6.7 Sketch of the relation between effective energy, multiplicity and leading energy (ZDC). A high (low) ZDC deposit corresponds to a low (high) effective energy available for particle production, and, consequently, low (high) midrapidity multiplicity. 128
- 6.8 Self-normalised ZN signal as a function of the self-normalised charged-particle multiplicity measured at midrapidity in pp collisions at $\sqrt{s} = 13$ TeV in all double-differential classes defined in this analysis. 130
- 6.9 Distributions of SPD tracklets (a proxy for charged particle multiplicity) and ZN energy for the Standalone class. 131
- 6.10 Distributions of SPD tracklets (a proxy for charged particle multiplicity) and ZN energy for the High Multiplicity class. 131
- 6.11 Distributions of SPD tracklets (a proxy for charged particle multiplicity) and ZN energy for the Low Multiplicity class. 132
- 6.12 Distributions of SPD tracklets (a proxy for charged particle multiplicity) and ZN energy for the High ZN class. 132
- 6.13 Distributions of SPD tracklets (a proxy for charged particle multiplicity) and ZN energy for the Low ZN class. 133
- 6.14 Charged and neutral kaons yields self-normalised to MB in VZEROM (a), RefMultEta5 (b), SPDClusters (c) and VZEROM + SPDClusters (d). 136
- 6.15 Pictorial representation of the topological variables used to identify V^0 and cascade candidates. 139
- 6.16 Invariant mass distributions for V^0 s: K_S^0 (a), Λ (b), $\bar{\Lambda}$ (c) in different p_T intervals. The candidates are reconstructed in $|y| < 0.5$. The red and grey areas delimited by the short-dashed lines are used for signal extraction in the bin counting procedure. The red dashed lines represent the preliminary fit to the invariant mass distributions used to define signal and background regions. 143
- 6.17 Peak positions retrieved from the signal extraction procedure for K_S^0 (a), Λ (b), $\bar{\Lambda}$ (c) as a function of p_T . The error bars correspond to the peak widths. 144

6.18	Invariant mass distributions for Cascades Ξ^- (a) and Ξ^+ (b) in different p_T intervals. The candidates are reconstructed in $ y < 0.5$. The red and grey areas delimited by the short-dashed lines are used for signal extraction in the bin counting procedure. The red dashed lines represent the preliminary fit to the invariant mass distributions used to define signal and background regions.	145
6.19	Peak positions retrieved from the signal extraction procedure for Ξ^- (a), and Ξ^+ (b) as a function of p_T . The error bars correspond to the peak widths. . .	145
6.20	Raw p_T spectra for K_S^0 (a), Λ (b), $\bar{\Lambda}$ (c) normalised to the number of events in the Standalone class.	146
6.21	Raw p_T spectra for Ξ^- (a), Ξ^+ (b) normalised to the number of events in the Standalone class.	147
6.22	Feed-down efficiency for Λ (a) and $\bar{\Lambda}$ (b) spectra obtained in the MB sample using the “ <i>MC Ratio</i> ” method.	148
6.23	Feed-down fraction removed in the Λ (a) and $\bar{\Lambda}$ (b) spectra obtained in the MB sample using the two different methods described in the text.	149
6.24	Feed-down fraction removed in the Λ and $\bar{\Lambda}$ spectra obtained as a function of VZERO multiplicity using the “ <i>MC Ratio</i> ” method.	149
6.25	Efficiency of K_S^0 (a), Λ ($\bar{\Lambda}$) (b), Ξ^- (Ξ^+) (c), as a function of p_T used in this analysis.	151
6.26	Efficiency of K_S^0 (a), Λ (b), Ξ^- (c), as a function of p_T in 3 VZEROM percentile classes compared to the MB one, used in this analysis.	152
6.27	Ratios of efficiency \times acceptance corrections with and without the GEANT4/GEANT3 correction for anti-particles $\bar{\Lambda}$ (a) and Ξ^+ (b).	153
6.28	Comparison of measured p_T shapes re-generated starting from Levy-Tsallis fits with the Monte Carlo p_T input distributions for $\Xi^- + \Xi^+$ in the Standalone event class.	154
6.29	Results from the iterative procedure relative to $\Xi^- + \Xi^+$ spectra in the Standalone event class. See text for more details. The bottom-right panels show the correction factors obtained at each iteration. The remaining panels show the ratio of the corrected spectra over the new MC input p_T shape for the three MC simulations.	156
6.30	Signal loss correction factors for K_S^0 (a), $\Lambda + \bar{\Lambda}$ (b), $\Xi^- + \Xi^+$ (c) in the Standalone Class selection.	158
6.31	Summary of the systematic uncertainties on the p_T spectra of K_S^0 (a), $\Lambda + \bar{\Lambda}$ (b) and $\Xi^- + \Xi^+$ (c) in the INEL>0 data sample.	163

6.32	Results from the fitting procedure of the spectra of $\Lambda + \bar{\Lambda}$ and $\Xi^- + \bar{\Xi}^+$ using different functional forms for the Standalone class.	164
6.33	Summary of the uncorrelated systematic uncertainties on the integrated yields for K_S^0 (a), $\Lambda + \bar{\Lambda}$ (b) and $\Xi^- + \bar{\Xi}^+$ (c) studied in the Standalone class selection. The contribution from the variation of selections and extrapolations is reported in blue and red, respectively. The total contribution is reported in black.	166
6.34	Comparison for different periods of the $\langle ZN \rangle$ for double differential SPDClusters + VZEROM selections. SPDClusters percentile selections are reported in the x-axis, while VZEROM is varied from top (VZEROM 70-100%) to bottom (0-10%).	167
7.1	Transverse momentum distribution of K_S^0 (a), Λ (b), and Ξ (c) in pp collisions at $\sqrt{s} = 13$ TeV in the Standalone selection (VZEROM classes). Statistical and total systematic uncertainties are shown by error bars and boxes, respectively. In the bottom panels ratios of the spectra to $INEL > 0$ are shown. The spectra are scaled by different factors to improve the visibility.	170
7.2	Transverse momentum distribution of Ξ in pp collisions at $\sqrt{s} = 13$ TeV in the High Multiplicity (a) and High ZN (b) selections (SPDClusters+VZEROM classes). The bottom panels show ratios of the two most extreme selections in the event class to the central one. The spectra are scaled by different factors to improve the visibility.	171
7.3	Transverse momentum distribution of Λ in pp collisions at $\sqrt{s} = 13$ TeV in the High Multiplicity (a) and High ZN (b) selections (SPDClusters+VZEROM classes). The bottom panels show ratios of the two most extreme selections in the event class to the central one. The spectra are scaled by different factors to improve the visibility.	172
7.4	Transverse momentum distribution of K_S^0 in pp collisions at $\sqrt{s} = 13$ TeV in the High Multiplicity (a) and High ZN (b) selections (SPDClusters+VZEROM classes). The bottom panels show ratios of the two most extreme selections in the event class to the central one. The spectra are scaled by different factors to improve the visibility.	173
7.5	Self-normalised yield ratios of K_S^0 , Λ , and Ξ in pp collisions at $\sqrt{s} = 13$ TeV in the Standalone selection (VZEROM classes). The ratios are shown as a function of the charged-particle multiplicity (left) and ZN energy (right) self-normalised to the minimum-bias $INEL > 0$ value. Statistical and total systematic uncertainties are shown by error bars and boxes, respectively. . .	175

7.6	Self-normalised yield ratios of K_S^0 , Λ , and Ξ in pp collisions at $\sqrt{s} = 13$ TeV in the High ZN and Low ZN selection (VZEROM+SPDClusters classes). The ratios are shown as a function of the charged-particle multiplicity (left) and ZN energy (right) self-normalised to the minimum-bias INEL > 0 value. Statistical and total systematic uncertainties are shown by error bars and boxes, respectively.	176
7.7	Self-normalised yield ratios of K_S^0 , Λ , and Ξ in pp collisions at $\sqrt{s} = 13$ TeV in the High Multiplicity and Low Multiplicity selection (VZEROM+SPDClusters classes). The ratios are shown as a function of the charged-particle multiplicity (left) and ZN energy (right) self-normalised to the minimum-bias INEL > 0 value. Statistical and total systematic uncertainties are shown by error bars and boxes, respectively.	178
7.8	Self-normalised ZN signal as a function of the self-normalised charged-particle multiplicity measured at midrapidity compared with model predictions. The PYTHIA8 Monash tune and with colour ropes are shown as a dashed and full line, respectively.	180
7.9	Average number of MPI as a function of the midrapidity multiplicity (left) and of the leading energy in the ZN acceptance (right) in the different multi-differential classes introduced in this work.	182
7.10	Average transverse momentum of charged pions as a function of the midrapidity multiplicity (left) and of the leading energy in the ZN acceptance (right) in the different multi-differential classes introduced in this work.	183
7.11	Self-normalised yield ratios of K_S^0 , Λ , and Ξ in pp collisions at $\sqrt{s} = 13$ TeV in the Standalone selection (VZEROM classes). The PYTHIA8 Monash generator and with colour ropes are shown with a dashed and full lines respectively.	184
7.12	Self-normalised yield ratios of K_S^0 in pp collisions at $\sqrt{s} = 13$ TeV in the Standalone, High Multiplicity, Low Multiplicity, High ZN and Low ZN selections compared to PYTHIA Monash and PYTHIA colour ropes results. The classes at fixed multiplicity are displayed in the top panels, and the classes at fixed leading energy are displayed in the bottom panels. The PYTHIA8 Monash generator without and with colour ropes are shown with dashed and full lines, respectively.	185

7.13	Self-normalised yield ratios of Λ in pp collisions at $\sqrt{s} = 13$ TeV in the Standalone, High Multiplicity, Low Multiplicity, High ZN and Low ZN selections compared to PYTHIA Monash and PYTHIA colour ropes results. The classes at fixed multiplicity are displayed in the top panels, and the classes at fixed leading energy are displayed in the bottom panels. The PYTHIA8 Monash generator without and with colour ropes are shown with dashed and full lines, respectively.	186
7.14	Self-normalised yield ratios of Ξ in pp collisions at $\sqrt{s} = 13$ TeV in the Standalone, High Multiplicity, Low Multiplicity, High ZN and Low ZN selections compared to PYTHIA Monash and PYTHIA colour ropes results. The classes at fixed multiplicity are displayed in the top panels, and the classes at fixed leading energy are displayed in the bottom panels. The PYTHIA8 Monash generator without and with colour ropes are shown with dashed and full lines, respectively.	187
8.1	Invariant mass distributions of $\Omega^- + \overline{\Omega}^+$ candidates in pp collisions at 13.6 TeV in the inclusive minimum bias INEL > 0 sample. Different plots refer to different p_T intervals, as indicated in the titles of the plots. The total fit function is shown in blue, the Gaussian functions in red and magenta, and the second degree polynomial as a black dotted line. The two vertical lines represent the outer limits of the invariant mass region from which the signal is extracted.	196
8.2	Invariant mass distributions of $\Omega^- + \overline{\Omega}^+$ candidates in pp collisions at 900 GeV in the inclusive minimum bias INEL > 0 sample. Different plots refer to different p_T intervals, as indicated in the titles of the plots. The total fit function is shown in blue, the Gaussian function in magenta, and the first degree polynomial as a black dotted line. The two vertical lines represent the outer limits of the invariant mass region from which the signal is extracted.	197
8.3	Raw yields of $\Omega^- + \overline{\Omega}^+$ for the 13.6 TeV (a) and 900 GeV (b) analyses. The bottom panels show the ratios between the values obtained in the different FT0M multiplicity classes and those obtained in the inclusive INEL > 0 selection.	198
8.4	Efficiency \times acceptance of $\Omega^- + \overline{\Omega}^+$ as a function of p_T for the 13.6 TeV (a) and 900 GeV (b) analyses.	198
8.5	Sketch of the event loss, signal loss and event splitting effects.	199
8.6	Event factor for the 13.6 TeV (a) and for the 900 GeV (b) analysis.	200
8.7	Signal loss correction for the 13.6 TeV (a) and for the 900 GeV (b) analysis.	201

8.8	Distributions of the deviation of the efficiency-corrected $\Omega^- + \overline{\Omega}^+$ yields obtained with default selections over the ones obtained with varied cuts in three p_T bins. The distributions, populated with 500 trials, are fitted with a Gaussian function, and the standard deviation is considered as a systematic uncertainty.	203
8.9	Distribution of relative deviation of integrated yields using multi-trials with respect to the ones using the default selections. The distribution is fitted with a Gaussian function.	204
8.10	Relative systematic uncertainty associated with the choice of the fit function. The uncertainty is given by the half-difference between the maximum extrapolated yield and the minimum extrapolated yield obtained with different fit functions.	205
8.11	Transverse momentum distribution of Ω in pp collisions at $\sqrt{s} = 13.6$ TeV for multiplicity classes selected using the FT0 detector. Statistical and total systematic uncertainties are shown by error bars and boxes, respectively. In the bottom panels, ratios of multiplicity dependent spectra to $\text{INEL} > 0$ are shown. The spectra are scaled by different factors to improve the visibility. .	206
8.12	Transverse momentum distribution of Ω in pp collisions at $\sqrt{s} = 900$ GeV for multiplicity classes selected using the FT0 detector. Statistical and total systematic uncertainties are shown by error bars and boxes, respectively. In the bottom panels, ratios of multiplicity dependent spectra to $\text{INEL} > 0$ are shown. The spectra are scaled by different factors to improve the visibility. .	207
8.13	Transverse momentum distribution of Ω in pp collisions at $\sqrt{s} = 900$ GeV for the inclusive $\text{INEL} > 0$ compared to the PYTHIA8 Monash tune, PYTHIA8 color ropes and EPOS-LHC event generators.	208
8.14	Statistical uncertainty reached in Run 2 [137] compared to the one reached with this analysis in Run 3 neglecting MC efficiency errors.	208
8.15	Ω/π ratio measured in Run 3 in pp collisions at $\sqrt{s} = 13.6$ and 0.9 TeV, compared to Run 1 measurement at $\sqrt{s} = 7$ TeV [138].	209
A.1	Distribution of the <i>ZDC Energy Sum</i> variable for the 2015 dataset. The events are grouped in percentile classes which reflect the fraction of events in each region over the total number. The pseudo-peaks visible in the region marked as 0-20 %, are fluctuations on the small energy deposit in the ZDC, which are almost empty in that range (pedestal effect).	228

A.2	(a) Cumulative distribution of the fraction of events in each bin of the distribution in Fig. A.1 over the total number of entries. (b) ZDC percentile distribution for all events.	228
A.3	Raw p_T spectra for K_S^0 normalised by the number of events in the High Multiplicity (a), Low Multiplicity (b), High ZN (c), Low ZN (d) event classes.	230
A.4	Raw p_T spectra for Λ normalised by the number of events in the High Multiplicity (a), Low Multiplicity (b), High ZN (c), Low ZN (d) event classes.	231
A.5	Raw p_T spectra for $\bar{\Lambda}$ normalised by the number of events in the High Multiplicity (a), Low Multiplicity (b), High ZN (c), Low ZN (d) event classes.	232
A.6	Raw p_T spectra for Ξ^- normalised by the number of events in the High Multiplicity (a), Low Multiplicity (b), High ZN (c), Low ZN (d) event classes.	233
A.7	Raw p_T spectra for $\bar{\Xi}^+$ normalised by the number of events in the High Multiplicity (a), Low Multiplicity (b), High ZN (c), Low ZN (d) event classes.	234
A.8	(a) Comparison of measured p_T shapes re-generated starting from Levy-Tsallis fits with the Monte Carlo p_T input distributions for $\Xi^- + \bar{\Xi}^+$ in the High Multiplicity event class. (b), (c), (d) Results from the iterative procedure relative to $\Xi^- + \bar{\Xi}^+$ spectra, see text for more details.	236
A.9	(a) Comparison of measured p_T shapes re-generated starting from Levy-Tsallis fits with the Monte Carlo p_T input distributions for $\Xi^- + \bar{\Xi}^+$ in the Low Multiplicity event class. (b), (c), (d) Results from the iterative procedure relative to $\Xi^- + \bar{\Xi}^+$ spectra, see text for more details.	238
A.10	(a) Comparison of measured p_T shapes re-generated starting from Levy-Tsallis fits with the Monte Carlo p_T input distributions for $\Xi^- + \bar{\Xi}^+$ in the High ZN event class. (b), (c), (d) Results from the iterative procedure relative to $\Xi^- + \bar{\Xi}^+$ spectra, see text for more details.	240
A.11	(a) Comparison of measured p_T shapes re-generated starting from Levy-Tsallis fits with the Monte Carlo p_T input distributions for $\Xi^- + \bar{\Xi}^+$ in the Low ZN event class. (b), (c), (d) Results from the iterative procedure relative to $\Xi^- + \bar{\Xi}^+$ spectra, see text for more details.	242
A.12	Signal loss correction factors for K_S^0 in the High Multiplicity (a), Low Multiplicity (b), High ZN (c) and Low ZN (d) Class selection.	243
A.13	Signal loss correction factors for Λ in the High Multiplicity (a), Low Multiplicity (b), High ZN (c) and Low ZN (d) Class selection.	244
A.14	Signal loss correction factors for Ξ in the High Multiplicity (a), Low Multiplicity (b), High ZN (c) and Low ZN (d) Class selection.	245

A.15	Summary of the uncorrelated systematic uncertainties on the integrated yields for K_S^0 studied in the High Multiplicity (a), Low Multiplicity (b), High ZN (c) and Low ZN (d) selections. The contribution from the variation of selections and extrapolations is reported in blue and red, respectively. The total contribution is reported in black.	246
A.16	Summary of the uncorrelated systematic uncertainties on the integrated yields for $\Lambda + \bar{\Lambda}$ studied in the High Multiplicity (a), Low Multiplicity (b), High ZN (c) and Low ZN (d) selections. The contribution from the variation of selections and extrapolations is reported in blue and red, respectively. The total contribution is reported in black.	247
A.17	Summary of the uncorrelated systematic uncertainties on the integrated yields for $\Xi^- + \bar{\Xi}^+$ studied in the High Multiplicity (a), Low Multiplicity (b), High ZN (c) and Low ZN (d) selections. The contribution from the variation of selections and extrapolations is reported in blue and red, respectively. The total contribution is reported in black.	248
B.1	Transverse momentum distribution of Ξ in pp collisions at $\sqrt{s} = 13$ TeV in the Low Multiplicity (a) and Low ZN (b) selections (SPDClusters+VZEROM classes). The bottom panels show ratios of the two most extreme selections in the event class to the central one. The spectra are scaled by different factors to improve the visibility.	249
B.2	Transverse momentum distribution of Λ in pp collisions at $\sqrt{s} = 13$ TeV in the Low Multiplicity (a) and Low ZN (b) selections (SPDClusters+VZEROM classes). The bottom panels show ratios of the two most extreme selections in the event class to the central one. The spectra are scaled by different factors to improve the visibility.	250
B.3	Transverse momentum distribution of K_S^0 in pp collisions at $\sqrt{s} = 13$ TeV in the Low Multiplicity (a) and Low ZN (b) selections (SPDClusters+VZEROM classes). The bottom panels show ratios of the two most extreme selections in the event class to the central one. The spectra are scaled by different factors to improve the visibility.	250

List of tables

4.1	Collision systems and energies at the LHC Run 1, 2 and 3. Run 3 energies are in bold.	67
4.2	Main characteristics of the ITS layers [99].	71
6.1	Average values of $dN_{\text{ch}}/d\eta$ and ZN energy for each event class.	134
6.2	Properties of K_S^0 , Λ and Ξ strange hadrons. The valence quark content, the mass, the main decay channel, their branching ratio (B.R.), and $c\tau$ are listed with the respective errors. The values are reported from [135].	137
6.3	Selections applied to K_S^0 , Λ and $\bar{\Lambda}$ candidates.	141
6.4	Selections applied to Ξ^- and Ξ^+ candidates.	142
6.5	Event loss corrections.	157
6.6	Variation of selections applied to K_S^0 candidates.	160
6.7	Variation of selections applied to Λ and $\bar{\Lambda}$ candidates.	160
6.8	Selections applied to Ξ^- and Ξ^+ candidates.	160
6.9	Main sources of systematic uncertainties (expressed in %) of the p_T differential yields, reported for low, intermediate and high p_T . These values are calculated for the $\text{INEL}>0$ data sample. Results in other classes are further affected by an uncertainty originating from the multiplicity dependence of the efficiency (2%) and, in the case of the Λ , of the feed-down contributions (2%).	162
8.1	Selections applied to identify Ω among the reconstructed cascade candidates.	194
8.2	The selections applied to $\Omega^- + \bar{\Omega}^+$ candidates are varied simultaneously within the limits reported in this table.	202

- 8.3 Main sources of systematic uncertainties (expressed in %) of the p_T differential yields, reported for low, intermediate and high p_T . The multi-trial approach includes topological and track quality selections, TPC energy loss selection, competing cascade decay rejection and the cut on the proper lifetime of the candidate. These values are calculated for the $\text{INEL}>0$ data sample, results in other classes are further affected by an uncertainty originating from the multiplicity dependence of the efficiency (2%). 204

Introduction

Strangeness enhancement, i.e. the enhanced production of strange hadrons in heavy-ion collisions compared to minimum-bias pp collisions, was historically considered one of the first signatures of quark-gluon plasma formation. At the LHC, the ALICE experiment demonstrated that small systems, such as pp and p-Pb, show striking similarities with Pb-Pb collisions when multiplicity dependent studies are performed. Notably, the ratio of strange to non-strange hadron yields increases with the charged-particle production at midrapidity, starting from pp collisions and smoothly evolving across interaction systems and energies, ultimately reaching Pb-Pb collisions. One of the main challenges in high-energy hadron physics remains the understanding of the origin of strangeness enhancement with multiplicity in small collision systems. This thesis exploits a novel approach to study strangeness production in pp collisions, introducing, for the first time, the concept of effective energy in hadronic interactions at the LHC.

In pp collisions, the emission of leading baryons at very forward rapidity reduces the effective energy available for particle production with respect to the nominal centre-of-mass energy. This phenomenon, known as leading effect, was extensively studied by past experiments at the CERN ISR (Intersecting Storage Rings) [1–9]. There, the correlation between the effective energy and collision event properties such as the charged-particle multiplicity was investigated in detail to shed light on the universal features of the QCD. In particular, in pp collisions, the charged-particle multiplicity at a fixed centre-of-mass energy is observed to be systematically lower than in e^+e^- at the same energy. However, a universal dependence can be found if the appropriate definition of the energy available for particle production, i.e. effective energy, is used. One way of estimating the effective energy event-by-event, is by measuring the energy of the leading baryons produced at very forward rapidities in each event hemisphere. This kind of analysis requires a detector able to measure particles with large longitudinal momenta with a good energy resolution. The ALICE experiment at CERN is well suited for this kind of measurement thanks to the Zero Degree Calorimeters (ZDC), dedicated detectors built to measure the energy of spectator nucleons in heavy-ion collisions. In this work, the ZDC are used to measure the energy carried by

leading baryons in pp collisions, providing an indirect measurement of the effective energy ($E_{\text{eff}} \simeq \sqrt{s} - E_{\text{ZDC}}$). This work complements previous studies on strange hadron production at midrapidity in pp collisions, performing an analysis as a function of the local charged-particle multiplicity and of the forward (leading) energy. This study provides new insights into the interplay, for strangeness production, between the initial stages of the collision and the produced final hadronic state. In fact, the particle production at midrapidity and the ZDC energy are measured in rapidity regions that are causally disconnected in the evolution of the system. In this analysis, the production of K_S^0 strange mesons, Λ ($\bar{\Lambda}$) strange baryons, and Ξ^- ($\bar{\Xi}^+$) multi-strange baryons is studied using pp collision data at $\sqrt{s} = 13$ TeV collected with the ALICE experiment in 2015, 2017 and 2018, with optimal run conditions for the ZDC data-taking.

Finally, this thesis presents the first Run 3 results on the production of Ω^- ($\bar{\Omega}^+$) multi-strange baryons in pp collisions at $\sqrt{s} = 13.6$ TeV and $\sqrt{s} = 900$ GeV, the highest and lowest collision energies reached so far at the LHC. In particular, the first ALICE measurement of Ω production in pp collisions at $\sqrt{s} = 900$ GeV is presented, complementing the results of lighter strange hadrons obtained in Run 1 at the same collision energy.

Most of the results discussed in this thesis were approved by the ALICE Collaboration and were presented at several international conferences [10, 11]. An article describing the results presented in this work is in preparation.

This thesis is organised in eight chapters. The first one is dedicated to the physics of heavy-ion collisions and to the observables that can be used to access the dynamic and thermal properties of the quark-gluon-plasma (QGP). The second chapter is focused on strangeness production in high energy hadronic collisions, discussing the state of the art and the motivations at the basis of the work carried out in this thesis. The third chapter focuses on the concept of effective energy, presenting an historical overview of the results on the leading effect obtained by past experiments at lower collision energies. The fourth chapter presents a detailed description of the ALICE detector with particular emphasis on the Zero Degree Calorimeters. The fifth chapter describes the work carried out on the Time-Of-Flight system, started during the Long Shutdown 2 (LS2), which allowed to monitor the data quality and performance of the detector during the Run 3 data-taking. The sixth chapter describes the analysis strategy used in this thesis, discussing details on the event selection, the particle identification techniques, and the systematic uncertainties. The seventh chapter presents the results on the production of K_S^0 , Λ , and Ξ in pp collisions at $\sqrt{s} = 13$ TeV as a function of the charged-particle multiplicity and the ZDC energy. Finally, the eighth chapter presents

the first Run 3 results on Ω production in pp collisions at $\sqrt{s} = 13.6$ TeV and 900 GeV, as well as a discussion on the perspectives for future analysis on strangeness production in pp collisions in Run 3 and beyond.

Chapter 1

High energy nuclear physics

The strong interaction between quarks and gluons, the elementary constituents of the hadronic matter, is described by Quantum Chromo-Dynamics (QCD). Under extreme conditions of high temperature and energy density, the QCD predicts a transition of the strongly interacting matter from the hadronic phase to a colour deconfined medium, called quark–gluon plasma (QGP). The QCD phase transition can be investigated in the laboratory through ultra-relativistic heavy-ion collisions by reproducing the temperature, pressure and energy density conditions that lead to the QGP formation. The product of the collision is a “fireball” in local thermal equilibrium that rapidly expands and cools down. The development of the fireball produced in heavy-ion collisions is expected to reproduce the evolution stages of the early Universe, when the partonic deconfined matter turned into confined hadrons, few μs after the Big Bang. In smaller systems like pp collisions, the initial energy density and system size are significantly lower, making it challenging to create and sustain a QGP-like state for a sufficient duration. However, the measurement of effects reminiscent of heavy-ion phenomenology in smaller systems has opened the opportunity to further extend our understanding of the underlying physics of high-energy hadronic collisions.

1.1 An introduction to QCD

The historical foundations of QCD date back to the early days of nuclear physics, when the binding energy of the nucleus was realised to be due to a new kind of interaction between nucleons. Scattering experiments then showed that this interaction had the properties of being very strong, but to act only over very short distances. The QCD is a non-Abelian quantum gauge field theory based on the invariance under local $SU(3)$ colour group transformations. This is embedded in the Standard Model (SM) of elementary particle physics with underlying gauge group $SU(3)_C \times SU(2)_L \times U(1)_Y$. The conserved charge of QCD is the colour charge,

which can assume three values: red, green, and blue. The colour interaction is mediated by eight massless coloured gauge bosons, the gluons. The general form of the QCD Lagrangian can be written as [12]:

$$\mathcal{L}_{QCD} = -\frac{1}{4}F_{\mu\nu}^a F_a^{\mu\nu} + \sum_q \bar{q}_i (i\gamma^\mu D_\mu - m_q)_{ij} q_j \quad (1.1)$$

where sums over repeated indices are implied. In the Lagrangian q_i is the field of a quark with flavour q , colour i and mass $(m_q)_{ij} = m_q \delta_{ij}$. The field strength tensor $F_{\mu\nu}^a$ and the covariant derivative $(D_\mu)_{ij}$ can be written as a function of the gluon fields $A_{\mu\nu}^a$ (with $a = 1, \dots, 8$) and the strong field coupling constant g_S :

$$F_{\mu\nu}^a = \partial_\mu A_\nu^a - \partial_\nu A_\mu^a - g_S f^{abc} A_\mu^b A_\nu^c \quad (1.2)$$

$$(D^\mu)_{ij} = \delta_{ij} \partial_\mu - ig_S T_{ij}^a A_\mu^a \quad (1.3)$$

where f^{abc} are the structure constants and $T^a = \lambda_a/2$ the generators of the Lie group which defines the gauge symmetry, with λ_a being the Gell-Mann matrices. The free parameters of the theory are the mass terms and the coupling constant g_S . The gluonic part derived from the field strength tensor consists of a free field term and two interaction terms where gluons couple to gluons. This coupling between gauge bosons is characteristic of a gauge theory based on a non-abelian group where the gauge bosons carry the charge of the interaction and thus can couple directly to themselves. As a consequence, the strong interactions not only have Feynman diagrams with quark loops but also gluon loops. The former leads to charge screening, making the force weaker at short distances, but also gluon loops, which lead to charge anti-screening, dominant in QCD, causing a stronger force at large distances. These diagrams are shown in Fig. 1.1. The fermionic part of the Lagrangian is a sum over all quarks flavours, containing a free field term and a term for the quark-gluon coupling. The amplitudes associated with the individual couplings depend on the detailed structure of the underlying symmetry group.

1.1.1 The running coupling α_S

The adimensional value g_S quantifies the intensity of the strong interaction and is defined as $g_S = \sqrt{4\pi\alpha_S}$, with α_S the strong coupling. A fundamental consequence of quarks and gluons loops in QCD is that α_S evolves with the transferred momentum Q . The corresponding trend has been measured experimentally and compared in Fig. 1.2 with predictions. In particular,

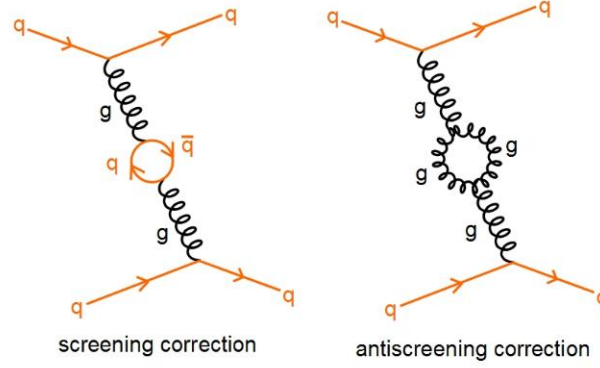


Fig. 1.1 Feynman diagrams of the strong interaction with quark loops (“charge screening”) and gluon loops (“charge anti-screening”).

the coupling runs such that it is small for increasing momentum transfers, $Q \gg \Lambda_{QCD}$, and large for small momentum transfers. To leading order one can write [12]:

$$\alpha_S(Q^2) \equiv \frac{g_S^2(Q^2)}{4\pi} = \frac{1}{\beta_0 \ln(Q^2/\Lambda_{QCD}^2)} \quad (1.4)$$

where Λ_{QCD} is the energy scale at which non-perturbative effects become significant. The evolution of the coupling is described by the β -function obtained from its renormalisation group equation (RGE) [12]. The corresponding potential has a completely different shape than the other fundamental interactions and can be expressed as a short range Coulomb-like term plus a long range linear term:

$$V_{QCD} = -\frac{4}{3} \frac{\alpha_S}{r} + kr \quad (1.5)$$

where r is the distance between colour charges generating the colour field and $k \approx 1$ GeV/fm. It is therefore possible to distinguish two different regimes in the strong interaction, at large and at short distances, known respectively as *confinement* and *asymptotic freedom*. In the large momentum transfer region (short distance), the weak coupling allows the use of perturbative methods to study QCD; however, perturbation theory cannot be used in the low- Q regions (large distance), where the coupling becomes stronger. In this case, the necessary tool to carry out such calculations is Lattice Quantum Chromodynamics (LQCD).

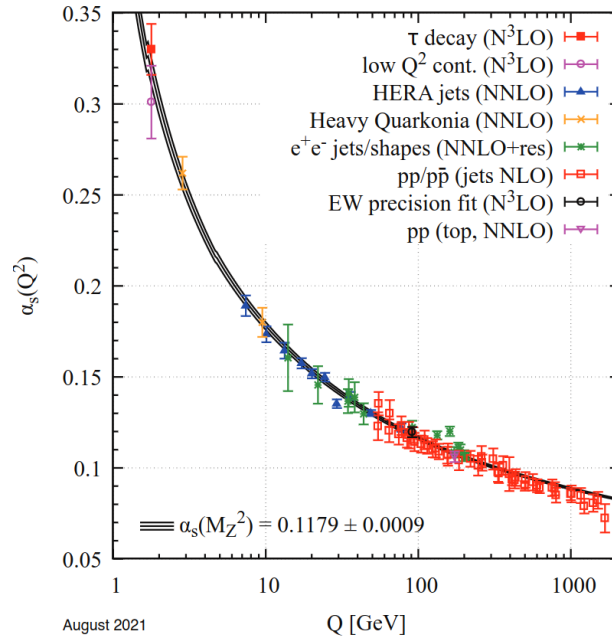


Fig. 1.2 Summary of α_s measurements as a function of the energy scale Q . Different colours indicate different measurements used to extract the α_s values. The QCD perturbation theory order used to extract α_s is indicated in parentheses. Figure from [13].

1.1.2 The QCD phase transition

Lattice QCD predicts a phase transition from a state in which quarks and gluons are confined into hadrons to a state in which they are deconfined: the quark-gluon plasma (QGP). A phase transition is a transformation of a thermodynamic system from one state of matter to another, where the properties of the medium rapidly change, continuously or discontinuously. Paul Ehrenfest's classification of phase transitions is based on the behaviour of the thermodynamic free energy as a function of other thermodynamic variables [14]:

- first order phase transition: characterised by a discontinuity in the first derivative of the free energy with respect to some thermodynamic variable (e.g. T);
- second order phase transition: characterised by a discontinuity in higher than first order derivatives of the free energy as a function of some thermodynamic variable (e.g. T);
- analytic crossover: characterised by the free energy and all its derivatives to be continuous at a critical value of the thermodynamic variable (e.g. T_c). In this case, the system changes smoothly from one phase to the other.

The phases of QCD matter can be summarised in a phase diagram as a function of the temperature T and the baryo-chemical potential μ_B , as displayed in Fig. 1.3. The baryo-

chemical potential is defined as the energy needed to increase by one unity the total number of baryons in a system (N_B):

$$\mu_B = \frac{\partial E}{\partial N_B}, \quad N_B = N(B) - N(\bar{B}) \quad (1.6)$$

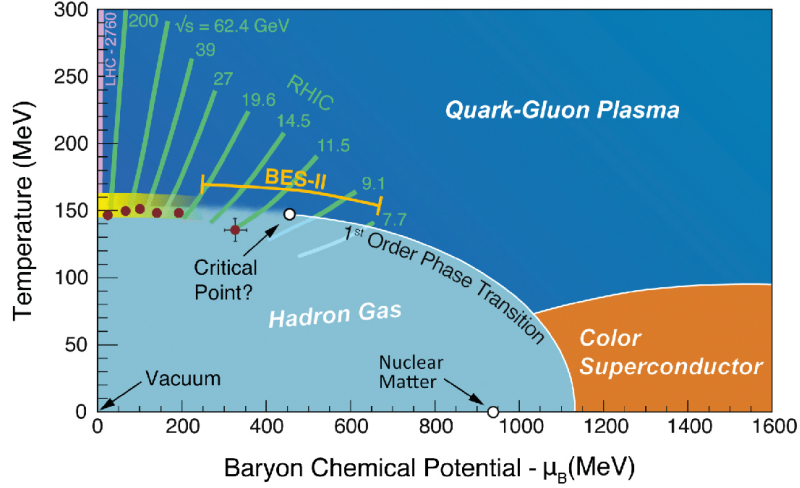


Fig. 1.3 QCD phase diagram.

The point at $T = 0$ MeV and $\mu_B = 0$ MeV corresponds to the QCD vacuum. Low temperatures and low baryo-chemical potential values ($T \approx 0$ and $\mu_B \approx 1$ GeV) in the diagram correspond to the ordinary nuclear matter. By moving towards higher temperatures the diagram reaches a phase of hadronic gas (HG) where nucleons interact and form hadrons. The deconfined phase of quark-gluon plasma is reached by further increasing temperature and energy density. At small values of T and large values of μ_B a transition to a Colour Superconductor phase is expected: this state of matter may be present in the core of the neutron stars [15]. At the LHC energies the region at $\mu_B \approx 0$ is investigated, where from lattice calculations, the transition of matter to the QGP occurs as a crossover at a temperature of $T \approx 154 - 174$ MeV [16]. The phase transition at larger values of μ_B can be studied at smaller centre of mass energies. Figure 1.4 shows the results of the Beam Energy Scan (BES) performed at RHIC, where the centrality dependence of the chemical freeze-out temperature as a function of the baryo-chemical potential for Au-Au collisions is displayed from 200 GeV to the lowest measured energy at 7.7 GeV.

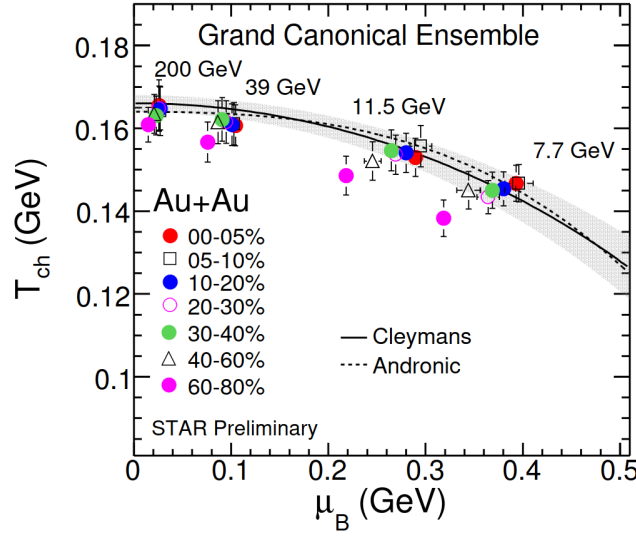


Fig. 1.4 Variation of T_{ch} with μ_B , fitted with the Grand Canonical approach in the THERMUS Model using all available particle ratios. Figure from [17].

1.1.3 Chiral symmetry in QCD

The phase transition is also characterised by changes in the symmetries of the system. In particular, it is found that such a crossover occurs in coincidence with a partial chiral symmetry restoration. To explain this concept, it is convenient to introduce the left- and right-handed projectors:

$$\gamma_L = \frac{1}{2}(1 - \gamma_5), \quad \gamma_R = \frac{1}{2}(1 + \gamma_5) \quad (1.7)$$

which satisfy the relations $\gamma_L^2 = \gamma_L$, $\gamma_R^2 = \gamma_R$ and $\gamma_L \gamma_R = 0$. We may decompose the quark fields from Eq. 1.1 into left- and right-handed components, $q_R = \gamma_R q$, $q_L = \gamma_L q$. A symmetry which acts separately on left- and right-handed fields is called a chiral symmetry. In the massless limit, these correspond to the positive and negative helicity states. Chiral symmetry is not apparent in QCD, if it was every hadron would be accompanied by a partner of opposite parity with the same mass and quantum numbers, instead it is spontaneously broken. Spontaneous breaking of a symmetry occurs when the ground state of the theory (the vacuum) is not invariant under the group of symmetry transformations. In QCD, the vacuum has a non-zero expectation value of the light-quark operator $\bar{q}q$ (referred to as a quark condensate):

$$\langle 0 | \bar{q}q | 0 \rangle = \langle 0 | (\bar{u}u + \bar{d}d) | 0 \rangle \simeq (250 \text{ MeV})^3 \quad (1.8)$$

Since the condensate connects left- and right-handed fields:

$$\langle 0 | \bar{q}q | 0 \rangle \equiv \langle 0 | (\bar{q}_R q_L + \bar{q}_L q_R) | 0 \rangle \quad (1.9)$$

the vacuum is not invariant under chiral rotations and it breaks the symmetry. If an exact symmetry of the Lagrangian is spontaneously broken, the theory will contain massless spin-zero particles called Goldstone bosons. According to the Goldstone theorem, the number of such particles will be equal to the number of spontaneously broken symmetry generators. In the case of chiral SU(2) breaking, this implies three pseudoscalar bosons, which are the three pions π^+ , π^- and π^0 in the massless quark limit. However, the light quark masses are not precisely zero, and therefore the chiral symmetry of the QCD Lagrangian is not exact. Nevertheless, the masses are small on the scale of strong interactions ($m_u \simeq 4$ MeV, $m_d \simeq 7$ MeV) and may be treated as a perturbation, therefore, the pions are not massless Goldstone bosons but their masses are much smaller than those of other hadrons. Similarly, considering also the strange quark mass ($m_s \simeq 100$ MeV) leads to a chiral SU(3) symmetry spontaneously breaking, with eight pseudoscalar Goldstone bosons corresponding to the flavour SU(3) octet (π^+ , π^- , π^0 , K^+ , K^- , K^0 , \bar{K}^0 and η). Chiral symmetry breaking is most apparent in the mass generation of nucleons from elementary light quarks, accounting for approximately 99% of their combined mass as baryons. As mentioned, the chiral symmetry is expected to be restored in the transition between the hadronic phase of matter and the deconfined state of plasma. As quarks become deconfined, the light quark masses go back to their bare values, an effect usually referred to as partial restoration of chiral symmetry because the masses do not go exactly to zero [18].

1.2 Heavy-ion collisions

The quark-gluon plasma can be investigated in the laboratory through ultra-relativistic heavy-ion collisions. The first heavy-ion experiments started in the 1980s at the Super Proton Synchrotron (SPS) [19] at CERN and at the Alternating Gradient Synchrotron (AGS) [20] at Brookhaven National Laboratory (BNL). There, several fixed-target experiments collected collisions at a centre-of-mass energy per nucleon-pair $\sqrt{s_{NN}}$ in the range $\approx 5 - 20$ GeV, probing the μ_B interval 200 - 500 MeV. This region is called *stopping regime*, the nucleons are stopped in the collision region, hence the net baryon density is high. Ultra-relativistic heavy-ion collisions were then studied at the Relativistic Heavy Ion Collider (RHIC) [21] since 2000 and at the Large Hadron Collider (LHC) [22] at CERN since 2010. The centre-of-mass energies per nucleon-nucleon pair reached the values of $\sqrt{s_{NN}} = 200$ GeV for Au–Au

collisions at RHIC and $\sqrt{s_{NN}} = 5.36$ TeV for Pb–Pb collisions at the LHC. At such high energies the colliding nuclei are not stopped at the collision point so the net baryon density is very small. This allows to explore the $\mu_B \approx 0$ region of the QCD phase diagram, called *Bjorken regime* or *transparency regime*.

1.2.1 Geometry of a heavy-ion collision

Since nuclei are extended objects, the volume of the interacting region depends on the impact parameter b of the collision, defined as the distance between the centres of the two colliding nuclei in the plane transverse to the beam axis. Relativistic nuclei are Lorentz contracted while travelling along the beam axis, and therefore, their transverse dimension is larger than their longitudinal dimension. A schematic picture of a heavy-ion collision is shown in Fig. 1.5. To characterise heavy-ion collisions it is useful to introduce the concept of

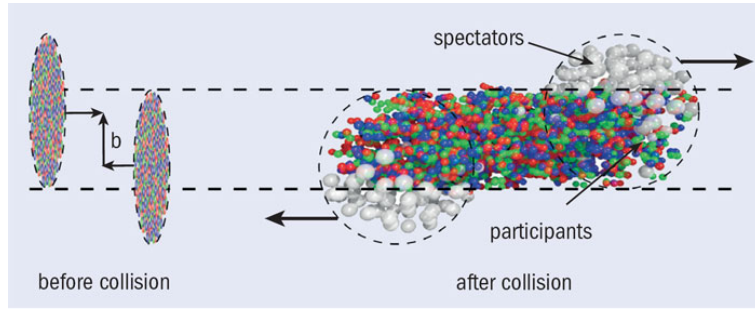


Fig. 1.5 Representation of an ultra-relativistic heavy ions collision.

centrality, which is directly related to the impact parameter. In so-called central collisions, the two nuclei collide almost head-on and almost all nucleons within the ion participate in the collision. This kind of interaction is characterised by a small impact parameter and the largest particle multiplicity production. On the contrary, a peripheral collision happens at large impact parameter. In this case, only a few nucleons interact with each other. Other useful parameters are the number of nucleons that participate in the collision, called “participants” (N_{part}), and those which do not interact, called “spectators” ($N_{\text{spect}} = 2A - N_{\text{part}}$). The Glauber model [23] relates N_{part} and N_{coll} to the impact parameter b by treating the collision of two nuclei as a superposition of individual nucleon-nucleon interactions. An example of collision simulated with such model showing participant and spectator nucleons is reported in Fig. 1.6. Centrality is usually measured by exploiting two main observables:

- the number of charged particles produced in the collision (average charged-particle multiplicity N_{ch});

- the number of spectator nucleons not involved in the collision.

In fact, neither the impact parameter nor the number of participants or the number of binary collisions N_{coll} , are directly measurable. In ALICE, during Run 1 and 2, centrality classes

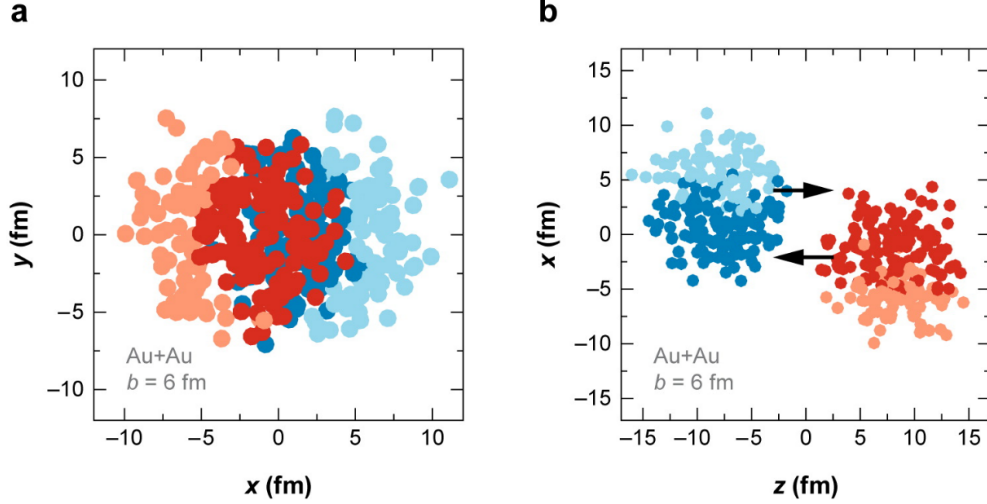


Fig. 1.6 A Glauber Monte Carlo simulation of an Au–Au collision event at $\sqrt{s_{\text{NN}}} = 200$ GeV with impact parameter $b = 6$ fm. (a) shows the transverse plane visualisation, while (b) the visualisation along the beam axis. Darker circles represent participating nucleons [23].

were defined starting from the distribution of the signal amplitudes measured by scintillators placed at forward rapidity, i.e. close to the beam axis, the VZERO detectors [24]. The signal amplitudes are proportional to the multiplicity of particles produced in the event, which is correlated to the centrality of the collision. An example of the VZERO amplitude distribution is shown in Figure 1.7. The 0-5% centrality class corresponds to the 5% of events with the highest VZERO amplitude, and the same principle applies to other classes. Centrality classes are therefore expressed via a percentage of the total hadronic interaction cross section.

1.2.2 Space-time evolution of the collision

The evolution of a heavy-ion collision is commonly described in terms of a series of stages illustrated schematically in Fig. 1.8 [22].

- At the time $t = 0$ fm/c the collision of the two nuclei takes place. As they collide, the ions will be highly Lorentz contracted, and an extremely dense region of partons deposits energy in the overlap region of the collision. The crossing time of the nuclei can be estimated as $\tau_{\text{cross}} = 2R/\gamma$, where γ is the Lorentz factor and R the radius of the nuclei ($R \simeq 7$ fm for large nuclei such as Pb and Au). The interval τ_{cross} is lower than the time-scale of strong interactions $\tau_0 = 1/\Lambda_{\text{QCD}} \simeq 1/200$ MeV $\simeq 1$ fm/c.

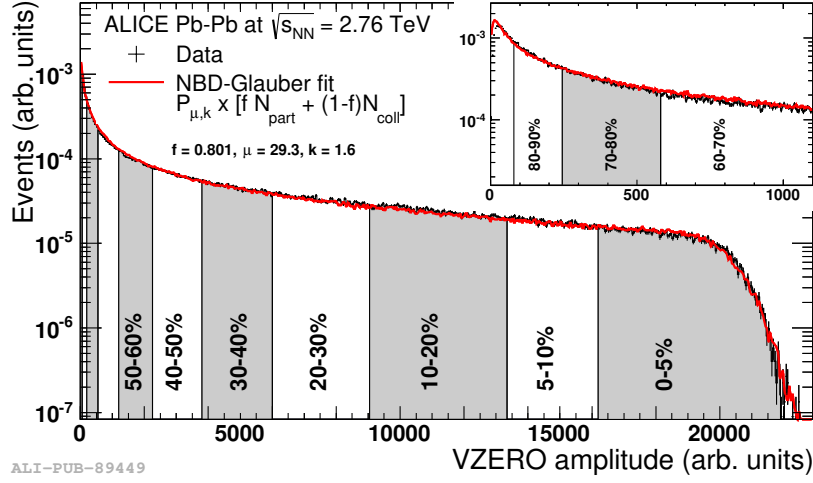


Fig. 1.7 Distribution of the sum of the signal amplitudes measured in the VZERO detectors in Pb–Pb collisions at $\sqrt{s_{NN}} = 2.76$ TeV. Figure from [25].

- For $t < 0.1$ fm/c the matter is in a stage called *pre-equilibrium*. In the early collision stages, most of the interactions between partons involve small momentum exchange (soft interactions). Some hard processes occur between partons and particles with either a large mass or large transverse momenta are created. In this phase, the production of direct photons is also expected.
- The particles produced in the primary collisions continue to mutually interact, giving rise to a region of high matter and energy density at the thermal equilibrium from which the QGP can be produced in less than 0.1-0.3 fm/c. This stage is referred to as *thermalisation*. The relative abundance of gluons, up, down and strange quarks changes in this phase. At this stage, due to the internal pressure, the thermalised system expands as the energy density decreases. The rapid expansion of the QGP is usually modelled using relativistic hydrodynamics [26], which provides useful insights to interpret the experimental data.
- When the critical density is reached ($\epsilon_c \sim 1$ GeV/fm³), the *hadronisation* stage starts, and the system gradually evolves into an interacting hadron resonance gas. In this phase, the expansion and contextual cooling of the system continues, as well as the elastic and inelastic interactions among the hadrons within the system.
- The relative abundance of hadron species can change until the hadron gas is able to interact inelastically. When the energy of the interactions becomes too small the abundances are fixed and the so-called *chemical freeze-out* is reached. At this stage elastic interactions are still present and continue to modify the kinetic properties of

the hadrons. When the distances between hadrons are larger than the range of the interaction, elastic collisions stop and the so-called *kinetical freeze-out* is reached. At this stage also the kinematical distributions of the hadrons are fixed.

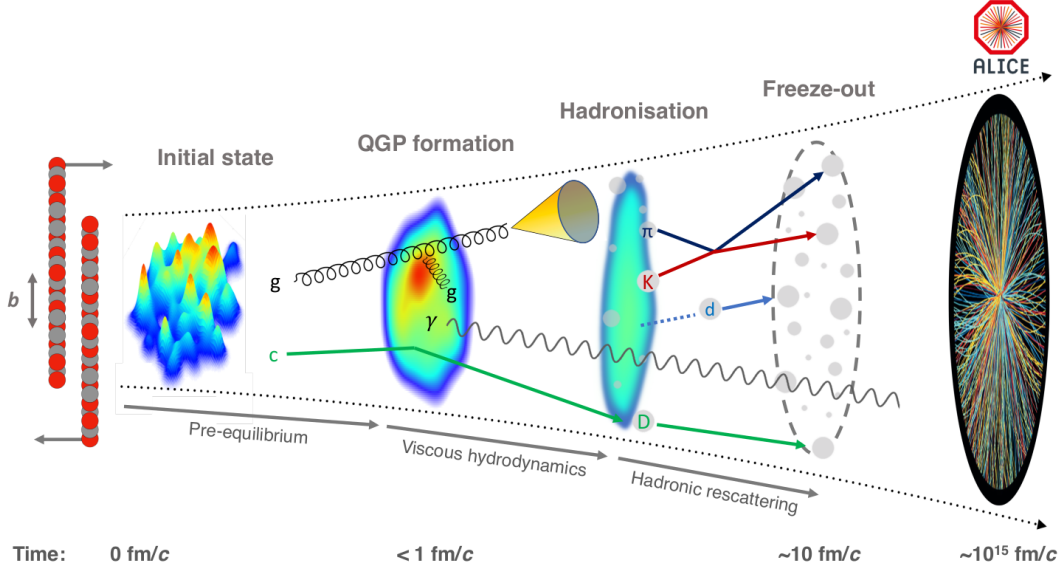


Fig. 1.8 The evolution of a heavy-ion collision at LHC energies [22].

1.2.3 QGP experimental probes

The QGP produced in heavy-ion collisions has a short lifetime ($\approx 10 \text{ fm}/c \approx 10^{-23} \text{ s}$), therefore it can not be studied directly, and we can only access the information available in the final state of the collision. However, theoretical models suggest some observables that can be studied as signatures of the production of the quark-gluon plasma. Depending on their properties and on the phase of the collision in which they are produced, these signatures are commonly referred to as electromagnetic, hard and soft probes:

- Electromagnetic probes consist of photons emitted before and after the thermalisation phase. They can be identified by measuring the lepton pairs they produce in the final state, but it is challenging to isolate their signal from the background coming from photons produced in later stages of the medium evolution.
- Hard probes are produced in high momentum transfer scatterings that occur at the early stages of the collision. They include jets and the production of particles containing heavy flavour quarks (c , b) in open charm/beauty and quarkonia ($q\bar{q}$).

- Soft probes include particles which are produced in soft processes of the collision. These probes come from the last stages of the fireball evolution and keep indirect information on the phase transition properties. These signatures are mainly measured from hadrons with light quarks (u, d, s) with momenta below 2 GeV/c.

In order to show how different probes allow access to different information on the nature of QGP, it is useful to report some examples.

Charged particle multiplicity

The measurement of the particle multiplicity produced in heavy-ion collisions provides important information about the properties of the created medium. This observable is typically expressed in terms of pseudorapidity density of charged particles per pair of participant nucleons $\frac{2}{N_{\text{part}}} dN_{\text{ch}}/d\eta$, and its dependence on energy and system size reflects the interplay between parton-parton scattering processes for particle production. When measuring particle production in the final state of the collision, it is crucial to introduce the definition of rapidity and pseudorapidity. The rapidity is defined as:

$$y = \frac{1}{2} \ln \left(\frac{E + p_L}{E - p_L} \right)$$

where E represents the energy and p_L the longitudinal momentum component. In the ultrarelativistic limit, rapidity may be approximated by pseudorapidity, which is defined as:

$$\eta = \frac{1}{2} \ln \left(\frac{p + p_L}{p - p_L} \right) = -\ln \left(\tan \left(\frac{\theta}{2} \right) \right)$$

where θ is the angle between the momentum of the particle and the beam axis. ALICE has provided results on the charged-particle multiplicity per unit of pseudorapidity ($dN_{\text{ch}}/d\eta$) in various collision energies and systems. To compare the particle production in different collision systems, the charged-particle multiplicity measured at midrapidity is usually scaled by the number of nucleon pairs participating in the collision $2/N_{\text{part}}$. Previous measurements of $dN_{\text{ch}}/d\eta$ for AA collisions were also performed at the LHC by ATLAS [27], and CMS [28] at $\sqrt{s_{NN}} = 2.76$ TeV, and at lower energies (in the range $\sqrt{s_{NN}} = 9$ -200 GeV) by experiments at the SPS [29] and RHIC [30–33]. All the results show an increase of charged multiplicity with energy steeper in AA compared to pp collisions. Figure 1.9 shows the midrapidity charged-particle multiplicity normalised by $2/N_{\text{part}}$, in pp, $p\bar{p}$, p(d)A and in central heavy-ion collisions as a function of the centre-of-mass energy per nucleon pair $\sqrt{s_{NN}}$. The dependence of $dN_{\text{ch}}/d\eta$ on the centre-of-mass energy is fitted with a power-law function

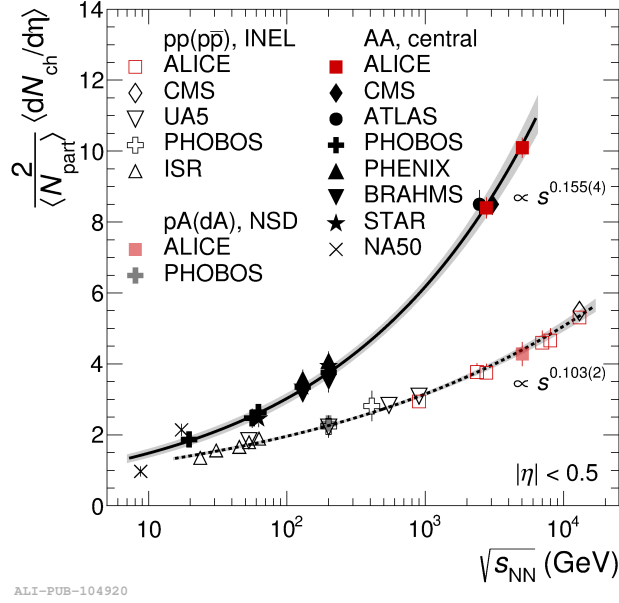


Fig. 1.9 Collision energy dependence of the charged-particle pseudorapidity density at midrapidity ($|\eta| < 0.5$) normalised to the average number of participants, $\frac{2}{\langle N_{\text{part}} \rangle} \langle dN_{\text{ch}}/d\eta \rangle$. Data from central AA collisions are compared to measurements in non-single diffractive p(d)A collisions and inelastic (INEL) pp and $p\bar{p}$ collisions. The lines are power-law fits to the data, and the bands represent the uncertainties on the extracted dependencies [22].

($\alpha \cdot s^\beta$) obtaining an exponent value of $\beta = 0.155 \pm 0.004$ for most central AA collisions. The dependence on \sqrt{s} is much stronger for AA collisions than for inelastic (INEL) pp and non-single-diffractive (NSD) p(d)A collisions, where a value of $\beta = 0.103 \pm 0.002$ is obtained. Notably, the pA results exhibit a similar trend to the pp results, suggesting that the significant increase observed in Pb–Pb collisions is not solely influenced by the multiple collisions undergone by the participant nucleons, as even in pA collisions protons interact with multiple nucleons. This indicates that heavy-ion collisions are more efficient in transferring the initial beam energy into particle production at midrapidity than pp or pA collisions.

Identified hadron abundances

Hadron yields measured at midrapidity in heavy-ion collisions are well described by a statistical hadronisation model (SHM), which assumes that the quark-gluon plasma reaches both chemical and thermal equilibrium [34]. The model contains three main parameters: the temperature T_{ch} at the chemical freeze-out, the baryo-chemical potential μ_{B} , which takes into account baryon number conservation, and the volume V of the hadron and resonance

gas (HRG) which is produced at the chemical freeze-out. The values of these parameters can be obtained by fitting the measurements of particle yields. In this model at the stage of the chemical freeze-out, strongly interacting hadrons form a grand-canonical ensemble and the abundance of a defined particle species i can be written as:

$$N_i(T, V, \mu_i) = \frac{g_i V}{2\pi^2} \int_0^\infty \frac{p^2 dp}{e^{(E-\mu_i)/T} \pm 1} \quad (1.10)$$

where g_i are the degrees of freedom of the species i and μ_i the baryo-chemical potential. Deviations from the grand-canonical description can be accommodated by introducing additional parameters to consider the incomplete thermalisation of strange (γ_s) or charm (γ_c) quarks. In case of non-equilibrium, these parameters are smaller than one. This adjustment is often necessary for peripheral AA collisions or in smaller systems, such as pp and p-Pb collisions. Fig. 1.10 shows the yields of different hadron species containing only light quarks (u, d, s) measured in central (0-10%) Pb-Pb collisions at $\sqrt{s_{NN}} = 2.76$ TeV compared to the results of four different implementations of such models, namely THERMUS [35, 36], SHARE [37–39], Thermal-FIST [40, 41], and GSI-Heidelberg [42]. The SHM describes the yields of all the measured species over nine orders of magnitude in abundance values. Among the parameters, the value for the baryo-chemical potential has been fixed to $\mu_B \approx 0$ in most models, given the almost equal abundances of particles and antiparticles at LHC energies. As a consequence, the corresponding fits are performed using the average of particle and antiparticle yields. An exception is the GSI-Heidelberg model, where μ_B is a free parameter determined to be zero with an uncertainty of about 4 MeV. The chemical freeze-out temperature derived from the fit is $T_{ch} \approx 156$ MeV, with uncertainties ranging from 2 to 3 MeV and minimal discrepancies (± 1 MeV) among the various implementations of the SHM. Another parameter estimated from the SHM fit is the volume of the fireball for one unit of rapidity at the chemical freeze-out, approximately 4500 fm^3 in SHARE, Thermal-FIST, and GSI-Heidelberg results. The fits using THERMUS give a significantly larger volume, incorporating an excluded-volume (Van-der-Waals like) correction [43], which accounts for the short-range repulsive interactions between hadrons, leading to a lower particle density within the fireball.

Dynamics of the fireball: flow

Essential insights into the understanding of strongly-coupled matter lie in the dynamical properties of the quark-gluon plasma. These properties are primarily identified through measurements sensitive to both anisotropic and radial flow, playing a significant role in the collective motion at play during heavy-ion collisions. A radial flow occurs due to a

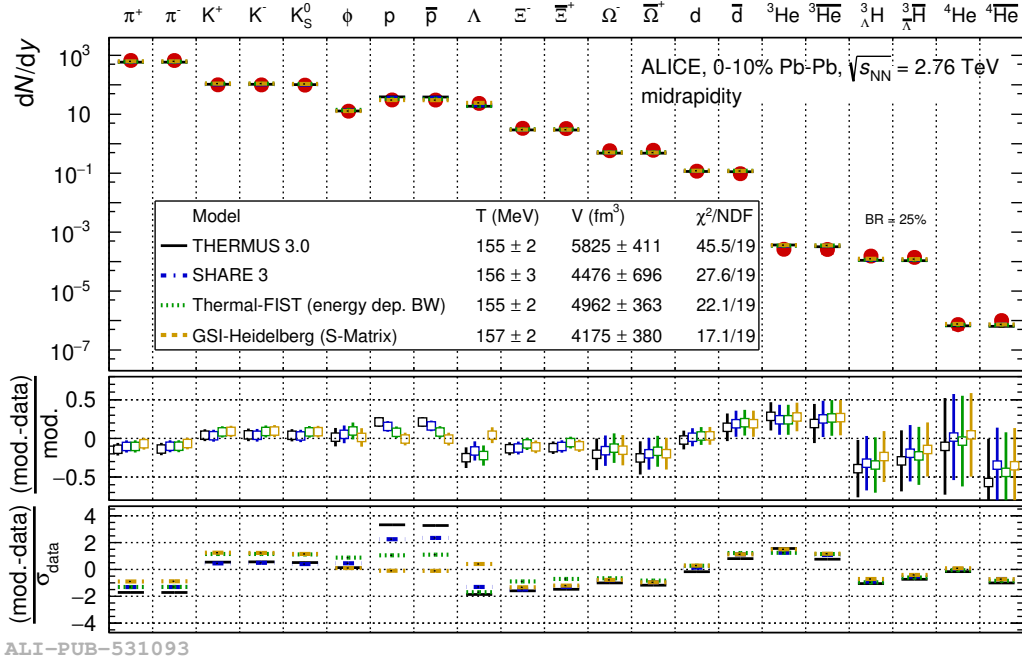


Fig. 1.10 Measured multiplicity per unit of rapidity of different hadron species and light nuclei compared to SHM fits from THERMUS, SHARE, Thermal-FIST, and GSI-Heidelberg (see text for references). Differences between the model calculations and the measured yields are shown in the bottom panels. Figure from [22].

greater pressure at the centre of the QGP compared to the outer regions, leading to a common velocity field outwards. The rate of the hydrodynamic expansion is influenced by the bulk viscosity, which is its resistance to volume growth. Anisotropic flow results from a directional dependence on these pressure gradients and occurs due to spatial anisotropies in the initial state. The radial flow, originating from the collective motion in the transverse plane, can be measured experimentally from the momentum distribution of identified particles. Radial flow leads to harder transverse momentum distribution with increasing mass, particularly at low p_T values. Within this region, the p_T distribution is shaped by two distinct contributions: random thermal motion and radial collective expansion. The latter depends on the hadron mass because all hadrons acquire an additional transverse momentum proportional to their mass and the common radial flow velocity. Figure 1.11 shows the p_T spectra of various particles in Pb-Pb collisions at $\sqrt{s_{\text{NN}}} = 2.76$ TeV for the 0-5% and 80-90% centrality intervals. The spectra shape depends on the centrality with the average transverse momentum located at higher transverse momenta in central collisions with respect to peripheral. The radial flow is the only collective motion which affects central heavy-ion collisions, however, when two nuclei collide with a non-zero impact parameter (non-central collisions) the overlapping

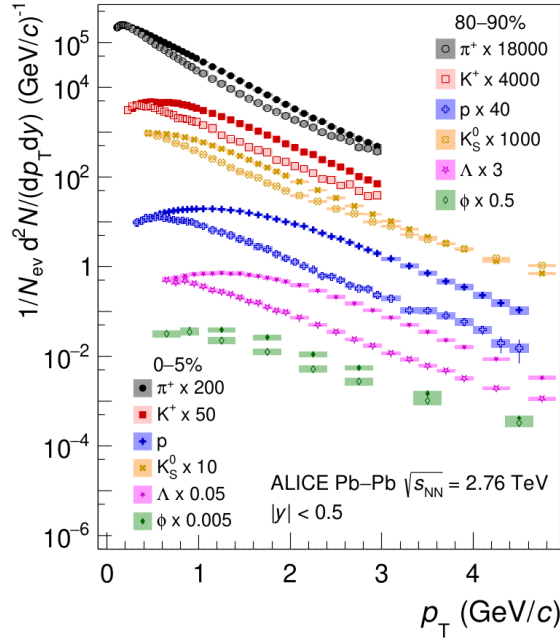


Fig. 1.11 Transverse momentum distributions of π^+ , K^+ , p , K_S^0 , and Λ , and the ϕ meson for 0-50% and 80-90% centrality intervals in Pb-Pb collisions at $\sqrt{s_{NN}} = 2.76$ TeV. The data points are scaled for better visibility. Statistical and systematic uncertainties are shown as bars and boxes, respectively. Figure from [22].

region is asymmetrical and this can produce further anisotropies in particle emission and momentum distribution. Since these anisotropies are generated before matter reaches the critical temperature and the hadronisation phase, the anisotropic flow is sensitive to the early and hot strongly interacting phase of the evolution of quark-gluon plasma. The final azimuthal distribution of emitted particles can be written in terms of the azimuthal Fourier coefficients of the transverse momentum spectrum:

$$E \frac{d^3N}{d^3p} = \frac{d^3N}{p_T dp_T dy d\phi} = \frac{d^2N}{p_T dp_T dy} \frac{1}{2\pi} \left[1 + \sum_{n=1}^{\infty} 2v_n \cos n(\phi - \Phi_R) \right], \quad (1.11)$$

where p_T is the transverse momentum, y the rapidity, ϕ the azimuthal angle of the particle momentum and Φ_R the angle of the reaction plane, known by measuring the transverse distribution of particles in the final state. The coefficients v_n are in general p_T and y dependent and are referred to as differential flow. In particular, the first coefficient v_1 is called direct flow. In a central collision (zero impact parameter) the final azimuthal distribution is isotropic, and therefore the coefficient v_n is equal to zero. In a non-central collision, the typical almond shape of the overlap region between the colliding nuclei generates a pressure gradient along the reaction plane. This collective motion is called elliptic flow and it contributes to the v_2

coefficient of Eq. (1.11). Thus, the measurements of these v_n coefficients are extremely important since they are related to the initial geometric conditions and in-homogeneities through the properties of the medium. Figure 1.12 shows the elliptic flow coefficient v_2 of charged pions, charged and neutral kaons, protons, ϕ mesons, and hyperons as a function of p_T for several centrality classes in Pb–Pb collisions at $\sqrt{s_{NN}} = 5.02$ TeV.

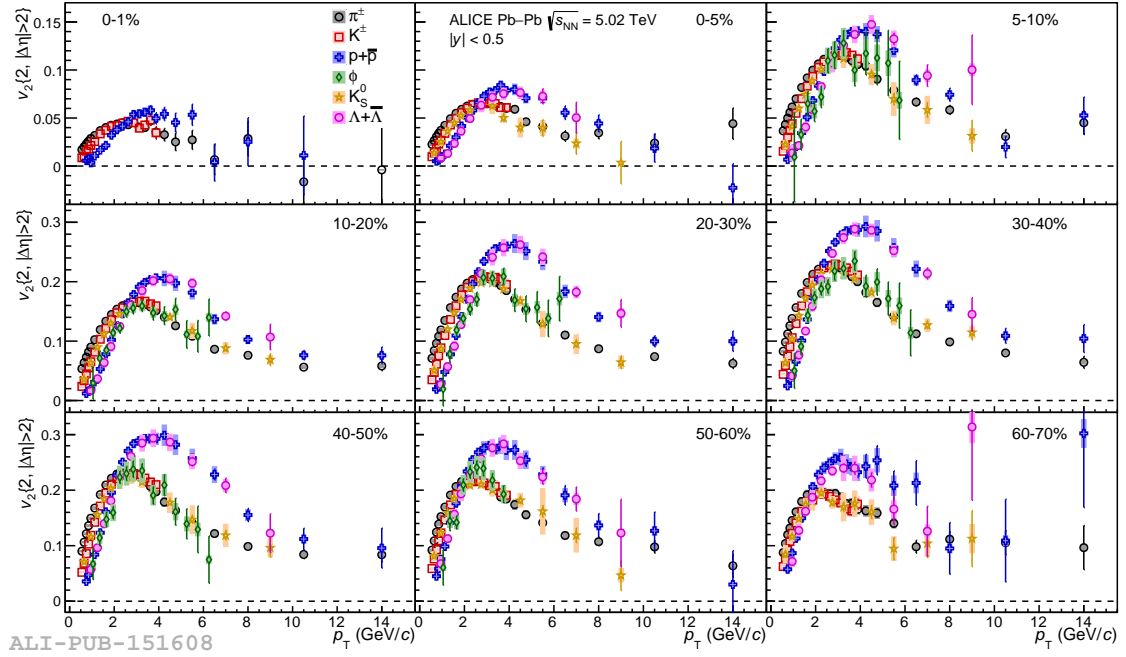


Fig. 1.12 Elliptic flow coefficient v_2 of charged pions, charged and neutral kaons, protons, ϕ mesons, and hyperons as a function of p_T for several centrality classes in Pb–Pb collisions at $\sqrt{s_{NN}} = 5.02$ TeV measured by the ALICE Collaboration. Figure from [44].

For $p_T < 2 - 3$ GeV/c, the v_2 of different particle species is mass-ordered, i.e. lighter particles have a larger elliptic flow than heavier particles at the same p_T . This indicates the presence of a strong radial flow which imposes an isotropic velocity boost to all particles in addition to the anisotropic expansion of the medium. For $3 < p_T < 8 - 10$ GeV/c, the v_2 depends on the number of constituent quarks: baryons have larger flow than mesons, as expected in the hypothesis of particle production via quark coalescence. For $p_T > 10$ GeV/c, the v_2 of different particle species are compatible within uncertainties and depend only weakly on the transverse momentum.

Hadronisation of the QGP

During the hadronisation of the fireball, two main processes compete: recombination and hadronisation of energetic (high- p_T) partons that escape from the QGP and hadronise in the

vacuum via string fragmentation. The final hadron spectra consist of a mixture of hadrons from recombination, with momentum determined by the sum of valence quark momenta, and fragmentation, with lower momentum than the parent parton. At low and intermediate p_T (up to a few GeV/c), recombination is expected to prevail over fragmentation, while at higher momenta, a transition occurs to a regime dominated by the fragmentation of jets. This transition is predicted to occur at higher values of p_T for baryons compared to mesons [45]. An intermediate p_T enhancement of heavier hadrons over lighter hadrons is expected from the collective hydrodynamic expansion of the system, as discussed in the previous section. Moreover, in coalescence models, baryon-to-meson ratios are further enhanced at intermediate p_T by the recombination of lower p_T quarks that leads to a production of baryons (3 quarks) with larger p_T than for mesons (2 quarks). Fig. 1.21 shows the p_T differential p/π and Λ/K_S^0 baryon-to-meson double ratio Pb–Pb/pp calculated at $\sqrt{s} = 5.02$ TeV and 2.76 TeV, respectively. The ratios exhibit a bump structure in $1.5 < p_T < 8.0$

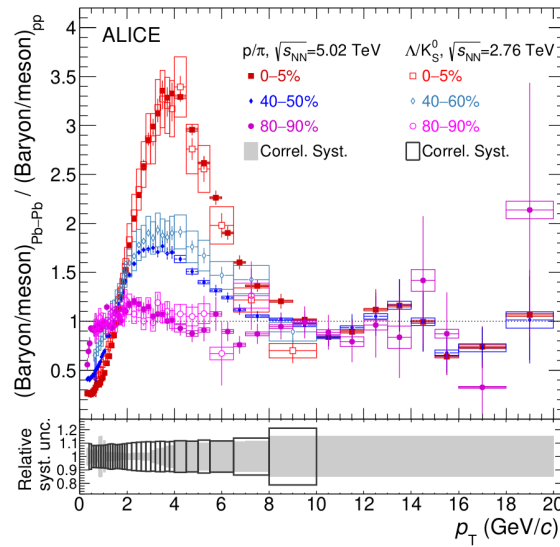


Fig. 1.13 p_T -differential baryon-to-meson ratios in Pb–Pb divided by the pp ones at the same colliding energy for $(p+p)/(\pi^+ + \pi^-)$ at $\sqrt{s_{NN}} = 5.02$ TeV and $(\Lambda + \bar{\Lambda})/(2K_S^0)$ at $\sqrt{s_{NN}} = 2.76$ TeV. Figure from [22].

GeV/c, gradually increasing with increasing centrality. The baryon-to-meson ratios in the strange-hadron sector show similar features as those for the p/π ratios, the two double ratios are compatible with each other within uncertainties in all centrality intervals, and they are consistent with unity for $p_T > 8\text{--}10$ GeV/c, where fragmentation dominates. For $p_T < 1.5$ GeV/c, a hierarchy of the baryon-to-meson ratios is observed as a function of centrality and the ratios are strongly reduced in central collisions compared to peripheral collisions.

Energy loss in the medium and jet quenching

As mentioned in the previous sections, the dominant production process for high p_T hadrons is the fragmentation of high p_T partons that originate in hard scattering in the early stages of the nuclear collision. These particles then propagate in the QGP losing energy interacting with the medium constituents via inelastic (gluon radiation) and elastic (scattering) processes. To quantify this effect, the so-called nuclear modification factor R_{AA} is used, which is constructed to be sensitive to changes in the dynamics of hard processes in heavy-ion collisions with respect to expectations from elementary pp collisions. It is defined as the ratio of the charged particle yield in Pb–Pb to that observed in pp collisions, scaled by the number of binary nucleon-nucleon collisions $\langle N_{\text{coll}} \rangle$:

$$R_{AA} = \frac{\left(\frac{d^3N}{dp^3} \right)_{AA}}{\left(\frac{d^3N}{dp^3} \right)_{pp} \langle N_{\text{coll}} \rangle} .$$

If $R_{AA}(p_T) = 1$, production from heavy-ion collisions can be considered as a superposition of nucleon-nucleon collisions, assuming no QGP formation in pp. In particular, R_{AA} is expected to be below unity at high- p_T for inclusive hadrons from partons undergoing energy loss. Figure 1.14 (a) shows the nuclear modification factor as a function of transverse momentum for charged particles at $\sqrt{s_{NN}} = 5.02$ TeV for central and peripheral Pb–Pb collisions and p–Pb collisions. The plot shows that a strong suppression is observed in central Pb–Pb collisions, due to final state partonic energy loss in the hot and dense QGP, while a weaker suppression is observed in peripheral collisions indicating an increasing parton energy loss with centrality. In p–Pb collisions, particle production approximately follows N_{coll} scaling for $p_T > 2$ GeV/c. The peak at 2 – 3 GeV/c for charged hadrons is partly due to collective radial flow and enhancement in the baryon-to-meson yield ratio observed at intermediate- p_T . Another effect which can occur from the energy loss of partons travelling through the QGP medium is called *jet quenching*. Typically, in the hadronisation jets are formed in a back-to-back arrangement, a result of momentum conservation during the initial collision. However, the two parent partons giving rise to these jets may encounter distinct path lengths within the QGP, leading to different degrees of energy loss for each parton. This results in an asymmetry in the p_T distributions of the jets measured in the final state. An example is shown in Figure 1.14 (b), where an ATLAS event display of a Pb–Pb collision shows a visible jet only on one side of the detector, while the opposite side shows only an overall higher activity, which corresponds to the other scattered jet.

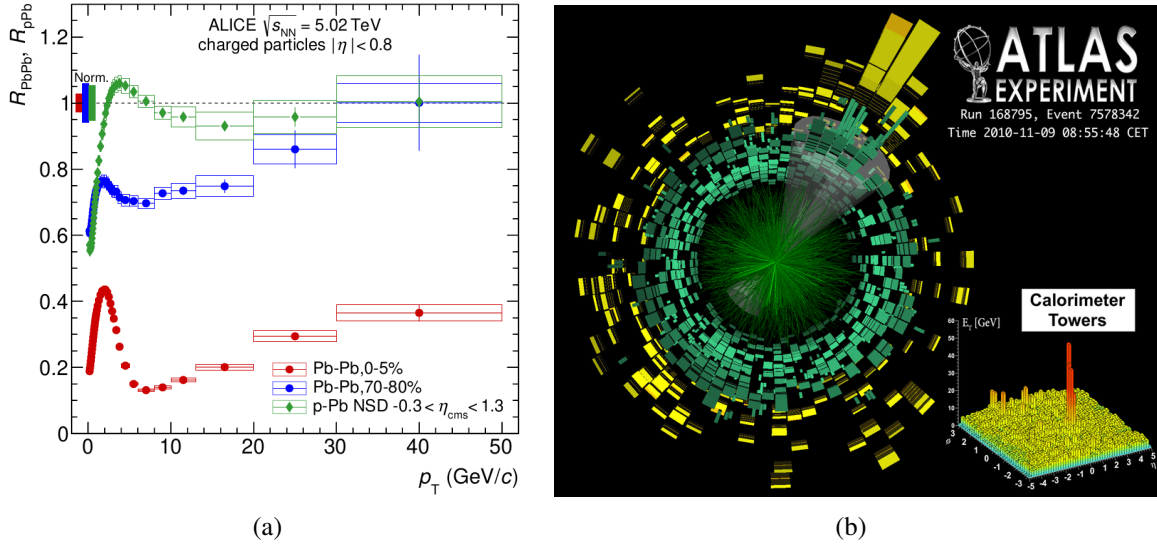


Fig. 1.14 (a) Nuclear modification factor R_{AA} for charged hadrons in central and peripheral Pb–Pb collisions and NSD p–Pb collisions [22]. (b) ATLAS event display of a Pb–Pb collision at $\sqrt{s_{NN}} = 2.76$ TeV showing jet quenching.

Heavy flavour production

As mentioned, due to the high mass of charm (c) and beauty (b) quarks ($m_c \simeq 1.3 \text{ GeV}/c^2$, $m_b \simeq 4.2 \text{ GeV}/c^2$), they are mainly produced in the hard scatterings among partons of the colliding hadrons. These processes take place with a characteristic timescale smaller than the typical QGP formation time, therefore, charm and beauty quarks live through the medium expansion, interacting with the free partons in the plasma. For these reasons, the measurement of open heavy-flavour hadrons, namely hadrons containing at least one heavy valence quark, and quarkonia, bound states of heavy quark-antiquark pairs $\bar{q}q$, are excellent tools to study the whole QGP space-time evolution. Examples of quarkonia states are the $\bar{c}c$ (charmonium), whose ground state is the J/ψ , and the $\bar{b}b$ (bottomonium), whose ground state is the Υ hadron. The QGP formation leads to a colour-screening effect which can dissociate the quarkonia in the medium, causing the so-called quarkonia suppression, which can be quantified by the nuclear modification factor R_{AA} . With increasing temperature the quarkonium state production is expected to be more suppressed and this can be studied experimentally with the increase of the centre of mass energy. Figure 1.15 (a) shows the R_{AA} of the J/ψ hadron measured in heavy-ion collisions at a different centre of mass energies as a function of the charged multiplicity produced in the collision. The R_{AA} measured by NA50 (green markers) and STAR (light blue markers) clearly decreases with the multiplicity. The ALICE results in Pb–Pb collisions at $\sqrt{s_{NN}} = 5.02$ TeV (red markers) show that at LHC

energies the J/ψ suppression is less pronounced and its multiplicity dependence is reduced. In fact, at higher energies, the cross-section for heavy-quark production is higher and thus more heavy quarks are produced: as a consequence, the recombination of a quark from a dissociated $\bar{q}q$ pair with an antiquark from another dissociated $\bar{q}q$ pair is more likely to happen. This effect is referred to as quarkonia regeneration and predicts that part of the charmonia production comes from the statistical recombination of charm and anti-charm quarks coming from unrelated hard-scatterings. This effect is expected to be stronger for charmonia than for bottomonia states since it is driven by the number of heavy-quark pairs produced in the collisions, which is smaller for bottom than for charm quarks.

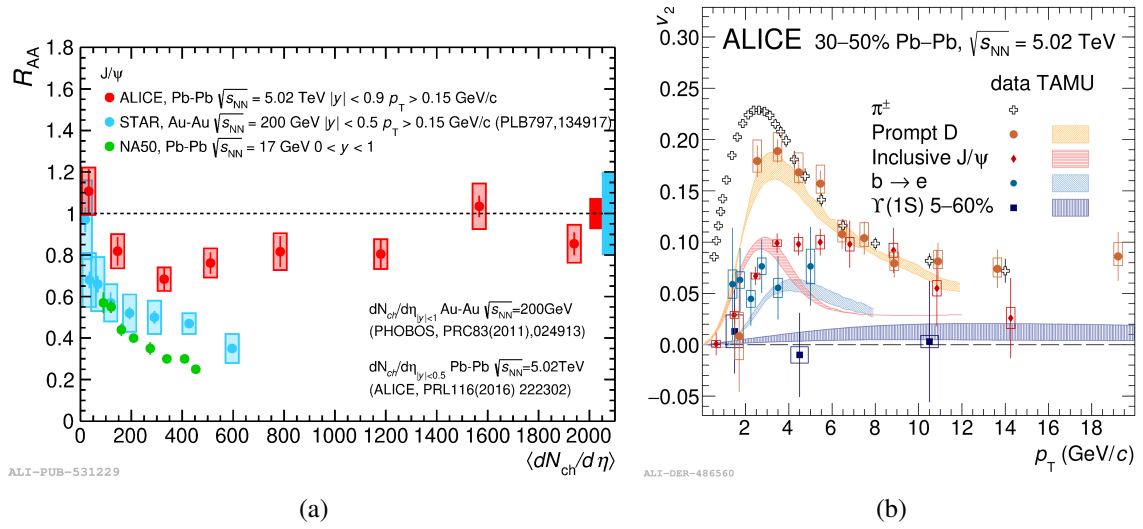


Fig. 1.15 (a) J/ψ R_{AA} as a function of the charged particle multiplicity. The results of NA50 (SPS), STAR (RHIC) and ALICE (LHC) are compared. Figure from [22]. (b) Elliptic flow of pions, prompt D mesons, inclusive J/ψ , electrons from beauty hadron decays and $\Upsilon(1S)$ in semicentral (30–50%) Pb–Pb collisions at $\sqrt{s_{NN}} = 5.02$ TeV.

The dynamics of heavy quarks are very different from that of the light partons since they are produced in the initial hard scattering processes. Therefore, heavy quarks are not expected to be in equilibrium at the formation time of the QGP, and thus, they only marginally take part in the build-up of the collective motions in the early stage of the system evolution. However, the bulk flow is transferred to the charm and beauty quarks via the multiple interactions with the medium constituents. Insights on the heavy quark elliptic flow come from the comparison of different open heavy-flavour hadrons and quarkonia. In Fig. 1.15 (b) the elliptic flow of pions, prompt D mesons, inclusive J/ψ , electrons from beauty hadron decays and $\Upsilon(1S)$ in semicentral (30–50%) Pb–Pb collisions at $\sqrt{s_{NN}} = 5.02$ TeV is reported. These results suggest that the beauty quark is less affected by flow effects. However, this might be

explained by the scaling to high p_T of the peak flow with the mass of the particle, where the uncertainties on the measurements are large.

1.3 Small hadronic collision systems

The first data from the LHC provided crucial insights into the understanding of the conditions necessary for quark-gluon plasma formation. Until then, small collision systems, such as pp and pA, were regarded as reference cases, wherein the conditions for QGP formation were thought not to be reachable. The discovery of collective phenomena within small collision systems, alongside the discovery of a continuous evolution of particle production (event multiplicity) from pp to Pb–Pb collisions, has surprised the scientific community. Historical signatures of QGP formation, like the measurement of long-range correlation structures (the ridge) and the increasing production of strangeness as a function of multiplicity, were also observed in these small systems. These observations triggered an extensive discussion on whether there can be a coherent understanding of hadronic collisions and particle production across colliding systems, in which a superposition of microscopic QCD processes transitions to a macroscopic QGP. The investigation of these effects in small systems is among the main novel aspects of the LHC physics programme, focusing on connecting results in small systems at multiplicity similar to the ones measured in semi-central AA collisions. Charged-particle multiplicity appears to be one of the simplest, even if not ideal, event classifiers which allows a direct comparison among different collision systems without any model dependence. The multiplicity dependence of identified particle yields relative to pions is compared to p–Pb and Pb–Pb results in Fig. 1.16. For all particle species, the evolution of yields with charged particle production smoothly connects different collision systems and energies. The ratio of strange-hadron yields to pion yields is observed to increase with multiplicity faster for particles with a larger strangeness content, as can be seen in the Λ/π , Ξ/π , and Ω/π ratios. The p/π ratio is observed to continuously decrease with increasing multiplicity, indicating that the increase of hyperon production with respect to pions with increasing multiplicity is a phenomenon that does not originate from mass differences but is rather connected to strangeness content. This effect will be discussed in detail in the next chapter.

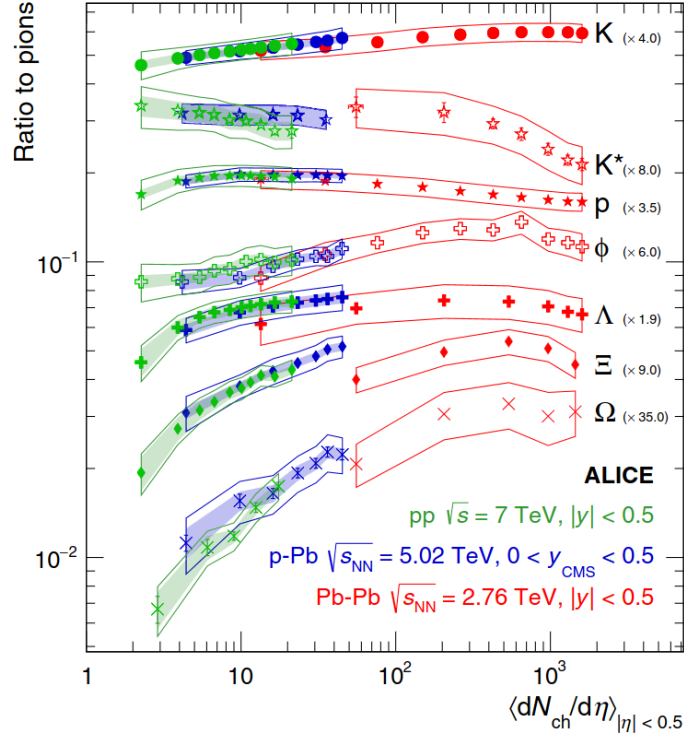


Fig. 1.16 Integrated particle-to-pion ratios as a function of the charged particle multiplicity for pp, p-Pb, and Pb-Pb collisions. Figure from [46].

1.3.1 Collectivity in small systems

In heavy-ion collisions, the emergence of collectivity can be traced back to the presence of a strongly-interacting QGP, where spatial anisotropies and correlations transform into anisotropies in momentum space. This phenomenon involves many particles spanning a wide rapidity range, and studies of multi-particle correlations play a major role in characterising the underlying mechanism of particle production in high-energy AA collisions. Particles emitted from a collective system display long-range correlations among numerous particles across a broad rapidity range, arising from their collective response to an initial anisotropy. The investigation of this phenomenon can be achieved through the study of azimuthal correlations and, in this context, the observed long-range (large $|\Delta\eta|$) structure in two-dimensional $\Delta\eta - \Delta\phi$ correlation functions is of particular interest. $\Delta\eta$ and $\Delta\phi$ are the differences in azimuthal angle ϕ and pseudorapidity η between the two particles. Fig. 1.17 shows the 2D two-particle correlation functions for (a) 2.76 TeV Pb-Pb and (b) 5.02 TeV p-Pb collisions measured by the CMS experiment. The peak centred in $(\Delta\eta, \Delta\phi) = (0, 0)$ is ascribed to particles produced in the same jet or coming from the decay of the same hadron. Long-range correlations are observed at $\Delta\phi \approx 0$ and $\Delta\phi \approx \pi$ (double-ridge), originating from

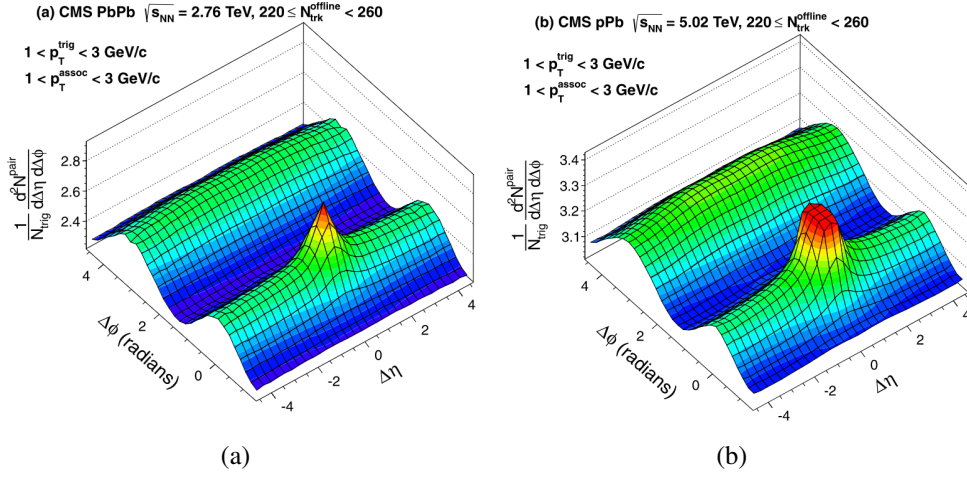


Fig. 1.17 2D two-particle correlation functions for (a) 2.76 TeV Pb–Pb and (b) 5.02 TeV p–Pb collisions for pairs of charged particles with $1 < p_T^{\text{trig}} < 3 \text{ GeV}/c$ and $1 < p_T^{\text{assoc}} < 3 \text{ GeV}/c$ within the $220 < N_{\text{trk}}^{\text{offline}} < 260$ multiplicity bin. Figures from [47].

the elliptic flow induced by the hydrodynamic evolution in non-central nucleus-nucleus interactions, discussed in section 1.2.3, contributing as a $\cos(2\phi)$ modulation to the two-particle correlation function over a broad $|\Delta\eta|$ range and an azimuthal structure is formed by the medium response to the initial transverse geometry. Remarkably, similar effects to collectivity have also been observed in small collision systems, although their underlying origins may differ from those in heavy-ion scenarios. In particular, a double-ridge structure was also observed in high multiplicity pp, but not in Minimum Bias (MB) pp collisions as displayed in Fig. 1.18 (a) and (b), respectively. Such a structure is not reproduced by pp Monte Carlo generators, e.g. PYTHIA, and the underlying origins of this effect have still to be fully understood. The fact that the ridge is observed independently of the collision system (if the multiplicity density is sufficiently high) suggests that a primordial collective evolution is already present in smaller systems. Further insights into the observation of collective effects in small systems are given by the measurement of anisotropic flow coefficients. Measurements of v_n using the two-particle cumulant method from pp, p–Pb, Xe–Xe and Pb–Pb collisions are shown in Fig. 1.19. An ordering of flow coefficients $v_2 > v_3 > v_4$ is observed in large collision systems, as well as a clear multiplicity dependence of v_2 reflecting the initial geometry of the overlapping region of the colliding nuclei. At low multiplicities, the values of v_n from Xe–Xe and Pb–Pb collisions are compatible with those measured in pp and p–Pb collisions, all exhibiting a weak multiplicity dependence. Similarly as in Xe–Xe and Pb–Pb collisions, an ordering of v_n is also observed in small collision systems.

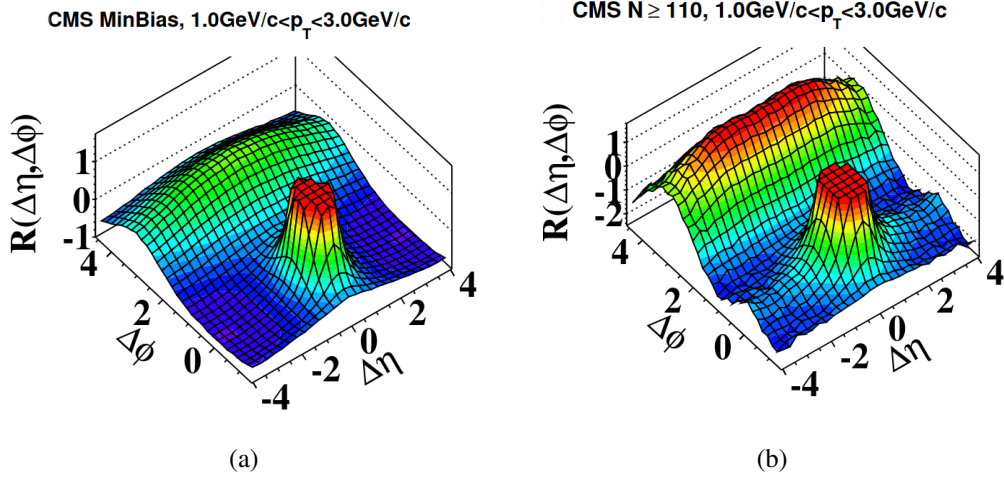


Fig. 1.18 2D two-particle correlation functions for 7 TeV pp (a) minimum bias events with $1 < p_T < 3$ GeV/c and (b) high multiplicity ($N_{\text{trk}}^{\text{offline}} \geq 110$) events with $1 < p_T < 3$ GeV/c. Figures from [48].

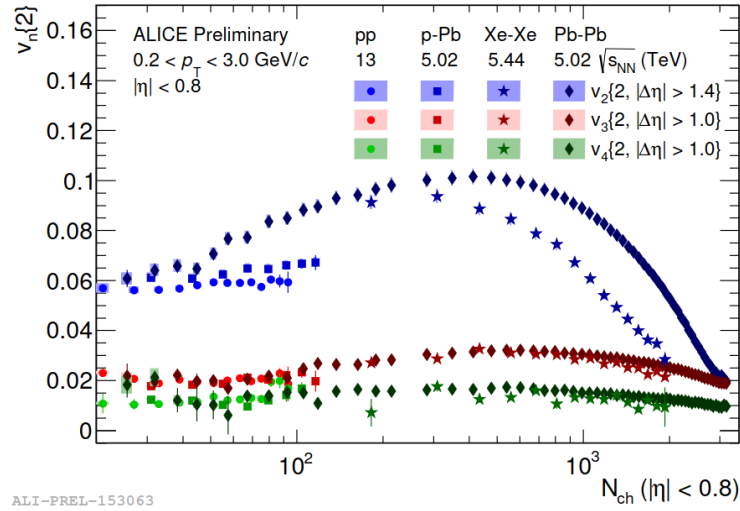
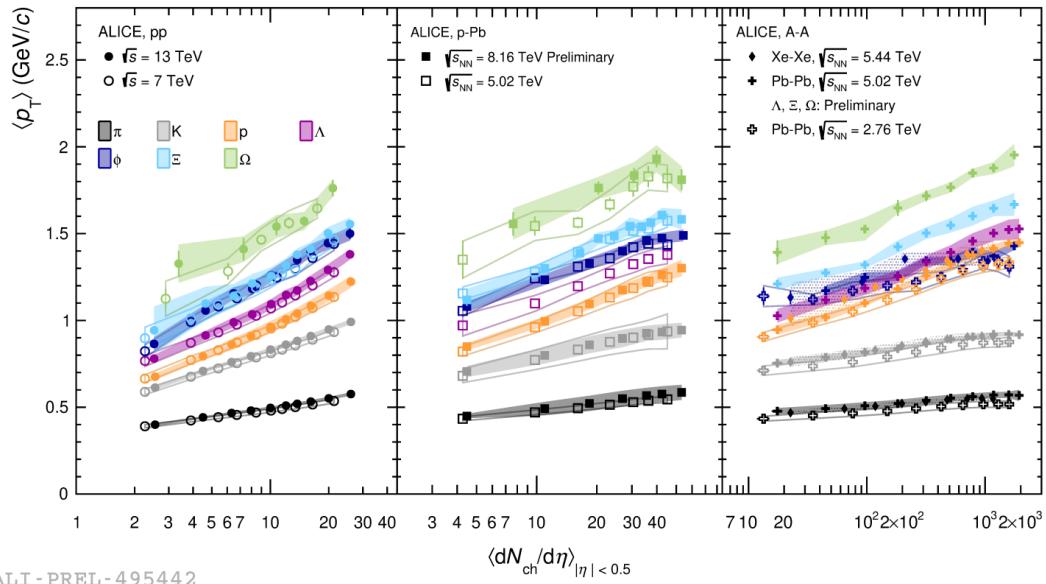


Fig. 1.19 Multiplicity dependence of v_2 , v_3 and v_4 measured using the two-particle cumulant method in small (pp and p-Pb) and large (Xe-Xe and Pb-Pb) collision systems [49].

1.3.2 Dynamics and hadrochemistry of particle production

As discussed in Sec. 1.2.3, in heavy-ion collisions, the average transverse momentum $\langle p_T \rangle$ increases with the centrality of the interaction following a mass-ordering. This is ascribed to the radial collective expansion of the strongly interacting system created in the collision, which boosts the momenta of the particles with a common velocity field. However, this effect has also been observed in p-Pb and pp collisions as a function of the multiplicity of charged

particles produced in the event, as shown in Fig. 1.20. The origin of this effect in small systems has still to be fully understood, in particular, whether the hardening of the spectra can only be attributed to a radial flow or if a different mechanism could explain the mass-dependent increase of $\langle p_T \rangle$ in the different collision systems. One way to further investigate this effect is to measure the p_T -differential ratios between baryon, and meson yields in pp and p-Pb interactions characterised by different final-state multiplicities. An example are the p/π and Λ/K_S^0 ratios, where the radial boost of a collectively expanding system should lead to the observation of an enhanced baryon-to-meson ratio at intermediate- p_T , as discussed in Sect. 1.2.3. Fig. 1.21 shows the baryon-to-meson ratio in pp (left), p-Pb (centre) and Pb-Pb (right) collisions, where red markers refer to events characterised by larger charged particle multiplicity with respect to the blue ones. In all collision systems, the ratios exhibit an increase at intermediate p_T values ($\langle p_T \rangle \simeq 3 \text{ GeV}/c$) which is observed to be enhanced with higher charged particle multiplicity.



ALI - PREL - 495442

Fig. 1.20 Average transverse momentum $\langle p_T \rangle$ as a function of the charged particle multiplicity at midrapidity $\langle dN_{ch}/d\eta \rangle$ in pp (left panel), p-Pb (central panel) and Pb-Pb and Xe-Xe (right panel) collisions. Different colours refer to different particle species, as indicated in the legend.

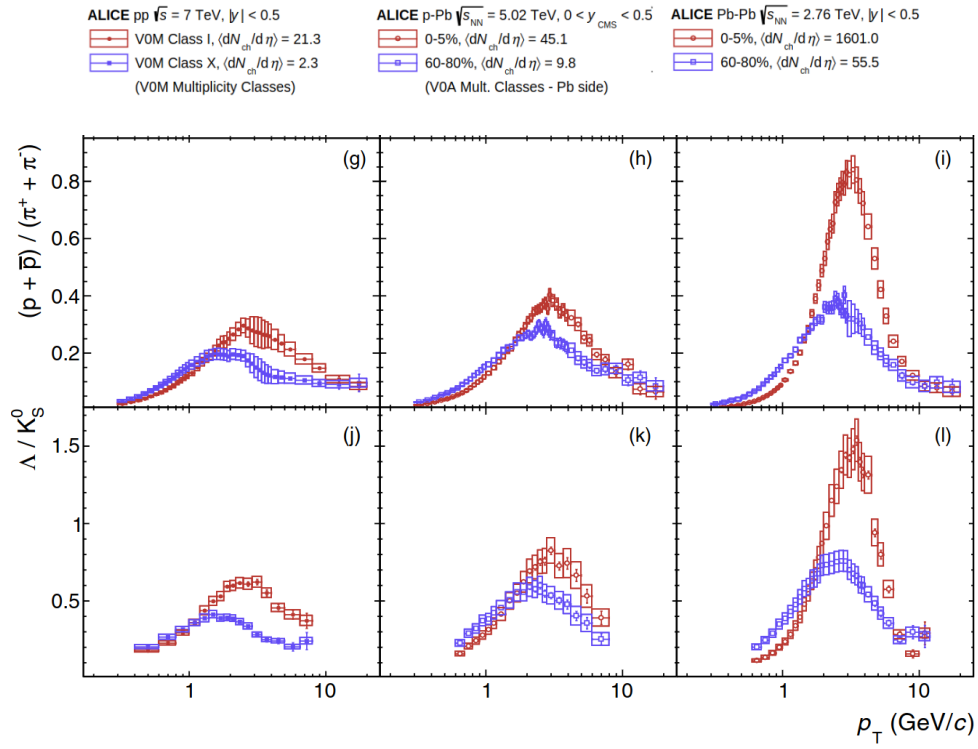


Fig. 1.21 Transverse momentum dependence of p/π and Λ/K_S^0 ratio in pp (left), p-Pb (centre) and Pb-Pb (right) collisions. The red markers refer to events characterised by larger charged particle multiplicity with respect to the blue ones. Figure adapted from [46].

Chapter 2

Strangeness production in high energy hadronic collisions

In the early 1950s, a quantum number, conserved under the strong interaction, was introduced (Gell-Mann, 1953) to explain the behaviour of the “strange” particles observed from cosmic rays. In the following years, several new particle species were discovered, and the idea that these could be the elementary constituents of matter was replaced by the intuition that they could be composite objects of more elementary particles. In 1961, Gell-Mann and Ne’eman introduced a $SU(3)$ symmetry where three different flavours of quark ($q = u, d, s$) combine to build mesons ($q\bar{q}$) and baryons (qqq). However, when cataloguing hadrons using the $SU(3)_f$ group, there are anomalous states, such as the $\Omega^-(sss)$, that are combinations of three quarks of the same flavour, in clear contrast with the Pauli exclusion principle for fermions. To resolve this issue, an additional colour quantum number was introduced within the $SU(3)$ gauge theory framework. In the Standard Model, quarks are now classified into six flavours: down (d), up (u), strange (s), charm (c), bottom (or beauty, b) and top (t). The first three are known as “light quarks”, while the others are usually called “heavy quarks”. Figure 2.1 provides an overview of the properties of quarks. Each elementary particle is described by a set of quantum numbers such as mass, spin, hypercharge, baryon number, strangeness, etc. The so-called strangeness quantum number of a particle is defined as:

$$S = -(n_s - n_{\bar{s}}) \quad (2.1)$$

where n_s represents the number of strange quarks (s) and $n_{\bar{s}}$ represents the number of strange antiquarks (\bar{s}) present in the hadron. Therefore, among the six flavours of quarks, only the strange quark has a nonzero strangeness, in particular -1 for s and +1 for \bar{s} . Strangeness is conserved in strong and electromagnetic interactions but not in weak ones. The family of

mass→	2.4 MeV	1.27 GeV	171.2 GeV
charge→	$\frac{2}{3}$	$\frac{2}{3}$	$\frac{2}{3}$
spin→	$\frac{1}{2}$	$\frac{1}{2}$	$\frac{1}{2}$
name→	u up	c charm	t top
Quarks	4.8 MeV	104 MeV	4.2 GeV
	$-\frac{1}{3}$	$-\frac{1}{3}$	$-\frac{1}{3}$
	$\frac{1}{2}$	$\frac{1}{2}$	$\frac{1}{2}$
	d down	s strange	b bottom

Fig. 2.1 Quarks in the Standard Model.

hadrons that contain at least one strange quark but no heavier quark (like charm or bottom) are called hyperons. These consist of: the $\Lambda(uds)$, the triplet $\Sigma^+(uus)$, $\Sigma^0(uds)$, $\Sigma^-(dds)$, the doublet $\Xi^-(dss)$, $\Xi^0(uss)$, the $\Omega^-(sss)$ and the corresponding antiparticles. Ξ and Ω are called multi-strange baryons since they are the only hyperons containing more than one strange quark. Unlike the other light quarks (up and down), strange quarks are not present as valence quarks in the initial state of pp and AA collisions. Therefore all the net strangeness present in the final state particles is created during the collision. Moreover, the strange quark has a mass value that is halfway between the two lighter and the three heavier quarks, which implies a lower production energy cost with respect to the latter. For these reasons, the s quark plays an interesting role in the study of particle production in hadronic collisions.

2.1 Strangeness as a signature of QGP

Strangeness is of great interest in the context of the study of the strongly interacting medium created in heavy-ion collisions. In 1982 Johann Rafelski and Berndt Müller [50] suggested an increased production of strange hadrons as a possible signature for the formation of quark-gluon plasma in AA collisions. At a fixed collision energy, the production mechanism of the strange quark is different within pp and AA colliding systems. The former is expected to produce a hadron gas (HG), with hadronic degrees of freedom, as quarks and gluons are confined. The latter allows the formation of the QGP, where the degrees of freedom are at partonic level, with deconfined quarks and gluons. In the QGP, the high gluon density plays a key role in strangeness production. Since gluons can be created and annihilated easily in interactions with other gluons and light quarks, the gluon density closely follows the temperature evolution during the quark-gluon phase lifetime. In a heavy-ion collision, strangeness can be produced in the first hard partonic scattering processes by flavour creation ($gg \rightarrow s\bar{s}$, $q\bar{q} \rightarrow s\bar{s}$) and flavour excitation ($gs \rightarrow gs$, $qs \rightarrow qs$), and it can also be created during the partonic evolution via gluon splittings ($g \rightarrow s\bar{s}$). Moreover, due to the partial

chiral symmetry restoration discussed in the previous Chapter, in these reactions, the energy threshold is equal to the bare mass of the two strange quarks, therefore, much lower than in a hadron gas. The Feynman diagrams corresponding to the dominant strangeness production processes are shown in Fig. 2.2.

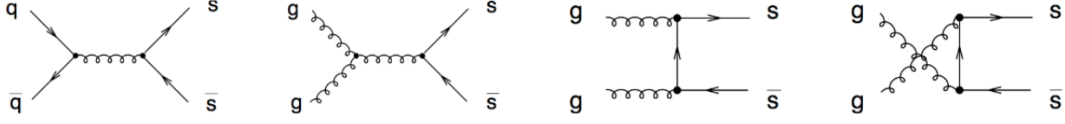


Fig. 2.2 Lowest-order production of $s\bar{s}$ by gluons and light quarks.

Calculations show that in the QGP strangeness is predominantly formed by reactions of gluons [50]. In Fig. 2.3 the rates for strangeness production by gluon splitting and quark annihilation are compared assuming $\alpha_S = 0.6$ and $m_s = 150$ MeV, and the gluon contribution is found to dominate the strangeness creation rate A . The evolution of the relative strangeness to baryon density produced in the plasma state is shown in Fig. 2.4 for various temperatures, showing that a saturation of the strangeness abundance is expected for $T > 200$ MeV within the QGP lifetime (≈ 10 fm/c).

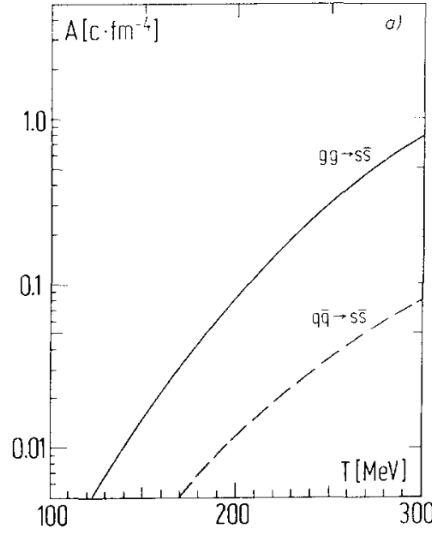


Fig. 2.3 Rates A of $s\bar{s}$ production as function of temperature T . The curves are for $\alpha_S = 0.6$ and $m_s = 150$ MeV [50].

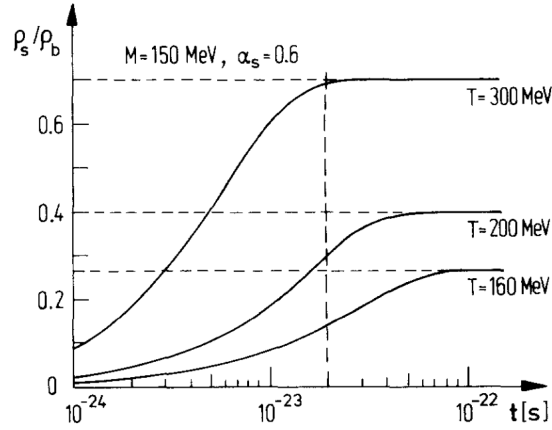


Fig. 2.4 Time evolution of the relative strangeness to baryon density in the plasma for various temperatures T . The curves are for $\alpha_s = 0.6$ and $m_s = 150$ MeV. The vertical line corresponds to a time of ≈ 6 fm/c [50].

The high gluon density in the QGP impacts the entire evolution of the plasma state, influencing also the hadronisation process. Therefore, the abundance of (multi-)strange hadrons produced in the final state reflects that of strangeness in the partonic phase.

As briefly introduced, in small collision systems no QGP is produced but rather a Hadron Gas, where the degrees of freedom are at the hadronic level. The energy needed to produce strange mesons or baryons in a thermally equilibrated HG is significantly higher than in the case of a QGP. Strangeness can be formed by direct production, e.g.:

$$\pi + \pi \rightarrow \pi + \pi + \Lambda + \bar{\Lambda} \quad (2.2)$$

$$\pi + \pi \rightarrow \pi + \pi + \Xi^- + \bar{\Xi}^+ \quad (2.3)$$

However, direct production is penalised due to strange number conservation, which requires the coupled production of strange particles and antiparticles. In this case, the reaction threshold corresponds to two times the rest mass of the strange hadrons. Strangeness can also arise from indirect production mechanisms, which are characterised by lower thresholds but are still quite penalised. In this case, to produce multi-strange hadrons, one would need two reactions in sequence, starting with the production of lighter hadrons and followed by a reaction of these intermediate products to produce the heavier hadrons.

$$\pi + N \rightarrow K + \Lambda \quad (2.4)$$

$$\pi + \Lambda \rightarrow K + \Xi \quad (2.5)$$

The common reaction feature of the processes in Eq. (2.4) and (2.5) is the $q\bar{q} \rightarrow s\bar{s}$ where three quarks are spectators, and a $q\bar{q}$ is annihilated and an $s\bar{s}$ is formed, as displayed in Fig. 2.5 (a). Finally (multi-)strange particles can be produced in strange quark exchange reactions, displayed in Fig. 2.5 (b), e.g.:

$$\bar{K} + N \rightarrow \Lambda + \pi \quad (2.6)$$

Experimentally, one finds for the strangeness exchange reaction in Eq. (2.6) has a cross section roughly ten times larger than the production cross section of the processes in Eq. (2.4) and (2.5). This means that strangeness is much faster redistributed among the strange particle families than produced.

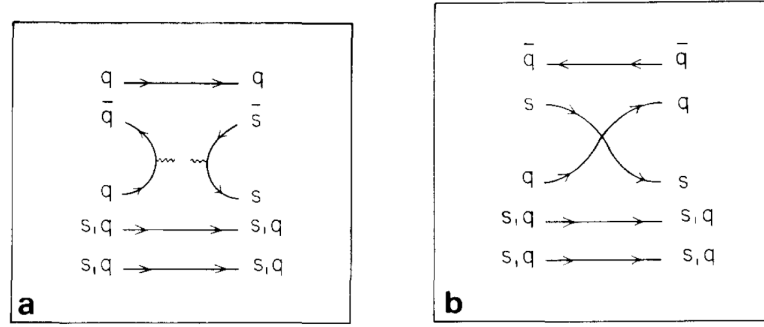
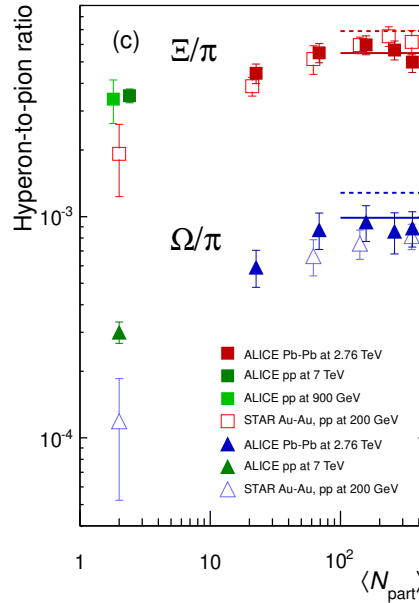


Fig. 2.5 (a) Quark flow diagram for indirect strangeness production reaction: annihilation of a $q\bar{q}$ pair and production of a $s\bar{s}$ pair. (b) Quark flow diagram for strangeness exchange reaction: exchange of the s quark from the initial K meson to the final baryon. Quark spectator lines are also indicated [50].

For all these reasons, strangeness production in small hadronic collision systems is much suppressed with respect to AA interactions. Therefore, the enhancement of strange hadron production in heavy-ion collisions with respect to minimum bias pp collisions (strangeness enhancement) was proposed as a signature of QGP formation in heavy-ion collisions.

2.1.1 Strangeness enhancement in heavy-ion collisions

Strangeness enhancement was first observed in 1988 by the CERN fixed-target experiment NA35 [51] at the Super Proton Synchrotron (SPS). The SPS accelerated beams of ^{32}S ions to 200 GeV per nucleon in the years 1987-1992, providing the first systematic studies of particle production using relativistic heavy ions at CERN. The NA35 collaboration first studied strangeness enhancement by comparing S-S collisions to p-S ones. In 1994, the CERN SPS accelerated ^{208}Pb nuclei to an energy of 158 GeV per nucleon, i.e. $\sqrt{s_{\text{NN}}} = 17.3$ TeV, measuring strangeness enhancement by comparing Pb-Pb to p-Pb and p-Be collisions [52–57]. At increasing collision energy, strangeness enhancement was later studied at RHIC by comparing Au-Au to pp collisions at $\sqrt{s_{\text{NN}}} = 130$ GeV and $\sqrt{s_{\text{NN}}} = 200$ GeV [58–60]. More recently, the ALICE experiment has provided results in ultra-relativistic Pb-Pb collisions at $\sqrt{s_{\text{NN}}} = 2.76$ TeV [61] compared to pp collisions. A collection of the available results is presented in Fig. 2.6 with the predictions from a thermal statistical model.



ALI-PUB-78357

Fig. 2.6 Hyperon-to-pion ratios as a function of $\langle N_{\text{part}} \rangle$ in AA collisions and pp collisions at LHC and RHIC energies. The lines are predictions from statistical hadronisation models. Figure from [61].

Figure 2.7 shows the ratios of Ξ and Ω yields measured in heavy-ion collisions at different centrality and the ones measured in pp (or pA) collisions, normalised by the average number of participant nucleons. The results obtained by ALICE in Pb-Pb collisions at $\sqrt{s_{\text{NN}}} =$

2.76 TeV are compared to those obtained at different centre-of-mass energies by the NA57 experiment (Pb–Pb and p–Pb collisions at $\sqrt{s_{NN}} = 17.2$ GeV) and by the STAR experiment (Au–Au collisions at $\sqrt{s_{NN}} = 200$ GeV). The strangeness enhancement factor is found to be larger than unity for all collision systems and energies and to increase with $\langle N_{part} \rangle$, reaching a saturation value at the LHC energies for $\langle N_{part} \rangle > 150$. The observed enhancement is larger for the triple-strange Ω baryon with respect to the double-strange Ξ baryon, consistently with the hierarchy expected for strange hadron production in a deconfined medium. The strangeness enhancement factor is also observed to be larger for smaller centre-of-mass energies, i.e. larger for NA57 results with respect to ALICE ones. This observation can be ascribed to the higher measured production of strange hadrons in the reference minimum bias pp collisions for higher centre-of-mass energies. In contrast, a similar yield is measured in AA collisions at different collision energies (strangeness saturation).

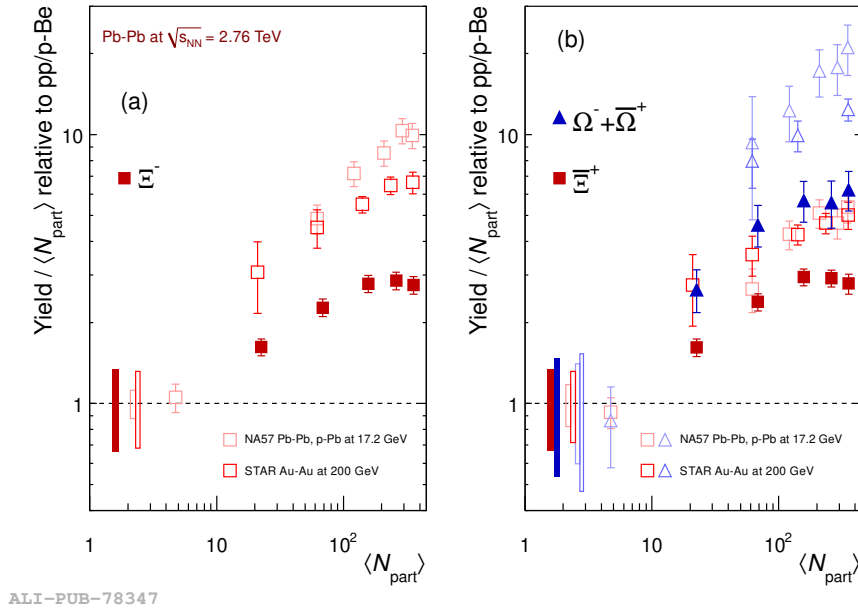


Fig. 2.7 Strangeness enhancement factors for Ξ and Ω hyperons as a function of the average number of participants measured in different centre-of-mass energies by NA57, STAR and ALICE experiments. ALICE data points are shown with full markers. Figure from [61].

2.2 Strange hadron production in small collision systems

As discussed in the Sec. 1.3 several effects have been observed in high-multiplicity pp and p–Pb collisions that are reminiscent of observations attributed to the creation of a medium in thermal and kinematic equilibrium. In particular, the charged-particle multiplicity appears to be a useful tool which allows for a direct comparison among different collision systems for these measurements, reflecting the final hadronic state produced in the collision and also being strongly related to the initial energy at play. The left panel of Fig. 2.8 shows the multiplicity dependence of identified particle yields relative to pions in different collision systems and centre-of-mass energies, namely pp, p–Pb, Xe–Xe and Pb–Pb for $2.76 < \sqrt{s_{NN}} < 13$ TeV. The ratios increase with $dN_{ch}/d\eta$, reaching in high-multiplicity pp collisions values comparable to those measured in peripheral Pb–Pb collisions. The evolution of yields with charged particle production smoothly connects all collision systems and energies for all particle species. The ratio of strange-hadron yields to pion yields is observed to increase with multiplicity faster for particles with a larger strangeness content, as can be seen in the K_S^0/π , Λ/π , Ξ/π , and Ω/π ratios ($|S_{\Omega^\pm}| > |S_{\Xi^\pm}| > |S_\Lambda| \approx |S_{K_S^0}|$). The p/π ratio is observed to continuously decrease with increasing multiplicity, indicating that the increase of open strange hadron production with respect to pions is a phenomenon that does not originate from mass differences but is rather connected to strangeness content. The relative production of the $\phi(s\bar{s})$ meson increases with $dN_{ch}/d\eta$ by a factor similar to the one measured for K_S^0 . This suggests that ϕ production cannot be described solely by considering net strangeness or the number of strange quark constituents. As seen in the right panel of Fig. 2.8, the ALICE Collaboration also measured the multiplicity evolution of particle ratios involving resonances and their non-resonant hadronic states. The scope of this study in heavy-ion collisions is to determine the presence and lifetime of the hadronic phase, which follows chemical freeze-out in heavy-ion collisions. Including the same results in small collision systems (pp and p–Pb) shows again a rather smooth trend across multiplicities.

2.2.1 Recent results in small systems

Important insights on the origin of strangeness production in small collision systems come from studying the strange hadron production associated to hard scattering processes and to the underlying event (UE). Hard processes are associated with the production of jets, showers of particles originating from a parton produced in a hard scattering interaction and undergoing subsequent parton fragmentation and hadronisation. Several processes contribute to the UE of a pp collision, such as initial and final state radiation (ISR/FSR), Multi-Parton

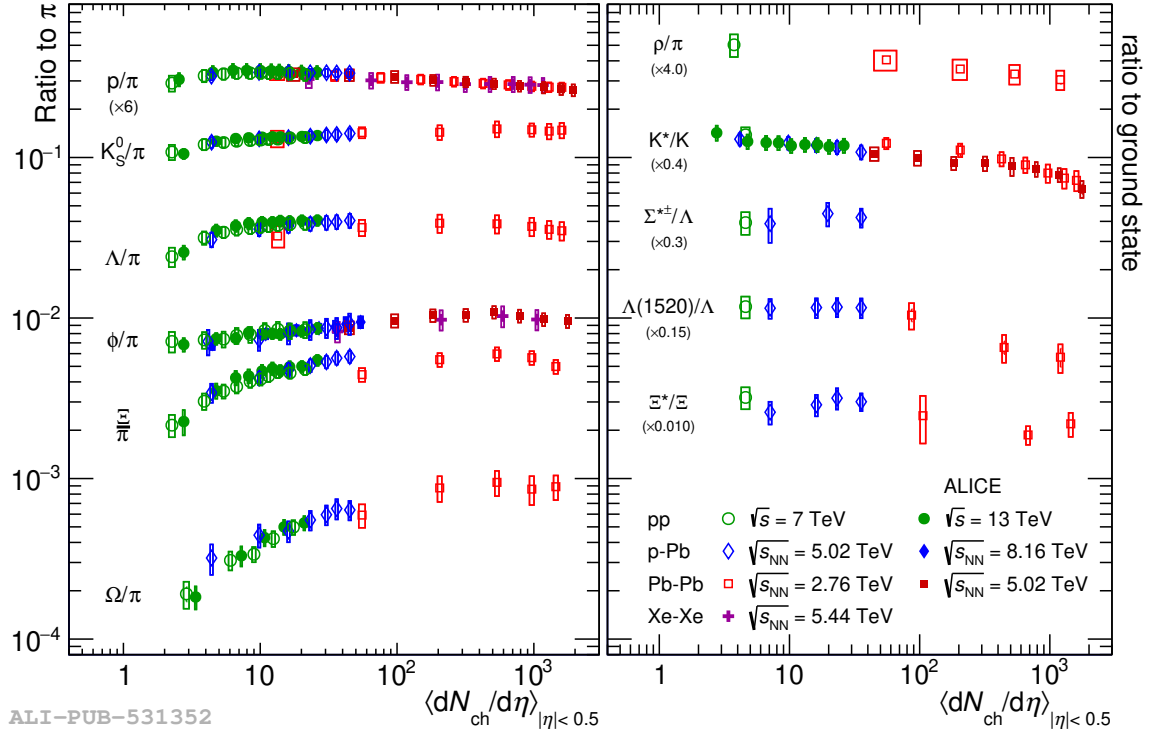


Fig. 2.8 (Left) Ratios of different hadron yields to pions as a function of the charged particle multiplicity measured at midrapidity in pp collisions at $\sqrt{s} = 7$ TeV and 13 TeV, p-Pb collisions at $\sqrt{s_{NN}} = 5.02$ TeV and at $\sqrt{s_{NN}} = 8.16$ TeV, Xe-Xe collisions at $\sqrt{s_{NN}} = 5.44$ TeV and Pb-Pb collisions at $\sqrt{s_{NN}} = 2.76$ TeV and at $\sqrt{s_{NN}} = 5.02$ TeV. (Right) Ratios involving ρ mesons, K^* , $\Sigma^{*\pm}$, $\Lambda(1520)$ and Ξ^* . All yields are obtained at midrapidity. Figure from [22].

Interactions (MPI) and beam remnants. ISR and FSR are due to partons undergoing a scattering process radiating gluons, respectively, before and after the interaction. The relative contribution of hard and soft processes to strangeness production in pp remains an open question and can be studied through different techniques involving full-jet reconstruction and/or two-particle correlations. The ALICE collaboration has measured the production of different (multi-)strange hadron yields in jets, exploiting jet-finder algorithms, and in the underlying event in pp collisions at $\sqrt{s} = 7$ TeV, $\sqrt{s} = 13$ TeV. The reconstruction of the jet is performed with the anti- k_T algorithm, applying a jet resolution parameter $R_{res} = 0.4$ and requiring $p_{T,jet}^{ch} > 10$ GeV/c. Strange hadrons are considered to be located inside a jet cone if their distance to the jet axis in the $\eta - \phi$ plane is smaller than $R_{cut} = 0.4$ equal to the jet resolution parameter. Strange hadrons not associated with hard scatterings, i.e. produced in the UE, are extracted from a cone perpendicular to the jet one with the same radius. The yield of strange hadrons produced in jets is obtained by subtracting the underlying event

contribution from the yield measured in the jet cone. Fig. 2.9 (a) shows the K_S^0 density yields, i.e. the yields normalised by the jet area $A = \pi R_{\text{cut}}^2$, measured in the jet cone (green markers), in the UE (blue empty markers) and in jets (red markers) as a function of the transverse momentum in pp collisions at $\sqrt{s} = 7$ TeV. The inclusive K_S^0 spectrum, i.e. the spectrum measured in all events, is shown in black markers. The spectrum of K_S^0 produced in jets is harder with respect to one measured in the perpendicular cone, in agreement with the jet being related to a hard scattering process. Similar results are observed for the Λ baryon.

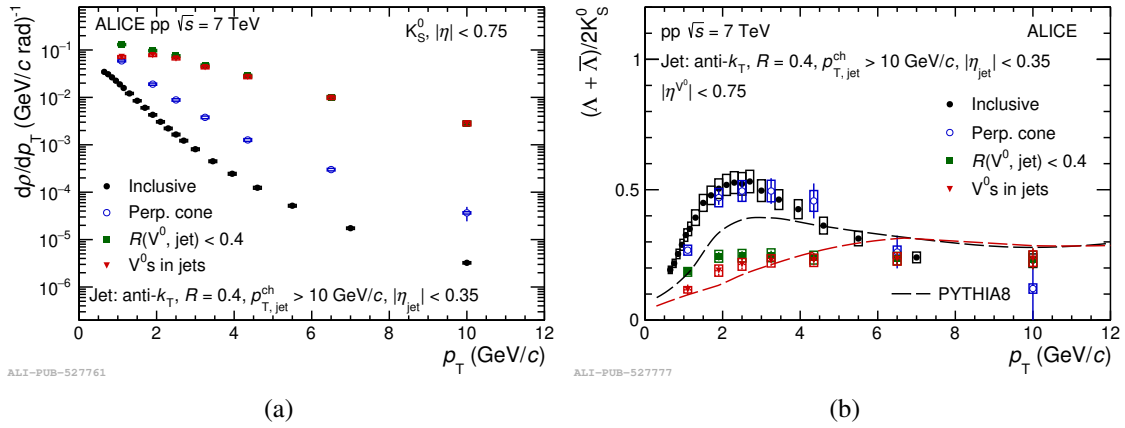


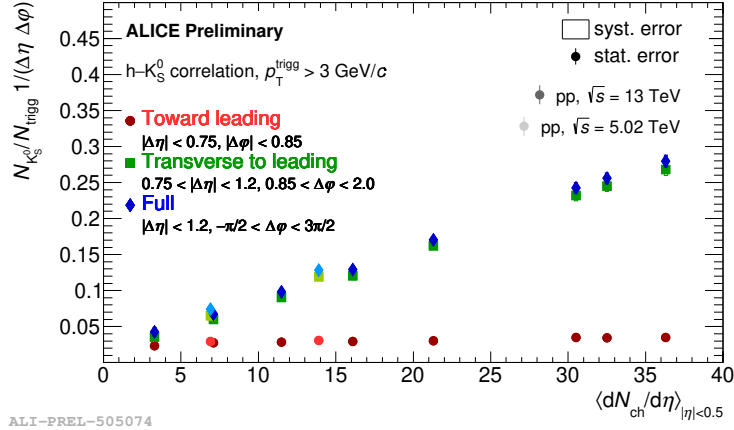
Fig. 2.9 K_S^0 density spectra (a) and $(\Lambda + \bar{\Lambda})/K_S^0$ (b) as a function of the transverse momentum p_T in pp collisions at $\sqrt{s} = 7$ TeV. The results are shown for inclusive K_S^0 and Λ produced in minimum bias events (black markers), in the underlying event (empty markers), in the jet cone (green markers) and in jets after the subtraction of the contribution from the underlying event (red markers). Figures from [62].

The baryon-to-meson ratio (Λ/K_S^0) is also studied in- and out-of-jets and the results are displayed in Fig. 2.9 (b). The ratio measured in the UE (blue empty markers) shows an enhancement at $p_T \approx 3$ GeV/c compatible with the one displayed by the inclusive yield ratio (black markers). The Λ/K_S^0 ratio in jets (red markers) shows little to no enhancement. These results show that the enhancement at intermediate p_T of the strange baryon-to-meson ratio (Λ/K_S^0) is found to be driven by particle production in the underlying event and that jet fragmentation alone is not sufficient to fully describe strange particle production in pp collisions at the LHC energies. The ALICE collaboration has also measured the production of Ξ and K_S^0 yields in jets as a function of the charged particle multiplicity, exploiting the angular correlation method. Extending this measurement as a function of multiplicity is crucial in order to shed light on the origin of the strangeness enhancement observed in small systems. The angular correlation technique is based on the observation that particles produced in the

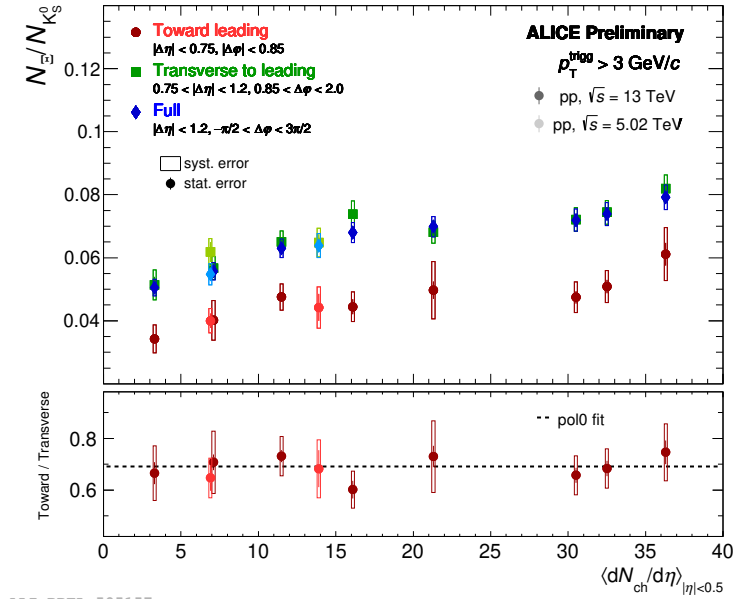
near-side jet region are characterised by a small angular separation from the trigger particle of the jet, which is identified as the particle with the highest transverse momentum in the event and $p_T > 3$ GeV/c. The angular distribution between the trigger particle and the associated strange hadron is studied in the $(\Delta\eta, \Delta\phi)$ plane, which is divided into three regions: a transverse-to-leading region, proxy for the out-of-jet production, a toward-to-leading region, proxy for the near-side-jet production, and a full inclusive region, which covers the entire angular correlation plane. The near-side-jet contribution is obtained subtracting the out-of-jet yield from the full yield in the toward-to-leading angular region. The K_S^0 yields per trigger particle and per unit of $\Delta\eta\Delta\phi$ are reported in Fig. 2.10 (a) as a function of the charged-particle multiplicity produced at midrapidity. The yields in the full and transverse-to-leading regions are found to increase with the charged particle multiplicity. In contrast, the toward-to-leading region yields show only a weak multiplicity dependence. Similar results are obtained for Ξ baryons. No energy dependence is observed when comparing the results obtained in pp collisions at $\sqrt{s} = 13$ TeV and $\sqrt{s} = 5$ TeV. The ratio of Ξ yields over K_S^0 yields as a function of midrapidity multiplicity is shown in Figure 2.10 (b). The full and transverse-to-leading yield ratios are found to increase with multiplicity, in agreement with the expected strangeness enhancement hierarchy with the hadron strangeness content. The toward-to-leading yield ratio shows an increasing trend with multiplicity as well within the uncertainties but is found to be lower with respect to full and out-of-jet ratios. The toward- and transverse-to-leading ratios are found to increase with increasing multiplicity with proportional slopes. These results suggest that out-of-jet processes are the dominant contributor to strange particle production in pp collisions. However, strangeness enhancement with multiplicity is also observed in hard processes. The ALICE Collaboration has also measured the production of (multi-)strange hadron yields selecting collision events based on the transverse sphericity estimator. The transverse sphericity allows to categorise events by their azimuthal topology, separating particle production in collisions dominated by soft initial interactions from collisions dominated by a single hard scattering. It is calculated as:

$$S_O^{p_T=1} = \frac{\pi^2}{4} \min_{\hat{n}} \left(\frac{\sum_i |p_{\hat{T},i} \times \hat{n}|}{N_{\text{trks}}} \right) .$$

where $p_{\hat{T},i}$ represents the transverse momentum unit vector, N_{trks} is the number of charged particles in a given event, and \hat{n} is the unit vector that minimises $S_O^{p_T=1}$. By construction, the value of transverse sphericity runs from 0 to 1, as the distribution of particles deviates from the jetty-like to an isotropic structure respectively, i.e. $S_O^{p_T=1} = 0$ corresponds to “pencil-like” (hard) events and $S_O^{p_T=1} = 1$ to the isotropic limit (soft events), as displayed in Fig. 2.11.



(a)



(b)

Fig. 2.10 (a) K_S^0 (a) yields per trigger particle and per unit of $\Delta\eta\Delta\phi$ in the full, toward- and transverse-to-leading azimuthal regions. The yields are reported as a function of the midrapidity multiplicity. (b) Ratio between Ξ and K_S^0 full, toward- and transverse-to-leading yields as a function of charged particle multiplicity at midrapidity [63].

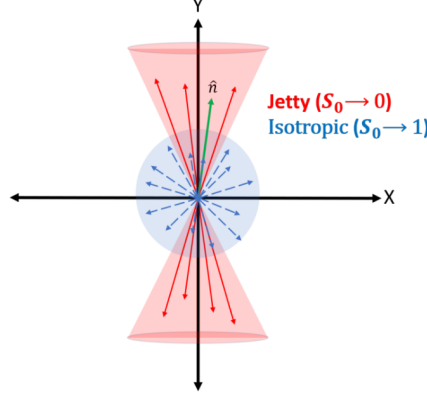


Fig. 2.11 Jetty and isotropic events in the transverse plane. Figure from [64].

The p_T -differential relative yields of Ξ hadrons to π mesons are shown in high multiplicity events (0-10% $N_{\text{tracklets}}^{|\eta|<0.8}$ class) for high ($S_O^{p_T=1} > 0.833$) and low ($S_O^{p_T=1} < 0.625$) values of transverse sphericity in Fig. 2.12. A suppression of strange hadrons across the entire measured p_T range is observed for events with jetty topologies, while an enhancement is observed for isotropic topologies. This observation suggests that the abundance of strange hadrons in high-multiplicity events is not driven by the hardest process in the collision, in agreement with the results discussed previously in this section.

2.2.2 Model description of strange hadron production

In order to understand the origin of the observed strangeness increase with multiplicity in small collision systems, the experimental data are compared with projections from various models. In this section, the strange hadron yields measured in pp collisions are compared to the predictions of a statistical hadronisation model based on the strangeness canonical suppression approach to Monte Carlo simulations implementing different microscopic models commonly used to describe particle production in pp collisions, namely PYTHIA8 [65] and HERWIG [66, 67], and finally to generators implementing core-corona models, such as EPOS LHC [68–70]. The results discussed in this section indicate that any of the available models cannot satisfactorily reproduce particle production in small systems and further experimental studies are needed to obtain a complete microscopic understanding of small hadronic collisions.

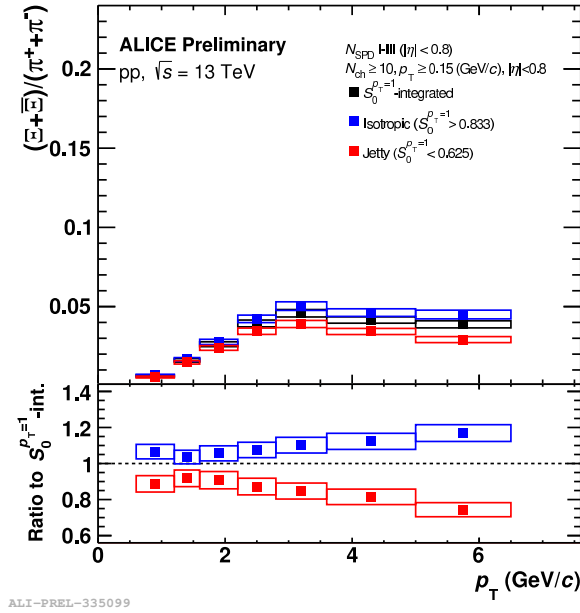


Fig. 2.12 p_T -differential Ξ to π ratio in the jetty, isotropic and spherocity-integrated events in the multiplicity class [0-10]%. The multiplicity estimation is based on the number of SPD tracklets within $|\eta| < 0.8$.

Canonical suppression

As discussed in Section 1.2.3, strange hadron production in central heavy-ion collisions is successfully described by statistical hadronisation models based on a grand canonical ensemble. The picture of statistical hadronisation can be extended to smaller systems such as pp or even e^+e^- collisions. In a small system, the conservation law of a quantum number, e.g. strangeness must be implemented locally on an event-by-event basis (canonical formulation). Therefore, the conservation of strangeness is guaranteed explicitly and not only on average, while the bulk of the particles is still well described in the grand-canonical ensemble. The canonical conservation of quantum numbers is known to severely reduce the phase space available for particle production, leading to canonical suppression (CS). Deviations from the grand-canonical description, which is based on the chemical freeze-out temperature (T_{ch}), the baryo-chemical potential μ_B and the correlation volume V_c , can be accommodated by introducing an additional parameter to consider the incomplete thermalisation of strange (γ_s) quarks. In the case of non-equilibrium, these parameters are smaller than one. Studies based on THERMUS [71] were used to describe the evolution of multi-strange particle production in pp and p-Pb collisions as a function of event multiplicity, displayed in Fig. 2.13. In these studies, the strangeness saturation parameter is fixed to $\gamma_s = 1$, and the chemical potentials μ_B of baryon and electric charge quantum number are set to zero. The chemical freeze-out

temperature T_{ch} is varied from 146 to 166 MeV, according to recent results from lattice QCD calculation and from fits to Pb–Pb experimental data [72]. All ratios are normalised to the high multiplicity limit, i.e. the mean ratio in the 0–60% most central Pb–Pb collisions for the data and the grand canonical saturation value for the model. This was done in order to decouple the influence of the freeze-out temperature and to isolate the dependence on the volume. The correlation volume V_c is imposed to be equal to the total volume of the system. From a quantitative point of view, almost all data points can be described within 1–2 standard deviations.

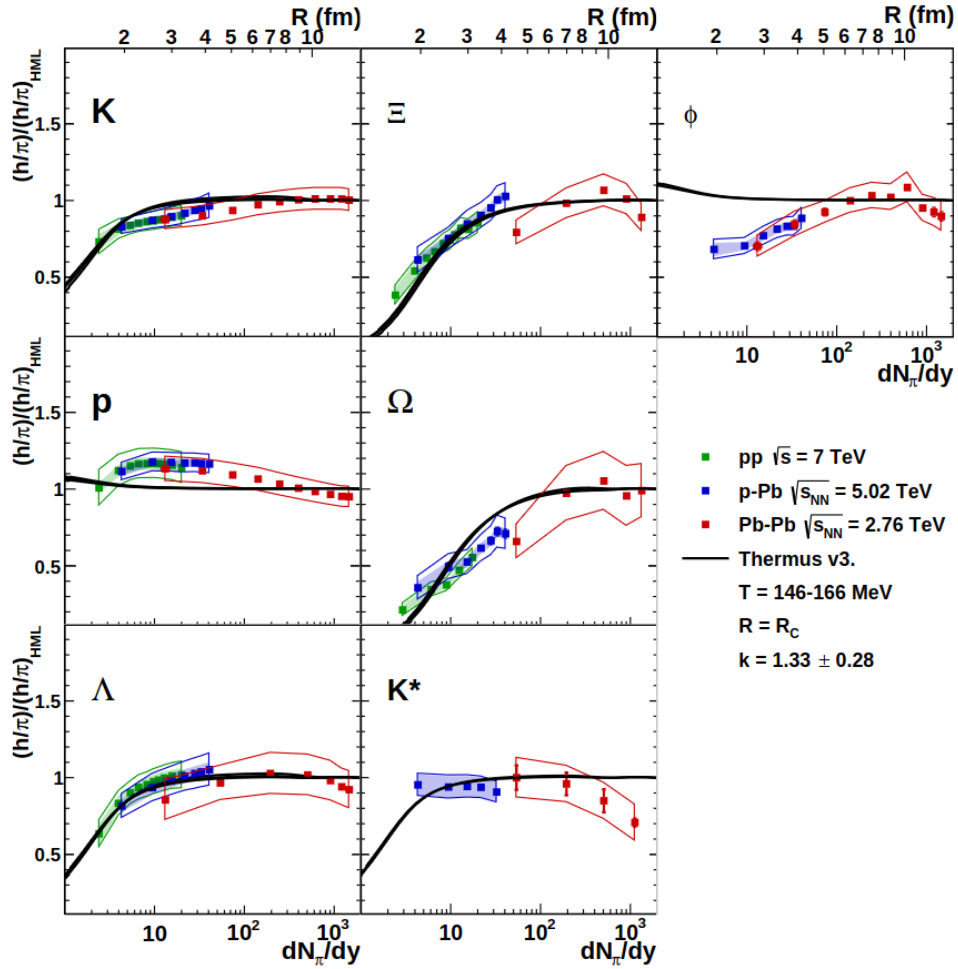


Fig. 2.13 Ratios of several particle species measured by the ALICE collaboration as a function of the midrapidity pion yields for pp, p–Pb and Pb–Pb colliding systems compared to the THERMUS strangeness canonical suppression model prediction (black line), in which only the system size is varied. The upper axis shows the radius R of the correlation volume $V = R^3$, which corresponds to the predicted particle ratios. Figure from [72].

A significantly different trend is observed for the proton and the ϕ meson, a strangeness neutral particle, for which a flat dependence as a function of event multiplicity is foreseen from the model but which shows an increasing trend in data. Overall, the strangeness canonical model provides a way to describe the strangeness enhancement with multiplicity across the different collision systems but fails to describe especially the proton and ϕ over pion yield ratios across different collision systems, indicating that a comprehensive description of all particle ratios has still to be achieved.

Common Monte Carlo models for pp collisions

As already mentioned, in a pp collision, the composite nature of the incoming protons can lead to multiple semi-perturbative parton-parton collisions, so-called Multi-Parton Interactions (MPI), as well as beam remnants and initial-state QCD radiation. Moreover, a high number of interacting partons can lead to the possibility of dynamically evolving colour topologies, collectively referred to as Colour Reconnection (CR) [73] phenomena. These are the baselines of the most commonly used generators in pp physics: PYTHIA and HERWIG. The description of the non-perturbative hadronisation process in PYTHIA is based on string fragmentation, in particular on the Lund String hadronisation Model [74]. The Lund String Model uses the massless relativistic string to model the QCD field between coloured objects. The string has a constant tension k , which gives rise to a linear potential, the endpoints of the string being the quark and the anti-quark. When it becomes energetically convenient for the string to break, a new $q\bar{q}$ pair forms through quantum mechanical tunnelling. This model is not able to describe the strangeness enhancement with multiplicity observed in pp collisions, as shown in Fig. 2.14. The predictions of PYTHIA8 (Monash tune 2013) underestimate the ratios and show no dependence with multiplicity, also if Colour Reconnection (CR) between partons is included. The description provided by PYTHIA8 improves if overlapping strings are allowed to interact with each other, forming colour ropes. The implementation of colour ropes results in a higher effective string tension, which determines the enhancement of strange baryon production, giving rise to larger rates of strange baryons. Fig. 2.14 shows PYTHIA8 with colour ropes can better describe the strangeness enhancement with multiplicity. The results in Fig. 2.14 are also compared to predictions from the HERWIG7 model, which implements hadronisation in a clustering approach including baryonic ropes, a reconnection scheme which increases the probability of forming baryons. HERWIG7 shows a larger deviation from the data than PYTHIA8, including colour ropes. Overall, the agreement between MC generators and measured hadron-to-pion ratios worsens for particles with a larger strangeness content.

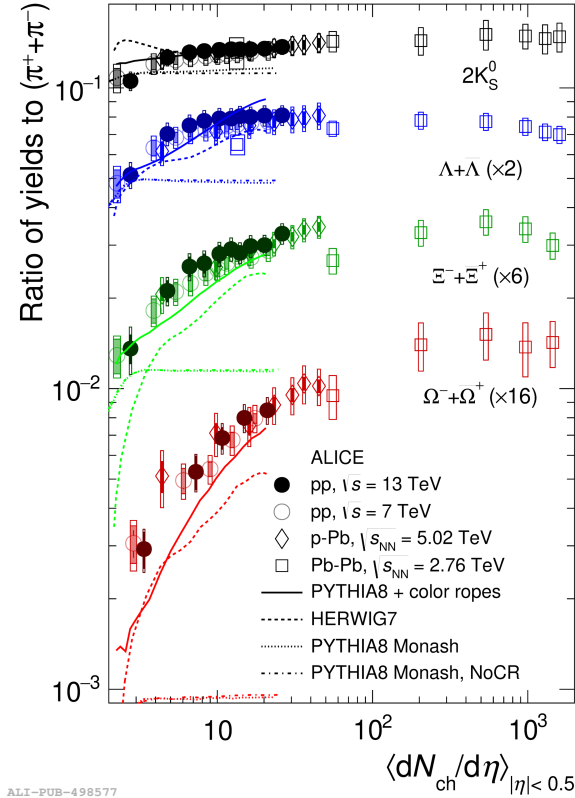


Fig. 2.14 Ratios of (multi-)strange hadron yields to pions as a function of the charged particle multiplicity measured at midrapidity. The open (shaded) boxes represent full (multiplicity uncorrelated) systematic uncertainties. Different lines represent predictions of different MC generators for pp collisions at $\sqrt{s} = 13$ TeV. Figure from [75].

Core-corona model

The core-corona model describes the strongly interacting system produced in a heavy-ion collision as divided into a *core* region, characterised by high energy density and by the formation of a deconfined medium, and a *corona*, a peripheral region with lower density. Hadronisation in the core occurs thermally, while particle production in the corona occurs through string breaking. In this model, the dominant process of final hadron production is supposed to change gradually from string fragmentation at the low-multiplicity limit to statistical hadronisation at the high-multiplicity limit. At intermediate multiplicity, final hadron production would be a superposition of these two contributions. As multiplicity increases, the high-density region, in which the matter is mostly thermalised, is supposed to become larger. As a result, the hadrons from thermalised matter dominate the final hadron yields. The core-corona model has also been implemented in the EPOS LHC event generator for smaller collision systems, such as $p\text{-Pb}$ and pp collisions. Recently, the

core-corona model has been implemented in the Dynamical Core-Corona Initialisation framework (DCCI) [69, 70], which deals with dynamics of the core (equilibrium) and the corona (non-equilibrium) at the same time. In the DCCI framework, the multiplicity dependence of multi-strange baryon production in small and large collision systems is attributed to a continuous change of the fractions of the core and the corona components as the multiplicity increases. This model generates the initial partons using PYTHIA8 or its heavy-ion implementation, PYTHIA8 Angantyr [76]. Figure 2.15 shows the particle yield ratios to charged pions produced at midrapidity as functions of charged particle multiplicity in pp and Pb–Pb collisions compared with the ALICE experimental data. Results from PYTHIA8 for pp collisions and PYTHIA8 Angantyr for Pb–Pb are also displayed. Figure 2.15 shows a smooth enhancement of (multi-)strange hadron to pion ratios, converging at low multiplicity to the value obtained from string fragmentation and at high multiplicity to the prediction from hydrodynamics. Overall, the core-corona model provides a way to describe the strangeness enhancement in small collision systems but fails to quantitatively reproduce the experimental data.

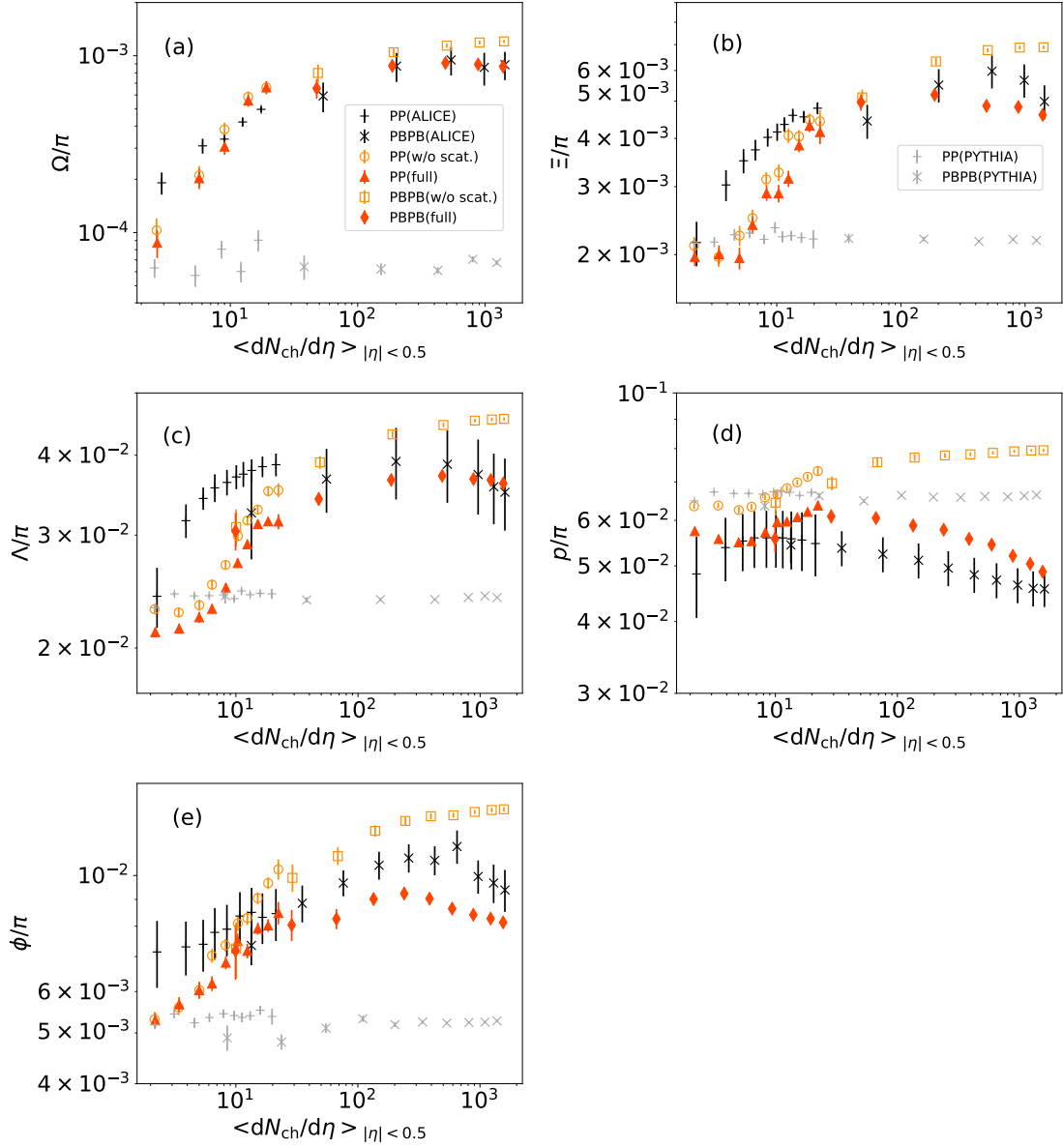


Fig. 2.15 Particle yield ratios of (a) Ω (Ω^\pm), (b) Ξ (Ξ^\pm), (c) Λ ($\Lambda + \bar{\Lambda}$), (d) protons ($p + \bar{p}$) and (e) ϕ to charged pions (π^\pm) as functions of charged particle multiplicity at midrapidity in pp and Pb–Pb collisions. Results from full simulations of DCC12 in pp collisions at $\sqrt{s} = 7$ TeV (full red triangles) and Pb–Pb collisions at $\sqrt{s_{NN}} = 2.76$ TeV (full red diamonds) collisions are compared with the ALICE experimental data in pp (black pluses) and Pb–Pb (black crosses) collisions. Results from Pythia8 in pp collisions (grey pluses) and from Pythia8 Angantyr in Pb–Pb (grey crosses) collisions are plotted as references. Results without hadronic rescatterings are also plotted for pp (open orange circles) and PbPb (open orange squared) collisions. Figure from [70].

Chapter 3

Effective energy and multiplicity

Studying the properties of the hadronic system produced in high-energy particle collisions is of fundamental interest to investigate the underlying mechanisms at play in different interaction systems. In particular, event properties such as the charged-particle multiplicity are key experimental observables, providing information on the final hadronic state produced in the interaction and on the initial dynamics of the collision. The results from several past experiments show that the dependence of the charged-particle multiplicity on the centre-of-mass energy is characteristic of the specific initial state under consideration. In particular, in the case of $pp(p\bar{p})$ collisions the charged particle multiplicity at a fixed centre-of-mass energy is observed to be systematically lower than in e^+e^- data at the same energy. However, a universal dependence can be observed if the appropriate definition of the energy available for particle production (“effective energy”) is used. In this chapter, we introduce the concept of effective energy in particle collisions and discuss the main results published on this topic. We then explore the possibility to perform effective energy studies in very high energy hadronic collisions with ALICE at the CERN Large Hadron Collider (LHC).

3.1 Multiplicity studies in different collision systems

The charged-particle multiplicity is an experimental observable of key relevance in high-energy particle collisions, being characteristic of the final state produced in the interaction but also strongly related to the energy available in the early stages of the collision. A detailed study of particle production in different collision systems and over a wide range of centre-of-mass energies is crucial to investigate analogies and differences between underlying production mechanisms at play in these interactions. The average charged-particle multiplicity was measured by several experiments in different interaction systems (e^+e^- , pp , $p\bar{p}$, pA , AA), and, at first sight, there seems to be no universality among different collisions

at fixed centre-of-mass energy. In particular, a discrepancy is observed between interactions involving only leptons in the initial state (i.e. e^+e^-) and hadronic collisions (i.e. pp), suggesting the possibility of different particle production mechanisms in the two interacting systems. For a long time, this fundamental difference was attributed to the nature of the interaction, driven by the strong force for hadronic collisions and by the electromagnetic force for leptonic ones. Some striking results regarding this observation were obtained by a Collaboration including the University of Bologna, CERN and LNF (National Laboratory of Frascati), which will be referred to as Bologna-CERN-Frascati (BCF) Collaboration in the following [1–9]. These results were obtained from data collected at the CERN ISR¹ (Intersecting Storage Rings), with the goal to investigate the analogies and the differences between pp and e^+e^- collision systems, and to explore the universality of charged-particle production across collision systems when an appropriate definition of “effective energy” is used.

3.1.1 Results from previous experiments

The average charged-particle multiplicity in e^+e^- collisions has been studied over the years by several experiments. A wide centre-of-mass energy range was explored, reaching the highest energies at LEP (Large Electron-Positron Collider) and DESY (Deutsches Elektronen-Synchrotron). The average charged multiplicity in e^+e^- collisions follows a logarithmic dependence on the centre-of-mass energy \sqrt{s} , as displayed in Fig. 3.1. However, when other initial states are considered, the average charged multiplicity is characterised by a significantly different dependence on \sqrt{s} . In particular, in the case of pp ($p\bar{p}$) collisions the charged particle multiplicity at a fixed centre-of-mass energy is observed to be systematically lower than e^+e^- at the same energy. Figure 3.2 shows this effect, displaying a collection of measures from different experiments in e^+e^- (full black symbols) and pp ($p\bar{p}$) (open symbols) collision systems. In particular, the multiplicities in the two collision systems become strikingly similar when the pp ($p\bar{p}$) points are plotted at half their collision energy. The Bologna-CERN-Frascati Collaboration provided some interesting insights into this observation, which will be discussed in the following, using data collected at the ISR at $(\sqrt{s})_{pp} = 30, 33, 62$ GeV [1–9]. The key point of their study was to explain the different dependence of the charged multiplicity on \sqrt{s} considering that, while in e^+e^- collisions the energy available for particle production coincides with the full centre-of-mass energy, in $pp(p\bar{p})$ this energy is reduced with respect to the full \sqrt{s} due to the so-called “leading effect”. This phenomenon consists in a high probability to emit (leading) baryons with large lon-

¹The ISR was the world’s first hadron collider, running at CERN from 1971 to 1984. The maximum centre-of-mass energy for pp and $p\bar{p}$ reached was 62 GeV.

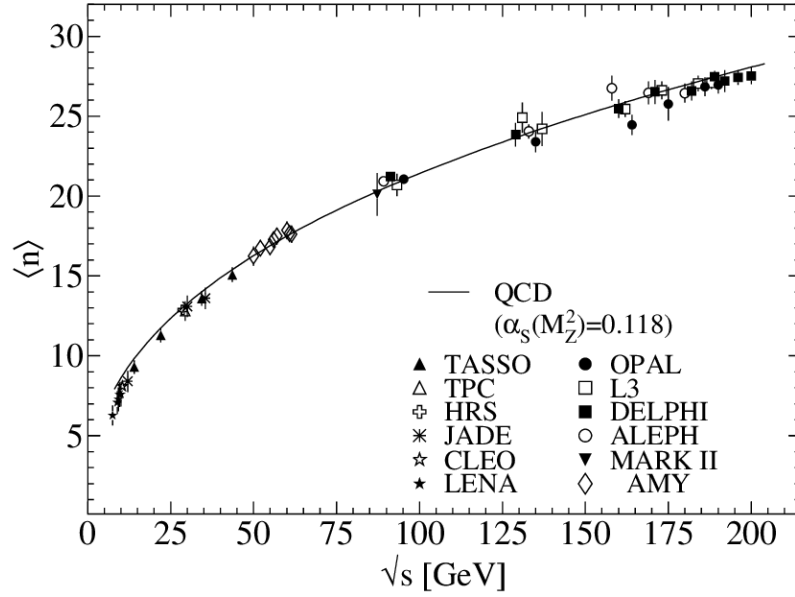


Fig. 3.1 Average multiplicity of charged particles measured in e^+e^- collisions by various experiments at LEP and DESY. Figure from Ref. [77].

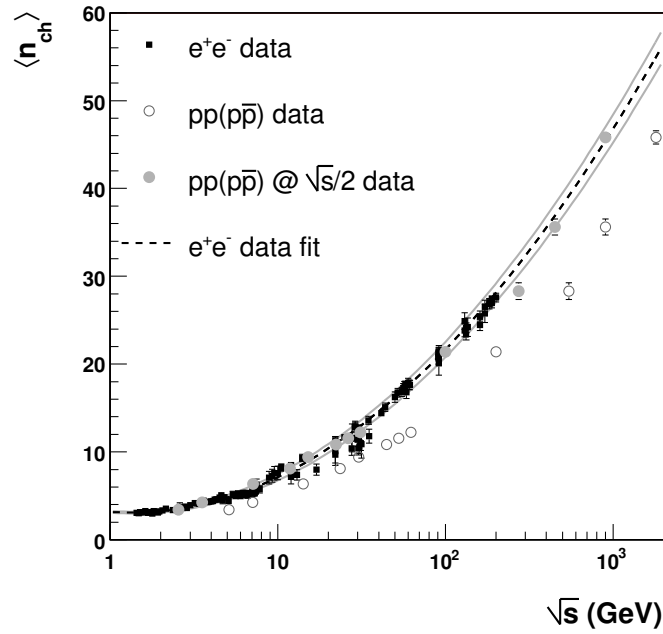


Fig. 3.2 Average charged particle multiplicity measured in e^+e^- (full black symbols) and $pp(p\bar{p})$ (open symbols) collisions. The full grey symbols indicate the $pp(p\bar{p})$ data after the centre-of-mass energies have been scaled by a factor $\frac{1}{2}$. Figure from Ref. [78].

itudinal momenta in the forward direction (along the incident beams), which carry away a fraction of the incident primary energy and reduce the “effective” energy available for particle production. The leading effect is related to the necessity of quantum number flow conservation between the initial and the final state of a hadronic interaction, and in pp collisions this consists mainly in proton and neutron emission. Considering the leading effect, and defining a new quantity called effective energy, common universal features among the leptonic and hadronic collision systems can be observed. According to the experimental results obtained up to the highest energies studied so far, e^+e^- collisions do not produce leading hadrons in their final state, in fact, the leading effect holds true provided a hadron is present in the initial state.

3.2 The effective energy

The leading effect reduces the total energy available for particle production in pp ($p\bar{p}$) collisions with respect to the full centre-of-mass energy. The definition of a novel quantity, the effective energy $E_{\text{effective}}$, allows to properly account for this “energy loss” when considering hadronic collisions, and helps to shed light on the differences between pp ($p\bar{p}$) and e^+e^- . Given two protons in the initial state, let $\mathbf{q}_1^{\text{inc}}$ and $\mathbf{q}_2^{\text{inc}}$ be their four-momenta, the total invariant four-momentum of the two colliding protons is:

$$\mathbf{q}_{\text{tot}}^{\text{inc}} = \mathbf{q}_1^{\text{inc}} + \mathbf{q}_2^{\text{inc}} \quad . \quad (3.1)$$

The centre-of-mass energy can be expressed as:

$$\sqrt{s} \equiv \sqrt{(\mathbf{q}_{\text{tot}}^{\text{inc}})^2} = E_1^{\text{inc}} + E_2^{\text{inc}} \quad , \quad (3.2)$$

where E_i^{inc} is the incident energy of each colliding proton. The total four-momentum carried away by leading baryons in the two hemispheres can be written as:

$$\mathbf{q}_{\text{tot}}^{\text{lead}} = \mathbf{q}_1^{\text{lead}} + \mathbf{q}_2^{\text{lead}} \quad . \quad (3.3)$$

The total effective energy $\sqrt{(\mathbf{q}_{\text{tot}}^{\text{had}})^2}$ will then be:

$$E_{\text{effective}} \equiv \sqrt{(\mathbf{q}_{\text{tot}}^{\text{had}})^2} = \sqrt{(\mathbf{q}_{\text{tot}}^{\text{inc}} - \mathbf{q}_{\text{tot}}^{\text{lead}})^2} \quad . \quad (3.4)$$

Equivalently, the leading effect can be conveniently studied using fractional energy or momentum variables such as the Feynman- x (x_F):

$$(x_F)_i = 2 \frac{(p_L)_i}{\sqrt{s}} \quad \text{for } i = 1 \text{ or } 2, \quad (3.5)$$

where $(p_L)_i$ is the longitudinal momentum of the leading baryon in the hemisphere i . The value of x_F ranges from 0 to 1. The effective energy can then be calculated as a function of the Feynman- x as:

$$E_{\text{effective}} \equiv \sqrt{(\mathbf{q}_{\text{tot}}^{\text{had}})^2} = \sqrt{s \cdot [1 - (x_F)_1] \cdot [1 - (x_F)_2]} \quad . \quad (3.6)$$

The definitions in Eq. 3.4 and 3.6 are Lorentz invariant. If the two hemispheres² were independent with respect to the leading effect, the total effective energy $E_{\text{effective}}$ in the event can be calculated as:

$$E_{\text{effective}} = 2(E_{\text{effective}})_i = 2 \left(\frac{\sqrt{s}}{2} - (E_{\text{leading}})_i \right) \quad \text{for } i = 1 \text{ or } 2 \quad , \quad (3.7)$$

where $(E_{\text{leading}})_i$ is the energy of the leading baryon in the hemisphere i . The independence of the two event hemispheres with respect to the emission of leading baryons was experimentally observed at the ISR by the BCF Collaboration [79], by studying the Feynman- x (x_F) distribution of emitted leading particles. The results of this study are presented in Fig. 3.3 (a) as a scatter plot of the quantities x_1^{leading} and x_2^{leading} , representing the Feynman- x of leading protons in the two hemispheres. The uniformity of the points in the plot confirms that no correlation is observed between the leading protons emitted in the two hemispheres. Moreover, Fig. 3.3 (b) shows the average value of x_2^{leading} , which displays a flat dependence with x_1^{leading} as expected in case of no correlation between the two observables.

3.2.1 Experimental results on the leading energy

In Sect. 3.1, we showed that at first sight there is no universality in the final state hadrons produced in leptonic and hadronic collision systems at fixed centre-of-mass energy. However, one can observe common universal features when accounting for the leading effect in hadronic interactions. The charged-particle multiplicity in e^+e^- collisions and pp ($p\bar{p}$) collisions becomes strikingly similar when the pp ($p\bar{p}$) points are plotted as a function of the effective energy as opposed to \sqrt{s} , as displayed in Fig. 3.4. This is a first evidence for

²The hemispheres are defined with respect to a plane transverse to the direction of the incident beams in the centre-of-mass system.

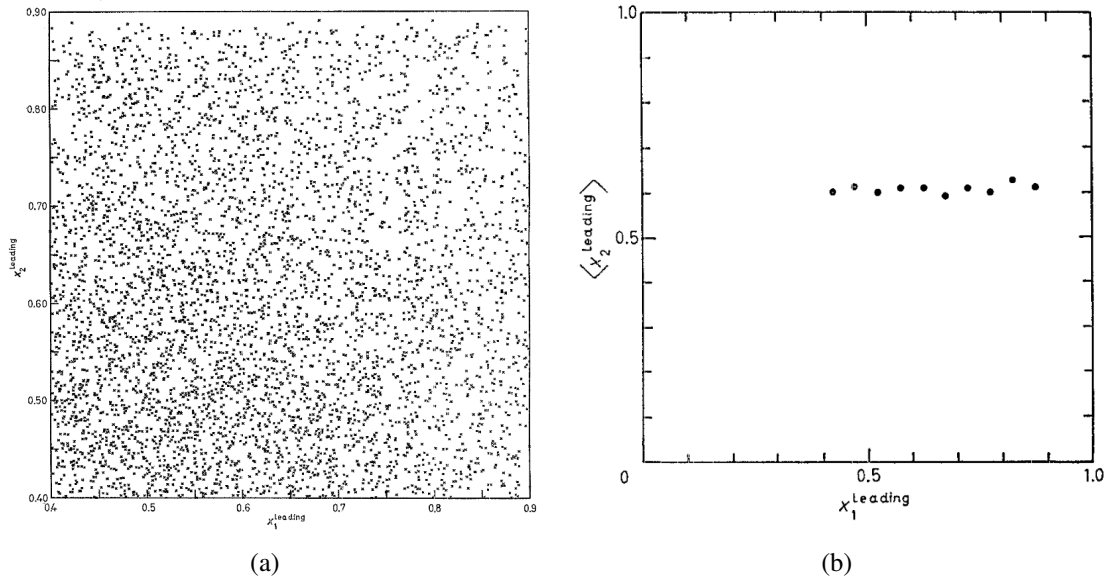


Fig. 3.3 (a) Scatter plot of the quantities x_1^{leading} and x_2^{leading} , representing the Feynman- x of leading protons in the two hemispheres. Each point in the scatter plot represents one collision event. (b) Average value of x_2^{leading} as a function of x_1^{leading} . Figures from Ref. [79].

universality features between pp and e^+e^- collisions, observed by the BCF Collaboration using pp collisions at $\sqrt{s} = 62$ GeV collected with the Split Field Magnet (SFM)³ experiment at the ISR. The pp data in this analysis refer to a minimum bias event sample, from which elastic and diffractive processes were excluded, with leading protons detected in the range $0.3 < x_F < 0.8$. Besides the average charged-particle multiplicity, other observables were considered by the Bologna-CERN-Frascati Collaboration to shed light on similarities between e^+e^- and pp collisions, such as the longitudinal and transverse momentum distributions of charged particles, the ratio of “charged” to total energy of the multiparticle hadronic system produced in the collision, the event planarity and sphericity etc. In this section, we will discuss some of these studies concerning the longitudinal and transverse momentum distributions, details on other results obtained by the BCF Collaboration can be found in Ref. [80, 81] and references therein. As reported in Fig. 3.5 each nominal centre-of-mass energy corresponds to a range of possible effective energies, which for $\sqrt{s} = 62$ GeV goes from few GeV up to about 40 GeV. A crucial point to prove the universality of the effective energy was to determine whether the hadronic systems produced at the same $E_{\text{effective}}$, but for different values of E_{inc} , had the same properties. For this purpose, results obtained in

³The Split Field Magnet (SFM) was the largest spectrometer for particles from collisions in the ISR. It could determine particle momenta in a large solid angle, but was designed mainly for the analysis of forward travelling particles.

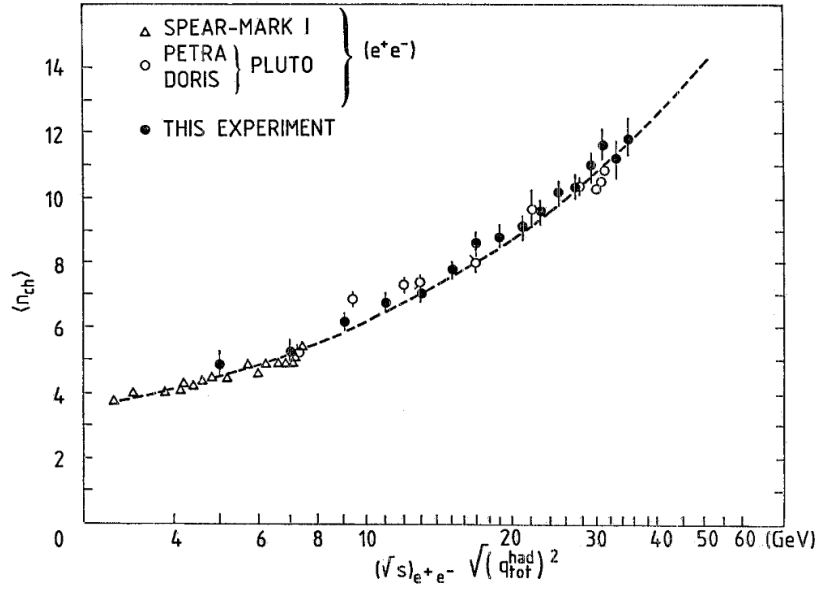


Fig. 3.4 Average charged multiplicity as a function of the effective energy $E_{\text{effective}}$, here indicated as $\sqrt{(q_{\text{tot}}^{\text{had}})^2}$, for e^+e^- and pp collisions. The pp data were collected by the SFM experiment at the CERN ISR (full circles). The results from e^+e^- collisions from different experiments are also shown (open circles and triangles). Figure from Ref. [82].

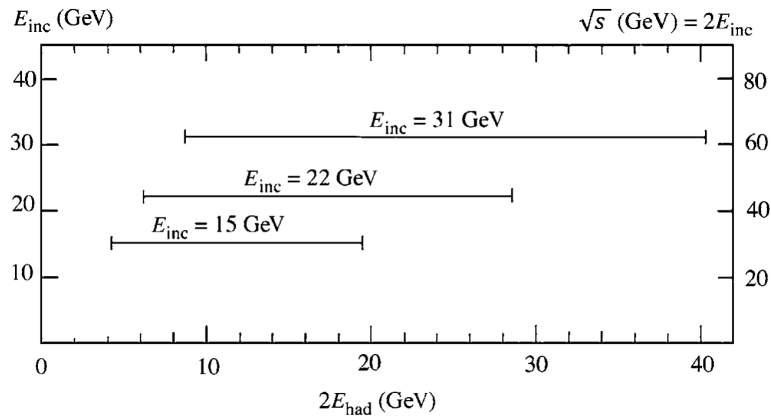


Fig. 3.5 In the abscissa the effective hadronic energy $2E_{\text{had}} \equiv E_{\text{effective}}$ (GeV) available for particle production. In the vertical axis on the left the beam energy, E_{inc} , on the right the total nominal energy of the ISR, $\sqrt{s} = 2E_{\text{inc}}$. Figure from Ref. [80].

the same range of effective energy but at different values of nominal \sqrt{s} were compared. In particular, three scenarios of incident energies were considered in this study: $E_{\text{inc}} = 15, 22$ and 31 GeV, corresponding to nominal energies of $\sqrt{s} = 30, 44$, and 62 GeV. Let's consider for instance the inclusive momentum distribution of particles produced in e^+e^- and pp collisions. This observable can be expressed as a function of the fractional variable x_R^* :

$$x_R^* = p/E_{\text{effective}} \quad , \quad (3.8)$$

obtained by dividing the momentum p of the particle by the effective energy of the system rather than by the centre-of-mass energy. Figures 3.6 (a) show the momentum distribution of charged particles at the nominal pp centre-of-mass energy of $\sqrt{s} = 30$ GeV, for effective energies in the range $4 \leq E_{\text{effective}} \leq 6$ GeV. Similarly, Fig. 3.6 (b) shows the momentum distribution at the nominal pp energies $\sqrt{s} = 44$ and 62 GeV, for $28 \leq E_{\text{effective}} \leq 32$ GeV. Assuming no leading effect in leptonic collisions, pp data are compared to e^+e^- collisions at $\sqrt{s} = 4.8$ GeV and $27.4 \leq \sqrt{s} \leq 31.6$ GeV, respectively. The e^+e^- and pp data at equivalent effective energies are found to be in remarkable agreement. Similar results are obtained when considering the inclusive transverse momentum distributions. Figure 3.7 shows the results obtained by the BCF Collaboration at $\sqrt{s} = 30$ GeV selecting a sample of events in the effective energy range $11 \leq E_{\text{effective}} \leq 13$ GeV. Results are compared with e^+e^- data at $\sqrt{s} = 12$ GeV, and, also in this case, data show an excellent agreement between the two collision systems.

3.2.2 Leading effect in heavy-ion collisions

In the most simple description of a pp collision, on average a single constituent quark from each nucleon takes part in the interaction and the rest can be considered as spectators. In this simplified case, the total $E_{\text{effective}}$ corresponds to the energy of a single quark pair, namely $1/3$ of the total \sqrt{s} . In addition, at high collision energies several models predict the possibility for multiple parton interactions to occur in the same collision, which would increase the fraction of initial energy available for particle production. In head-on heavy-ion collisions, described by the Glauber model, each participating nucleon is typically struck on average 3 to 6 times as it passes through the oncoming nucleus, the exact value of this number is determined by the energy-dependent nucleon-nucleon inelastic cross-section $\sigma_{NN}(s)$. As a consequence, in AA collisions a much larger fraction of the energy from the colliding nucleons (participants) is expected to be available for particle production. Figure 3.8 shows the average charged-particle multiplicity for pp ($p\bar{p}$), e^+e^- , Au–Au and Pb–Pb events as a function of the centre-of-mass energy per binary collision, where the multiplicity is scaled by a factor $\langle N_{\text{part}}/2 \rangle$. Heavy-ion

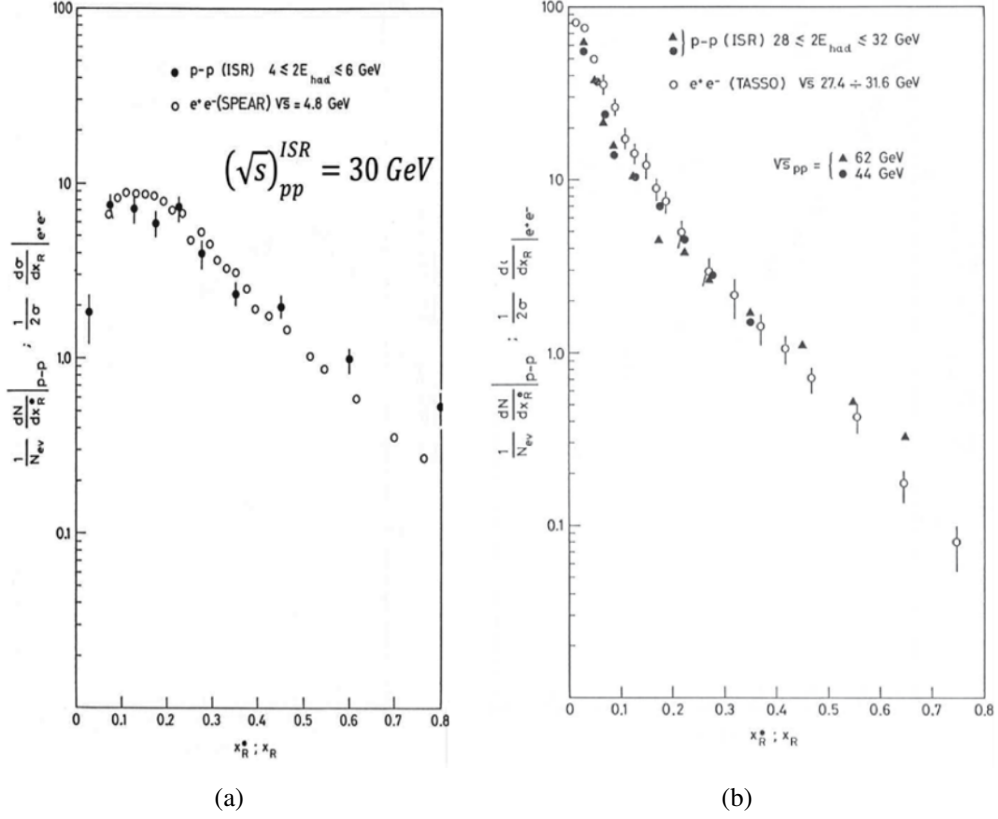


Fig. 3.6 Inclusive momentum distributions in pp collisions for $4 \leq E_{\text{effective}} \leq 6$ GeV (a) and $28 \leq E_{\text{effective}} \leq 32$ GeV (b), produced at three ISR nominal energies: $\sqrt{s} = 30, 44, 64$ GeV. TASSO and SPEAR e⁺e⁻ data are shown at \sqrt{s} compatible with pp effective energies. Figures from Ref. [80].

data are shown for central Au–Au events collected with PHOBOS at RHIC [83] and with E895 at the AGS [84], and Pb–Pb events recorded with NA49 at the SPS [85]. The scaled total charged multiplicity in AA collisions is in good agreement with the one measured in e⁺e⁻ for $20 < \sqrt{s_{\text{NN}}} < 200$ GeV, suggesting a substantially reduced leading particle effect in heavy-ion collisions at high energies. For $\sqrt{s_{\text{NN}}} < 20$ GeV, heavy-ion data do not follow the e⁺e⁻ trend, which may indicate a non-negligible leading effect in this energy range.

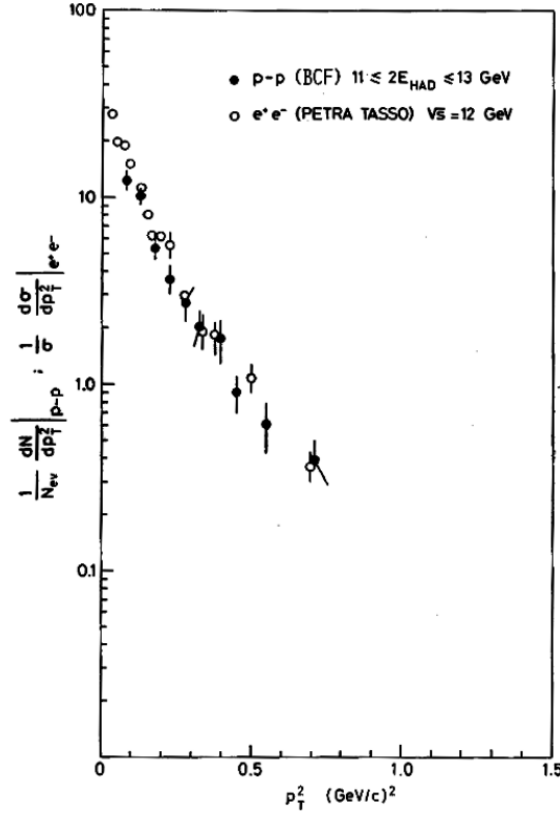


Fig. 3.7 Inclusive transverse momentum distribution measured in pp collisions at the ISR nominal energy $\sqrt{s} = 30$ GeV, for $11 \leq E_{\text{effective}} \leq 13$ GeV. The results are compared with e^+e^- data at $\sqrt{s} = 12$ GeV measured by TASSO at the PETRA electron-positron collider. Figure from Ref. [4].

3.2.3 Studying the leading effect at the LHC

An analysis in terms of the leading energy can be extended to higher centre-of-mass energies at the LHC. We mentioned that one way of estimating the effective energy is by measuring the energy of the leading baryons (E_{leading}) emitted in each event hemisphere. This kind of analysis requires a detector able to measure particles with large longitudinal momenta with a good energy resolution. The ALICE experiment at CERN has a very good capability for this kind of measurement thanks to the Zero-Degree Calorimeters (ZDC), detectors covering very forward rapidities on both sides with respect to the interaction point. A detailed description of the ZDC detectors will be provided in the next Chapter. In Ref. [78] an exploratory study on the possibility to measure the leading energy through the ZDC is reported, proving that ALICE is well suited to measure forward-going nucleons over a wide range of energies. In Fig. 3.9 the different effective energy ranges explored at ISR are compared to the one reached at the LHC are reported [86, 87]. The ALICE Collaboration has also recently published new

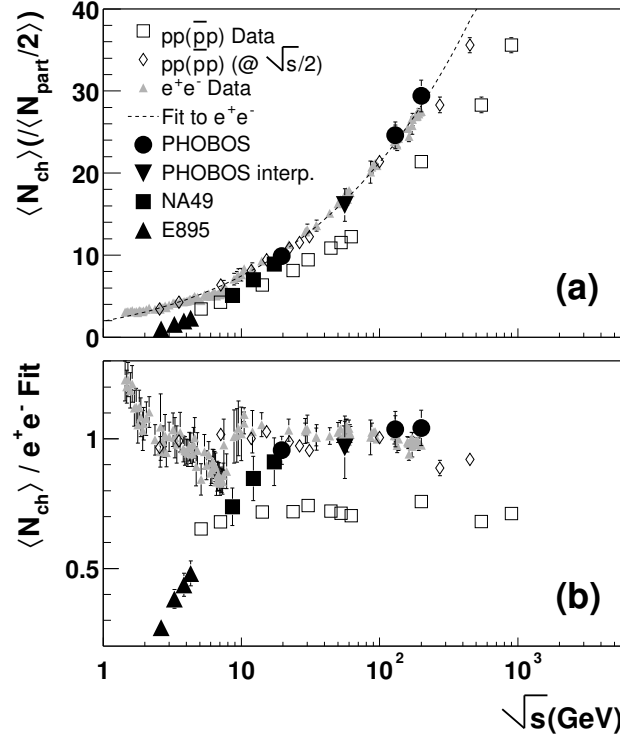


Fig. 3.8 (a) Charged multiplicity $\langle N_{\text{ch}} \rangle$ in pp, $p\bar{p}$, e^+e^- , Au–Au and Pb–Pb events as a function of centre-of-mass energy per binary collision. The heavy-ion data are normalised by $\langle N_{\text{part}}/2 \rangle$. (b) The data in (a) are divided by a perturbative QCD fit to the e^+e^- data (dotted line). Figure from Ref. [83].

results on the correlation between central rapidity particle production and the energy detected by the ZDC in pp and p–Pb collisions [88]. Indeed, the correlation between observables measured in rapidity regions that are causally disconnected in the evolution of the system provides key information on how the energy of the colliding protons is transferred from beam to central rapidities. These results confirm that the charged particle multiplicity produced in the central rapidity region is strongly anti-correlated with the very forward (“zero degree”) activity. In this thesis, we perform the first analysis addressing the characterisation of strange particle production at midrapidity with the leading energy, unlocking the unique possibility to shed light on strange quark production mechanisms in high-energy pp collisions. In fact, the nature of the similarities observed between pp and Pb–Pb collisions in terms of strangeness production is still not fully understood, as discussed in Chapter 2. This work introduces a novel approach to study strangeness production in pp collisions, introducing, for the first time, the concept of effective energy in hadronic collisions at the LHC. Disentangling the dependence of strange particle production on the multiplicity and on the effective energy

could be crucial to understand the nature of the similarities observed between small and large collision systems.

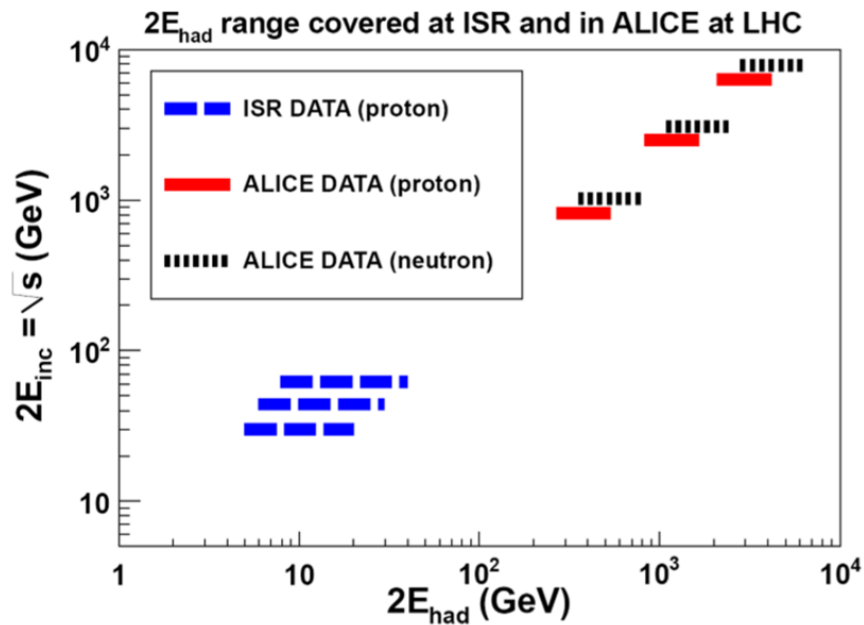


Fig. 3.9 Effective energy range (here indicated as E_{had}) covered at ISR and LHC as a function of \sqrt{s} . Figure from Ref. [86, 87].

Chapter 4

ALICE: A Large Ion Collider Experiment

ALICE (A Large Ion Collider Experiment) is a dedicated heavy-ion detector operating at the Large Hadron Collider (LHC) at CERN. In order to achieve its physics program ALICE was designed to study the high particle-multiplicity environment of ultra-relativistic Pb–Pb collisions, addressing the study of particle production in the widest possible momentum range, from the soft to the hard sector. By the time the LHC and ALICE became operative in 2010, the search for the quark-gluon plasma and its characterisation was already the main physics goal of various existing experiments. The heavy-ion collider at RHIC entered operation at the Brookhaven National Laboratory in 2000, and the first round of results from its experiments was an essential input for shaping the physics program for heavy-ion collisions at the LHC. The main goals of ALICE during its first physics program were to investigate the QGP properties to a new level of precision and to explore the phase diagram of strongly interacting matter at vanishing net baryon number density. However, besides focusing on heavy ion collisions, ALICE also exploits proton-proton and proton-lead collisions in LHC runs. The comparison between the three collision systems proved to be crucial not only to distinguish QCD properties with and without medium effects but also to test the limit conditions necessary for QGP formation.

4.1 The Large Hadron Collider

The Large Hadron Collider (LHC) [89] is a two-ring superconducting hadron collider operating at the European Organization for Nuclear Research (CERN) near Geneva. The LHC ring has a circumference of 26.7 km and is located underground between 50 m and 175 m deep.

It consists of ~ 1200 dipole magnets, used for bending the beams, and ~ 400 quadrupole magnets, for beam focusing. Inside the ring, two beams of protons or heavy ions circulate in opposite directions. The LHC is the last step of the CERN accelerator complex, shown in Fig. 4.1, a series of machines which accelerate particles to increasingly high energies in which each step boosts the energy of the particles before injecting them into the next accelerator of the sequence.

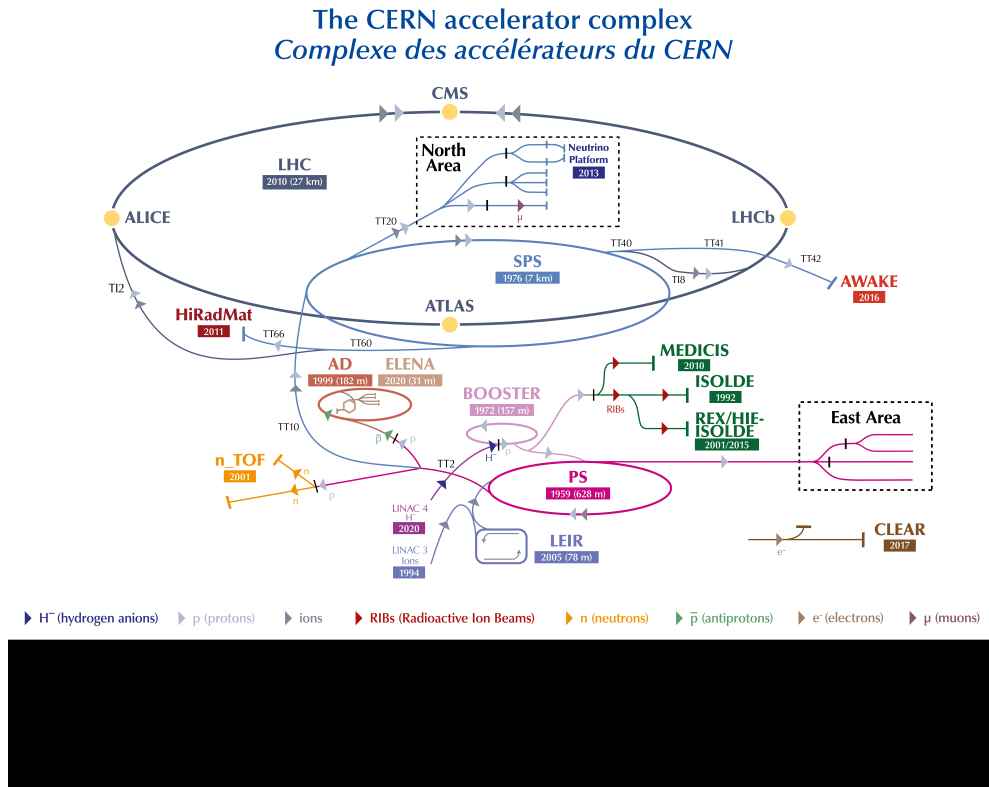


Fig. 4.1 The CERN accelerator complex. Figure from [90].

To create a proton beam, hydrogen atoms are stripped of electrons by applying an electric field. These protons are then injected from a linear accelerator (LINAC) [91] into the Proton Synchrotron Booster (PSB) [92] where the proton energy is increased. Afterwards, the beams pass to the Proton Synchrotron (PS) [93] for further acceleration and then are sent to Super Proton Synchrotron (SPS) [94] before the injection into the LHC. Each interaction point along the LHC ring is covered by a large detector system, each with its unique physical goals and research objectives. CMS (Compact Muon Solenoid) [95] and ATLAS (A Toroidal LHC ApparatuS) [96] were conceived to study the creation and the properties of the Higgs boson and to explore the physics beyond the Standard Model. The main purpose of LHCb (Large Hadron Collider beauty) [97] experiment is to study the CP violation in the heavy-

quark sector. Finally, ALICE was built to study the properties of the quark-gluon plasma (QGP) in heavy-ion collisions. The LHC is capable of accelerating pp and heavy ions at ultra-relativistic energies, summarised in Table 4.1.

Collision system	Collision energy (\sqrt{s} , $\sqrt{s_{NN}}$)
pp	0.9 , 2.76, 5.02, 7, 8.16, 13, 13.6 TeV
p-Pb	5.02 , 8.16 TeV
Pb-Pb	2.76, 5.02, 5.36 TeV
Xe-Xe	5.44 TeV

Table 4.1 Collision systems and energies at the LHC Run 1, 2 and 3. Run 3 energies are in bold.

4.2 ALICE 1 (Run 1 and 2)

The ALICE detector is located at the interaction point IP2 of the LHC. The apparatus that was in operation in the LHC Runs 1 and 2 (“ALICE 1”), and its performance is described in detail in Ref.[98] and [99]. The detector has been designed to cope with the high particle multiplicity environment expected in heavy-ion collision systems and to provide unique Particle IDentification (PID) performance that allows a comprehensive study of particle production down to very low transverse momentum (0.1 GeV/c). The ALICE detector setup is shown in Fig. 4.2.

4.2.1 ALICE sub-detectors

ALICE sub-detectors can be classified into three main groups, which will be discussed in the following: the barrel detectors, covering central pseudorapidities, the forward detectors, placed at forward rapidity, and the muon arm dedicated to muon identification. The ALICE reference coordinate system is a right-handed orthogonal Cartesian system with origin $(x, y, z) = 0$ at the interaction point (IP), where the z axis is parallel to the beam direction. The two sides of the detector along the z axis are labeled A (anti-clock wise, for positive z) and C (clock-wise, for negative z).

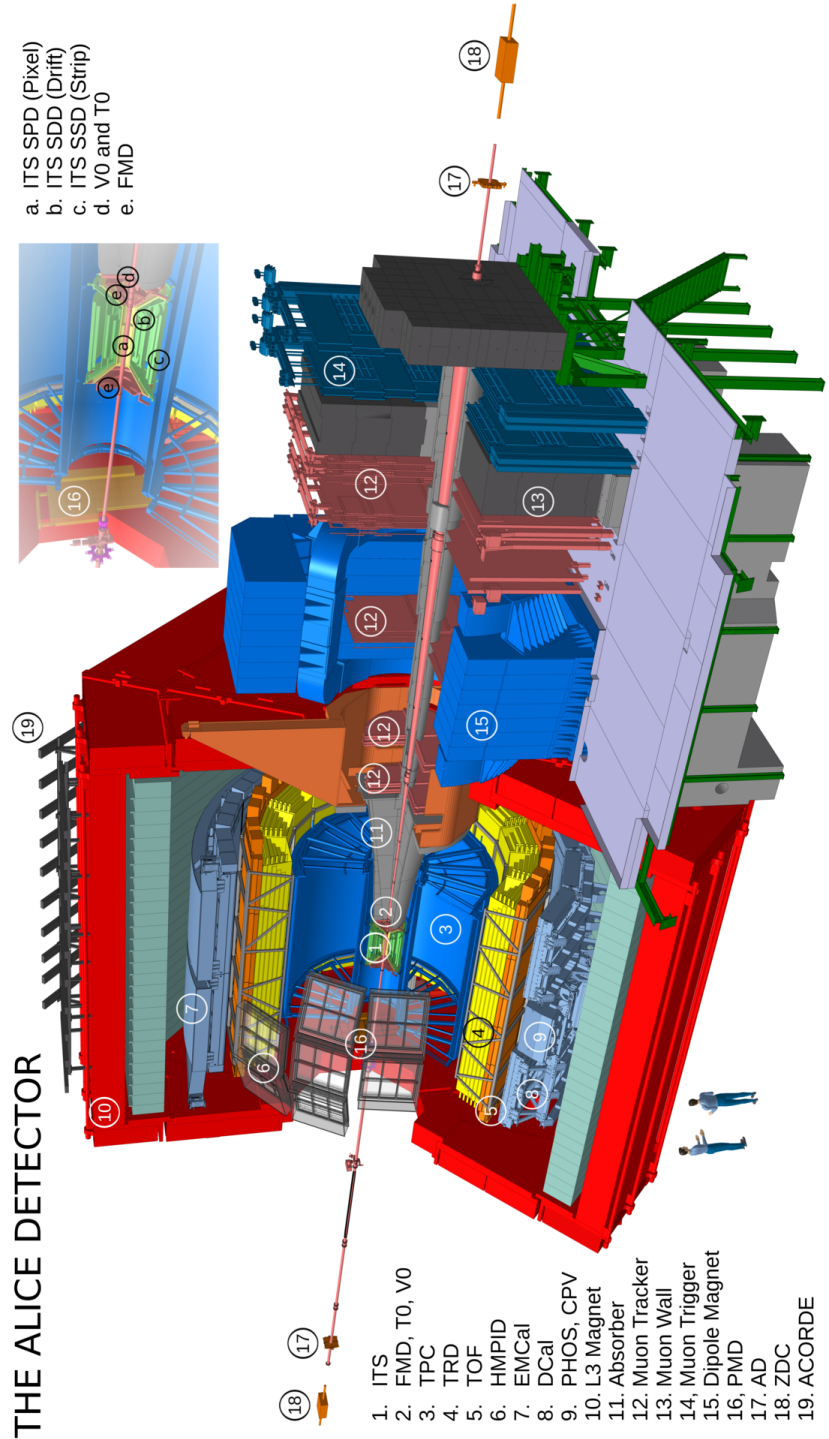


Fig. 4.2 Schematic view of the ALICE detector.

- **The central barrel detectors**, which include, starting from the interaction point and going outward:
 - the Inner Tracking System (ITS);
 - the Time Projection Chamber (TPC);
 - the Transition Radiation Detector (TRD);
 - the Time of Flight (TOF).

This group of subsystems have full azimuthal ($0 \leq \phi < 2\pi$) coverage with rapidity acceptance $|\eta| < 0.9^+$ and is enclosed in the L3 solenoid magnet, which provides a 0.5 T nominal magnetic field. They are mostly dedicated to vertex reconstruction, tracking, particle identification and momentum measurement. In the mid-rapidity region, there are also some specialised detectors with limited acceptance:

- High-Momentum Particle Identification Detector (HMPID);
 - PHOton Spectrometer (PHOS);
 - ElectroMagnetic CALorimeter (EMCAL) and Di-jet Calorimeter (DCal).
- **The muon spectrometer**, placed in the forward pseudorapidity region ($-4.0 \leq \eta \leq -2.5$). This detector consists of a dipole magnet, tracking and trigger chambers; it is optimised to reconstruct heavy quark hadrons through their $\mu^+\mu^-$ decay channel and single muons.
 - **The forward detectors** are placed in the high pseudorapidity region with different acceptances. These detectors are specialised systems for event triggering and measuring global event characteristics. They include:
 - Forward Multiplicity Detector (FMD) ($-3.4 < \eta < 5.1$);
 - Photon Multiplicity Detector (PMD) ($2.3 < \eta < 3.7$);
 - Zero Degree Calorimeters (ZDC) ($|\eta| > 8.8$ for ZN, $6.5 < |\eta| < 7.4$ for ZP, $4.8 < |\eta| < 5.7$ for ZEM);
 - VZERO Detectors ($2.8 < \eta < 5.1$ for VZERO-A and $-3.7 < \eta < -1.7$ for VZERO-C);
 - TZERO Detectors ($4.6 < \eta < 4.9$ for TZEROA and $-3.3 < \eta < -2.9$ for TZERO-C).

This section presents details regarding some of these detectors, focusing on the ones more relevant for this thesis. A specific section (Sect. 4.2.2) is dedicated to the Zero Degree Calorimeters since they are especially important for this work.

The Inner Tracking System (ITS)

The Inner Tracking System (ITS) [100] is the innermost detector of the central barrel. The detector is attached to the beam pipe, covering the region from 3.9 cm to 43 cm in radius. Starting from the beam pipe and proceeding radially outwards, the ITS, which operated in Run 2, is composed of a total of six layers:

- two Silicon Pixel Detector (SPD) layers, based on hybrid silicon pixels. The purpose of the SPD is to provide ALICE with adequate secondary vertexing capability for charm and beauty detection in such a high multiplicity environment. In particular, the first layer of the SPD is used to measure the charged-particle multiplicity produced at midrapidity. Each readout chip of the SPD layers provides a binary output, providing only hit information on the track and no energy loss measurements. The spatial resolution is $100\ \mu\text{m}$ along the z direction and $12\ \mu\text{m}$ in the transverse plane ($r\phi$ plane).
- two Silicon Drift Detector (SDD) layers, the two intermediate layers of the ITS, which, together with the two outermost layers SSD (see later), have analogue readout and can be used for Particle IDentification via dE/dx measurement for low momentum particles.
- two Silicon Strip Detector (SSD) layers, besides providing energy loss measurements, play a crucial role in tracking the particles produced in the collisions connecting the tracks from the external detectors (i.e. Time Projection Chambers) to the ITS inner layers.

Since multiple scattering effects dominate the momentum and impact parameter resolution, the amount of material used for the detector was minimised as much as possible in the design. The detector effective thickness is equal to 0.4% of one radiation length X_0 and, considering all the additional material in the active volume (support structures, cooling systems, et cetera), the total material traversed by a track perpendicular to the detector surface is approximately 7.2% of X_0 . A schematic view of the detector is shown in Fig. 4.3, and a summary of the main characteristics of the ITS layers is reported in Table 4.2.

Time Projection Chamber (TPC)

The Time Projection Chamber (TPC) is the main tracking detector of the central barrel [101]. It provides the charged particle momentum measurement ($0.1\ \text{GeV}/c < p_T < 100\ \text{GeV}/c$), contributes to the vertex determination and performs particle identification via the

Layer	Type	r (cm)	Acceptance
L0	pixel	3.9	$ \eta < 2.0$
L1	pixel	7.6	$ \eta < 1.4$
L2	drift	15.0	$ \eta < 0.9$
L3	drift	23.9	$ \eta < 0.9$
L4	strip	38.0	$ \eta < 0.97$
L5	strip	43.0	$ \eta < 0.97$

Table 4.2 Main characteristics of the ITS layers [99].

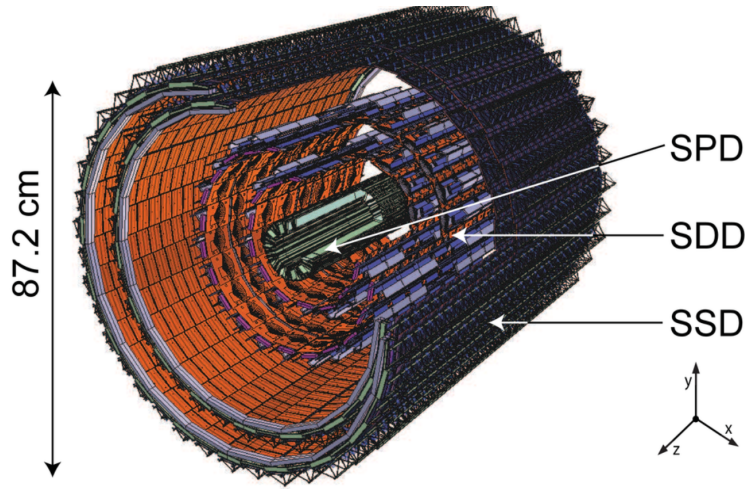


Fig. 4.3 Schematic view of ALICE 6 layers Inner Tracking System. Figure from [98].

measurement of the ionisation energy loss dE/dx . The TPC is a 88 m^3 cylinder filled with gas with an inner radius of 85 cm, an outer radius of 250 cm and an overall length along the beam direction of 5 m. It covers the pseudorapidity region of $|\eta| < 0.9$ and provides full azimuthal acceptance. The detector is divided into two drift regions by a central electrode. During Run 1, the detector was filled with a mixture of Ne and CO_2 (2009-2012), while at the beginning of the LHC Run 2 (2015-2018), a mixture of Ar and CO_2 was used to improve the PID resolution in the relativistic rise region. Charged particles traversing the TPC volume ionise the gas along their path, creating free electrons and ions. The drift field separates the two charges, and the electrons drift to the end-plates. The parameters of the particle trajectory inside the known magnetic field are then used to measure the momentum of the particle. The applied external electric field accelerates the electrons and ions produced in the ionisation process, drifting them towards the readout chambers and the Central Electrode (CE), respectively. The readout chambers consist of multi-wire proportional chambers (MWPC) with cathode pad readout. An electron avalanche is produced in the high electric fields in the vicinity of the anode wires, and this avalanche process amplifies the primary

ionisation signal. The electrical signal induced by the positive space charge onto a segmented pad plane is shaped, amplified, digitalised, processed and read from each readout pad by the data acquisition system. A schematic view of the TPC detector is shown in Fig. 4.4.

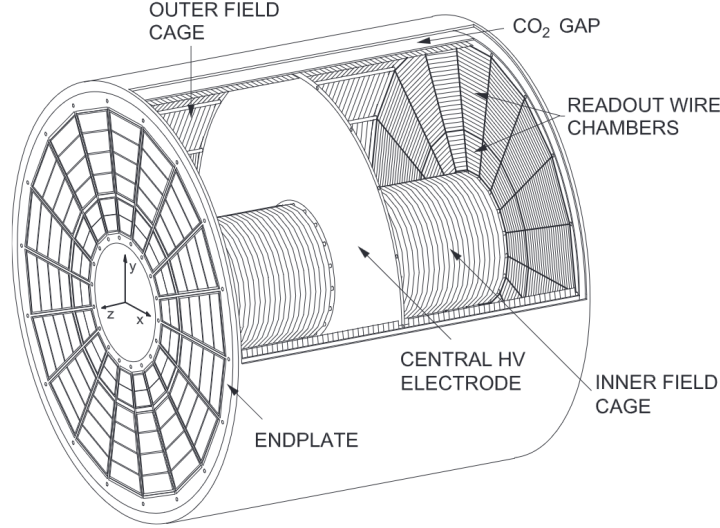


Fig. 4.4 3D view of the TPC field cage [102].

VZERO detector

The VZERO detectors [103] consist of two arrays of scintillator counters, referred to as VZERO-A and VZERO-C. VZERO-A is located on the positive z -direction at about 3.4 m from the ALICE vertex opposite to the muon spectrometer and provides pseudorapidity coverage $2.8 < \eta < 5.1$. VZERO-C is located on the other side of the vertex on the negative z -direction, at a distance of about 90 cm with pseudorapidity coverage $-3.7 < \eta < -1.7$. Each of the VZERO arrays is segmented into four rings in the radial direction, and each ring is divided into eight sections in the azimuthal direction as shown in Fig. 4.5. This detector system has several functions, among which providing minimum-bias (MB) and high multiplicity (HM) triggers for the central barrel detectors in pp, p-Pb and AA collisions. In the first data-taking periods (2009), the ALICE MB trigger was achieved by requiring a hit in the Silicon Pixel Detector (SPD) or in either of the VZERO arrays (VZERO-A or VZERO-C). Given the increasing LHC luminosity and beam background in the most recent data taking periods, the trigger required a stricter condition using the coincidence between both VZERO arrays and the LHC bunch crossing signals. A non-negligible background comes from interactions between the beams and the residual gas within the beam pipe and between the

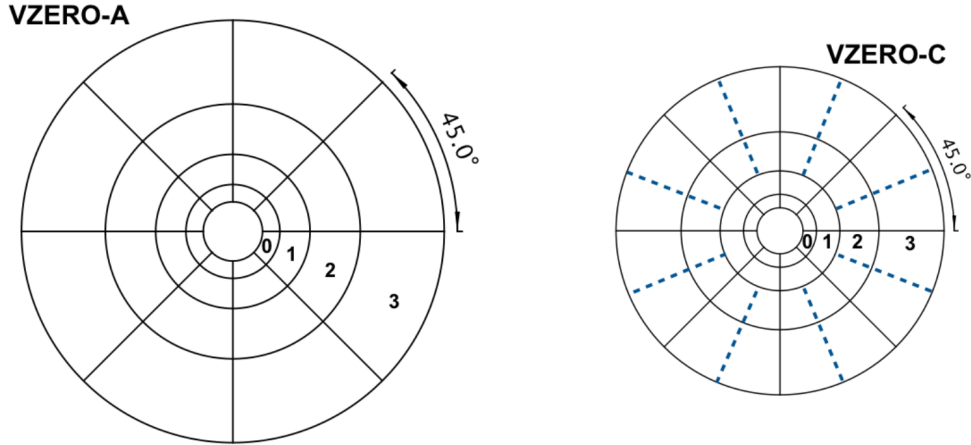


Fig. 4.5 Segmentation of the VZERO-A/VZERO-C arrays [103].

beam halo and various accelerator components, such as the collimators. However, using the time of flight of particles detected by each VZERO array, particles from collisions and from beam-gas backgrounds can be efficiently distinguished. Finally, the VZERO detector provides a charged particle multiplicity measurement based on the signal amplitude in the scintillators, which is used to define percentile classes as discussed in Chapter 1 Sec. 1.2.1.

4.2.2 The Zero Degree Calorimeters (ZDC)

In Sec. 1.2.1, we introduced the concept of impact parameter (b) and of participant and spectator nucleons. The energy E_S carried away by the spectator nucleons in a collision is one measurable quantity, directly related to the definition of centrality as it allows a direct estimate of the number of participant nucleons N_p through the simple relation:

$$N_p = A - E_S/E_A \quad (4.1)$$

where A is the mass number of the ion and E_A is the beam energy per nucleon. Some simple considerations can be made to link the average number of participant nucleons with the impact parameter b of the collision in the case of identical nuclei, and a more detailed calculation can be made in the framework of the Glauber theory. At fixed-target experiments, the spectator nucleons, which typically fly away in the forward direction, are usually detected using zero-degree calorimeters placed close to the beam axis, which measure E_S . This technique has been successfully adopted by several SPS heavy-ion experiments, such as WA80 [104], NA49 [105], and NA50 [106]. It has been shown that the measurement of projectile spectators in a ZDC is well correlated with other centrality estimators, such as

charged-particle multiplicity. However, the design of devices for the detection of spectator nucleons for an ion collider experiment, like ALICE, differs significantly with respect to a fixed-target environment. In particular, in the case of LHC, the beams are deflected by means of two separation dipoles at a defined distance from the interaction point (≈ 50 m in ALICE). These magnets will also deflect the spectator protons, separating them from the spectator neutrons, which instead fly at $\approx 0^\circ$. Therefore, it is necessary to place two devices on the two sides of the interaction point: one positioned at 0° , between the two beam pipes, to detect spectator neutrons, and one placed externally to the outgoing beam pipe, to collect the spectator protons.

Detection technique of the ALICE ZDC

ALICE Zero Degree Calorimeters (ZDC) [107] consist of two sets of hadronic calorimeters, located at ≈ 112.5 m on each side of the interaction point, and of two small electromagnetic calorimeters (ZEM), placed at ≈ 7.5 m on the A side of the detector. As mentioned, at this distance from IP, spectator protons are spatially separated from neutrons by the magnetic dipoles of the LHC beam line and therefore, two distinct detectors are used: one for spectator neutrons, placed at zero degrees relative to the LHC axis ($|\eta| > 8.8$), and one for protons, placed close to the external side of the outgoing beam pipe where positive particles are deflected. For the proton calorimeters, the geometric coverage is $6.5 < |\eta| < 7.4$, but since the actual pseudorapidity interval covered by ZP depends strongly on the LHC beam optics, this was further studied through Monte Carlo simulations. For pp collisions at $\sqrt{s} = 13$ TeV, the acceptance of ZP was found to be $7.8 < |\eta| < 12.9$ [88]. The amount of space between the separating dipoles which could be allocated to the hadronic ZDC was quite reduced, and the transverse dimensions of the neutron device can not exceed the distance between the two beam pipes in that region. Figures 4.6 and 4.7 show a schematic representation of the ZDC location in ALICE. The detection technique adopted for the Zero Degree Calorimeters is the quartz fibre calorimetry. The shower generated by incident particles in a dense passive material produces Cherenkov radiation in quartz fibres (active material) embedded in the absorber. This technique has been chosen because it fulfils two fundamental requirements. Due to severe space constraints, the detectors needed to be compact and therefore, a very dense passive material had to be used as an absorber to contain the shower. Moreover, the ZDC operates in a very high radiation environment, and radiation hardness must be guaranteed, leading to the choice of high radiation-resistant quartz fibres. Moreover, Cherenkov radiation ensures a high-speed signal due to the intrinsic speed of the emission process. Finally, two small electromagnetic calorimeters (ZEM1, ZEM2) are placed on the A side at ≈ 7.5 m from the IP, at 8 cm from the LHC axis covering the pseudorapidity region $4.8 < \eta < 5.7$, detect a

small fraction of the energy released in the collisions and allow the separation of hadronic and electromagnetic interactions.

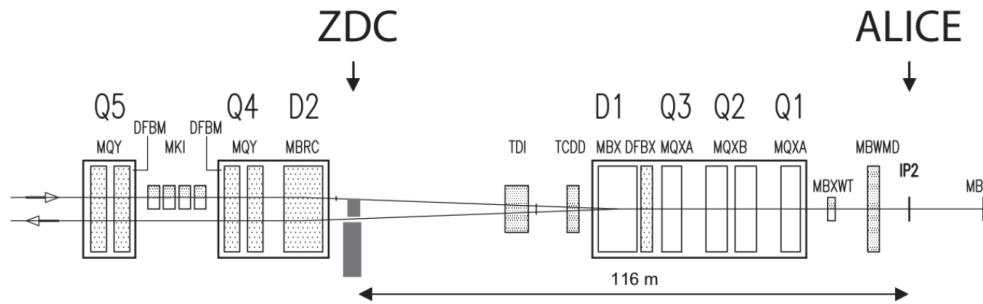


Fig. 4.6 Schematic view of the beamline and the ZDC location.

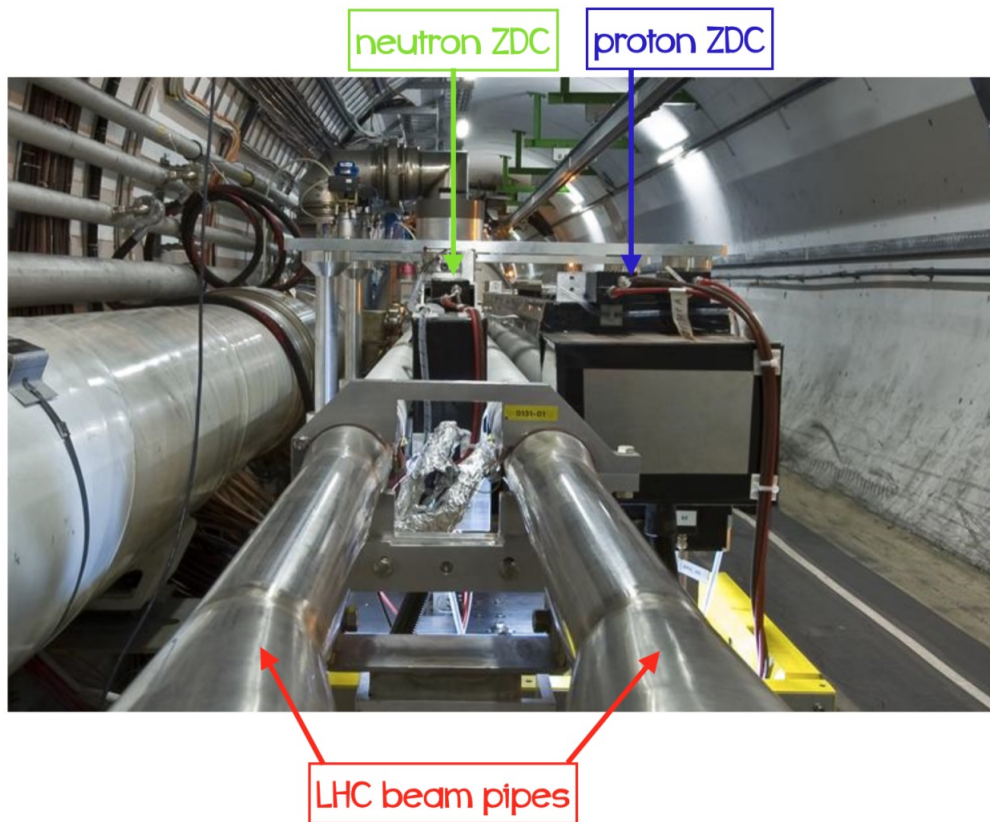


Fig. 4.7 View of the ZDC location.

The neutron calorimeter (ZN)

The design of the neutron calorimeter consists of heavy metal absorber plates stacked to form a parallelepiped. The quartz fibres embedded in the absorber are placed parallel with respect to the LHC axis (spaghetti calorimeter). The spectator neutrons, impinging on the front face of the detector, produce showers in the absorber/quartz matrix, and the charged particles above the Cherenkov threshold produce photons transmitted through the quartz fibres up to the photodetectors. The optical readout was divided into four independent towers to verify that the calorimeter was centred, this configuration can also be exploited to monitor the relative damage that can affect the different sections. On the other hand, to make the energy calibration easier, it is also important to receive the measured light from the whole calorimeter, reading from a single photodetector. To fulfil these requirements, one out of every two fibres is sent to a single photodetector (PMTc) and the remaining fibres to four different photodetectors (PMT1 to PMT4) collecting the light from the four towers. The connections of the fibres to the different photodetectors are shown in Fig. 4.8.

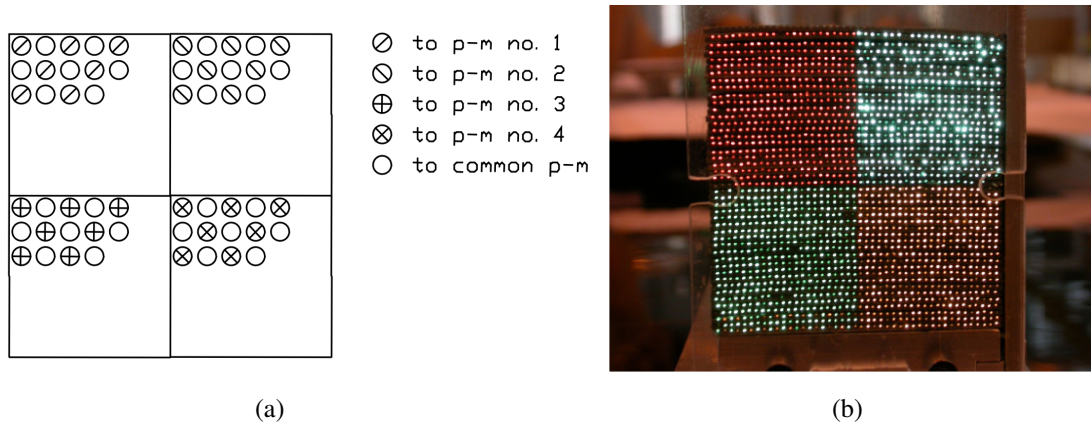


Fig. 4.8 (a) Schematic connections of the fibres to the PMTs for the neutron calorimeter. (b) Picture of one Zero Degree Calorimeter for neutrons.

Proton calorimeter (ZP)

The design of the proton calorimeter is similar to the one discussed for the ZN. The primary constraint in this case comes from the need to optimise the detection of the spectator protons, which are spread over the horizontal coordinate by the separator magnet. The optical readout is divided into five PMTs, one of which collects the light of half of the fibres uniformly distributed inside the calorimeter. With the remaining fibres, four towers are defined and read out by four PMTs. The schematic arrangement of the fibres is shown in Fig. 4.9.

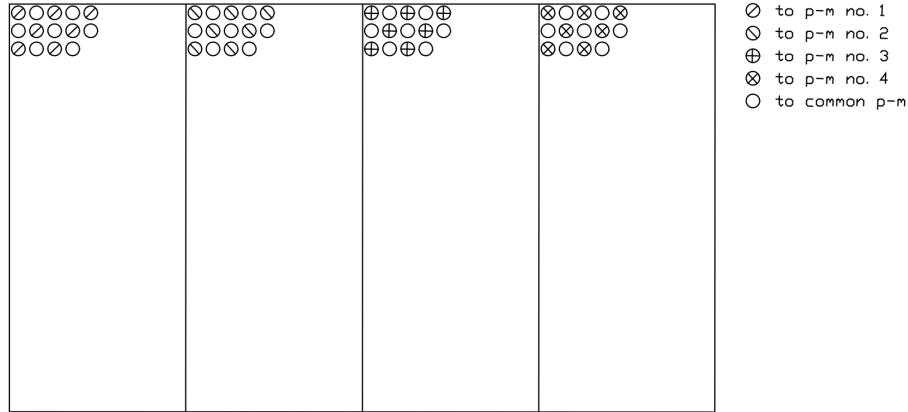


Fig. 4.9 Schematic connections of the fibres to the PMTs for the proton calorimeter.

Performance of ALICE ZDC

In Pb–Pb collisions, the ZDC allow a direct estimate of the number of participant nucleons through the detection of the energy carried away by the spectators, which is directly related to the centrality of the collision. However, unlike the fixed target experiments, the correlation between the impact parameter and the ZDC response at colliders is not exactly monotonic. In particular, in central AA collisions, a small amount of energy is deposited in the ZDC. Still, a similar effect can be measured for very peripheral collisions, where spectator nucleons can bound into fragments which do not get out from the beam pipe and cannot be detected from the hadronic calorimeters. In this context, the information provided by the electromagnetic calorimeter ZEM is crucial to remove the ambiguity between central and peripheral collisions. Centrality classes can be defined by selections on the two-dimensional distribution of ZDC vs ZEM energy as shown in Fig. 4.10 since the energy measured in the ZEM calorimeter is monotonic with centrality. In addition to the determination of the centrality of the collision, the ZDC can also monitor the LHC luminosity. The minimum bias rate on the ZDC is dominated by electromagnetic dissociation processes, which can occur even in ultra-peripheral collisions when the impact parameter of the two colliding ions is larger than the sum of the nuclear radii, and therefore, hadronic interactions are not possible. The event rate in the ZN is usually used to measure the delivered luminosity. The cross section for electromagnetic processes is dominated by nuclear excitation and following de-excitation, with the emission of one or more neutrons or protons at very forward rapidities. These reactions can also occur with a double photon exchange, leading to neutron emission from both ions (mutual electromagnetic dissociation). The energy spectrum for the ZNA is shown in Fig. 4.11, together with the fit obtained by summing four Gaussians. The event selection for this measurement requires a signal in one of the ZNs and nothing in the other.

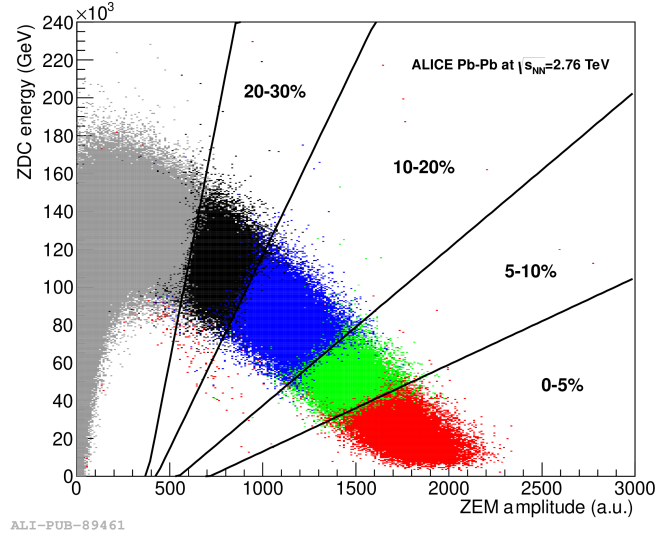


Fig. 4.10 Spectator energy deposited in the ZDC calorimeters in Pb–Pb collisions as a function of ZEM signal amplitude. The correlation is used to define centrality classes [108].

In this way, hadronic events, which mostly lead to the disintegration of both colliding nuclei, are rejected, and pedestal effects at $E = 0$ are neglected (e.g. events with no signal detected by the ZNA but fired by the ZNC). In the energy spectrum, a pronounced $1n$ peak at 1.38 TeV is present, but also $2n$, $3n$, and $4n$ peaks are clearly identified. The ALICE ZDC detectors are calibrated in Pb–Pb collisions through this technique, which allows a direct absolute measurement of the LHC luminosity, once the cross-section for the process is known. In pp collisions there is no reliable way to calibrate the calorimeters spectra in energy units without introducing model dependencies, therefore, the ZDC energy is commonly reported in arbitrary units.

Measuring the leading effect with the ZDC

As discussed in Chapter 3, in pp collisions the effective available energy for particle production is reduced with respect to the full centre-of-mass energy due to the emission of forward baryons with large longitudinal momenta (leading effect). Through the measurement of the energy carried away by the leading baryons it is possible to estimate the effective energy event-by-event from Eq. 3.7. ALICE has a good capability for this kind of analysis thanks to the Zero-Degree Calorimeters. Even though optimised for Pb–Pb collisions, several results show that the ZDC have a sufficient energy resolution to allow a pp data analysis in terms of the effective energy. The ALICE Physics Performance Report [110] states that for positively charged particles measured by the ZP, the beam optics constraints the measurable energy

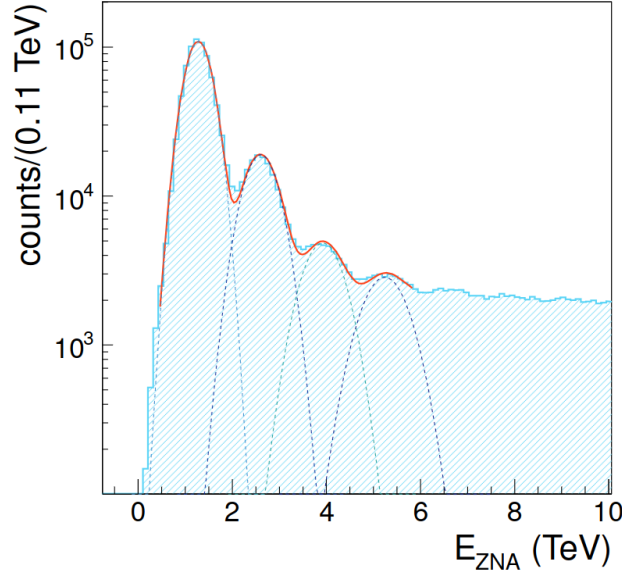


Fig. 4.11 ZNA energy spectrum requiring signal over the threshold in ZNA but not in ZNC, rejecting thus neutron emission on the opposite side. The dashed lines represent the single fits of the different peaks (1n, 2n, 3n, 4n), while the continuous line is the sum of all the contributions [109].

interval between 2.2 and 4.5 TeV, corresponding to a Feynman- x range $0.30 < x_F < 0.64$. For neutral particles, all those emitted in a cone of 0.3 mrad around the beam direction are expected to fall in the ZN acceptance [110]. In Ref. [78] a PYTHIA event generator is used to test the ZDC capabilities to efficiently measure the effective energy in pp collisions, using the GEANT package to simulate the detector response. Figure 4.12 shows the average charged-particle multiplicity n_{ch} as a function of the generated effective energy (circles) and reconstructed with the ZDC (squares). The results are in good agreement between generator and reconstruction levels, indicating that the limitations related to the leading energy reconstruction in the ZDC and the background from other particles in the forward region do not introduce a significant bias in the measurement. These results confirm that an analysis of pp events in terms of the effective energy with ALICE is possible. In addition, the Collaboration has recently published the first results on the correlation between central rapidity particle production and the energy detected by the ZDC in pp collisions [88]. The forward energy is found to decrease with increasing charged-particle multiplicity at midrapidity, in agreement with the expectations from the leading effect.

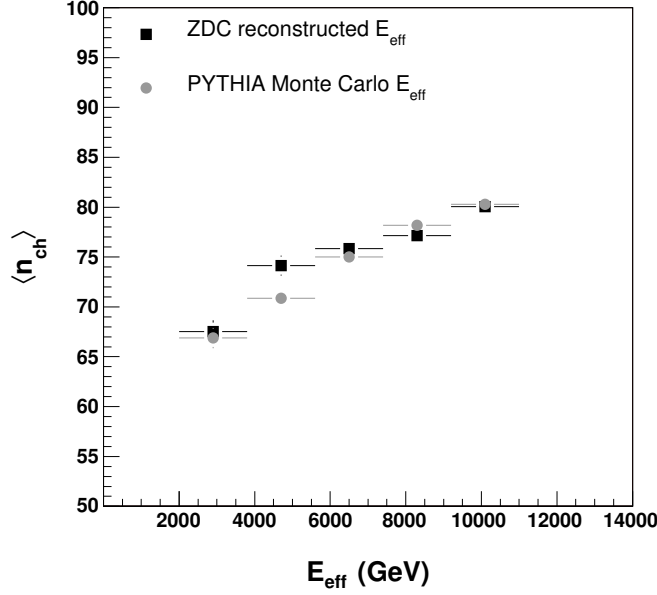


Fig. 4.12 Correlation between the average charged multiplicity and the average effective energy in PYTHIA pp events, using the leading energy measurement in the ZDC calorimeters (squares), and at the generator-level (circles). Figure from [78].

4.2.3 Data acquisition and offline framework

ALICE data taking activities in Run 1 and 2 were controlled by the following central online systems: the Detector Control System (DCS), which allowed to operate the detector hardware from a central interface, the Data Acquisition (DAQ) system, which controlled the configuration of the detectors during data taking, and the Trigger (TRG) systems, which allowed for the selection of interesting physics events. The ALICE trigger system was composed by a low-level hardware trigger, called Central Trigger Processor (CTP), and a High-Level software Trigger (HLT). The CTP generated the trigger decision by combining the information from the different detectors, and, since these have different readout times, the system was divided into three levels called L0, L1 and L2. The Level 0 trigger decision (L0) was taken $\sim 0.9 \mu s$ after every collision, and the events that successfully passed this selection were then propagated through Level 1 (L1). The L1 trigger decision was taken $\sim 6.5 \mu s$ after L0, in order to account for the computation time and the signal propagation from farther detectors. If both L0 and L1 conditions were met, a Level 2 (L2) decision was issued after $\sim 100 \mu s$, time gap necessary to allow the complete drift of ionisation charges in the TPC. The collision events which successfully passed the hardware trigger selections

were accepted, and handled by the Data Acquisition (DAQ) system. The DAQ was interfaced to the HLT, which performed a fast reconstruction of each event and a further skimming, in order to reduce the data size without losing physics information. Finally, events were permanently stored in the CERN computing centre. The huge amount of data collected by the ALICE experiment requires an infrastructure to process and analyse the events. Data processing is distributed in several worldwide computing centres and coordinated by the Worldwide LHC Computing Grid (WLCG) project [111]. The WLCG is a hierarchical computing infrastructure developed on three levels: the largest computing centre is located at CERN (Tier-0), and other large computing centres (Tier-1) are logically clustered around the Tier-0 and contribute to the storage of raw data. Finally, smaller Tier-2 centres are logically clustered around Tier-1. The grid infrastructure is used to store the data and for data processing, including calibration, reconstruction, simulation and analysis. The ALICE collaboration has developed a service called AliEn (ALICE Environment) [112] that allows the collaboration to easily access the data on the Grid. The data collected in Run 1 and Run 2 is analysed using the ALICE software environment called AliRoot [113], based on ROOT, a data analysis framework mainly written in C++. AliRoot is interfaced with several Monte Carlo generators, e.g. PYTHIA [65] among others, that simulate particle production in the collisions. The interaction of the particle with the material is simulated in detail by using the GEANT3 [114], GEANT4 [115] and Fluka [116] transport codes. The final analysis code is collected in a data repository called AliPhysics [117]. The output of the whole reconstruction operation is the Event Summary Data (ESD), which contains all the information about the event at the track and collision level. A summary of the most relevant information is extracted from the ESDs in the format of Analysis Object Data (AOD) to allow a more efficient analysis.

4.2.4 Tracking and vertex reconstruction

The procedure used to track charged particles in the central barrel and to determine the position of the interaction vertex consists of several steps [118]. The first step of the reconstruction is a local cluster-finding algorithm executed by each detector within its sensitive volumes. The signals of particles crossing the sensitive area of the detectors are combined into a single cluster, characterised by positions, signal amplitudes, times and their associated errors. Then, a preliminary determination of the primary vertex is performed using the SPD tracklets, defined as lines connecting two clusters found in the two SPD layers of the ITS. The primary vertex is defined as the space point to which a maximum number of tracklets converge. Track finding and fitting are performed using ITS and TPC clusters through the Kalman filter technique [119] in three stages, following an inward-outward-inward scheme.

The first inward stage starts with finding tracks in the TPC: track seeds are built first with two TPC clusters and the vertex point, then with three clusters and without the vertex constraint. The seeds are propagated inward and, at each step, updated with the nearest cluster provided that it fulfils a proximity cut. Only tracks with a minimum number of clusters (20 out of 159 possible) are accepted. Since the clusters can be shared by different seeds, the same physical track can be reconstructed multiple times at this stage. This problem is addressed at a later stage using an algorithm to search for pairs of tracks with a fraction of common clusters exceeding a specific limit. Surviving tracks are then propagated inwards to the inner TPC radius, and at this stage, a preliminary particle identification is made based on the particular energy loss in the TPC. The reconstructed TPC tracks are then propagated to the outermost ITS layer, becoming the seeds to start the track finding in the ITS, which follows an inward propagation similar to the one described for the TPC. The TPC acceptance does not allow for efficient track finding at $p_T < 200 \text{ MeV}/c$, therefore, in this region a standalone ITS reconstruction is performed, taking into account those clusters not used to build ITS-TPC tracks. Once the reconstruction in the ITS is completed, the second tracking stage starts, and tracks are refitted by the Kalman filter in the outward direction using the clusters previously found where they can be matched to TRD and TOF clusters. The track length integration and time-of-flight calculation are finalised at this stage. The tracks are then propagated further for matching with signals in EMCAL, PHOS, and HMPID. At the final stage of the track reconstruction, all tracks are propagated inwards, starting from the outer radius of the TPC. In each detector (TPC and ITS), the tracks are refitted with the previously found clusters. The track's position, direction, inverse curvature, and its associated covariance matrix are determined. Global ITS-TPC tracks are used to find the interaction vertex with a higher precision than with SPD tracklets alone.

4.2.5 Particle Identification with ALICE

The goal of Particle IDentification (PID) is to determine the mass of each reconstructed track, which, together with its charge, provides the identity of the particle itself. The PID in ALICE is performed by direct measurements (such as the time-of-flight, the specific energy loss, et cetera) or by reconstructing the particle decay products [118]. The ALICE experiment relies on the following subsystems for identifying charged particles with direct measurements:

- ITS: the four outermost layers of the ITS have analogue readout and can be used for PID via dE/dx measurement for low momentum particles, where the ITS is used for standalone tracking. An example of the ITS PID performance is shown in Fig. 4.13 (a).

- TPC: the TPC identifies particles via the measurement of their specific energy loss dE/dx in the gas volume. An example of the TPC PID performance is shown in Fig. 4.13 (b).
- TOF: the Time-Of-Flight detector provides a measurement of the velocity of the particle. An example of the TOF PID performance is shown in Fig. 4.13 (c).
- HMPID: the High Momentum Particle Identification Detector provides PID through the Cherenkov technique. An example of the HMPID PID performance is shown in Fig. 4.13 (d).

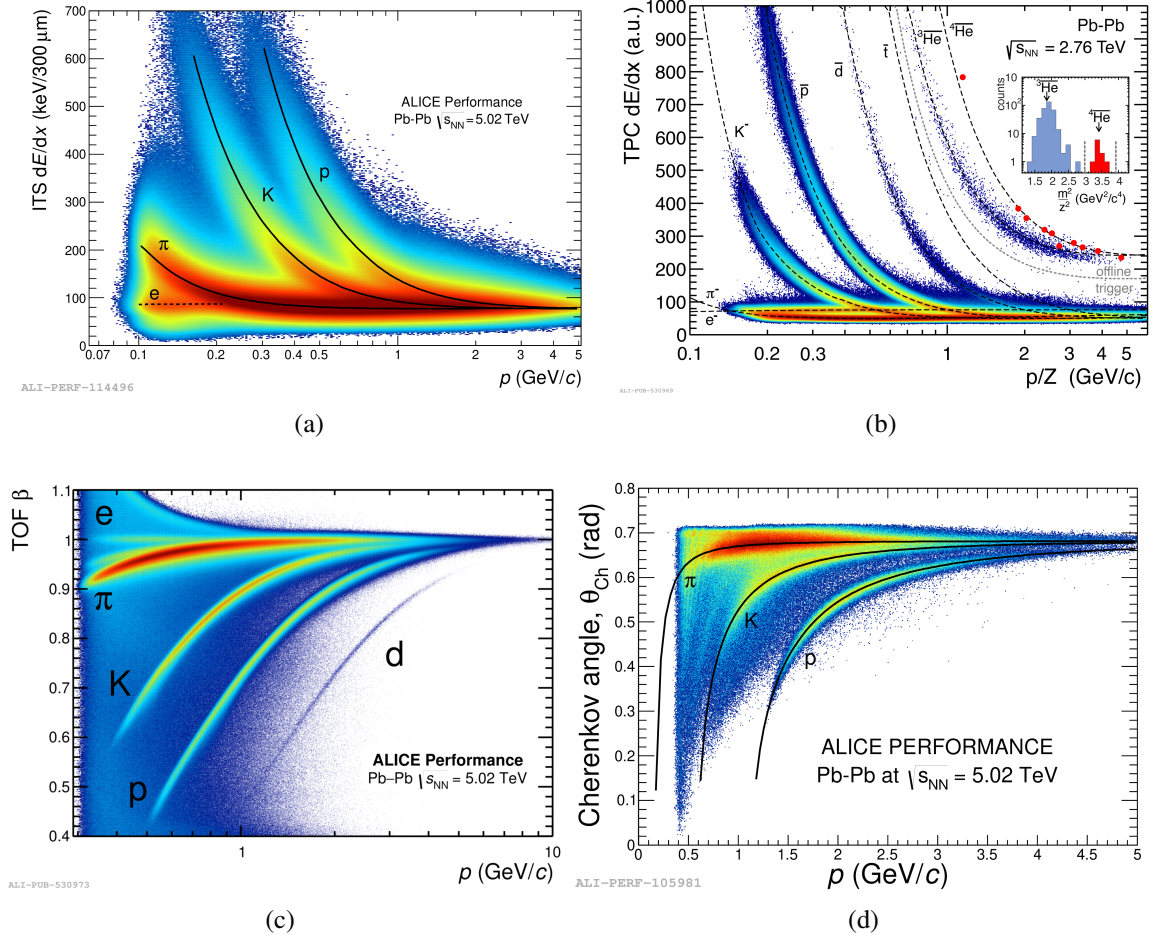


Fig. 4.13 PID performance of ITS (a), TPC(b), TOF (c), and HMPID (d) detectors.

The particle identity is defined based on a discriminating quantity, which can be evaluated using the detector signal S and the expected average response S_{exp} under the particle species hypothesis. The discriminating quantity for the particle species j can be evaluated using

detectors with Gaussian response in units of σ ($n\sigma$):

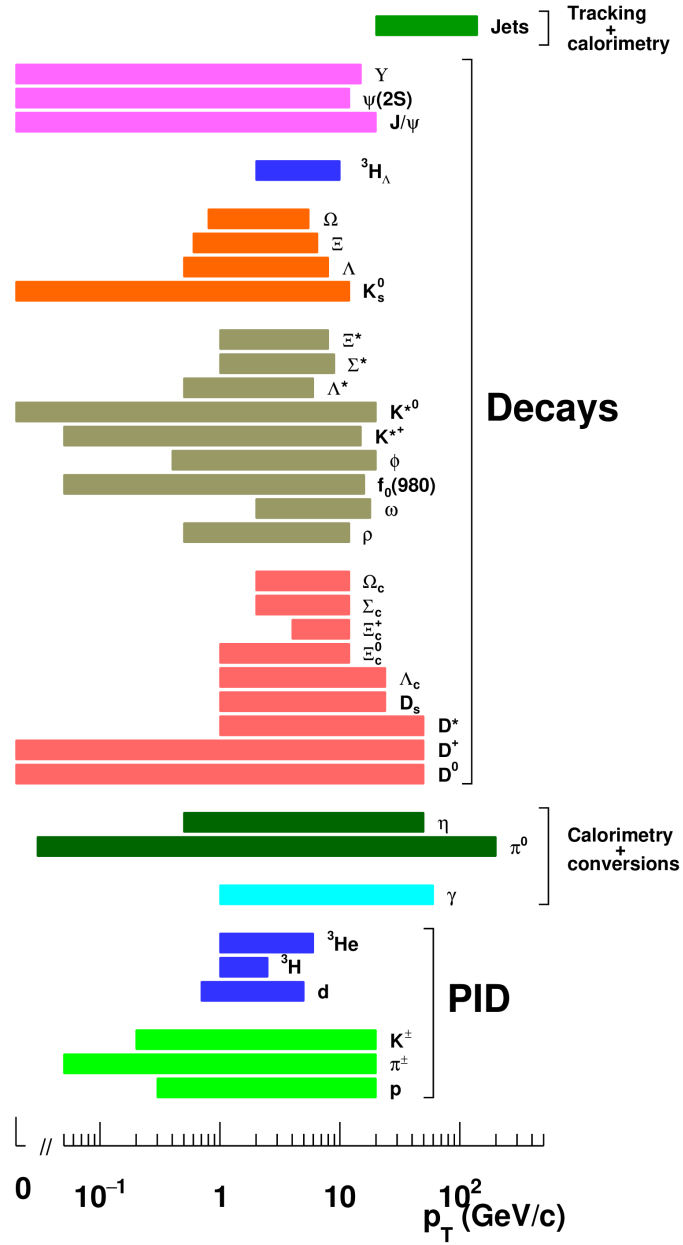
$$n\sigma \equiv \frac{S_j - S_{exp,j}}{\sigma_j} . \quad (4.2)$$

A convolution of track parameters and detector characteristics usually gives the resolution. The information from different detectors can also be combined to obtain track samples with extremely low contamination. The identification of charged particles is possible only if they live long enough to reach the mentioned detectors located further away from the interaction point. For shorter-lived particles, secondary vertices can be reconstructed thanks to high-precision tracking in the inner layers of the ITS, allowing the identification of hadrons from their weak decay topology. This technique significantly extends the number of particle species detected, including (multi-)strange and heavier hadrons. A summary of ALICE particle identification and reconstruction capabilities, with the p_T coverage corresponding to the published measurements based on pp or Pb–Pb data samples, is shown in Fig. 4.14.

4.3 Run 3 upgrade: ALICE 2

During the LHC Long Shutdown 2 (LS2), ALICE performed several crucial upgrades, which marked a new era for the experiment, now operating in the Run 3 [120]. ALICE proposes to address some leading physics topics in the following years of data-taking, requiring the measurement of heavy flavour hadrons, quarkonia, and low-mass di-leptons down to low transverse momenta. These measurements are characterised by a very small signal-over-background ratio, which calls for large statistics and new physics-based triggering techniques. Moreover, these measurements require significantly improving the pointing resolution and tracking efficiency while preserving the excellent particle identification capabilities of the old ALICE detector. The LHC in Run 3 delivers Pb–Pb collisions at up to $L = 6 \cdot 10^{27} \text{ cm}^{-2}\text{s}^{-1}$, corresponding to an interaction rate of 50 kHz. Therefore, the new ALICE detector must also cope with the higher interaction rates at play. The main upgrades which took place during the LS2 will be discussed in this section and can be summarised as follows:

- A new beam pipe with smaller diameter;
- An upgraded ITS;
- An upgraded TPC;
- Upgrade of the readout electronics of other detectors, such as TRD, TOF, PHOS and Muon Spectrometer;



ALI-PUB-530977

Fig. 4.14 ALICE particle identification and reconstruction capabilities, with the p_T coverage corresponding to the published measurements based on pp or Pb–Pb data samples [22].

- Upgrade of the forward trigger detectors;
- New online systems, offline reconstruction and analysis framework.

4.3.1 Detectors upgrade

ITS Upgrade

The ITS2 consists of seven layers of Silicon Pixel Detector based on Monolithic Active Pixel Sensors (MAPS). The pixel size was reduced with respect to the ITS1, and the first layer is now positioned closer to the interaction point (at ~ 22.4 mm), also thanks to a new beam pipe with a smaller diameter. Moreover, the material budget of the detector was reduced to $0.35\% X_0$ per layer. The ITS2 has a better impact parameter resolution, which is expected to improve by a factor 3 in the $r\phi$ plane and by a factor 5 in the z direction for tracks with $p_T \sim 500$ MeV/c. The improved impact parameter resolution reached so far in Run 3 compared to Run 2 is shown in Fig. 4.15 in the $r\phi$ plane. The tracking efficiency and the momentum resolution also improved at low p_T , allowing for a very precise reconstruction of secondary vertices from the decays of charm and beauty hadrons. Finally, the readout rate was increased from 1 kHz to 100 kHz in Pb–Pb collisions, allowing the ITS2 to cope with the new running conditions in Run 3.

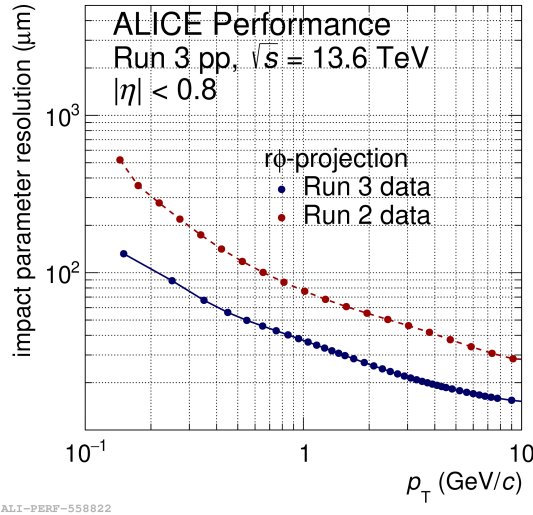


Fig. 4.15 Impact parameter resolution in $r\phi$ vs p_T in pp collisions at $\sqrt{s} = 13.6$ TeV extracted from Run 3 data compared with Run 2 collisions at $\sqrt{s} = 13$ TeV.

TPC Upgrade

During the LS2, the TPC underwent a major upgrade, which allowed the detector to cope with the higher interaction rates and data-taking modes of Run 3 and 4. The Multi-Wire Proportional Chambers (MWPCs) used in Run 1 and 2 were replaced by gas electron multiplier (GEM) chambers. The use of MWPCs required to suppress the ion backflow into the drift region by using a *gating grid* technique, which strongly limited the readout rate. On the other hand, the newly employed GEMs have an intrinsic ion-blocking capabilities that avoid massive charge accumulation in the drift volume. This upgrade allows for a paradigm shift in the operation of the TPC, and ALICE in general, where the concept of event triggers is replaced by a continuous readout of all detector data.

New Fast Interaction Trigger detector (FIT)

The new Fast Interaction Trigger (FIT) consists of three detectors: FV0, FT0 and FDD, displayed in Fig. 4.16. The FV0 consists of a large-acceptance ring made of a plastic

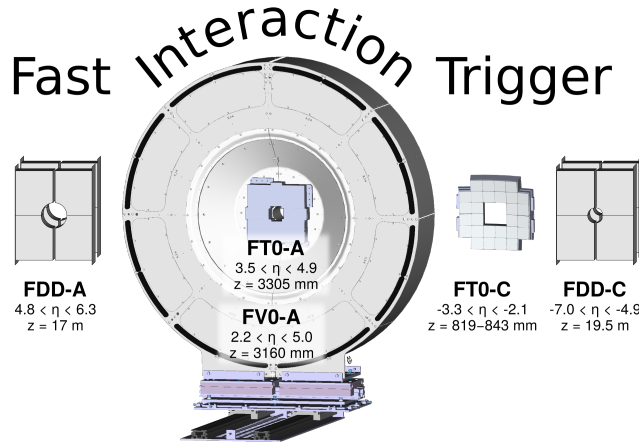
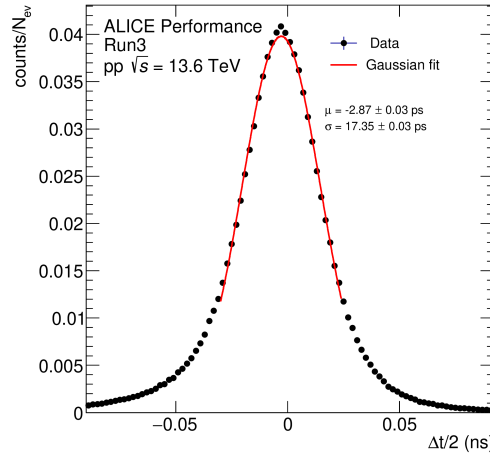


Fig. 4.16 FIT detector layout [121].

scintillator divided into 5 rings with equal η coverage and placed on the A-side of the detector. The FT0 comprises two arrays of Cherenkov modules placed asymmetrically on the opposite sides of the interaction point. Finally, the FDD consists of two arrays surrounding the beam pipe at +17 m and -19.5 m from the interaction point of two plastic scintillator layers. The FIT serves as the main triggering detector of ALICE in Run 3, providing a minimum bias (MB) trigger and the possibility to select events based on recorded forward multiplicity. FIT provides online the z coordinate of the vertex and a precise estimation of the collision time with a resolution of 20 ps, as displayed in Fig. 4.17. Finally, the FIT operates as a luminometer, providing direct, real-time feedback to the LHC for beam tuning.



ALI-PERF-542879

Fig. 4.17 FT0 time resolution in pp 13.6 TeV collected in Run 3.

4.3.2 Upgrade of data taking, processing and reconstruction

In ALICE Run 3 operations, the concept of event triggers is replaced by a continuous readout of all detector data. Compared to Runs 1 and 2, the new running conditions are significantly more challenging for the online and offline computing systems [122]. In particular, the resulting data throughput from the detector is greater than 1 TB/s for Pb–Pb events, roughly two orders of magnitude more than in Run 1. To minimise the cost and requirements of the computing system for data processing and storage, the ALICE Computing Model for Runs 3 is designed for a maximal reduction of the data volume read out from the detector as early as possible in the data flow. This is achieved by partially reconstructing the data synchronously with data taking. An important example is the TPC, the most significant contributor to the data volume, for which the raw data are first rapidly reconstructed to suppress clusters not associated to tracks, using a first tracking algorithm and early calibrations. The synchronous processing phase performs data compression, calibration, and quality control on the online computing farm. The output of these steps is then stored on an on-site disk buffer. The second reconstruction stage is performed asynchronously, using the final detector calibrations to reach the desired data quality. The new computing scheme for Run 3 replaces the traditionally separate online and offline frameworks with a unified one called O² (Online Offline processing). The hardware consists of two computing farms: the FLP (First Level Processors) and the EPNs (Event Processing Nodes). As already mentioned, ALICE now operates using a continuous data-taking mode, i.e. the readout of the detectors is not based on a trigger decision but is done continuously. Data arrive at the FLPs from the detector readout

links, where a first data compression (zero suppression) is performed, and the continuous streams of data are split into Sub-Time Frames (TF) ~ 10 ms long. Sub-time frames are then sent to the EPNs, where the information from different detectors is assembled into complete timeframes and a first synchronous reconstruction of the events is performed. In the EPNs, data are compressed into the Compressed Time Frames (CTF), which are written to a disk buffer. At the asynchronous stage, a second reconstruction with final calibrations is run on the EPN farm or GRID nodes, and Analysis Object Data (AO2D) are produced and saved on permanent storage. At this processing stage, all detectors are included in the reconstruction and global track fitting, primary and secondary vertexing and particle identification are performed. Therefore, it is possible to use data selection algorithms to skim the interesting physics events. Since the Run 3 data-taking applies a continuous readout mode, the event selection is not based on hardware triggers but is performed at the software level. Specific triggers taking advantage of the full reconstruction of each event are applied to study rare probes with high precision [123]. At the end of this event selection, the original CTFs are deleted from the disk buffer to make space for new data. The skimming procedure is applied only to pp collisions, to reduce the amount of data stored on tape, while all recorded Pb–Pb data are saved. On top of processing, calibration, and data compression, quality control procedures are performed in real-time to validate the detector data on the EPNs and the FLPs. Given the integration of the online and offline computing systems into the common O² project, the offline Quality Assurance (QA) and the online Data Quality Monitoring (DQM) are combined into a single Quality Control (QC), which is critical to promptly identify and overcome possible problems during data taking and to ensure that the calibration and reconstruction behave as expected both synchronously and asynchronously. The analysis software of the experiment was also significantly changed to improve its performance and integrate it into the new O2 Data Processing Layers (DPL) to provide a coherent environment from data taking to analysis [124]. Compared to the Run 2 framework, the underlying data model is organised in a set of tables arranged in a relational-database-like manner (using the Apache Arrow layout [125]). Because of the continuous nature of the data-taking in Run 3, the vertex-to-track association is no longer unambiguous, and thus, collisions and tracks are represented as separate tables, connected by an index and stored as a set of flat ROOT trees. Therefore, the analysis data model differs considerably from the hierarchical “event contents” of Runs 1 and 2. In general, the new data-taking scheme with continuous readout also requires the tracking to work without a primary vertex constraint. The description of the track reconstruction strategy for Run 3 and Run 4 is reported in Ref. [126, 127].

Chapter 5

TOF data quality assurance and performance in Run 3

The Time Of Flight (TOF) is one of the main detectors of the ALICE central barrel, providing charged particle identification in the intermediate momentum range and a trigger for cosmic ray events and ultra-peripheral heavy-ion collisions. The TOF detector is located at ~ 3.7 m from the interaction point. It has a cylindrical symmetry, covering an active area of ~ 141 m² in the central rapidity region ($|\eta| < 0.9$), with full azimuthal coverage. The technology of the ALICE Time-Of-Flight detector is based on Multigap Resistive Plate Chambers (MRPC), which provide excellent intrinsic time resolutions while being able to operate in the high track multiplicity and detector occupancy environment typical of Pb–Pb collisions at the LHC. The TOF measures the time needed for the particles produced in the interaction point to reach its sensitive surface (*time-of-flight*), which is used to determine the particle velocity. This information is combined with the momentum p and the track length L measured by the ALICE tracking systems to estimate the particle mass m , according to the relativistic relation:

$$m = \frac{p}{\beta\gamma c} = \frac{p}{c} \sqrt{\left(\frac{ct}{L}\right)^2 - 1} \quad , \quad (5.1)$$

where $\beta = \frac{v}{c}$, γ is the Lorentz factor and t is the particle time-of-flight, defined as:

$$t = t_{\text{TOF}} - t_0 \quad , \quad (5.2)$$

where t_{TOF} is the time measured by the TOF detector and t_0 is the event time of the collision, measured on an event-by-event basis from the information of the TOF detector itself or by other dedicated systems. In this chapter, we discuss the performance of the TOF detector in Run 3, focussing on the contribution of the work presented in this thesis to the monitoring

of the detector data quality during the commissioning phase in the Long Shutdown 2 (LS2) and the Run 3 data taking. Section 5.1 briefly describes the TOF detector and its readout system. Section 5.2 discusses how this work contributed to the TOF data quality assurance and monitoring during the commissioning phase and the data-taking. Finally, in Section 5.3, the first results on the performance of the detector in Run 3 are shown.

5.1 The Time-Of-Flight detector

The active area of the ALICE Time-Of-Flight is based on the Multigap Resistive Plate Chamber (MRPC) technology [128], which will be discussed in detail in Sect. 5.1.1. The experimental setup of the TOF detector is shown in Fig. 5.1. The TOF contains a total of 1593 MRPC strips, located in 87 modules distributed over 18 azimuthal Super Modules (SM) in the ALICE “space-frame” structure. Each SM is ~ 9.3 m long, positioned parallelly to the beam line, and covers approximately 20° of azimuthal angle. Five modules are hosted in each Super Module: the two external and two intermediate modules contain 19 MRPCs each, while the central one contains 15 strips, for a total of 91 MRPCs per SM. Due to the ALICE Photon Spectrometer (PHOS) requirements to reduce the material budget in its acceptance region, the central modules of SM 13, 14 and 15 are not installed. Inside each module, the MRPCs are positioned such that their active area is overlapped by 2 mm, being slightly rotated with respect to the horizontal position, as displayed in Fig. 5.2. This is done in order to minimise the dead areas and to orient the strips perpendicularly to the interaction point. The sensitive elements of the detector are highly segmented to guarantee a low detector occupancy in the high charged-particle density environment of Pb–Pb collisions. Each MRPC strip is divided into two rows of 48 pickup pads, for a total of 96 pads for each strip and 152928 total readout channels.

5.1.1 The Multigap Resistive Plate Chamber technology

The basic unit of the TOF detector is a Multigap Resistive Plate Chamber strip, which is an evolution of the Resistive Plate Chamber (RPC). An RPC is constituted of two parallel electrode planes of high resistivity filled with a specific gas mixture. The charged particles that traverse the active area (gas gap) of an RPC ionise the gas into ion-electron pairs. If a sufficiently strong electric field is applied, the electrons created in this process migrate towards the anode, generating an “avalanche”. The motion of the electrons in the avalanche induces a fast signal on the electrodes (~ 1 ns) that is read by the electronics. The intrinsic resolution on the measured time is determined by the time needed by the drift electrons to

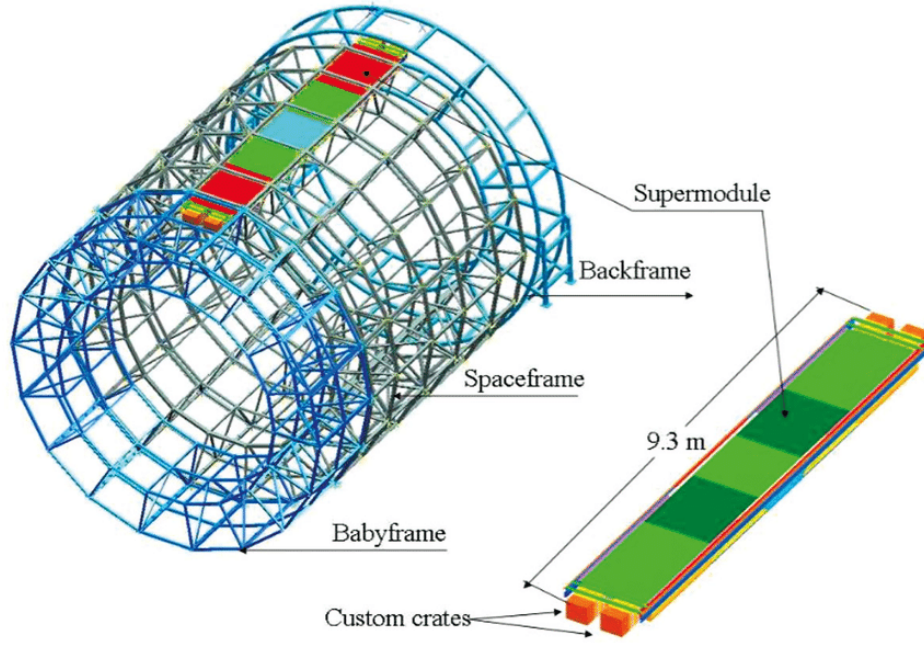


Fig. 5.1 Layout of the TOF detector in the ALICE space-frame. One of the 18 Super Modules inserted is highlighted, divided into five modules.

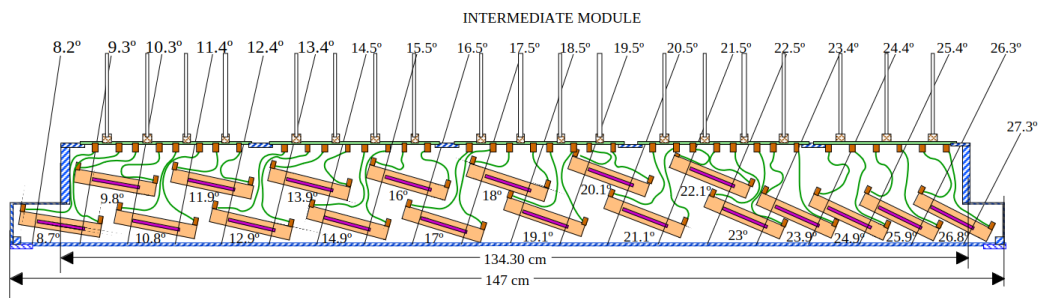


Fig. 5.2 Longitudinal cross-section of the intermediate module. The strips are slightly rotated with respect to the horizontal position, oriented inside a module to be perpendicular to the interaction point.

generate a signal above the threshold in the readout pads. The application of RPCs in the TOF detector design was precluded for two main reasons: the need to achieve time resolutions of the order of ~ 100 ps and the high charged-particle density environment of Pb–Pb collisions. In order to meet these requirements, solutions were investigated during the detector R&D phase. A larger gas gap would mean a longer path available for the avalanche formation but worse timing resolutions. On the contrary, a smaller gap would lead to better timing resolutions at the cost of significant inefficiencies. A combination of good time resolution and efficiency is provided by the Multigap RPCs, formed by two parallel resistive planes where the gas gap is divided into smaller gaps by intermediate planes. This detector was developed specifically to meet the requirements of the ALICE experiment, and the design implemented in the TOF detector is called “double stack”, consisting of five gas gaps per stack (ten gaps in total) [128]. The cathode pickup electrodes are located at the top and bottom of the chamber, and the anode is placed in the middle, shared between the two stacks, as displayed in Fig. 5.3. Ionising particles create independent avalanches in each gap. In this way, the dimension of the avalanches is constrained, and the time resolution is improved. The total signal on

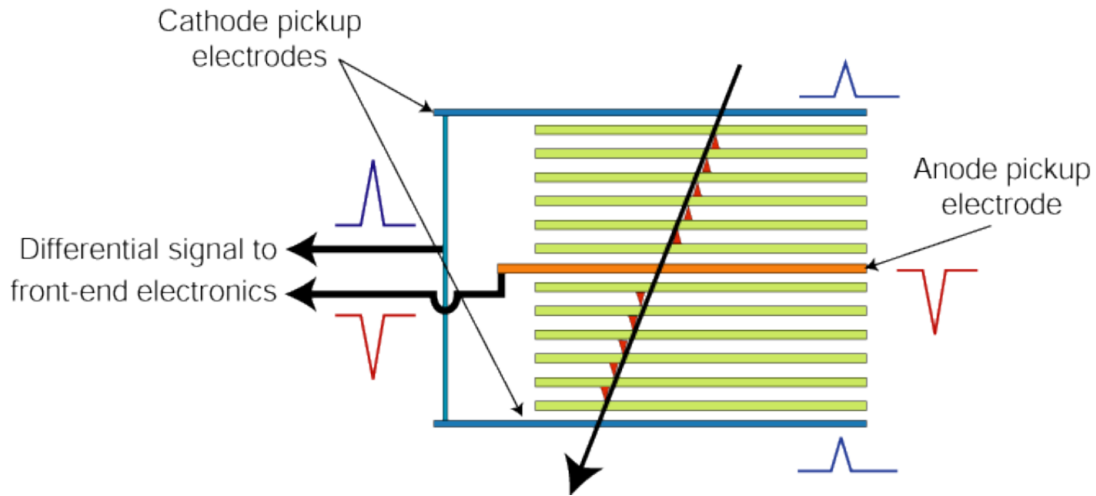


Fig. 5.3 Representation of the design of the ALICE TOF MRPC. The charge deposited by the ionising particle is shown with the corresponding signals on the pickup electrodes.

the pickup electrodes has the shape of a Landau distribution and is the analogue sum of the signals given by each avalanche. The active area of the TOF MRPC ($7 \times 120\text{cm}^2$) is filled with a non-flammable freon-rich gas mixture containing $\text{C}_2\text{H}_2\text{F}_4$ (tetrafluoroethane or freon) and SF_6 (sulfur hexafluoride) in the concentration of 93% and 7% respectively.

5.1.2 Detector readout

The readout of the TOF detector consists of custom electronics located close to the MRPCs (front-end) and at the edges of each SM in four readout crates [129]. The signal from each pad is first amplified and discriminated by a Front End Analogue card (FEA) mounted on the TOF module. The discriminated signal is then shaped to provide a Time over Threshold (ToT) output; the leading edge of the ToT provides the time of the hit, and the width of the signal is proportional to the charge deposited during the interval in which the signal is above the threshold. In particular, the signal amplitude is essential to extract corrections for time slewing¹. The leading edge and the width of the ToT signal are then transmitted to dedicated readout boards at the ends of the SM: the TDC Readout Modules (TRM), equipped with High Performance TDCs (HPTDC) with high timing resolution. All TRMs are read by Data Readout Module (DRM) boards that collect and process the data, which are later sent to the central DAQ via dedicated optical links (Detector Data Link or DDL). One Local Trigger Module (LTM) and a dedicated TRM for trigger readout complete the readout modules of each SM. A sketch of the TOF readout system is shown in Fig. 5.4.

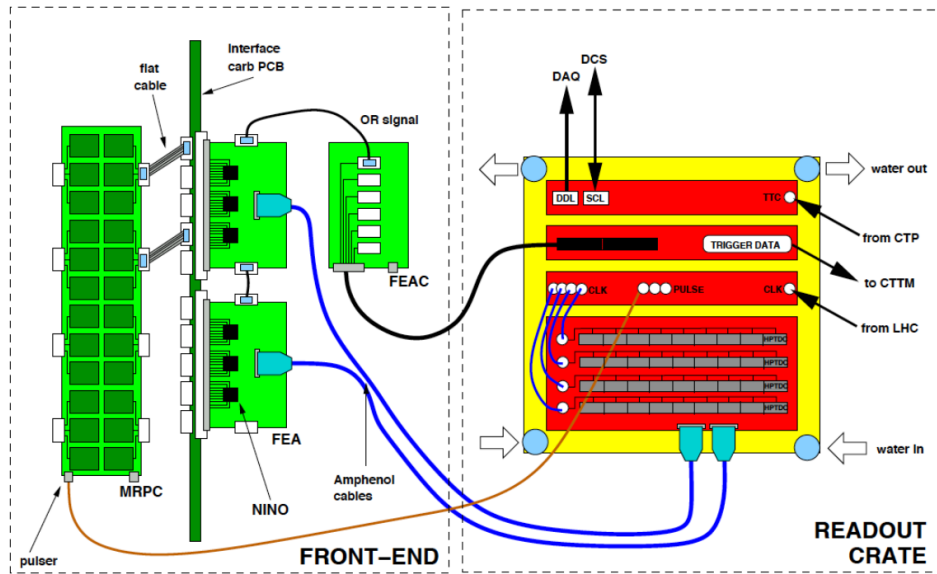


Fig. 5.4 Sketch of the TOF front-end and readout electronics.

¹Time slewing corrections are needed to correctly handle two analogue signals with different amplitudes and the same arrival time. In this case, due to their different amplitudes, the two signals would be assigned to different time-of-flight as they cross the fixed threshold in successive instants due to their different amplitudes.

Front-End electronics

The Front-End electronics provide very fast amplification and signal discrimination as they are mounted and attached to the MRPC strips. Each FEA contains three NINO ASIC chips, 8-channel amplifiers and discriminators, for a total of 24 channels per FEA. A total of 4 FEAs and 12 NINO chips read the 96 pads of each MRPC strip. The discriminated signal is then transmitted to the TRM readout boards. In addition to the time-of-flight measurement, the TOF detector provides a fast pre-trigger to the Transition Radiation Detector (TRD) and, in Run 1 and 2, contributed with an L0 trigger to ALICE event selection.

Readout electronics

The discriminated output from the Front-End electronics is transferred to a custom VME crate, where the signals are digitised. Each side of a Super Module hosts two crates, as displayed in Fig 5.1, which contain the TDC Readout Modules (TRM), the Local Trigger Module (LTM), the Clock and Pulser Distribution Module (CPDM) and the Data Readout Module (DRM).

- The TDC Readout Module, TRM:

The TRM manages the time-to-digital conversion of the signal coming from the FEAs. The left crates contain 10 TRMs (slots numbered from 3 to 12), while the right crates contain only 9 since one TRM slot is dedicated to trigger readout (slots from 4 to 12). Each TRM hosts 3 HPTDC chips that can read 8 channels. During Run 1 and Run 2 operations, when ALICE Central Trigger Processor provided an L1 trigger signal, the HPTDCs recorded hits that fell in a matching window of 600 ns, starting $t_{\text{latency}} = 9 \mu\text{s}$ before the L1 signal (which is provided with a latency of $6.8 \mu\text{s}$). The readout configuration of the TOF detector in Run 1 and Run 2 is shown in Fig. 5.5. In Run 3, the TOF detector is required to operate in continuous readout. To achieve this condition, the internal buffering capabilities of the HPTDC are fully exploited, using a matching window of $\sim 30 \mu\text{s}$ and a pseudo-trigger at a fixed frequency of 33 kHz. The readout configuration of the TOF detector in Run 3 is shown in Fig. 5.6.

- The Local Trigger Module, LTM:

The Local Trigger Module is the first level of the TOF trigger. It is responsible for receiving the output from the Front End Analogue Control board (FEAC) and transferring it to the CTTM (Cosmic and Topology Trigger Module). It is also responsible for setting and monitoring low voltages and temperatures of the Front-End electronics.

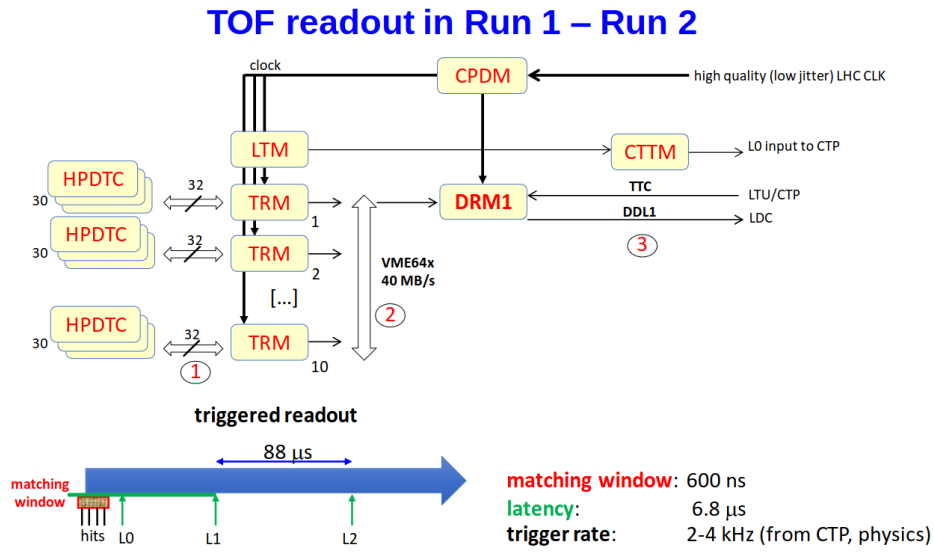


Fig. 5.5 TOF readout scheme in Run 1 and 2.

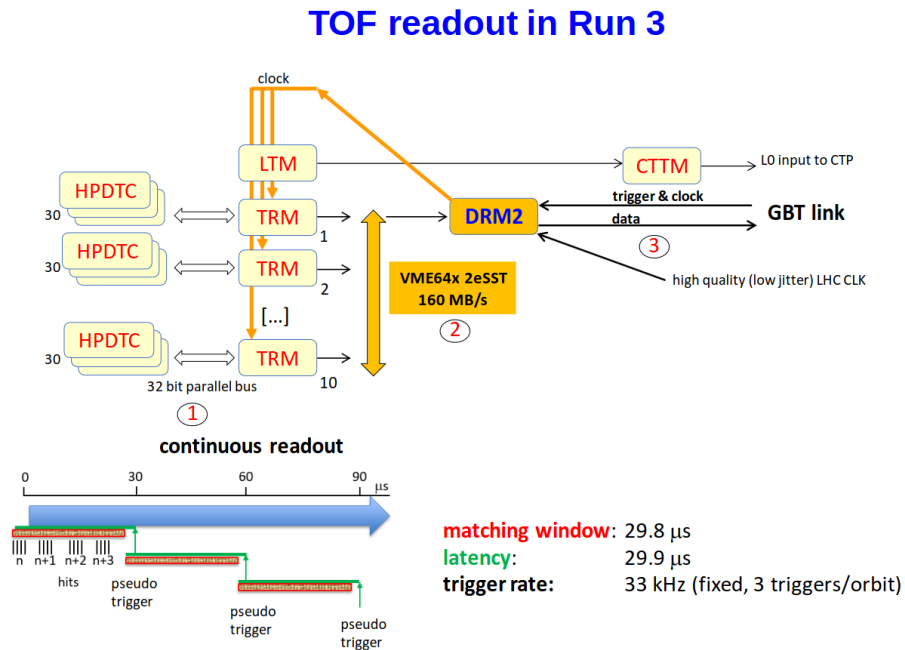


Fig. 5.6 TOF readout scheme in Run 3.

- The Clock and Pulser Distribution Module, CPDM:
Two CPDMs per Super Module propagate the LHC clock to every board of the SM crates. The common clock source ensures the synchronisation of all the TOF electronics.

- The Data Readout Module, DRM:

Each crate is equipped with a Data Readout Module (DRM) card that acts as the primary interface between the Central ALICE DAQ and TOF readout electronics. One DRM is placed in each crate and reads the data from the TRM modules. The connection with the central DAQ is ensured through optical links (DDL). In order to cope with the increase in interaction rate in Run 3, a new readout board was designed, the DRM2. This board is equipped with a faster link towards the DAQ system using the GBTx ASIC and the VTRX transceiver. During the Long Shutdown 2, the DRM2 board replaced the old DRM1. Moreover, the VME64 readout (40 MB/s) was also upgraded to VME64 2eSST protocol, yielding a data throughput of 160 MB/s over the VMEbus.

5.2 Monitoring the TOF data quality in Run 3

As discussed in Chapter 4, the new computing scheme for Run 3 replaces the traditionally separate online and offline frameworks with the unified O² (Online Offline processing). Given the integration of the online and offline computing systems, the offline Quality Assurance (QA) and the online Data Quality Monitoring (DQM), used in Run 1 and 2, are combined into a single Data Quality Control and Assessment (QC) [130]. The QC is critical to promptly identify and overcome possible problems during the data taking and to ensure that the calibration and reconstruction behave as expected synchronously and asynchronously to the data acquisition. For this purpose, it was crucial during the commissioning phase of the TOF detector in the Long Shutdown 2 (LS2) and is being successfully used in the Run 3 data-taking. The components of the Quality Control framework are illustrated in Fig. 5.7. In this scheme, there are two major computing layers: the FLP (First Level Processors) and the EPN (Event Processing Nodes). Data arrives first at the FLPs from the detector readout links, where a first data compression is performed, and the continuous data streams are split into Sub-Time Frames (TF). These frames are then transferred to the EPNs, where the information from different detectors is assembled into complete time-frames and a first synchronous reconstruction of the events is performed. During the full processing chain, QC tasks monitor the data quality and provide feedback to the central system. The QC tasks can run on the FLPs, on the EPNs or on dedicated QC servers, and the input varies depending on the processing stage and covers the whole range of data types, from raw to digitised to analysis-level objects. The output of these tasks is called QC Object (or Monitor Object, MO) and typically consists of ROOT histograms. Since the processes run on many servers in parallel, specific Merger tasks are used to unify the different outputs into a single object.

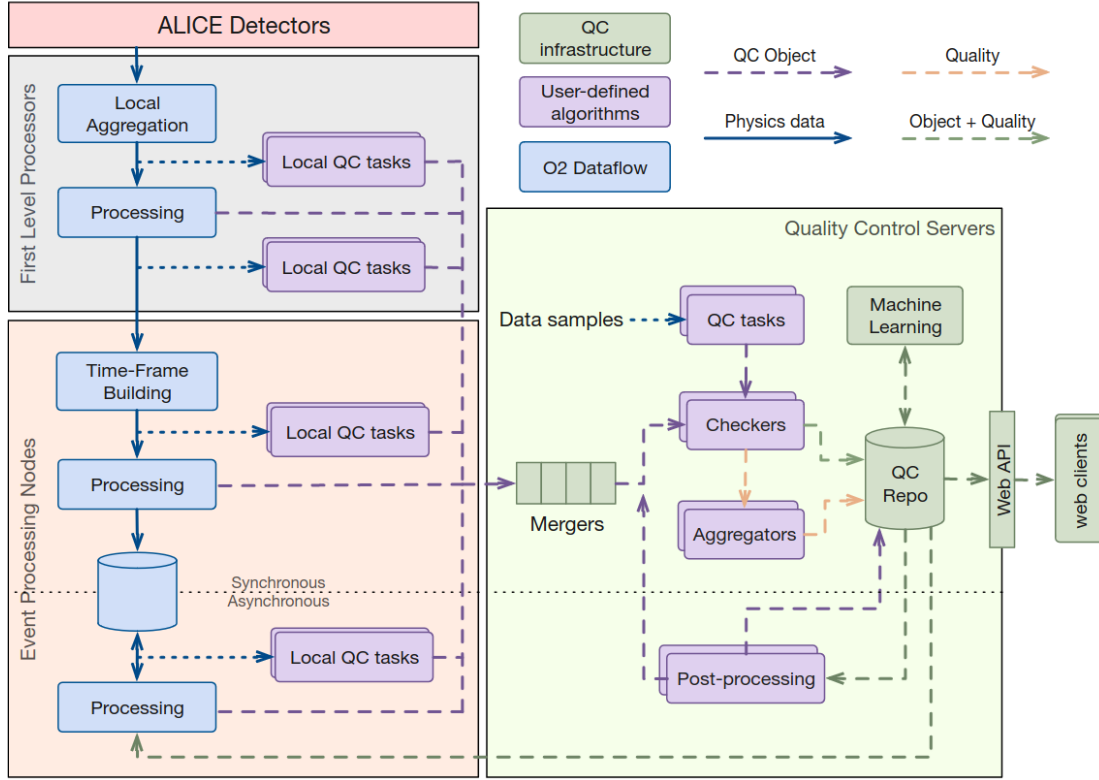


Fig. 5.7 The Data Quality Control and Assessment (QC) architecture.

Moreover, dedicated processes called Checkers automatically evaluate the data quality by running defined algorithms over the MOs. Once the QC objects are produced, they are stored in the Condition and Calibration Data Base (CCDB). The ALICE shifters and detector experts can access the MO through the QC GUI (QCG) to promptly visualise them. Specific instructions were prepared and provided to the shift crew to take action in case of problems.

5.2.1 TOF quality control during the data-taking

The status of the TOF hardware, the readout electronics, the detector occupancy, and the entire data-processing chain must be monitored during the data-taking. For this purpose, in this work, we developed specific monitoring tasks within the QC framework, which have been used since the beginning of the commissioning phase of the detector during the Long Shutdown 2 (LS2) and are being successfully used in the Run 3 data-taking. The TOF QC is composed of specialised modules which monitor the TOF raw data stream in all the steps along the reconstruction chain, i.e. before and after data reduction/compression. The TOF data-processing chain consists of several steps: the raw data (RAW) from the detector are first received and compressed at the level of the FLPs; the output of the compressor (CRAW

data) is monitored by a specific QC module ("Raw Task") and then sent to the EPNs. On the EPN nodes, the compressed raw data are handled by a decoder that converts them into a digitised format (DIGI). In case of issues in the decoding procedure, a set of diagnostic words is produced and monitored by a specific QC module ("Digits Task"). The digits are then processed by a clusterer, which groups them into clusters that contain the information needed for the final reconstruction procedure, matching the TOF hits with the tracks reconstructed by the ALICE tracking detectors. The output of the matching procedure is monitored by a specific QC module ("Matching Task"). These modules produce ~ 200 objects per run, which are stored in the CCDB and monitored online by the ALICE shift crew on the QC GUI. The TOF QC has been fundamental to quickly detect faulty conditions and wrong detector configurations during the data-taking, ensuring an excellent performance of the TOF detector in Run 3. The TOF data-processing chain consists of the following steps. During the run, it is crucial to verify that each strip is correctly recording hits. It is possible to build a map of the reconstructed hits in the whole active area of the TOF detector, which can then be compared to a reference map of the enabled channels to spot runtime readout or decoding issues. Figure 5.8 shows the hit map obtained in one run of pp collisions at $\sqrt{s} = 13.6$ TeV and Interaction Rate $IR = 500$ kHz collected in Run 3.

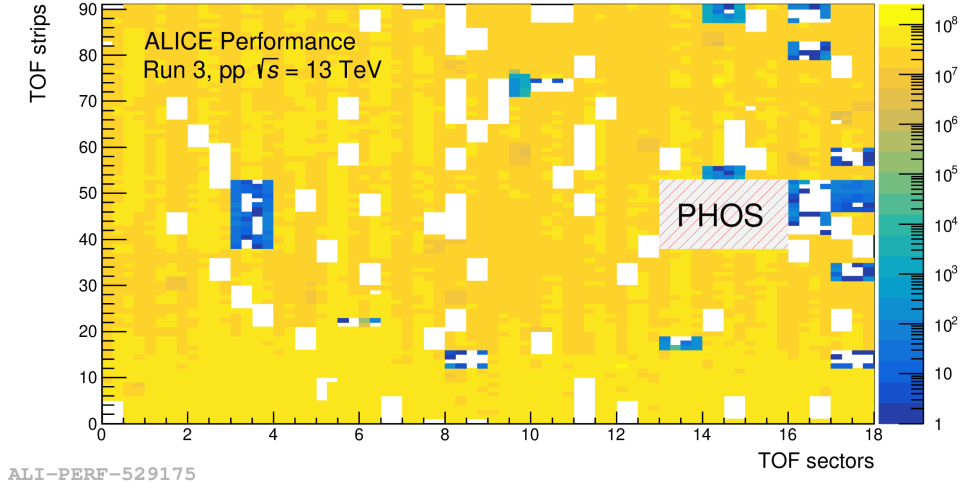


Fig. 5.8 Hit map from a pp run at $\sqrt{s} = 13.6$ TeV collected in 2022. Each bin groups hits from the 24 channels read by one FEA. To reduce the material budget in the PHOS acceptance region, the central modules of SM 13, 14 and 15 are not installed, here displayed with a box.

The x-axis displays the Super Module index ($r\phi$ coordinate), while the vertical axis refers to the strip index along the SM (z coordinate). Each bin of the histogram corresponds to 24 channels read by one FEA. Empty bins are due to the exclusion of some readout components from the data acquisition, while very high occupancy bins are related to noisy channels.

The noise level of each channel can be monitored by the QC tasks as displayed in Fig. 5.9, which shows the single channel hit rate of each channel, identified by a specific electronics index on the x-axis. Channels are flagged as noisy if their rate is above a specific threshold, configurable run-by-run. These channels are then masked in reconstruction and simulation.

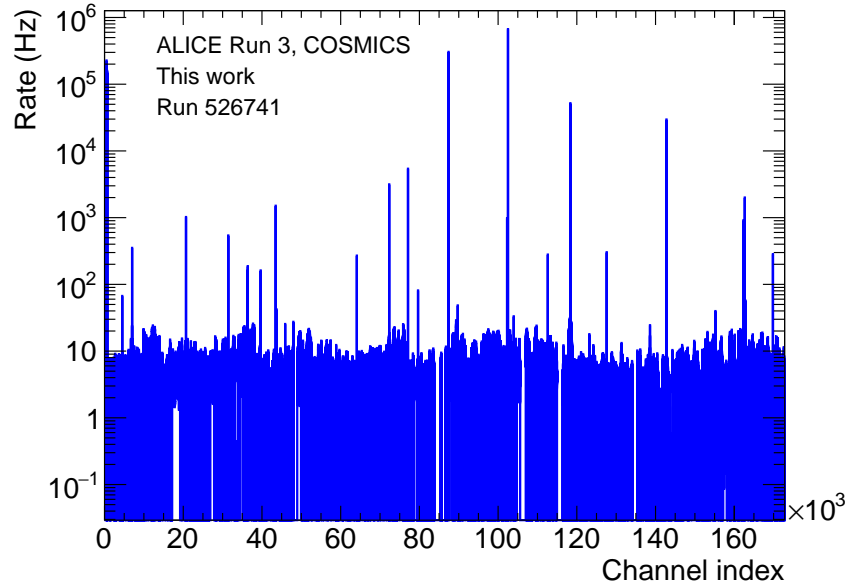


Fig. 5.9 Hit rate in TOF channels, which are flagged as noisy if their rate is above a specific threshold, configurable run-by-run. The x-axis displays the electronics index of the channel. The run displayed is a COSMIC run, i.e. without collisions.

Another interesting quantity to monitor during the data acquisition is the time recorded by the TOF detector. As discussed in Sect. 5.1.2, since the TOF is now operating in continuous readout, it is able to record all collisions in the LHC orbit. Figure 5.10 (a) shows the hit times recorded by TOF in one LHC orbit for one run of pp collisions at $\sqrt{s} = 13.6$ TeV and $IR = 500$ kHz. The pattern of the peaks in the hit time distribution reflects the LHC filling scheme² used during the acquisition of this specific run, proving that TOF is effectively able to collect all collisions in the LHC orbit. Figure 5.10 (b) shows the number of hits in the TOF detector as a function of the bunch crossing ID. This quantity also reflects the LHC filling scheme and provides a more precise discrimination of single bunch crossings. Monitoring Fig. 5.10 (b) is essential to verify the noise level of the detector, checking that the majority of the hits are grouped around a bunch crossing with filled buckets. Another critical quantity to monitor during the data-taking is the distribution of the total hit multiplicity on the TOF

²A fill starts when protons or ions are injected into the LHC, and its lifetime is related to the bunch intensity, luminosity and beam conditions. The filling scheme reflects how the LHC orbit is filled with bunches, depending on the number of full packets and the spacing between them.

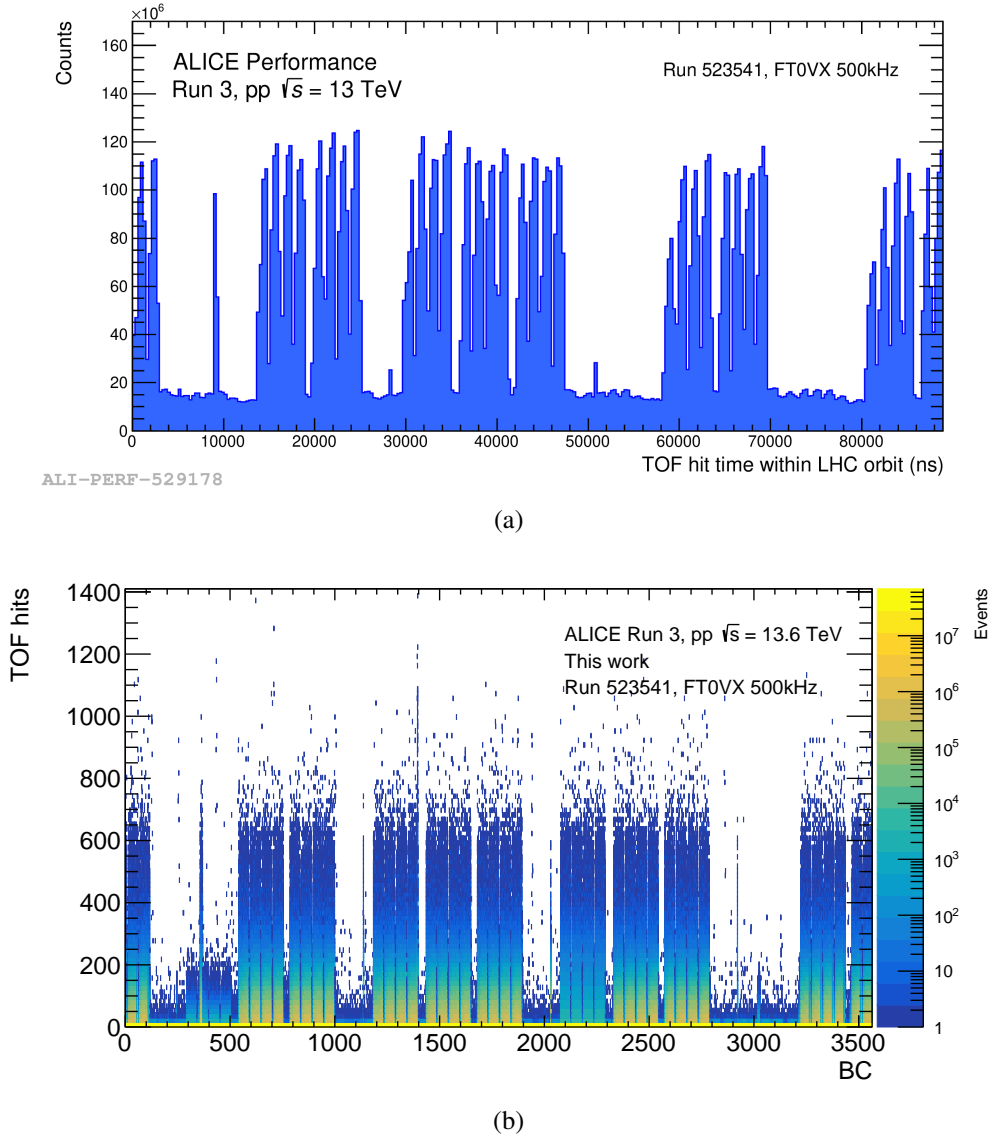


Fig. 5.10 (a) TOF hit time distribution within one LHC orbit ($88.92 \mu\text{s}$). (b) TOF hit multiplicity as a function of the Bunch Crossing ID within one LHC orbit.

detector, shown in Fig. 5.11. This distribution is important to control the detector occupancy, a crucial parameter to ensure the correct operation of the detector over the full duration of the run. An average multiplicity higher than expected could indicate the presence of noisy channels, while a lower occupancy could be a sign of readout inefficiencies. Finally, the QC tasks are also crucial to monitor possible readout errors detected during the compression and decoding procedures performed on the raw data. Different types of errors are identified through specific diagnostic words and monitored separately for each create and readout slot by the QC. Figure 5.12 reports a summary of the crates and corresponding TRM slots

where decoding errors occurred during the run. Further details on the nature of these errors are provided by complementary QC plots. This information is crucial to evaluate the true acceptance of the detector during the run, and it is accounted for in the simulation procedure.

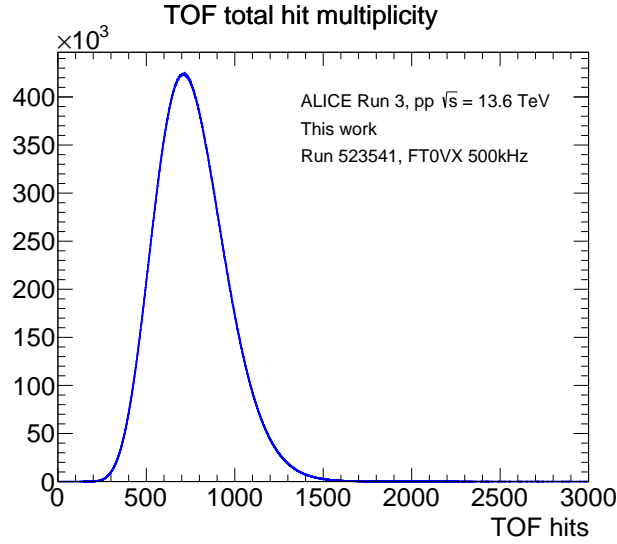


Fig. 5.11 Hit multiplicity on the TOF detector integrated in one readout window.

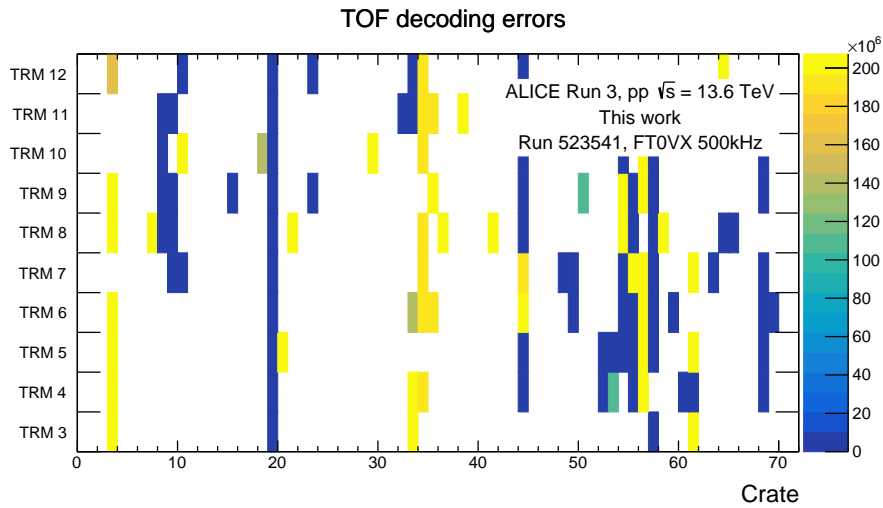


Fig. 5.12 Summary of the TRM slots and crates where readout errors detected during the run. Further details on the nature of the errors are provided by complementary QC plots.

TOF data quality in Pb–Pb collisions at 50 kHz

In October 2023, the LHC provided the first Pb–Pb collisions at $\sqrt{s_{NN}} = 5.36$ TeV and 50 kHz interaction rate. The Run 3 upgrade of the ALICE experiment was designed to allow all detectors to operate and collect data at this increased interaction rate, as discussed in Chapter 4. Therefore, monitoring the performance of the Time-Of-Flight in this new data-taking condition was crucial to ensure the correct operation of the detector in Run 3. The hit multiplicity on the TOF detector in one of these runs is shown in Fig. 5.13 (a), and the TOF multiplicity as a function of the bunch crossing ID is shown Fig. 5.13 (b), reflecting the LHC filling scheme in this run.

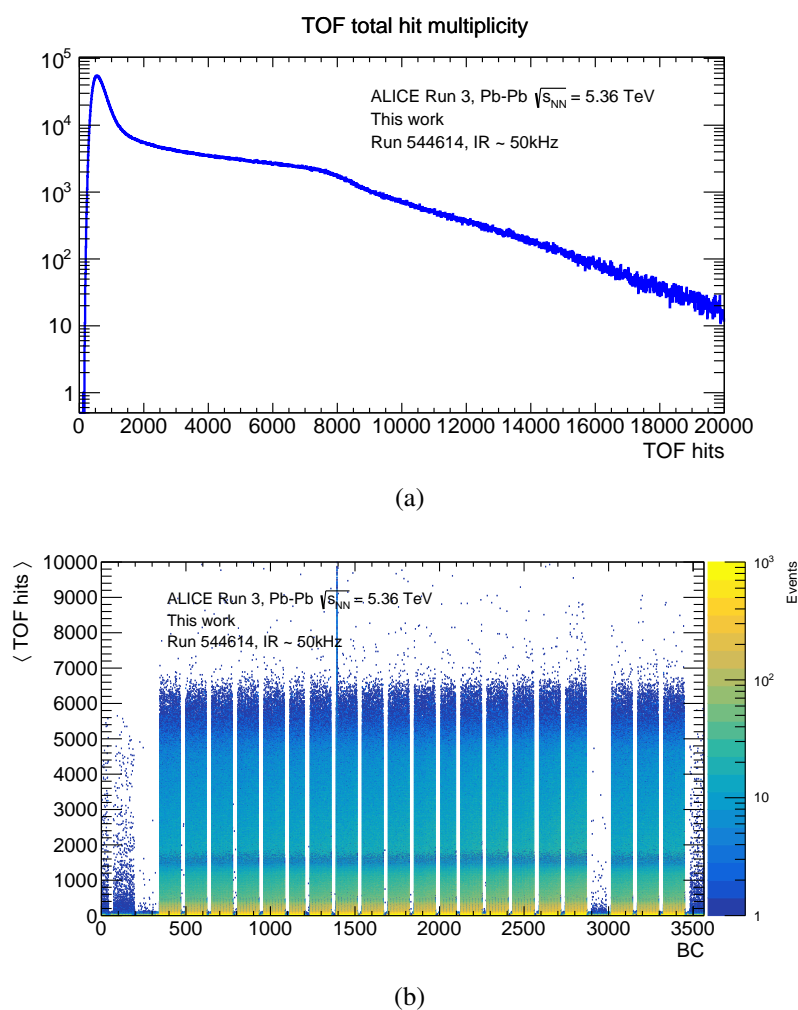


Fig. 5.13 (a) Hit multiplicity on the TOF detector in one of the first Pb–Pb collision runs at $\sqrt{s_{NN}} = 5.36$ TeV at 50 kHz interaction rate. (b) TOF hit multiplicity as a function of the Bunch Crossing ID within one LHC orbit.

5.3 TOF performance in Run 3

The TOF detector measures the times-of-flight of particles produced in the collision. This is then combined with the momentum p and the track length L measured by the ALICE tracking systems to perform the particle identification and estimate the particle mass m , obtained according to the relativistic relation in Eq. 5.1. The relative uncertainty on the mass measurement is given by:

$$\left(\frac{\Delta m}{m}\right)^2 = \left(\frac{\Delta p}{p}\right)^2 + \gamma^4 \left[\left(\frac{\Delta t}{t}\right)^2 + \left(\frac{\Delta L}{L}\right)^2 \right] . \quad (5.3)$$

The total resolution on the time-of-flight measurement ($\sigma_{\text{TOF}} \equiv \Delta t$) can be divided into several contributions:

$$\sigma_{\text{TOF}}^2 = \sigma_{\text{MRPC}}^2 + \sigma_{\text{TDC}}^2 + \sigma_{\text{FEE}}^2 + \sigma_{\text{Cal}}^2 + \sigma_{t_0}^2 , \quad (5.4)$$

where σ_{MRPC} is the intrinsic resolution of the MRPC, σ_{TDC} accounts for the resolution on the signal digitisation and σ_{FEE} accounts for the delay of the signal distribution to the Front-End Electronics (FEE). The contribution associated with the calibration procedure (σ_{Cal}) and the time resolution of the event time measurement (σ_{t_0}) also contribute to the total resolution. To ensure an excellent PID performance of the detector, it is crucial to achieve the following conditions:

- a precise measurement of the interaction time t_0 ;
- an optimal calibration of the TOF signal;
- a good matching efficiency between the TOF and the tracking detectors.

In this section, we will discuss the studies performed in this thesis to evaluate the performance of the TOF detector in Run 3. These results are obtained using the QC framework, with a set of dedicated tasks, developed in this work, that run at the level of the asynchronous reconstruction, before the creation of analysis-level objects. These tasks have been crucial to monitor the quality of reconstructed data and provide a prompt feedback to the analysers on the performance of the TOF detector in Run 3 data periods.

5.3.1 Time calibration

TOF calibrations consist of a set of corrections applied to the signal from the readout channels needed to reach the best performance of the detector in terms of efficiency, noise rejection,

and resolution. Calibrations are also applied at the simulation level, allowing to reproduce with high accuracy the conditions of the data taking. The extraction of the calibration constants requires a full track reconstruction; therefore, they are affected, to some degree, by the calibration of the tracking detectors. The TOF calibration procedures in Run 3 are performed at different stages of the data-taking and reconstruction and are calculated at the level of a single run or sub-frames of a run when conditions are expected to change rapidly. The first level of calibration is performed at the Start Of Run (SOR) from the TOF slow control system (DCS calibration). At this stage, a map of TOF active channels is stored on the CCDB. If, during the run, channels are switched off, the map is updated accordingly, keeping track of the time of the change. The second level of calibration is performed during the data-taking at the level of the EPNs (synchronous calibration). At this stage, a first synchronous reconstruction is performed on the EPN nodes, and three main corrections are extracted:

- a global offset, common to all readout channels, to account for the TOF clock shift with respect to the LHC phase;
- a single offset for each channel accounting for electronics/cable delays;
- the frequency of decoding errors occurring for each readout module.

Finally, the third level of calibration is performed asynchronously, with a better data reconstruction quality. The online calibration objects are updated at this stage, including time-slewing corrections evaluated channel-by-channel.

5.3.2 Event time measurement

The event time (t_0) is a crucial parameter in the measurement of the time-of-flight in Eq. 5.2. The collision time has a natural spread with respect to the nominal beam crossing. In fact, the bunch crossing time provided by the LHC clock (t_0^{fill}) can vary slightly within a fill and has a significant uncertainty ($\sigma_{t_0^{\text{fill}}} \approx 200$ ps), related to the finite size of the bunches (longitudinal spread σ_z) [131]. Therefore, the t_0 has to be measured on an event-by-event basis, either from information from the TOF detector itself or by other dedicated systems. In Run 3, the FT0 detector (described in Sect. 4.3.1) is specifically dedicated to the measurement of the collision event time. This detector consists of two Cherenkov arrays located on both sides of the interaction point (FT0-A and FT0-C). If the information from both FT0-A and FT0-C is available, the two measurements are combined to achieve the best quality event time (t_0^{FT0AC}) in terms of resolution, reaching values of ~ 20 ps for minimum-bias pp collisions. The collision time can also be calculated using the information of the TOF detector itself via a

dedicated combinatorial algorithm by means of a χ^2 -minimisation procedure [131]. In events with $n_{\text{trk}} \geq 3$ tracks matched to a corresponding hit on the TOF detector and satisfying a set of quality cuts, the algorithm compares the measured TOF times to the expected times, for π , K, or p mass hypotheses. We define a combination of masses \vec{m}_i , assigned independently for each track, where the index i indicates one of the possible combinations ($m_1, m_1, \dots, m_{\text{tracks}}$). The event time is the weighted average of $(t^{\text{TOF}} - t_{\text{exp},i})$:

$$t_0^{\text{TOF}}(\vec{m}_i) = \frac{\sum_{n_{\text{trk}}} w_i (t^{\text{TOF}} - t_{\text{exp},i})}{\sum_{n_{\text{trk}}} w_i} , \quad (5.5)$$

where the weights w_i are defined as:

$$w_i = \frac{1}{\sigma_{\text{TOF}}^2 + \sigma_{\text{exp},i}^2} . \quad (5.6)$$

The resolution on the event time is then given by:

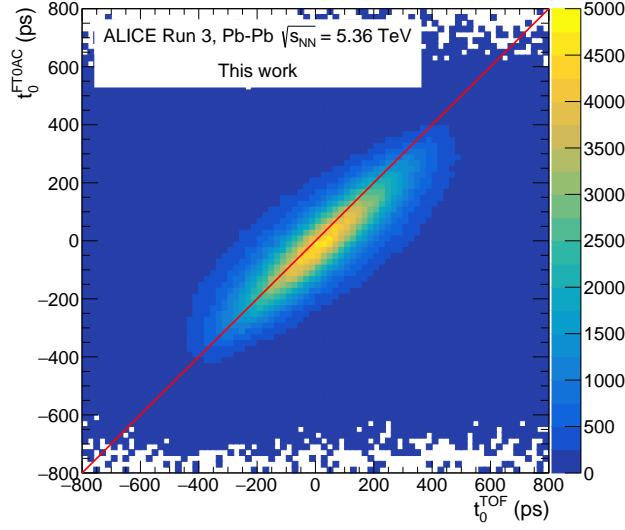
$$\sigma_{t_0^{\text{TOF}}}(\vec{m}_i) = \frac{1}{\sqrt{\sum_{n_{\text{trk}}} w_i}} . \quad (5.7)$$

The χ^2 is defined as:

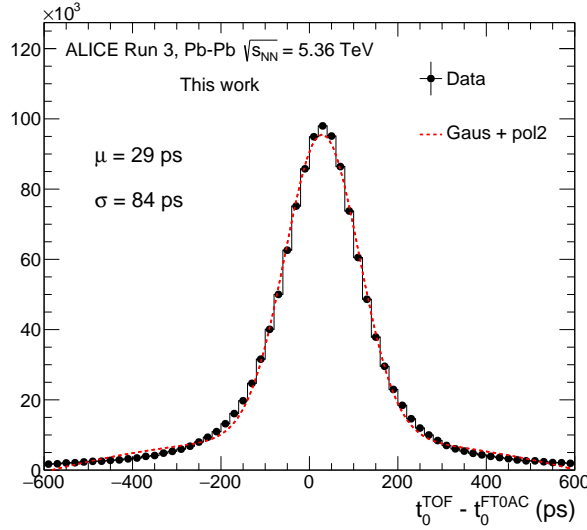
$$\chi^2(\vec{m}_i) = \sum_{n_{\text{trk}}} \frac{((t^{\text{TOF}} - t_0^{\text{TOF}}(\vec{m}_i)) - t_{\text{exp},i})^2}{\sigma_{\text{TOF}}^2 + \sigma_{\text{exp},i}^2} . \quad (5.8)$$

The combination \vec{m}_i^* which minimizes the χ^2 is used to derive via $t_0^{\text{TOF}}(\vec{m}_i^*)$ via Eq. 5.5. The procedure described above calculates the average t_0 minimisation for all n_{trk} tracks, but in reality, this has a significant computational cost, implying $3^{n_{\text{trk}}}$ operations. Therefore, the minimisation procedure is performed by classifying the tracks into sub-samples of ten tracks each. Within each sub-sample, the χ^2 value of each track is checked in order to verify that the measured time is compatible with at least one particle mass hypothesis and is not entirely uncorrelated. In the case of a track with a χ^2 value above a certain threshold, this is removed from the sub-sample, and the minimisation procedure is repeated. Moreover, to avoid auto-correlation biases, the event time calculated for each track is corrected by the contribution of that specific track in the average. This is achieved by subtracting the t_0 of the track from the average, obtaining the unbiased event time for that track. In Fig. 5.14 (a), we report the correlation between the event time measured by the TOF detector (for $n_{\text{trk}} \geq 3$) and the event time measured by the FT0 detector for Pb–Pb collisions at $\sqrt{s_{\text{NN}}} = 5.36$ TeV collected in Run 3. In addition, Fig. 5.14 (b) shows the distribution of the difference between

the two event times ($t_0^{\text{TOF}} - t_0^{\text{FT0AC}}$). The two event times are found to be very well correlated, and this correlation is expected to improve with an increasing number of tracks available for the t_0^{TOF} measurement in the event. In fact, $\sigma_{t_0^{\text{TOF}}}$ scales with the event track multiplicity as $\sim 1/\sqrt{n_{\text{trk}}}$, according to Eq. 5.7.



(a)



(b)

Fig. 5.14 (a) Correlation between the event time measured by the TOF detector and the event time measured by the FT0 detector for Pb–Pb collisions at $\sqrt{s_{\text{NN}}} = 5.36$ TeV collected in Run 3. (b) Difference between the TOF event time and the FT0 event time.

5.3.3 TOF-tracks matching efficiency

The strategy for track reconstruction in Run 3 is similar to the one used in Run 2, with few notable differences [126, 127]. In Run 3, the full tracking chain involves four main detectors: the ITS (Inner Tracking System), the TPC (Time Projection Chamber), the TRD (Transition Radiation Detector) and the TOF (Time Of Flight). The ALICE new data-taking scheme with continuous readout leads to a crucial challenge in the tracking procedure: the data are not delimited by physics triggers but composed of several continuous data streams, leading to the overlap of multiple collisions in the TPC drift time (5 collisions for 50 kHz Pb–Pb). Therefore, the TPC clusters do not have a well-defined z coordinate but only a definite time t , which requires the TPC tracking to work without a primary vertex constraint. Therefore, TPC standalone tracking is not used in Run 3, but TPC tracks are matched in a specific space-time window to the ITS, TRD or TOF detectors in order to constrain their z -coordinate. The TOF-track matching procedure has the purpose of associating each track propagated outside the TPC to a hit in the Time-Of-Flight detector. A geometrical matching window of 10 cm is used to match the intercept of the extrapolated track with a TOF sensitive layer. The matching algorithm looks for triggered TOF pads within this matching window, and if any are found, the closest one to the track extrapolation is associated to the track. Figure 5.15 shows a section of one MRPC, displaying the readout pads.

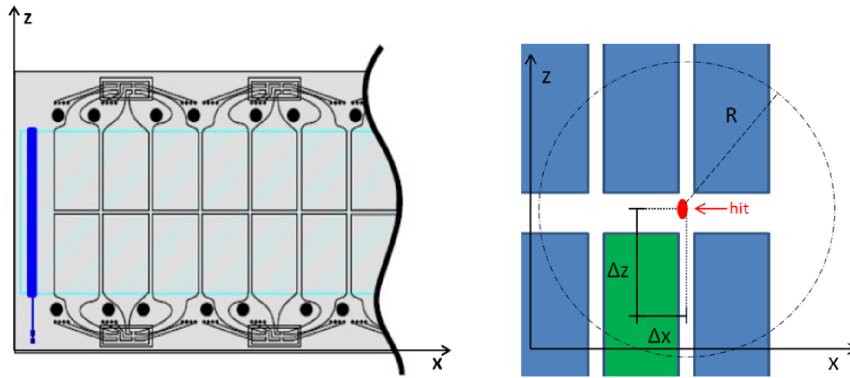


Fig. 5.15 Section of one MRPC, displaying the readout pads, after the hit of a particle. Δx and Δz are the residuals with respect to the centre of the triggered (green) pad, and R is the matching window.

We mentioned that each MRPC is segmented into two rows of 48 pickup pads, for a total of 96 pads for each strip. The variables Δx and Δz are called “residuals” and represent the spatial distances, along the x and z axes, between the centre of the triggered TOF pad and the

track extrapolation point. From the residuals, the matching χ^2 can be calculated as:

$$\chi^2 = \sqrt{\Delta x^2 + \Delta z^2} \quad . \quad (5.9)$$

For the track extrapolation to be successfully matched to a TOF hit, the χ^2 must satisfy the condition $\chi^2 < 10$ cm. Once a cluster is matched, it is removed from the sample of matchable hits to avoid double assignments. The distribution of the x and z residuals as a function of ϕ and η , respectively, are shown in Fig. 5.16 for Pb–Pb collisions at $\sqrt{s_{NN}} = 5.36$ TeV collected during the heavy-ion Pilot Run in 2022 at interaction rate ~ 30 Hz.

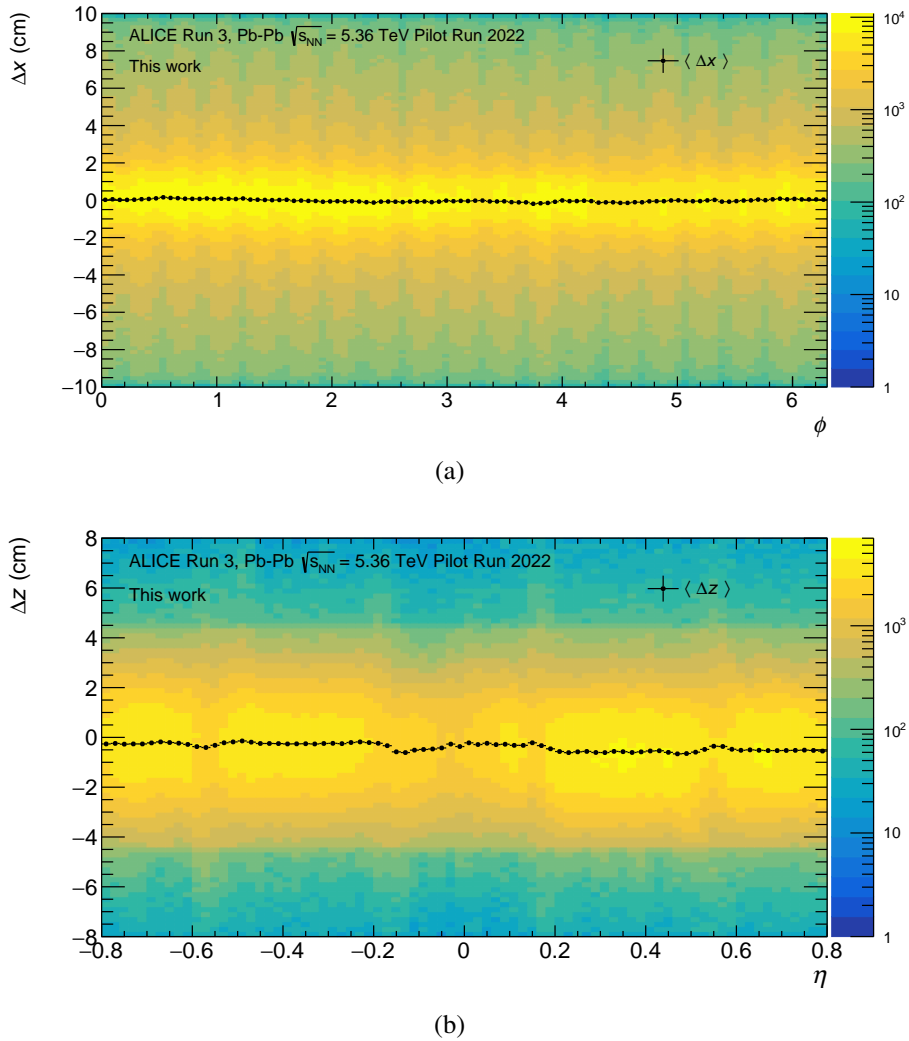


Fig. 5.16 TOF residuals along the x (a) and z (b) directions as function of ϕ and η , respectively, for ITS constrained tracks (ITS-TPC and ITS-TPC-TRD) in Pb–Pb collisions at $\sqrt{s_{NN}} = 5.36$ TeV. The average value of the residuals is indicated with black points.

The distributions are centred around zero, as expected in the case of good quality of the matching and tracking procedure. The different widths of the distributions in the x and z directions reflect the dimension of the pad, $2.5 \times 3.5 \text{ cm}^2$, and the different track resolutions along the axes. The TOF-track matching efficiency is defined as:

$$\epsilon_{\text{match}} = \frac{N_{\text{reco+matched}}}{N_{\text{reco}}} , \quad (5.10)$$

where $N_{\text{reco+matched}}$ is the number of tracks matched to a TOF hit, and N_{reco} is the total number of reconstructed tracks. Of course, the matching procedure is not immune to erroneous matching (“mismatch”). In fact, several factors can affect the matching efficiency, such as the particle interactions in the TRD passive material placed between the TPC and TOF, dead zones and switched-off channels in the detector, and possible inefficiencies of the matching algorithm itself. Moreover, the matching efficiency is also influenced by the TOF readout efficiency, as well as by the tracking performance. As a matter of fact, during the commissioning and Run 3 data-processing phases, monitoring the matching efficiency has proved to be a powerful tool to identify issues in the tracking reconstruction procedure, in addition to the TOF detector itself. The matching efficiency as measured in 2022 Pilot Run Pb–Pb collisions at $\sqrt{s_{\text{NN}}} = 5.36 \text{ TeV}$ ($\text{IR} \sim 30 \text{ Hz}$) for tracks with $|\eta| < 0.8$ is reported as a function of the particle transverse momentum in Fig. 5.17. A comparison between the efficiency obtained in the data and in the anchored MC simulation, still under development, is shown. Tracks with $p_{\text{T}} < 0.3 \text{ GeV}/c$ do not reach the TOF detector due to the curvature in the magnetic field. For higher p_{T} values, the efficiency rapidly increases saturating for $p_{\text{T}} > 1 \text{ GeV}/c$. As mentioned, the matching efficiency depends on the readout efficiency and on the number of dead zones and switched-off channels in the detector. In order to compare the efficiency among different runs, it is essential to consider these factors, which are monitored by specific QC tasks. The trending plot of the matching efficiency value for tracks with $p_{\text{T}} \sim 1.5 \text{ GeV}/c$ is reported in Fig. 5.18 for different Pb–Pb runs collected in 2022, where a comparison with the matching efficiency corrected for acceptance and readout inefficiencies (normalised) is carried out. The normalisation is expected to level the differences between runs with different readout configurations. Any further discrepancy from the trend is usually investigated in detail.

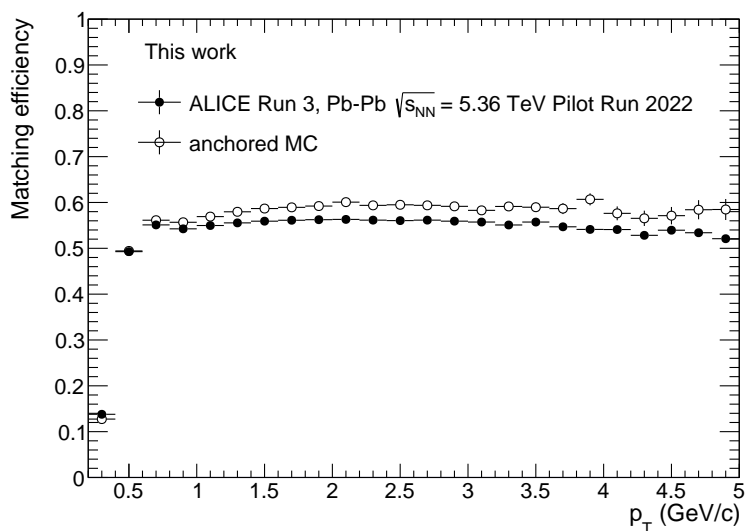


Fig. 5.17 Matching efficiency for ITS constrained tracks (ITS-TPC and ITS-TPC-TRD) with $|\eta| < 0.8$ as function of the particle transverse momentum Pb-Pb collisions at $\sqrt{s_{NN}} = 5.36$ TeV. A comparison between the efficiency obtained in the data and in the anchored MC simulation is shown.

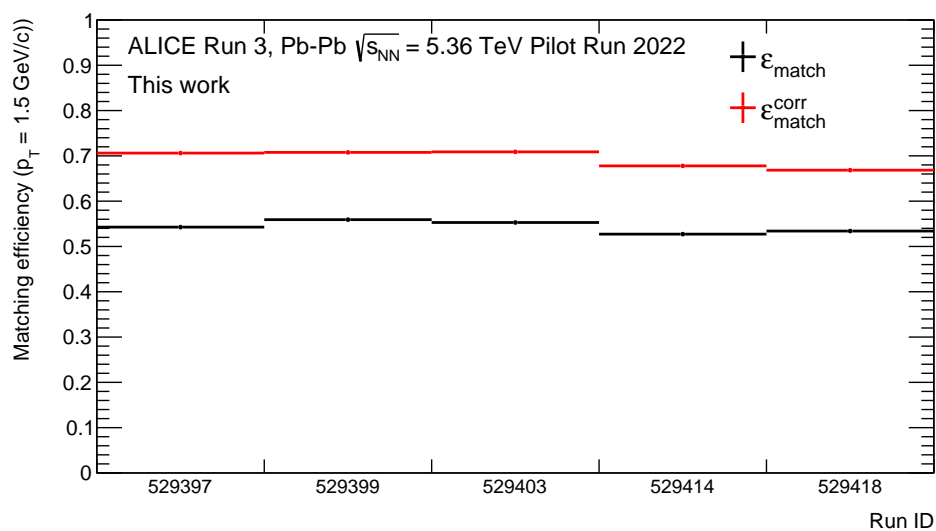


Fig. 5.18 Matching efficiency for ITS constrained tracks (ITS-TPC and ITS-TPC-TRD) with $|\eta| < 0.8$ as function of the Run ID in Pb-Pb collisions at $\sqrt{s_{NN}} = 5.36$ TeV. A comparison between the normalised efficiency, i.e. corrected for readout inefficiencies and dead channels, is shown.

5.3.4 TOF PID

In order to perform the particle identification, the time of flight t of the particle measured by TOF from Eq. 5.2 is compared to the expected flight time for a given particle species. The discriminating quantity Δt_{PID} is defined as:

$$\Delta t_{\text{PID}} = t - t_{\text{exp}} = t_{\text{TOF}} - t_0 - t_{\text{exp}} \quad , \quad (5.11)$$

The expected arrival times for a given mass hypothesis, $t_{\text{exp},i}$ for $i = \pi, K, p, \dots$, is calculated during the track reconstruction procedure as the sum of small time increments during the track propagation steps. At each reconstruction step, the track parameters are updated. Therefore, the expected times take into account the variations in the momentum along the trajectory due to the particle energy loss and interaction with the material. The resolution (σ_{PID}) on the quantity Δt_{PID} includes the contribution from the TOF time resolution in Eq. 5.4 (σ_{TOF}), defined in Eq. 5.4, and the contribution from the tracking (σ_{trk}):

$$\sigma_{\text{PID}}^2 = \sigma_{\text{TOF}}^2 + \sigma_{\text{trk}}^2 \quad . \quad (5.12)$$

The separation power is measured in terms of $n\sigma$, and for Δt_{PID} can be defined as:

$$n\sigma = \frac{\Delta t_{\text{PID}}}{\sigma_{\text{PID}}} \quad . \quad (5.13)$$

A higher separation power is reached for a better resolution on Δt_{PID} . Figure 5.19 shows the distribution of Δt_{PID} for pions, kaons and protons as a function of the transverse momentum in Pb–Pb collisions at $\sqrt{s_{\text{NN}}} = 5.36$ TeV. From the time-of-flight measurement, it is possible to extract the particle $\beta = v/c$ and the particle mass from Eq. 5.1. An example of the separation achieved by the TOF detector in the measurement of hadron masses in Pb–Pb collisions at $\sqrt{s_{\text{NN}}} = 5.36$ TeV is shown in Fig. 5.20 for $1.4 < p < 1.5$ GeV/c. The performance in Fig. 5.19 and 5.20 are obtained using the QC framework, which implements a rather loose set of quality cuts on the tracking and matching procedures. At the analysis level, this performance can be further improved by applying tighter cuts on the track quality and by constraining the TOF matching window to reduce the impact of mismatch.

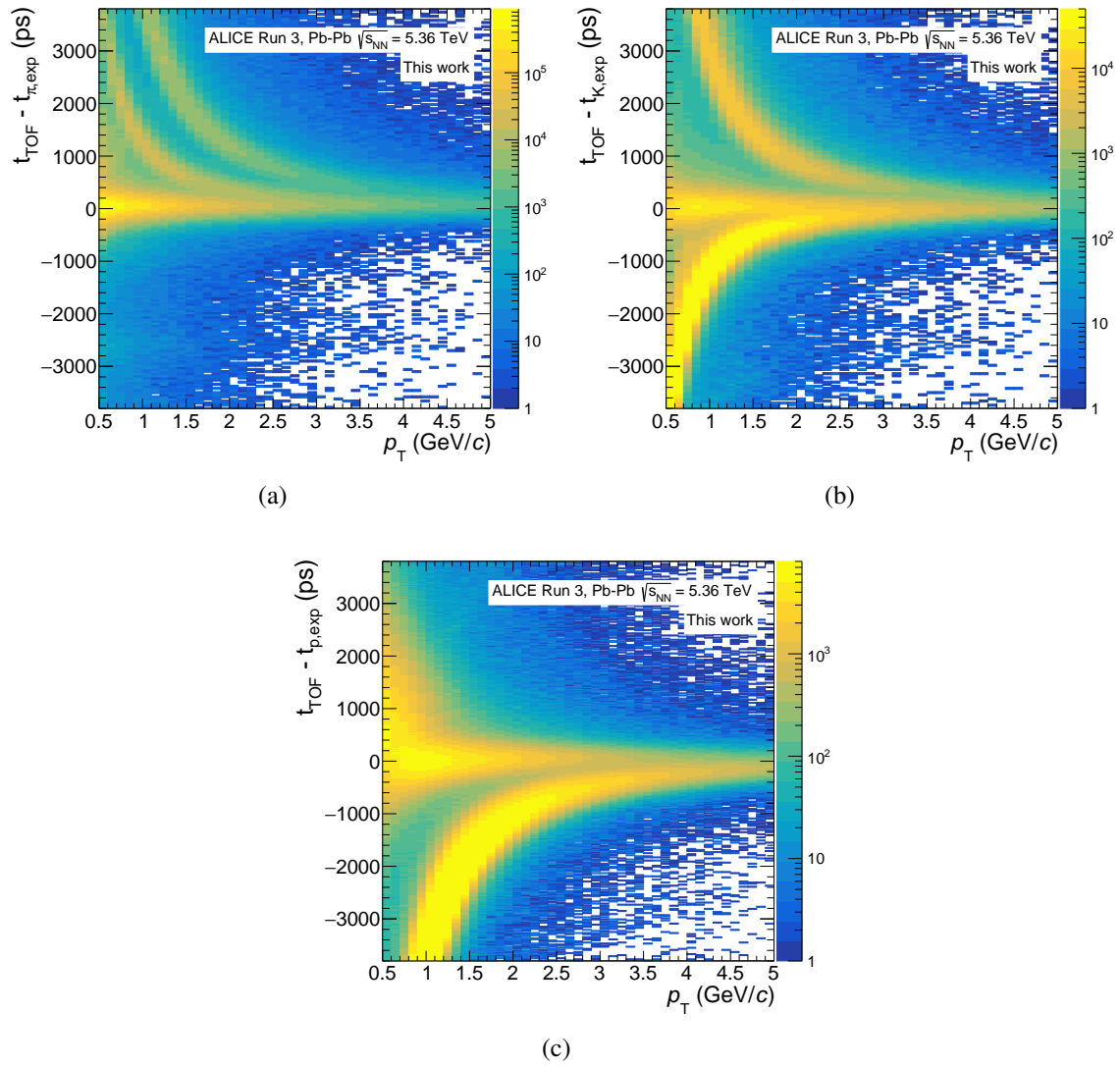


Fig. 5.19 ($t - t_{\text{exp}}$) for pions (a), kaons (b) and protons (c) mass hypotheses in Pb-Pb collisions at $\sqrt{s_{\text{NN}}} = 5.36$ TeV.

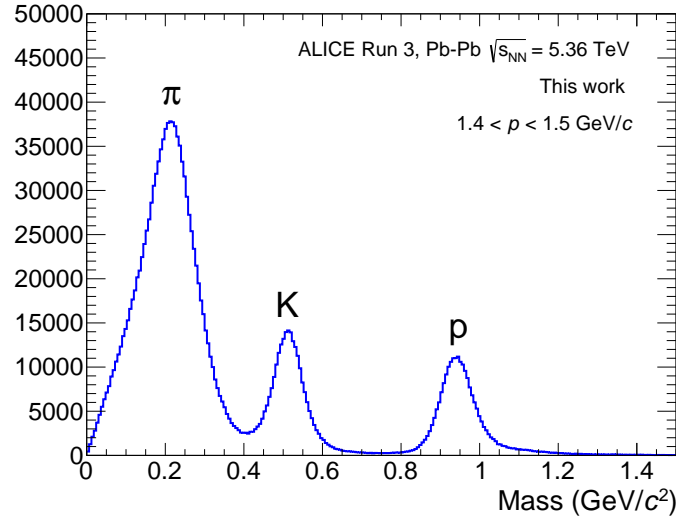
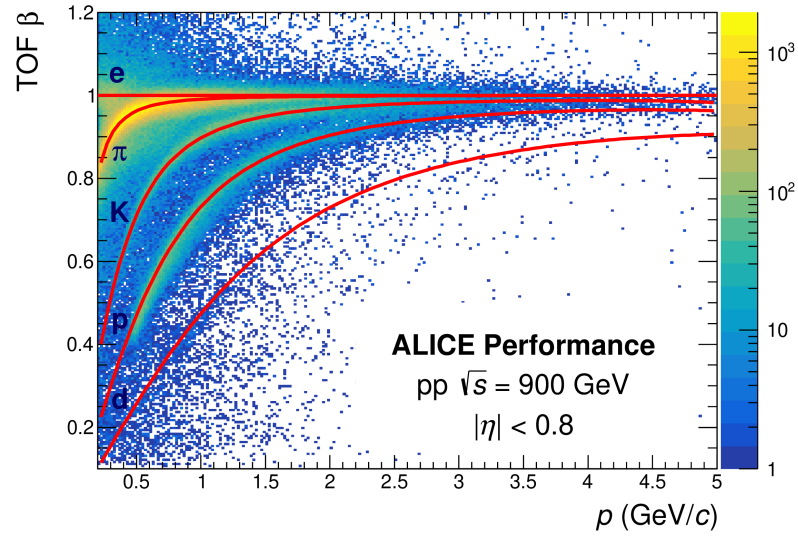


Fig. 5.20 Particle mass extracted from the time-of-flight measurement in Pb–Pb collisions at $\sqrt{s_{\text{NN}}} = 5.36$ TeV.

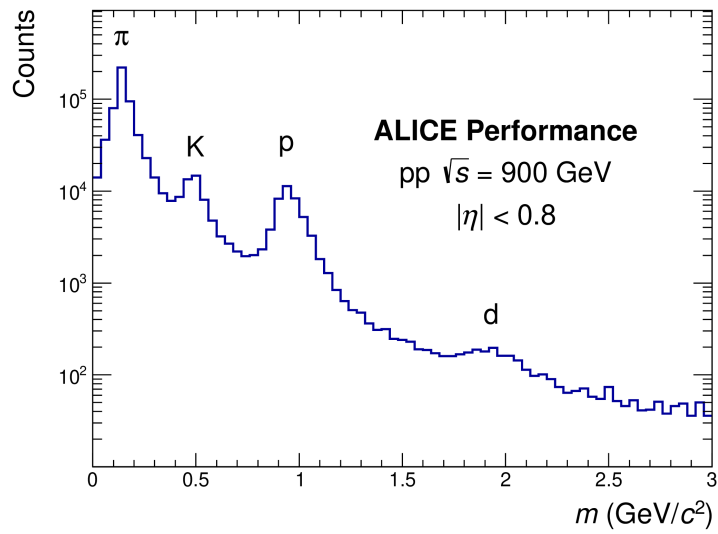
5.3.5 Commissioning and Pilot Run 2021

In 2021, the TOF detector started its commissioning phase after the Long Shutdown 2 (LS2). During this period, the detector was mainly operated in a standalone mode, i.e. without other ALICE detectors, collecting cosmic data and testing the detector performance, readout chain and quality assurance procedures. The tasks developed in the context of this work within the QC framework were crucial in this phase in order to monitor the detector performance through the entire data flow. During November 2021, the LHC delivered the first pp collisions at $\sqrt{s} = 900$ GeV after years of technical stop. On this occasion, ALICE performed the first global data-taking, called Pilot Run, with almost all detectors in operation. TOF was operated for the first time in continuous readout mode with 68/72 active data links, corresponding to 96% of the detector's active area. Figure 5.21 shows the first results on the performance of the TOF detector operating in continuous readout. In particular, the particle β as a function of momentum and the particle masses distribution are reported in Figure 5.21 (a) and (b), respectively. The pions, kaons, and protons separation can be clearly observed in these plots, and the preliminary performance of the TOF detector in the first data-taking after LS2 proved to be in line with the expectations. We obtained these results just a few days after the Pilot Run, proving the readiness of the TOF detector for Run 3 several months before the data-taking started.



ALI-PERF-499091

(a)



ALI-PERF-499095

(b)

Fig. 5.21 (a) Particle β as a function of the momentum and (b) particle mass extracted from the time-of-flight measurement in the first Pilot Run pp collisions at $\sqrt{s} = 900$ GeV during November 2021.

5.3.6 Performance in Run 3

After 15 years from the LHC start, the ALICE TOF detector evolved to operate in Run 3 in continuous readout mode, showing very stable operations and excellent PID performance. In this chapter, we showed several results on the performance of the TOF detector in Run 3, mostly obtained using the QC framework, which implements a basic set of quality cuts on the reconstructed data. A more detailed analysis of the detector performance can be carried out at the analysis level, where tighter cuts on the track quality, the matching procedure, and the event time determination can be applied. The first high-quality measurement of TOF time resolution in Run 3 was obtained in pp collisions at $\sqrt{s} = 13.6$ TeV, finding results at the level of ~ 80 ps. Figure 5.22 shows the distribution of the variable $(t - t_0^{\text{FT0}} - t_{\text{exp},\pi})$ for tracks with $p_T \sim 1.5$ GeV/c. The event time is measured using the FT0 detector, which is expected to provide the most precise measurement of the collision time with a resolution of 20 ps.

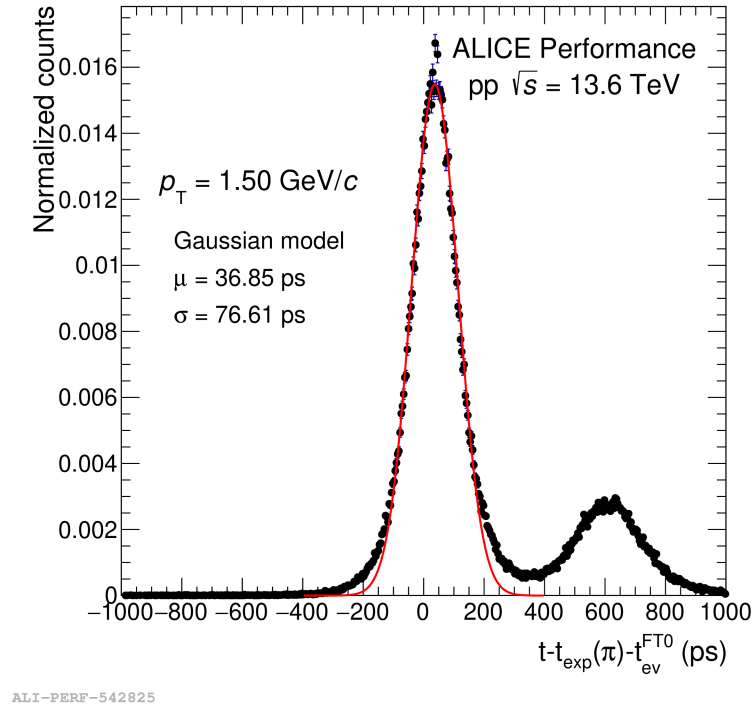


Fig. 5.22 Difference between the TOF and expected time-of-flight $(t - t_0^{\text{FT0}} - t_{\text{exp},\pi})$ for tracks with $p_T \sim 1.5$ GeV/c in $\sqrt{s} = 13.6$ TeV collected in Run 3. The event time is measured using the FT0 detector.

Chapter 6

Strangeness enhancement with multiplicity and effective energy

In Chapter 2, we introduced the concept of strangeness enhancement, i.e. the enhanced production of strange hadrons in heavy-ion collisions relative to that in minimum-bias pp collisions. At the LHC, the ALICE experiment proved that small systems show striking similarities with Pb–Pb collisions when multiplicity dependent studies are performed. The ratio of strange hadron yields to pions was found to increase with the charged particle multiplicity starting from pp and p–Pb collisions, evolving smoothly across different collision systems and energies, reaching Pb–Pb collisions. One of the main challenges in high-energy hadron physics remains the understanding of the origin of strangeness enhancement with multiplicity in small collision systems. This work exploits a novel approach to study strangeness production in pp collisions, introducing, for the first time, the concept of effective energy in hadronic collisions at the LHC. As presented in Chapter 3, the multiplicity of charged particles in pp collisions is characteristic of the final hadronic state of the interaction and also provides information on its initial stages, being strongly correlated with the effective energy available for particle production. This energy is reduced with respect to the total centre-of-mass energy due to the production of leading nucleons, which carry away a fraction of the available energy. In particular, the energy of very forward emitted baryons is measured through the ALICE Zero Degree Calorimeters (ZDC), which are well suited to detect the energy deposits of leading nucleons, as discussed in Chapter 4. This analysis investigates for the first time the dependence of strange particle production with the multiplicity and the leading energy through a multi-differential technique, in order to disentangle effects correlated with the initial stages of the collision from processes connected to final state effects. In fact, the charged-particle multiplicity and ZDC energy are measured in rapidity regions that are causally disconnected in the evolution of the system. Disentangling the

dependence of strange particle production on the multiplicity and on the effective energy could be crucial to shed light on the nature of the similarities observed between small and large collision systems.

6.1 Analysis Strategy

As a first step, this analysis selects Minimum Bias pp collision events, which successfully pass a list of quality requirements. A description of all the event selections applied for this purpose is reported in Sect. 6.3. The selected events are then divided into several percentile classes, defined from the information provided by VZERO and ITS detectors. The VZERO classes are built from the total charge deposited in the forward region in the VZERO-A and VZERO-C detectors, while the ITS classes are defined from the number of hits (clusters) measured by the Silicon Pixel Detectors (SPD) layers. These selections are optimised to classify events based on two topologies:

- events characterised on average by the same charged-particle multiplicity produced in the event;
- events characterised on average by the same very forward energy detected by the ZDC.

The definition of multi-differential classes is discussed in Section 6.3. The average pseudorapidity density of primary charged particles is measured at midrapidity $|\eta| < 0.5$ from the number of short track segments (tracklets) extracted from hits between the two SPD layers and the primary vertex. The measurement of the average forward energy is extracted from the signal distribution measured in the ZN detectors, as described in Sect. 6.3. The identification of K_S^0 , Λ , $\bar{\Lambda}$, Ξ^- and $\bar{\Xi}^+$ hadrons is performed through their weak decays into charged hadrons, as discussed in Sect. 6.6. In each event class, the invariant mass of the hadron candidates is then extracted in different p_T intervals. Through a signal extraction procedure, the yields of the different particle species are obtained in each p_T bin (raw p_T spectra), as described in Sect. 6.6.1. The contamination from secondary Λ and $\bar{\Lambda}$ originating from Ξ^\pm decays is calculated using the measured Ξ^\pm p_T spectra and MC simulations. Details on this procedure are provided in Sect. 6.6.2. The raw yields are then corrected by several factors before obtaining the final p_T dependent yields. First, the transverse-momentum distributions are corrected by the reconstruction efficiency of the specific particle species, which is obtained from MC simulation as the ratio between the number of reconstructed and generated strange hadrons. Details on the efficiency correction procedure are provided in Sect. 6.6.3. The measured transverse momentum spectra are then corrected for normalisation corrections to account for event and signal loss due to the event selection. These corrections

are computed using MC simulations and are described in Sect. 6.6.5. The p_T integrated yields are then computed from the corrected spectra in the measured ranges and using a fit extrapolation for the unmeasured regions. Finally, a detailed description of the systematic uncertainties considered for this analysis is provided in Sect. 6.7.

6.2 Data and Monte Carlo samples

The data used for this analysis were collected in 2015, 2017, and 2018 during LHC pp runs at $\sqrt{s} = 13$ TeV, in specific data-taking periods where the ZDC were switched on. A limited half-crossing angle of the beams in the vertical plane was applied in these runs, corresponding to $+45 \mu\text{rad}$ for 2015 data and $+70 \mu\text{rad}$ for 2017 and 2018 data. This configuration guarantees that all the neutrons emitted at very forward rapidities fall within the ZN geometric acceptance. The acceptance of the neutron calorimeter is not affected provided that the vertical half-crossing angle is smaller than $+60 \mu\text{rad}$ for a nominal vertex vertical position on the LHC axis ($y_{\text{vtx}} = 0$ mm), and smaller than $+79 \mu\text{rad}$ for a position of $y_{\text{vtx}} = -1$ mm. The y_{vtx} is found to be equal to 0 mm for 2015 data, and equal to -1 mm for 2017 and 2018 data. The selected dataset contains 43 runs collected in 2015 (42×10^6 events), 9 runs collected in 2017 (37×10^6 events) and 9 runs collected in 2018 (50×10^6 events), for a total of $\sim 130 \times 10^6$ collisions. Monte Carlo (MC) simulations are needed to compute the reconstruction efficiency of strange hadron candidates and to calculate the correction factors applied to the p_T spectra. The MC samples used for this work are generated with the PYTHIA8 (PYTHIA6) event generator, based on GEANT4 (GEANT3), to describe the propagation of particles through the detector. The simulations are anchored to the data samples, reproducing the configuration of the detector during the data acquisition. In particular, the MC samples anchored to the data collected in 2015 were simulated with the PYTHIA6 generator, while the samples anchored to the data collected in 2017 and 2018 are based on the PYTHIA8 event generator. The reconstruction efficiency of Ξ baryons is calculated using a dedicated MC sample simulated injecting one Ξ^- or Ξ^+ particle per event to increase the statistics of the simulated dataset. For all other corrections, a General Purpose MC is used.

6.3 Event selection and classification

A minimum bias (MB) event trigger is used in this analysis, which requires coincident signals in the VZERO detectors to be synchronous with the bunch crossing time defined by the LHC clock. In order to keep the conditions of the detectors as uniform as possible and

reject background collisions, the coordinate of the primary vertex along the beam axis is required to be within 10 cm from the nominal interaction point. The contamination from the beam-induced background is removed offline using the VZERO detectors and taking into account the correlation between tracklets and clusters in the SPD detector [99]. Events with more than one reconstructed primary interaction vertex (in-bunch pile-up) identified with the SPD are tagged as pile-up and removed from the analysis [99]. In addition, events with pile-up occurring during the drift time of the TPC are rejected based on the correlation between the number of SDD and SSD clusters and the total number of clusters in the TPC, as described in Ref. [132]. To further suppress the pile-up contribution, mostly from out-of-bunch collisions, it is requested that at least one of the tracks from the decay products of the (multi-)strange hadron under study is matched in either the ITS or the TOF detector. The final results are reported for the $\text{INEL} > 0$ event class, defined by requiring at least one reconstructed primary charged particle within the pseudorapidity interval $|\eta| < 1$. After applying these requirements, a total of 1.29×10^8 MB events were selected. The collisions which successfully pass these quality requirements are divided into event classes based on three topologies:

- **Fixed multiplicity selection:** event classes characterised on average by the same charged-particle multiplicity produced in the event and different energy detected by the ZDC;
- **Fixed leading energy selection:** event classes characterised on average by the same very forward energy detected by the ZDC and different multiplicity produced;
- **Standalone selection:** event classes characterised on average by different multiplicity and ZDC energy deposits.

The event classes are defined through two event estimators, a forward one (VZEROM) and a midrapidity one (SPDClusters). The VZEROM estimator is based on the signal amplitude measured by the VZERO detectors (VZERO-A + VZERO-C), which reflects the total charge deposited in the forward region and is proportional to the multiplicity of charged particles produced at midrapidity. The SPDClusters estimator is based on the number of hits (clusters) measured at midrapidity by the two SPD layers (Layer0 + Layer1). The signals measured by the VZERO and SPD detectors are divided into percentile classes, which reflect the fraction of events in each interval over the total number of events. For instance, the VZEROM class 0-1% corresponds to the 1% of events characterised by the highest VZERO amplitude, and the same applies to the other percentile classes. The VZERO signal amplitude distribution and the SPD number of clusters divided into percentile classes are shown in Fig. 6.1.

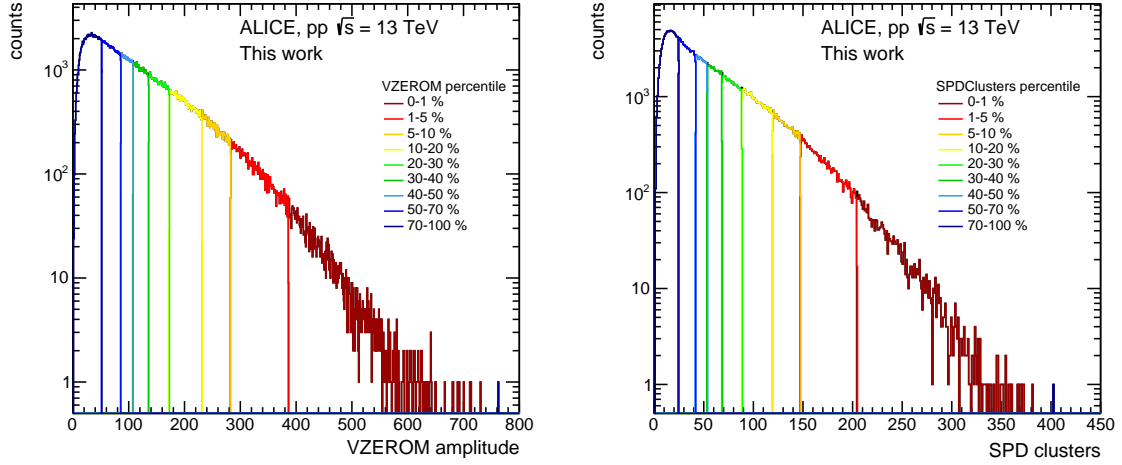


Fig. 6.1 Distribution of the VZERO amplitude (left) and SPD clusters (right) in a subset of pp collisions at $\sqrt{s} = 13$ TeV considered for this analysis. VZERO and SPDClusters percentile classes are defined starting from these distributions.

6.4 Multiplicity and forward energy measurement

In this analysis, the strange hadron production is studied as a function of the charged-particle multiplicity and the forward energy deposited in the ZDC. The average pseudorapidity density of primary charged-particles $dN_{\text{ch}}/d\eta$ is measured at midrapidity $|\eta| < 0.5$ from the number of short track segments formed using the position of the primary vertex and all possible combinations of hits between the two SPD layers. The value is then corrected for the background from secondary particles as well as for efficiency and detector acceptance using the technique described in Ref. [133]. The very forward energy is measured as the amplitude of the signal detected by the Zero Degree Calorimeters. In pp collisions, the energy detected by ZN is mainly due to neutrons, with a small contribution from photons at low energies, while the energy detected by ZP is primarily due to protons, with a small contribution from positive pions. As described in Section 4.2.2, in Pb–Pb collisions, the energy calibrations of ZN and ZP spectra are performed using the narrow peaks measured from the detection of single nucleons. In pp collisions, there is no reliable way to calibrate the calorimeter spectra in energy units without introducing model dependencies. In this analysis for the final results, we use self-normalised quantities, namely signals normalised to their average minimum-bias value, which allow us to overcome this problem and be directly comparable to model predictions. Quality checks on the ZDC signals were performed, prior to the complete analysis, to ensure that the events selected contained good quality information from the forward calorimeters. The correlation between the energy emitted at forward and

backward rapidities is shown in Fig. 6.2, for ZN (left) and ZP (right). The detected energy in the calorimeters shows no significant correlation between the A and C sides, suggesting no correlation between the leading protons and neutrons emitted in the event, as discussed in Chapter 4. However, a subset of the event sample seems to be partially correlated, in particular for neutron emission. In both cases, the detected energies show some asymmetric features, i.e. a high energy deposit on one side corresponds to a very low energy deposit on the opposite side. This effect was investigated in Ref. [88] using MC generators, and the observed asymmetry is ascribed to an effect of the limited and not overlapping pseudorapidity ranges covered by the neutron and the proton detectors.

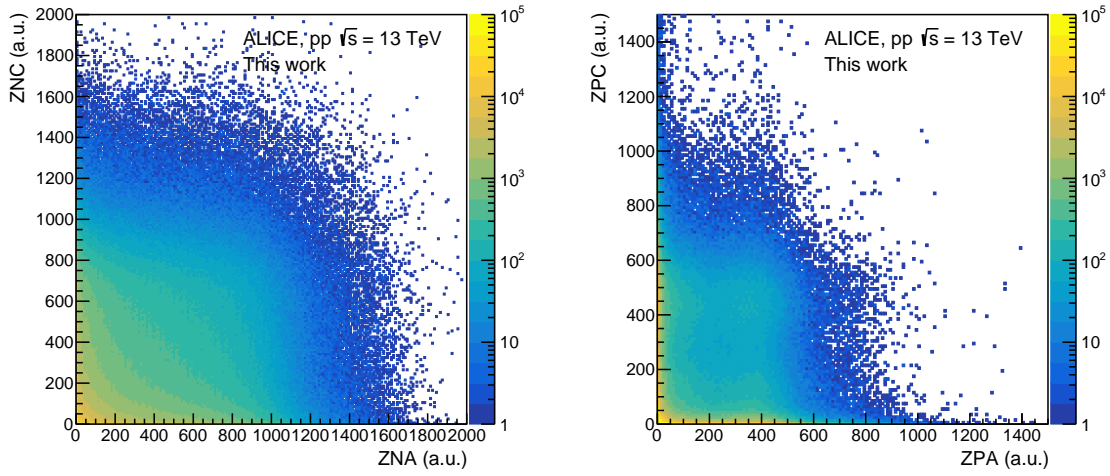


Fig. 6.2 A- vs. C-side signal in ZN (left) and ZP (right).

6.4.1 ZDC energy calibration

The ZDC response was compared for the three data-taking periods, and few differences were observed. For this reason, a calibration procedure was applied to get a uniform average response through the entire data sample by re-absorbing the discrepancies between datasets. The ZN and ZP signals were calibrated separately for A and C sides using as a reference the distribution of the signal measured in the A-side neutron calorimeter in the 2017 data sample. For each run, a calibration constant was applied to the ZN-A, ZP-A, ZN-C and ZP-C signals, as reported in Fig. 6.3. After this calibration procedure, the signals measured in the three data-taking periods are found to be compatible within the uncertainties, as shown in Fig. 6.4. The capability of the ZDC to estimate the effective energy, measuring the energy deposits of leading baryons, mainly depends on its acceptance, as discussed in Sect. 4.2.2.

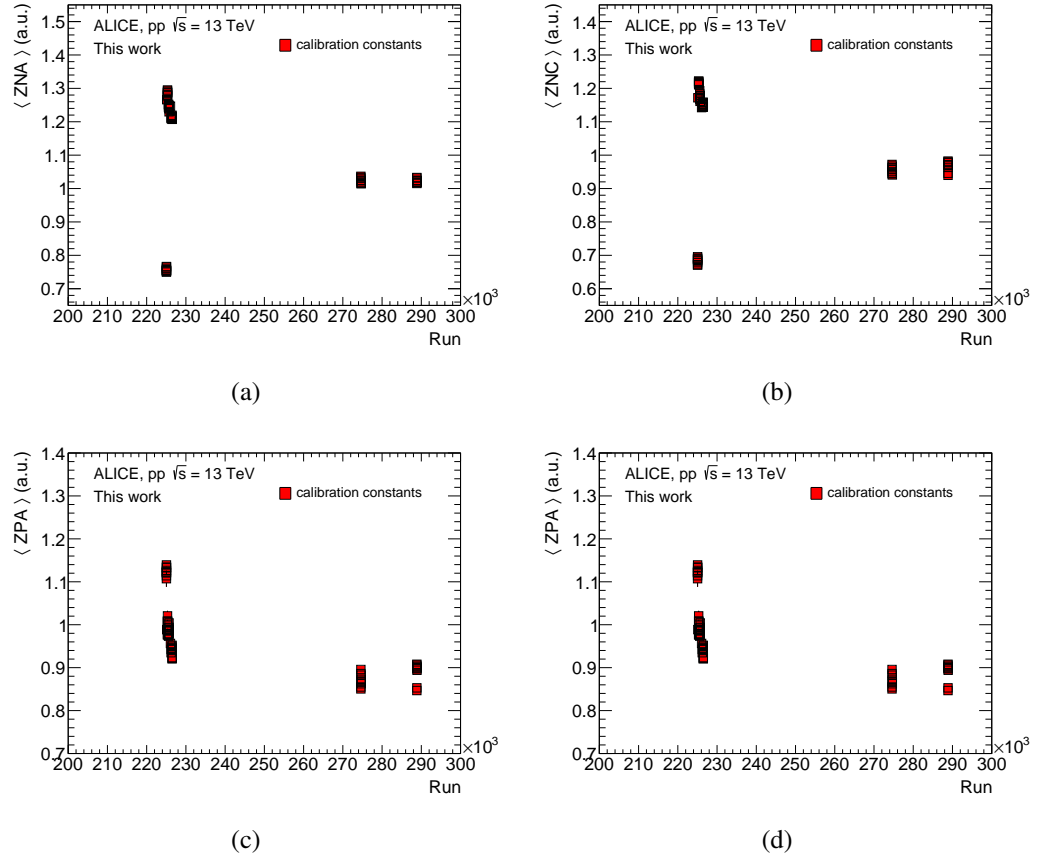


Fig. 6.3 Run-by-run ZDC calibrations aligned to LHC17j A-side neutron calorimeters.

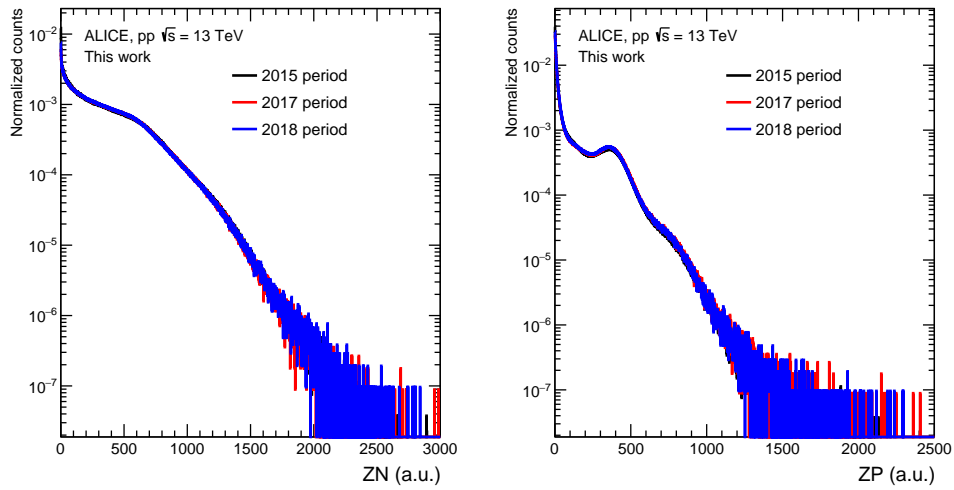


Fig. 6.4 Signal in the neutron and proton calorimeters for the three data-taking periods after calibrations were applied.

In particular, the proton calorimeter is also affected by the limitations related to the beam optics deflection of protons. This can lead to underestimating the energy event-by-event due to hadronic showers not being fully contained. Therefore, the signal from ZP is found to be much less clean with respect to the one from ZN. In order to avoid introducing any bias in our measurement, we decided to use only the signal from ZN in our final results. This choice does not affect our capability to use the forward energy as a proxy for the effective energy. In fact, in pp collisions, the proton beams carry a baryon number flux, which must be conserved in the interaction through both leading protons and neutrons emission. The final results were also cross-checked using the ZP and ZN+ZP signals, and no significant differences were observed. The correlation between the energy detected by ZN and the leading energy ($E_{(|\eta|>8)}$) was studied using full GEANT3 simulations with four MC generators (Pythia8, EPOS-LHC, Pythia6 and Phojet). Figure 6.5 (a) displays the correlation between the reconstructed ZN energy in arbitrary units and the true leading energy in VZEROM and SPDClusters classes. The ZN energy shows a strong correlation with the true leading energy in all models, consistent for the two percentile estimators. Figure 6.5 (b) shows the correlation between the self-normalised quantities, namely signals normalised to their average minimum-bias value, which is found to be model-independent. For this reason, in this analysis, we make use of self-normalised quantities, which allow us to be directly comparable to the leading energy in model predictions.

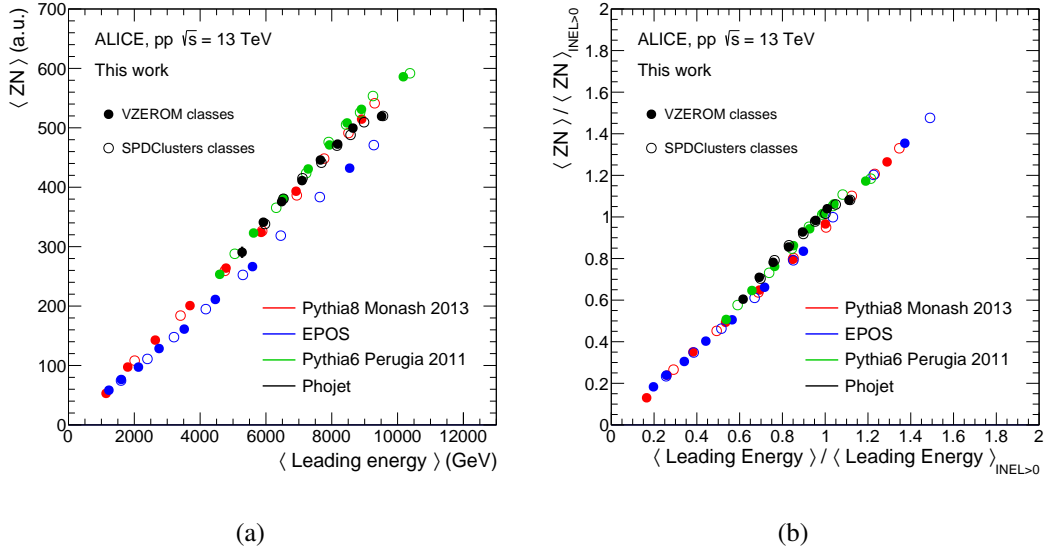


Fig. 6.5 (a) Leading energy correlation with ZN energy in VZEROM and SPClusters classes using full GEANT3 simulations with four MC generators: Pythia8, EPOS-LHC, Pythia6 and Phojet. Self-normalised quantities are shown in (b). The leading energy is defined as the energy of primary particles with $|\eta| > 8$.

6.5 Definition of multi-differential classes

The ALICE Collaboration has studied the forward energy detected by the ZDC as a function of the charged-particle multiplicity produced at midrapidity [88]. This measurement showed that the two quantities are anti-correlated: the higher the activity measured at midrapidity, the smaller the forward energy. We reproduced this result in Fig. 6.6, which shows the self-normalised ZN signal as a function of the self-normalised charged-particle multiplicity measured at midrapidity in pp collisions at $\sqrt{s} = 13$ TeV. In this plot collision events are divided into VZEROM percentile classes, from here referred to as Standalone selection. The observed behaviour in Fig. 6.6 can be explained in terms of the leading effect, since the energy deposit in the calorimeters is proportional to the energy of leading particles. Therefore, a high (low) ZDC deposit corresponds to a low (high) effective energy available for particle production, and, consequently, low (high) midrapidity multiplicity, as displayed in the sketch in Fig. 6.7. As discussed in Section 6.3, in the final results of this analysis, the events are classified using a combination of percentile selections based on the total charge deposited in the forward region in the VZERO detectors (VZEROM amplitude) and on the number of hits (clusters) measured by the SPD. In the preliminary stages of this work, several estimators based on different detector information were considered.

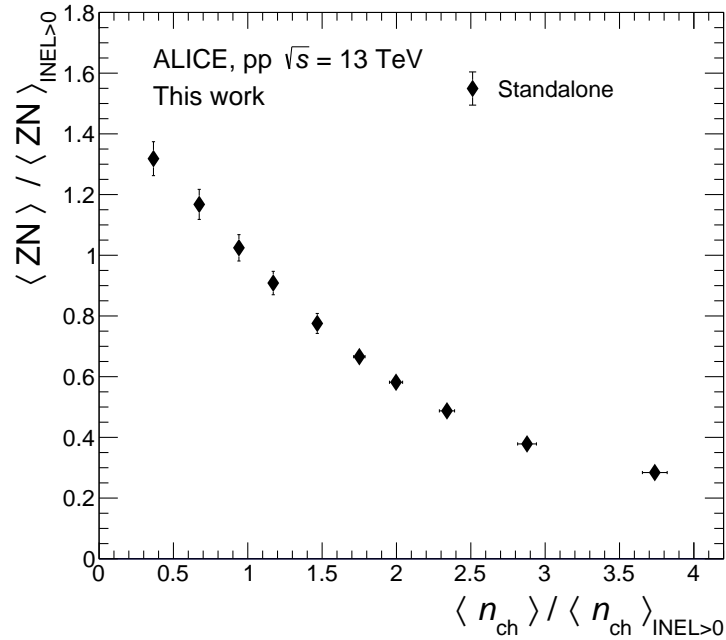


Fig. 6.6 Self-normalised ZN signal as a function of the self-normalised charged-particle multiplicity measured at midrapidity ($|\eta| < 0.5$) in pp collisions at $\sqrt{s} = 13$ TeV.

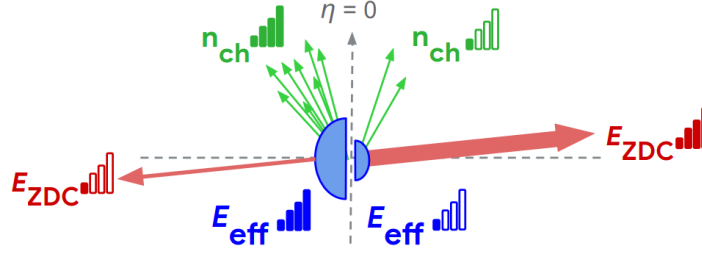


Fig. 6.7 Sketch of the relation between effective energy, multiplicity and leading energy (ZDC). A high (low) ZDC deposit corresponds to a low (high) effective energy available for particle production, and, consequently, low (high) midrapidity multiplicity.

In particular, the ZDC energy was first considered at the event-by-event level to build a percentile estimator, used in combination with the VZEROM percentile [11]. Details about the ZDC percentile estimator are provided in Appendix A. However, an event-by-event estimator based on the ZDC energy was found to be strongly correlated with the VZEROM amplitude, therefore the discriminatory power in terms of multiplicity and effective energy was strongly limited. The outcome of further studies, combining different event estimators at central and forward rapidity, showed that using VZEROM and SPDClusters combined was the most efficient way to select events based on the three topologies introduced in Section 6.3: fixed multiplicity, fixed forward energy and standalone classes. This configuration allowed us to exploit the ZDC energy as an average observable, property of the event class and complementary to the charged-particle multiplicity. In fact, midrapidity multiplicity and ZDC energy are measured in rapidity regions that are causally disconnected in the evolution of the system. In summary, this analysis introduces two main novelties with respect to previous studies on strangeness production in pp collisions: we introduce the leading energy as an average observable correlated to midrapidity (strange) particle production, and we exploit a multi-differential approach to classify events characterised by fixed multiplicity and fixed forward energy, respectively. The multi-differential approach used in this analysis is very similar to the so-called “Event Shape Engineering”, used in the context of flow-coefficient studies in Pb–Pb collisions within the ALICE Collaboration [134], which allows to experimentally select events with different shapes of initial spatial asymmetry.

6.5.1 Estimators selectivity: VZEROM and SPDClusters

As discussed above, using the estimators VZEROM and SPDClusters combined is found to be the most efficient way to select events based on the event topologies introduced in Section 6.3.

Several event classes were defined to select collisions with fixed average multiplicity at midrapidity and forward energy detected by ZN, respectively. The distributions of SPD tracklets (a proxy for charged particle multiplicity) and ZN energy were also studied in each selection class to ensure not only a fixed average value of these observables in the selected events but also similar distributions. A total of five groups of event classes are defined in this analysis:

- **Standalone selection:** event classes characterised on average by different multiplicity and ZN energy deposits. The number of tracklets and ZN energy distributions obtained with these selections are reported in Fig. 6.9.
- **High Multiplicity selection:** event classes characterised on average by the same multiplicity ($\langle n_{\text{ch}} \rangle \approx 13$) and different ZN energy deposits. Fig. 6.10 shows the distributions of the number of tracklets and ZN energy in these classes, proving that we are actually selecting events with similar multiplicity distributions.
- **Low Multiplicity selection:** event classes characterised on average by the same multiplicity ($\langle n_{\text{ch}} \rangle \approx 6$) and different ZN energy deposits. The distributions of the number of tracklets and ZN energy are shown in Fig. 6.11. Also in this case we can select events with similar multiplicity distributions.
- **High ZN selection:** event classes characterised on average by the same ZN energy ($\langle \text{ZN} \rangle \approx 250$ a.u.) and different multiplicity. Fig. 6.12 shows the distributions of the number of tracklets and ZN energy in these classes, proving that we are selecting events with similar ZN energy distributions.
- **Low ZN selection:** event classes characterised on average by the same ZN energy ($\langle \text{ZN} \rangle \approx 175$ a.u.) and different multiplicity. The distributions of the number of tracklets and ZN energy are shown in Fig. 6.13. Also in this case we are able to select events with similar ZN energy distributions.

The average values of multiplicity and forward energy in each class are reported in Table 6.1. Figure 6.8 summarises the relation between the self-normalised ZN signal and the self-normalised charged-particle multiplicity at midrapidity for the five selections listed above. For two values of midrapidity multiplicity, the High Multiplicity and Low Multiplicity selections (red and orange circles) classify events with different ZN energy deposits. In particular, the self-normalised ZN energy values cover a range between 0.4 and 1.0 for the High Multiplicity selection, and between 0.7 and 1.3 for the Low Multiplicity selection. The total average forward energy interval covered by the Standalone selection ranges between

0.3 and 1.3, therefore, also at fixed multiplicity, we are able to select events covering a wide range of ZN energies, compared to the Standalone selection. Similarly, for two values of ZN energy, the High ZN and Low ZN selections (blue and azure squares) classify events with different midrapidity multiplicity. In particular, the self-normalised multiplicity values cover a range between 0.5 and 2.0 for the High ZN selection, and between 1.1 and 2.7 for the Low ZN selection. The total average multiplicity interval covered by the Standalone selection ranges between 0.4 and 3.8, therefore, also at fixed ZN energy, we are able to select events covering a wide range of multiplicities, compared to the Standalone selection.

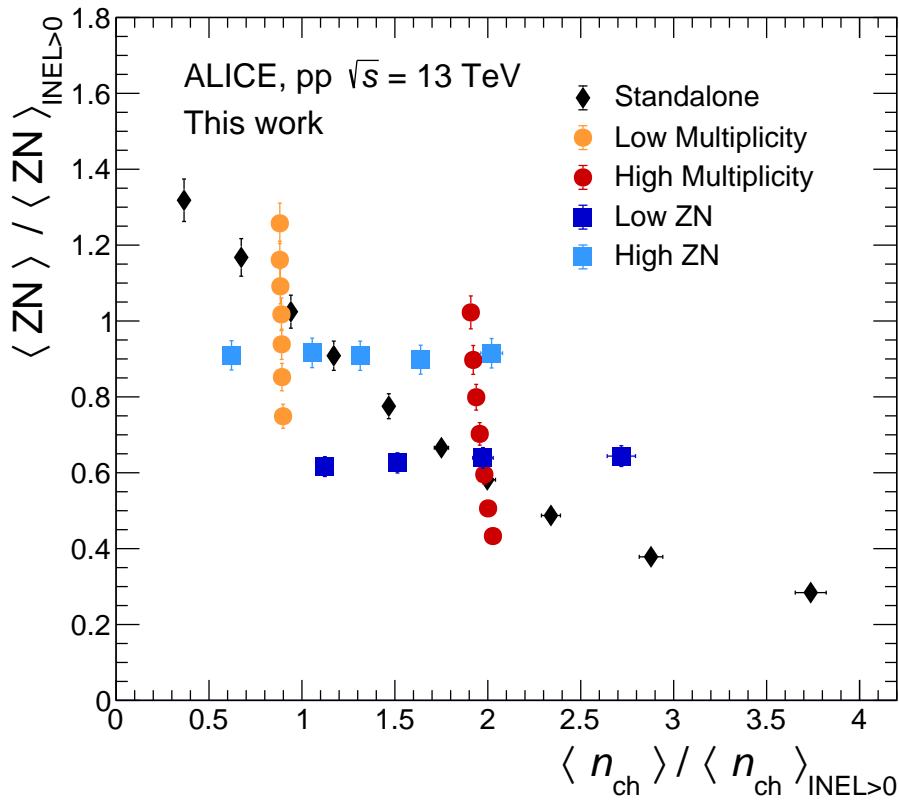


Fig. 6.8 Self-normalised ZN signal as a function of the self-normalised charged-particle multiplicity measured at midrapidity in pp collisions at $\sqrt{s} = 13$ TeV in all double-differential classes defined in this analysis.

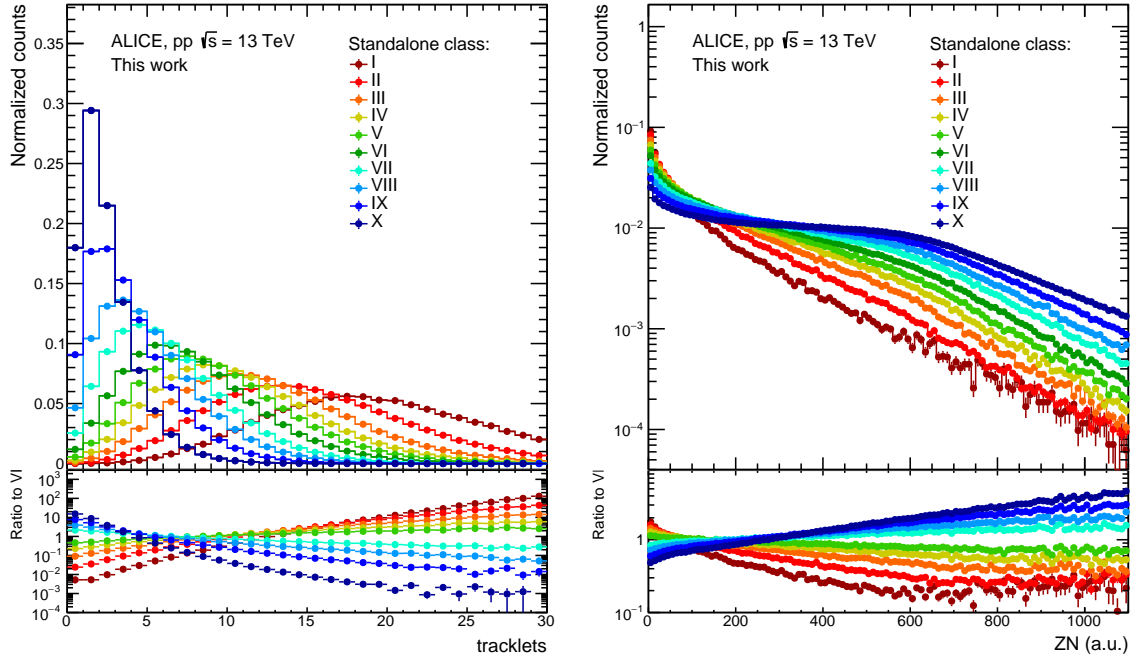


Fig. 6.9 Distributions of SPD tracklets (a proxy for charged particle multiplicity) and ZN energy for the Standalone class.

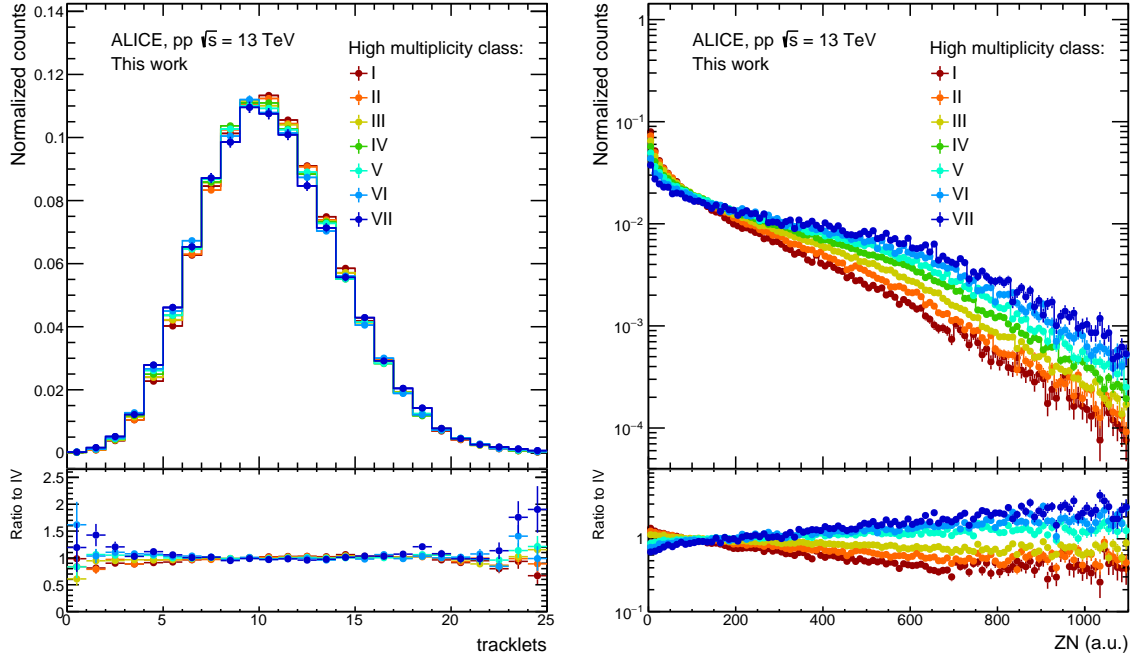


Fig. 6.10 Distributions of SPD tracklets (a proxy for charged particle multiplicity) and ZN energy for the High Multiplicity class.

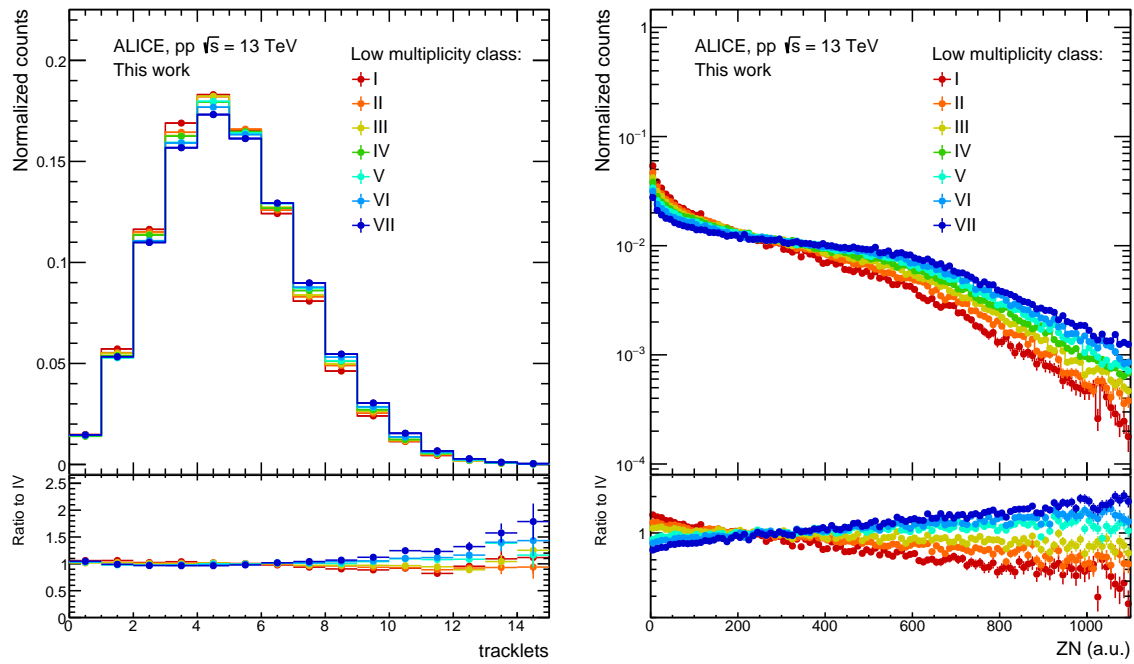


Fig. 6.11 Distributions of SPD tracklets (a proxy for charged particle multiplicity) and ZN energy for the Low Multiplicity class.

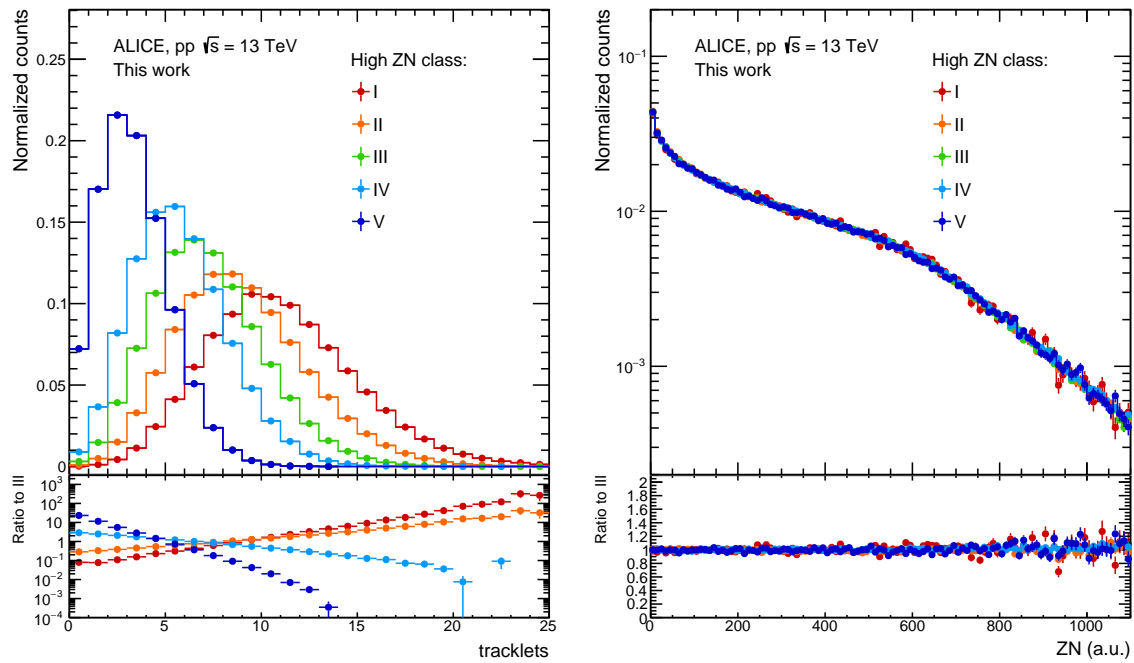


Fig. 6.12 Distributions of SPD tracklets (a proxy for charged particle multiplicity) and ZN energy for the High ZN class.

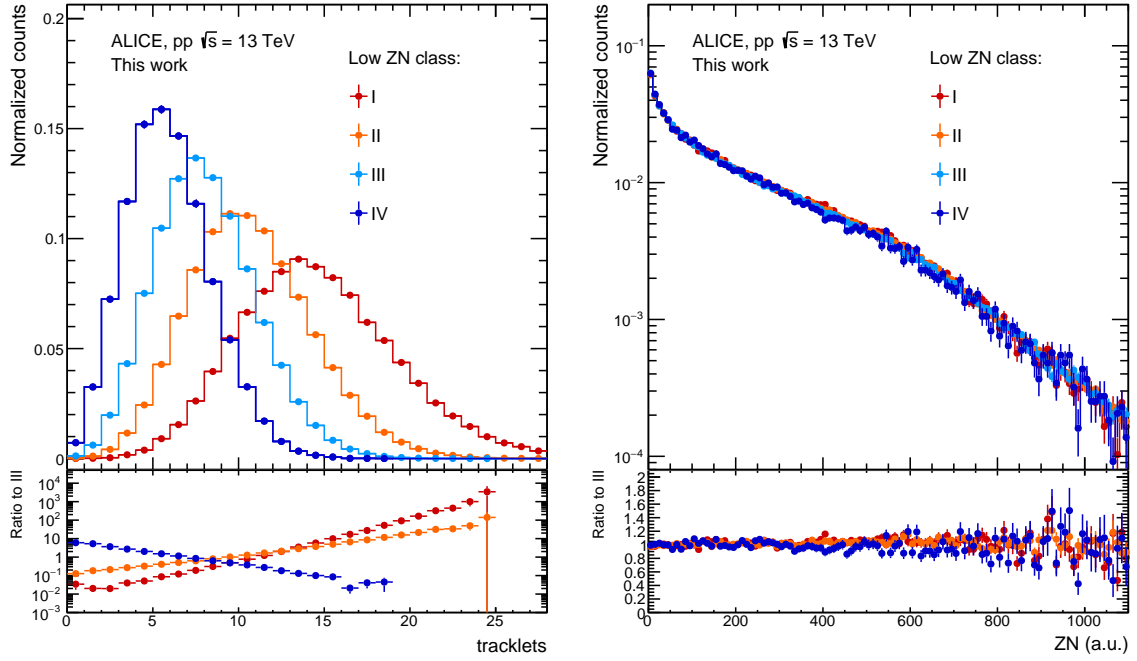


Fig. 6.13 Distributions of SPD tracklets (a proxy for charged particle multiplicity) and ZN energy for the Low ZN class.

Table 6.1 Average values of $dN_{\text{ch}}/d\eta$ and ZN energy for each event class.

Event Class	Selection	V0M	SPDclusters	$\langle dN_{\text{ch}}/d\eta \rangle_{ \eta <0.5}$	$\langle \text{ZN} \rangle$ (a.u.)
INEL>0	I	0–100%	0–100%	6.89 ± 0.11	280 ± 8
Standalone	I	0–1%	0–100%	25.75 ± 0.40	80 ± 2
	II	1–5%	0–100%	19.83 ± 0.30	106 ± 3
	III	5–10%	0–100%	16.12 ± 0.24	136 ± 4
	IV	10–15%	0–100%	13.76 ± 0.21	163 ± 5
	V	15–20%	0–100%	12.06 ± 0.18	186 ± 6
	VI	20–30%	0–100%	10.11 ± 0.15	217 ± 7
	VII	30–40%	0–100%	8.07 ± 0.12	254 ± 8
	VIII	40–50%	0–100%	6.48 ± 0.09	287 ± 9
	IX	50–70%	0–100%	4.64 ± 0.06	327 ± 10
	X	70–100%	0–100%	2.52 ± 0.03	369 ± 11
High Multiplicity	I	0–5%	10–20%	13.97 ± 0.16	121 ± 4
	II	5–10%	10–20%	13.79 ± 0.17	141 ± 4
	III	10–20%	10–20%	13.65 ± 0.17	167 ± 5
	IV	20–30%	10–20%	13.48 ± 0.17	197 ± 6
	V	30–40%	10–20%	13.35 ± 0.17	224 ± 7
	VI	40–50%	10–20%	13.24 ± 0.17	251 ± 8
	VII	50–100%	10–20%	13.15 ± 0.16	286 ± 9
Low Multiplicity	I	0–20%	40–50%	6.19 ± 0.07	210 ± 6
	II	20–30%	40–50%	6.15 ± 0.07	239 ± 7
	III	30–40%	40–50%	6.14 ± 0.07	263 ± 8
	IV	40–50%	40–50%	6.13 ± 0.08	285 ± 9
	V	50–60%	40–50%	6.09 ± 0.08	306 ± 9
	VI	60–70%	40–50%	6.07 ± 0.09	325 ± 9
	VII	70–100%	40–50%	6.07 ± 0.09	352 ± 11
High ZN	I	40–60%	0–20%	13.92 ± 0.34	256 ± 8
	II	30–70%	10–30%	11.29 ± 0.27	251 ± 8
	III	30–50%	20–40%	9.05 ± 0.22	254 ± 8
	IV	20–50%	30–50%	7.27 ± 0.17	256 ± 8
	V	0–30%	50–100%	4.28 ± 0.10	255 ± 8
Low ZN	I	20–30%	0–10%	18.73 ± 0.43	180 ± 5
	II	10–30%	10–20%	13.6 ± 0.31	179 ± 5
	III	0–20%	20–30%	10.43 ± 0.23	175 ± 5
	IV	0–10%	30–50%	7.74 ± 0.17	173 ± 5

6.5.2 Cross-check for auto-correlation biases

In this work, the event classification relies on both midrapidity and forward-backwards pseudorapidity-based selections, respectively, through SPDClusters and VZEROM estimators. Performing the event classification using midrapidity estimators can lead to possible auto-correlation biases, possibly altering the measured hadrochemistry. In fact, both the average $dN_{\text{ch}}/d\eta$ and the strange hadron yields are measured at central rapidities. To verify that correlation biases did not affect our selections, we studied the progression of charged and neutral kaon abundances with multiplicity in pp collisions simulated with the PYTHIA8 event generator. Figure 6.14 (a) and (b) show the charged and neutral kaon yields as a function of multiplicity using the VZEROM and RefMultEta5 estimators. The latter is based on the so-called reference multiplicity, i.e. the number of tracks reconstructed in the central barrel, which include global tracks reconstructed by ITS and TPC and complementary tracks found with ITS only information. The kaon yields are self-normalised to the average MB value in order to study only effects related to the multiplicity selection. However, similar amounts of charged and neutral kaons are found on average as expected due to their similar masses. If a selection based on the reference multiplicity is used (RefMultEta5), the integrated yields of K^\pm for high-multiplicity events are found to be higher than the ones for K^0 . Similarly, for low-multiplicity events, K^\pm yields are found to be lower than K^0 ones. Therefore, the measurement of charged kaon yields is biased by selecting primary charged-particles in the same pseudorapidity range. If the selection is performed using the multiplicity measured in a different pseudorapidity range than the one in which K^\pm and K^0 production rates are measured (i.e. using the VZEROM estimator), similar amounts of charged and neutral kaons are found as a function of multiplicity [46]. Figure 6.14 (c) shows that similarly to VZEROM, also the SPDClusters estimator is not altered by selection biases. This can be explained considering that the SPDClusters estimator is not based on a direct measurement of the primary charged particle multiplicity at midrapidity. In fact, the number of clusters in the SPD is proportional to the primary charged multiplicity but also includes secondary tracks. The choice of an SPD estimator based on clusters, as opposed to the number of tracks, in this analysis, is motivated by this observation. Finally, the combination of VZEROM and SPDClusters was also considered for this check. Similar amounts of charged and neutral kaons are found across multiplicity as displayed in Figure 6.14 (d), confirming that the selections used in this analysis are not affected by auto-correlation biases.

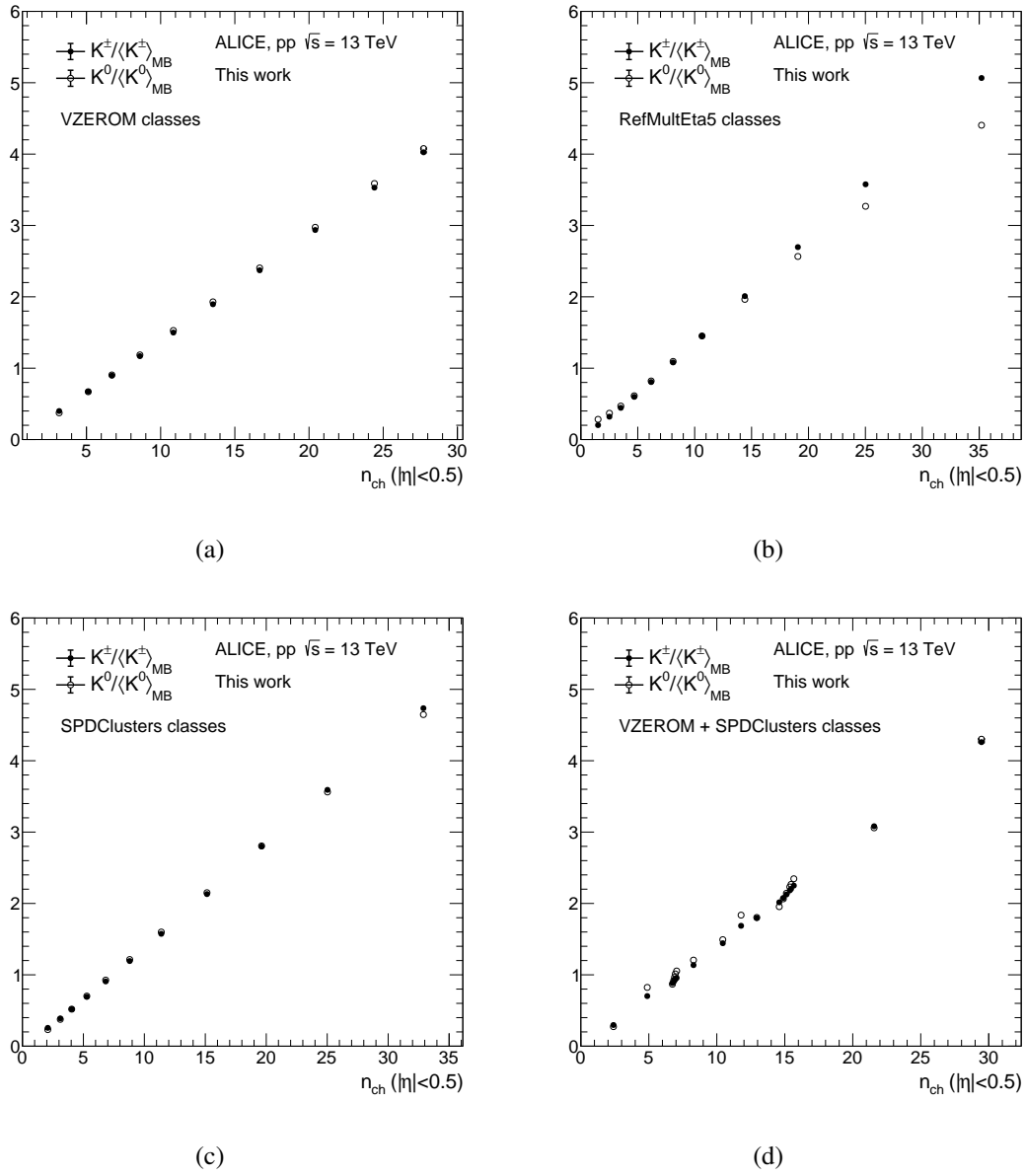


Fig. 6.14 Charged and neutral kaons yields self-normalised to MB in VZEROM (a), RefMultEta5 (b), SPDClusters (c) and VZEROM + SPDClusters (d).

6.6 Strange hadron reconstruction

In this analysis, we study the production of strange mesons K_S^0 , strange baryons Λ and multi-strange baryons Ξ . The ALICE experiment identifies strange hadrons via the topological reconstruction of their weak decays in the central pseudorapidity region. These particles, once created, travel for a few centimetres before decaying weakly. The travelled distance depends on the particle momentum and its mean lifetime, expressed as the product $c\tau$ (decay length), e.g. for Ξ^- , it is equal to 4.91 cm (for a momentum equal to m_Ξ). Geometrical and kinematic selections are applied to the reconstructed strange hadron candidates to identify specific decay topologies and improve the signal/background ratio. Strange hadrons are divided into two topological classes:

- V^0 : such as Λ baryons and K_S^0 mesons, characterised by a V-shaped decay topology.
- Cascade: such as Ξ baryons, which decay into a charged meson (*bachelor*) and a Λ , which further decays into a proton and a pion;

A summary of K_S^0 , Λ , $\bar{\Lambda}$, Ξ^- and $\bar{\Xi}^+$ properties is reported in Table 6.2.

Particle	Mass (MeV/ c^2)	Decay channel	B.R.(%)	$c\tau$ (cm)
K_S^0 ($\frac{d\bar{s}-s}{\sqrt{2}}$)	497.611 ± 0.013	$K_S^0 \rightarrow \pi^- + \pi^+$	69.20 ± 0.05	2.68
Λ (uds)	1115.683 ± 0.006	$\Lambda \rightarrow p + \pi^-$	63.9 ± 0.5	7.89
$\bar{\Lambda}$ ($\bar{u}\bar{d}\bar{s}$)	1115.683 ± 0.006	$\bar{\Lambda} \rightarrow \bar{p} + \pi^+$	63.9 ± 0.5	7.89
Ξ^- (dss)	1321.71 ± 0.07	$\Xi^- \rightarrow \Lambda + \pi^-$	99.887 ± 0.035	4.91
$\bar{\Xi}^+$ ($\bar{d}\bar{s}\bar{s}$)	1321.71 ± 0.07	$\bar{\Xi}^+ \rightarrow \bar{\Lambda} + \pi^+$	99.887 ± 0.035	4.91

Table 6.2 Properties of K_S^0 , Λ and Ξ strange hadrons. The valence quark content, the mass, the main decay channel, their branching ratio (B.R.), and $c\tau$ are listed with the respective errors. The values are reported from [135].

The reconstruction of strange hadrons starts with the V^0 finding procedure. For K_S^0 , Λ , and $\bar{\Lambda}$, the first step is the selection of secondary tracks, i.e. tracks having a sufficiently large impact parameter to the primary vertex. All possible combinations between two secondary

tracks of opposite charge are then considered, and they are accepted as V^0 candidates only if their Distance of Closest Approach (DCA) is smaller than a selected value. Charged particles compatible with two pions for K_S^0 and with a pion and a (anti)proton for Λ ($\bar{\Lambda}$) are identified through their specific energy loss in the TPC. The V^0 vertex position is defined as the point where the two tracks have the closest approach. Once their position is determined, only V^0 candidates located inside a given fiducial volume are kept. Finally, the V^0 finding procedure checks whether the particle momentum p associated with the V^0 candidate points back to the primary vertex by applying a cut on the cosine of the pointing angle (θ_p), i.e. the angle between the momentum p and the vector connecting the primary vertex and the V^0 position. The invariant mass of these candidates can then be calculated either under the $\pi^- + \pi^+$ hypothesis for K_S^0 , or the $p(\bar{p}) + \pi^- (\pi^+)$ hypotheses for Λ ($\bar{\Lambda}$). After finding V^0 candidates, the search for cascade decays is performed, looking for V-shaped decays of the daughter Λ ($\bar{\Lambda}$) plus a negatively or positively charged bachelor track. The V^0 -bachelor association is performed if the DCA between the bachelor track and the V^0 trajectory is less than a selected value. Charged particles compatible with the pion hypothesis are identified as bachelors using the TPC PID. Finally, the cascade candidate is selected if its reconstructed momentum points back to the primary vertex using the cosine of the cascade pointing angle. A pictorial representation of V^0 and cascade decay topology is shown in Figure 6.15. The specific kinematic and topological selections used in this analysis are described in the following and are listed in Table 6.3 and 6.4 for V^0 and cascades, respectively.

- **Topological selections**

A specific set of geometrical requirements is applied to identify V^0 and cascade decay topologies. For V^0 candidates, the distance of closest approach (DCA) of the daughter tracks to the primary vertex is required to be greater than 0.06 cm to reject particles coming from the primary vertex. For cascades, this value is set to 0.04 cm for the bachelor track and 0.06 cm for the Λ daughter. To select daughter pairs coming from the decay of the same V^0 , the DCA between the daughter tracks is required to be smaller than 1σ , where the σ reflects the resolution with which the DCA is measured. The same kind of selection is applied to the daughter tracks of the Λ produced in the Ξ decay. In this case, considering the different decay topology, the DCA is required to be smaller than 1.5σ . For cascades, the V^0 -bachelor association is performed if the DCA between the bachelor track and the V^0 trajectory is less than 1.3 cm. A selection on the decay radius, defined as the radial distance of the secondary vertex from the primary one, is also applied to V^0 and cascade candidates in order to remove daughter tracks coming from the primary interaction vertex. To reject V^0 and cascade candidates coming from secondary vertexes, a selection on the cosine of the pointing angle θ_p

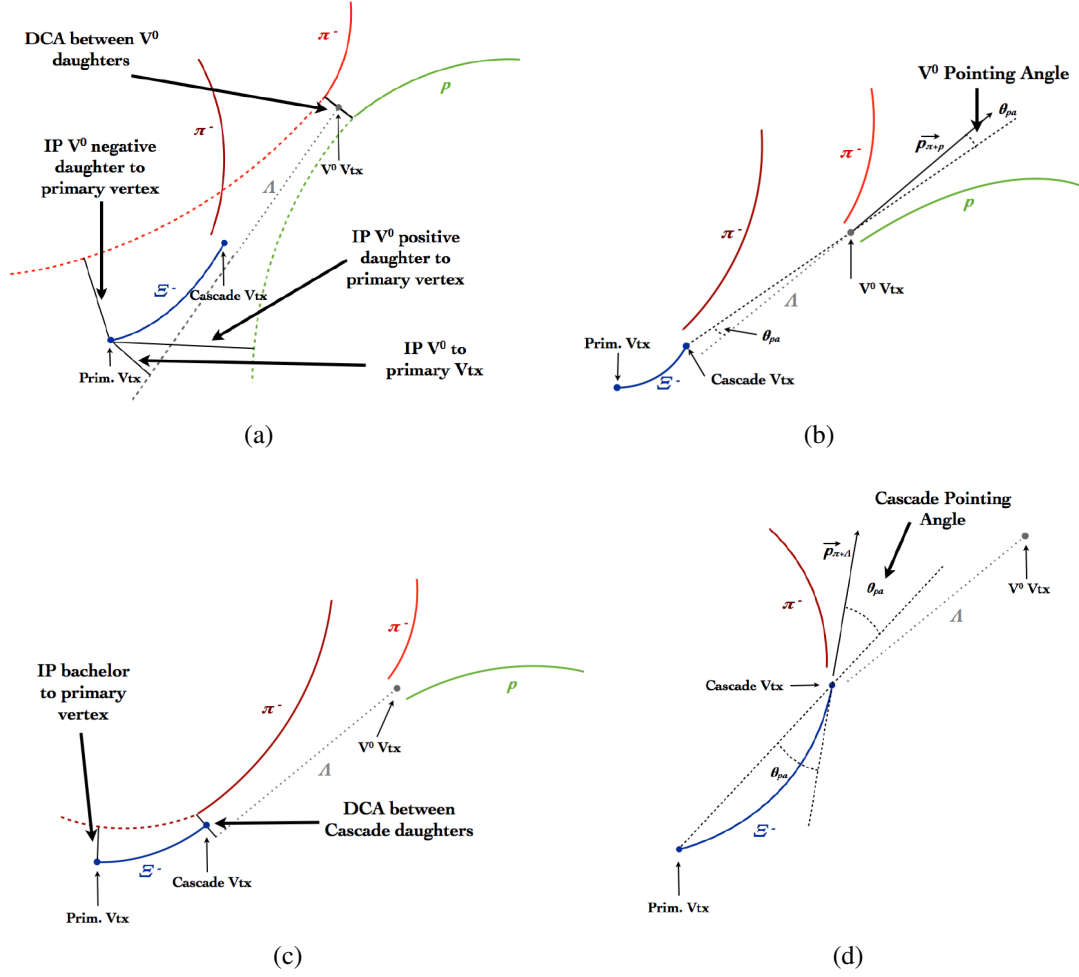


Fig. 6.15 Pictorial representation of the topological variables used to identify V^0 and cascade candidates.

is applied. The selection $\cos(\theta_{V^0}) > 0.97(0.995)$ is applied to K_S^0 (Λ) candidates and $\cos(\theta_{casc}) > 0.97$ to Ξ candidates. A condition on the cosine of the pointing angle of the V^0 daughter of the cascade is also applied, which in this case refers to the angle between the direction of the reconstructed momentum p of the V^0 and the line connecting the V^0 decay vertex to the cascade decay vertex. A selection $\cos(\theta_{V^0}) > 0.97$ is found to efficiently reject V^0 candidates not coming from the decay of a Ξ .

- **Kinematic selections**

Strange particles are reconstructed within $|y| < 0.5$, and daughter tracks are required to lie within the fiducial tracking region $|\eta| < 0.8$. A proper lifetime selection is also applied as $mL/p < 3 \cdot c\tau$, where m is the candidate mass, L is the linear (3D) distance

between the candidate decay point and the primary vertex, p the total momentum and $c \cdot \tau$ is the lifetime of the candidate. A selection to reject the background of the competing V^0 species is applied to both K_S^0 and Λ candidates. For this purpose, the invariant mass calculated under the competing hypothesis is required to differ from the nominal mass value by more than $5 \text{ MeV}/c^2$ for K_S^0 and $10 \text{ MeV}/c^2$ for Λ ($\bar{\Lambda}$). To identify Ξ candidates, the invariant mass of the daughter Λ is required to differ from the nominal mass value by less than $6 \text{ MeV}/c^2$.

- **Track quality selections**

Daughter tracks are required to cross at least 70 TPC readout pads out of a maximum of 159. Tracks are also required not to have large gaps in the number of expected tracking points in the radial direction. This is achieved by checking that the number of clusters expected based on the reconstructed trajectory and the measurements in neighbouring TPC pad rows do not differ by more than 20%.

- **PID selections**

The specific energy loss (dE/dx) measured in the TPC is used for the particle identification of the decay products, requiring it to be compatible within 5σ with the one expected for the corresponding particle specie hypothesis.

- **OOB pile-up rejection**

In order to reject the residual out-of-bunch pile-up background on the measured yields, it is requested that at least one of the tracks from the decay products of the strange hadron is matched in either the ITS or the TOF detector.

6.6.1 Signal extraction

The K_S^0 , Λ , and Ξ signal extraction is performed starting from the invariant mass distributions of their decay daughters in different p_T bins. The distributions obtained in the MB sample are preliminarily fitted with a Gaussian function for modelling the signal and a linear function to model the background. The peak region is defined within $\pm 6(4)\sigma$ for V^0 s (cascades) with respect to the Gaussian mean extracted in each p_T bin, being σ the standard deviation of the Gaussian function. Adjacent background bands, covering a mass interval as wide as the peak region, are defined on both sides. The signal is extracted in each p_T interval and percentile selection with a bin counting procedure subtracting counts in the background region from those of the signal region.

V^0	
Topological selections	Cut $\Lambda (K_S^0)$
V0 transv. decay radius	> 0.50 cm
DCA Negative Track to PV	> 0.06 cm
DCA Positive Track to PV	> 0.06 cm
V0 Cosine of Pointing Angle	> 0.995 (0.97)
DCA V0 Daughters	$< 1.0\sigma$
Other selections	Cut
Rapidity Interval $ y $	< 0.5 (MC value for MC analysis)
Daughter Track Pseudorapidity Interval $ \eta $	< 0.8
Proper Lifetime (mL/p)	< 30 cm (20 cm)
Competing V0 Rejection	$10 \text{ MeV}/c^2$ (5 MeV/c)
TPC dE/dx Selection (Real data only)	$< 5\sigma$
Primary Selection (MC Only)	Is physical primary
MC Association (MC Only)	PDG code (V^0 and dau.)
Daughter Track Pseudorapidity Interval	$ \eta < 0.8$
Daughter Track Ncrossedrows	≥ 70
Daughter Track Ncrossed/Nfindable	≥ 0.8
OOB pile-up rejection	ITS TOF matching
p inner wall TPC (proton only)	$> 0.3 \text{ GeV}/c$

Table 6.3 Selections applied to K_S^0 , Λ and $\bar{\Lambda}$ candidates.

The following p_T bins are used for the signal extraction:

- K_S^0 : {0.0, 0.1, 0.2, 0.3, 0.4, 0.5, 0.6, 0.7, 0.8, 0.9, 1.0, 1.1, 1.2, 1.3, 1.4, 1.5, 1.6, 1.7, 1.8, 1.9, 2., 2.2, 2.4, 2.6, 2.8, 3.0, 3.3, 3.6, 3.9, 4.2, 4.6, 5, 5.4, 5.9, 6.5, 7, 7.5, 8, 8.5, 9.2, 10};
- $\Lambda (\bar{\Lambda})$: {0.4, 0.6, 0.8, 1., 1.2, 1.4, 1.6, 1.8, 2, 2.2, 2.5, 2.9, 3.4, 4, 5, 6.5, 8};
- $\Xi^- (\bar{\Xi}^+)$: {0.6, 1.0, 1.2, 1.4, 1.6, 1.8, 2.0, 2.2, 2.5, 2.9, 3.4, 4.0, 5.0, 6.5};

The invariant mass distributions and the fit functions used for the signal extraction in different p_T bins are shown in Fig. 6.16 for K_S^0 , Λ , $\bar{\Lambda}$ and in Fig. 6.18 for Ξ^- and $\bar{\Xi}^+$. The peak

Cascade	
Topological variable	Cut Ξ
Cascade transv. decay radius R_{2D}	$> 0.6 \text{ cm}$
V0 transv. decay radius	$> 1.2 \text{ cm}$
DCA bachelor - PV	$> 0.04 \text{ cm}$
DCA V0 - PV	$> 0.06 \text{ cm}$
DCA meson V0 track - PV	$> 0.04 \text{ cm}$
DCA baryon V0 track - PV	$> 0.03 \text{ cm}$
DCA V0 tracks	$< 1.5 \sigma$
DCA bach - V0	$< 1.3 \text{ cm}$
cascade cos(PA)	> 0.97
V0 cos(PA)	> 0.97
Other selections	Cut
Primary Selection (MC Only)	Is physical primary
MC Association (MC Only)	PDG code (casc. and dau.)
Rapidity Interval $ y $	< 0.5
Daughter Track Pseudorapidity Interval $ \eta $	< 0.8
TPC dE/dx Selection (Real data only)	$< 5\sigma$
Proper Lifetime (mL/p)	$< 3 \times c\tau$
OOB pile-up rejection	ITS TOF matching
Daughter Track NTPCclusters	≥ 70
V0 invariant mass window	$\pm 0.008 \text{ GeV}/c^2$

Table 6.4 Selections applied to Ξ^- and Ξ^+ candidates.

positions in each p_T bin are displayed in Fig. 6.17 for V^0 s and Fig. 6.19 for cascades, where the error bars correspond to the related width (σ) of the invariant mass distribution. Once the signal extraction is completed, the so-called raw p_T spectra are obtained. The yields in each p_T interval are divided by the bin width and normalised to the rapidity interval $|y| < 0.5$ to obtain the raw p_T spectra normalised to the number of events ($1/N_{\text{ev}} d^2N_{\text{raw}}/(dy dp_T)$). These spectra are still subject to all the inefficiencies and the acceptance limitations of the detector and must be corrected for these effects. The raw yields for the Standalone class are displayed in Fig. 6.20 for V^0 s and Fig. 6.21 for cascades, the yields for the other event classes are reported in Appendix A.

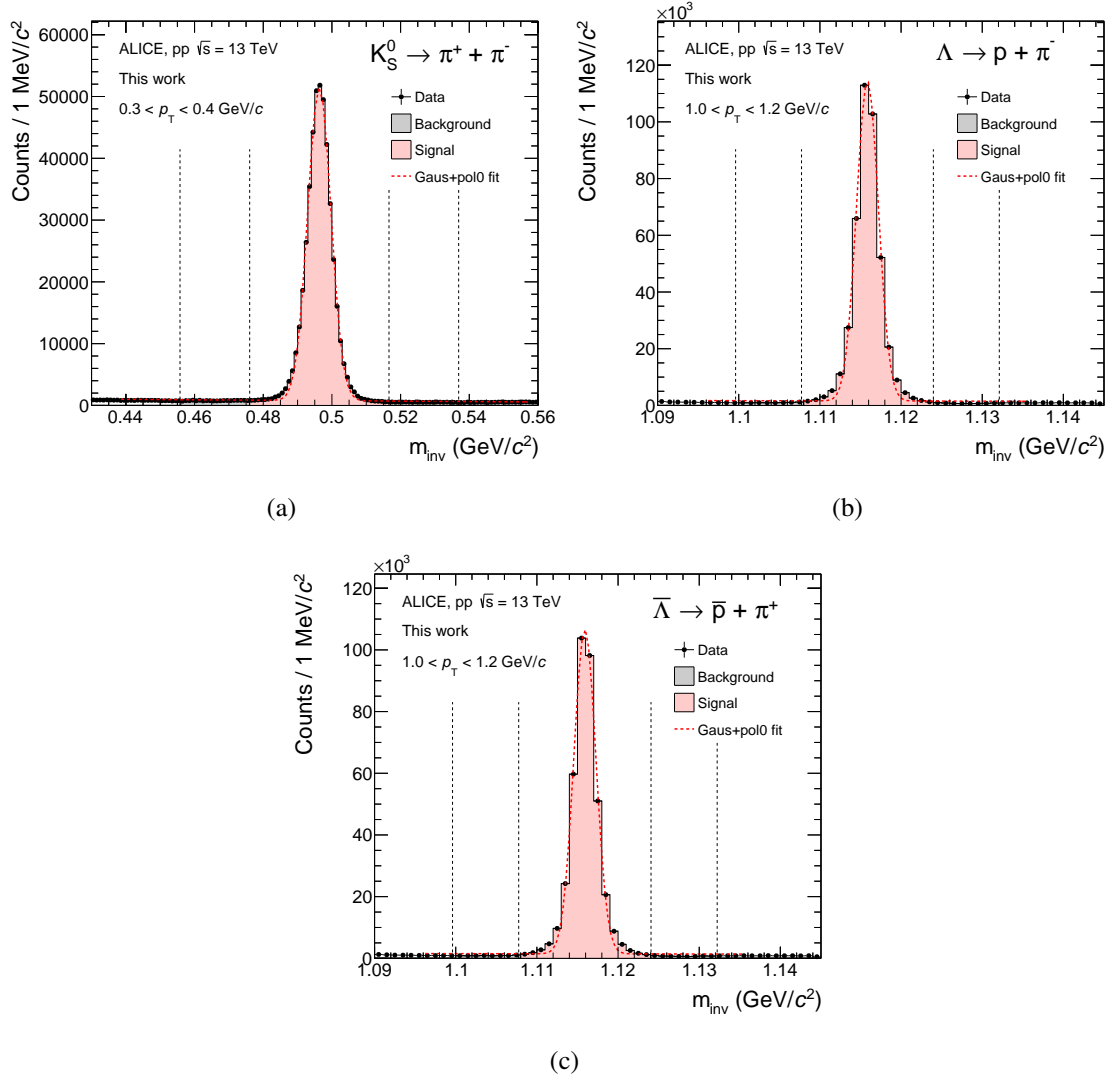


Fig. 6.16 Invariant mass distributions for V^0 s: K_S^0 (a), Λ (b), $\bar{\Lambda}$ (c) in different p_T intervals. The candidates are reconstructed in $|y| < 0.5$. The red and grey areas delimited by the short-dashed lines are used for signal extraction in the bin counting procedure. The red dashed lines represent the preliminary fit to the invariant mass distributions used to define signal and background regions.

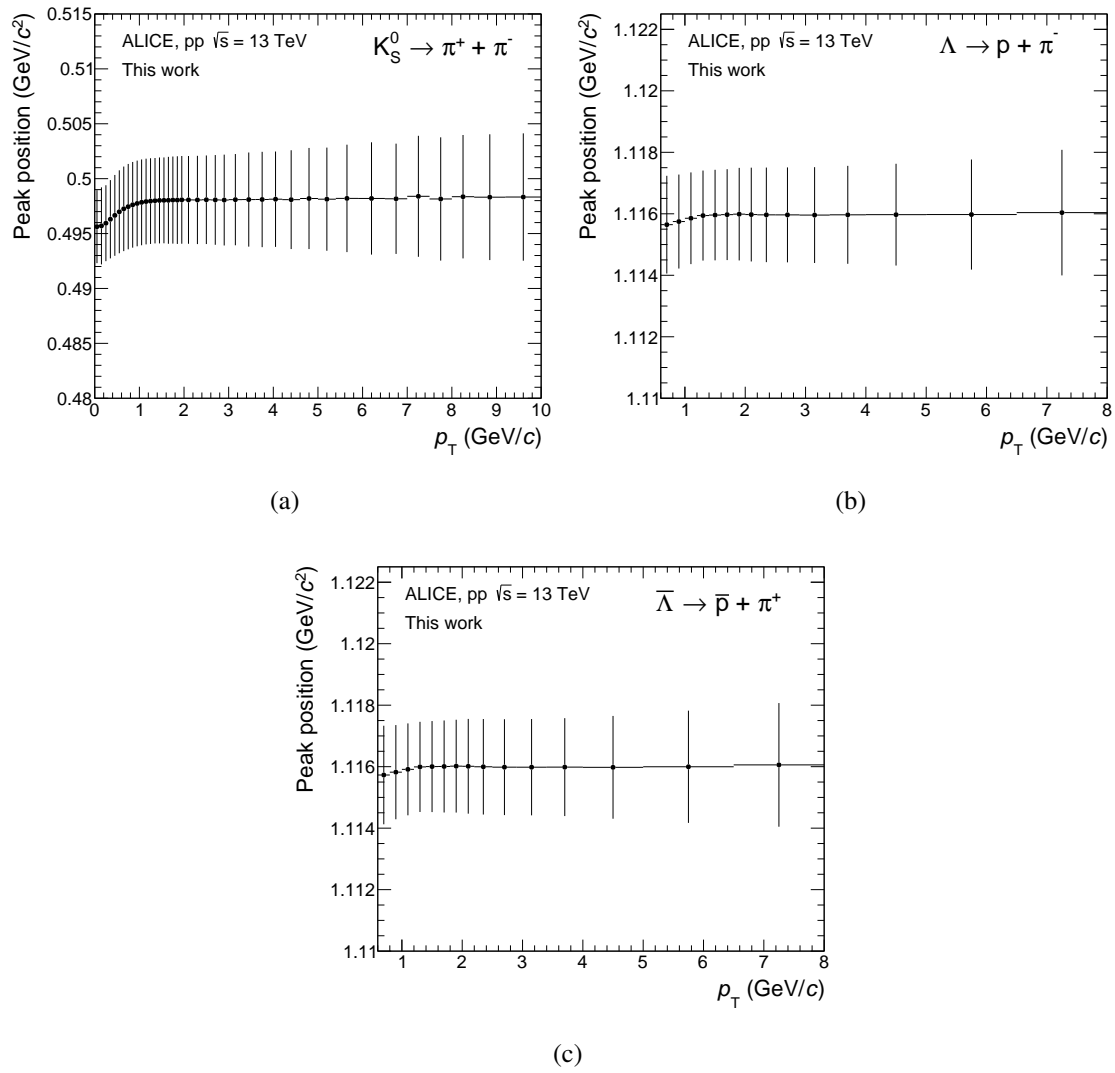


Fig. 6.17 Peak positions retrieved from the signal extraction procedure for K_S^0 (a), Λ (b), $\bar{\Lambda}$ (c) as a function of p_T . The error bars correspond to the peak widths.

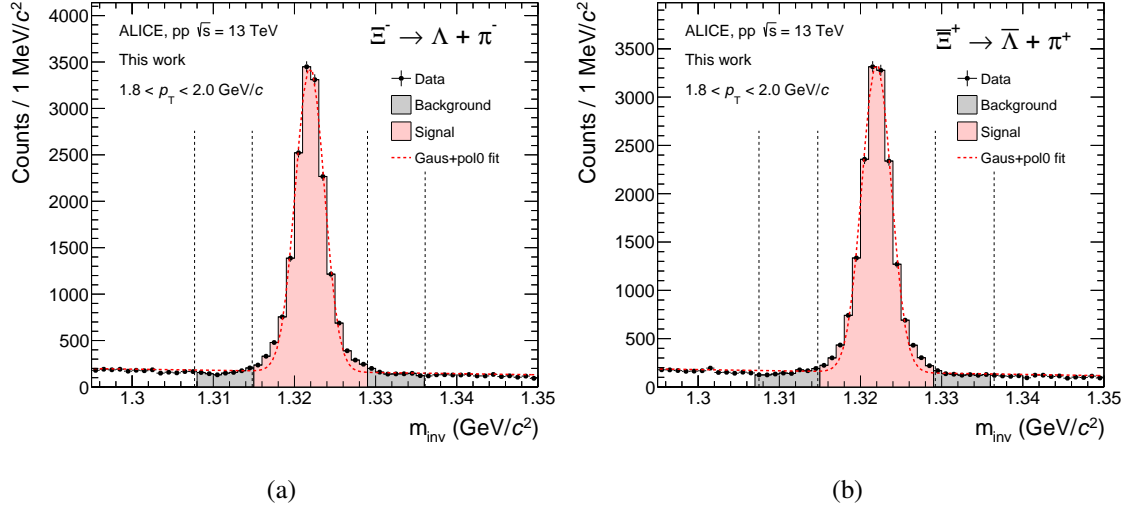


Fig. 6.18 Invariant mass distributions for Cascades Ξ^- (a) and Ξ^+ (b) in different p_T intervals. The candidates are reconstructed in $|y| < 0.5$. The red and grey areas delimited by the short-dashed lines are used for signal extraction in the bin counting procedure. The red dashed lines represent the preliminary fit to the invariant mass distributions used to define signal and background regions.

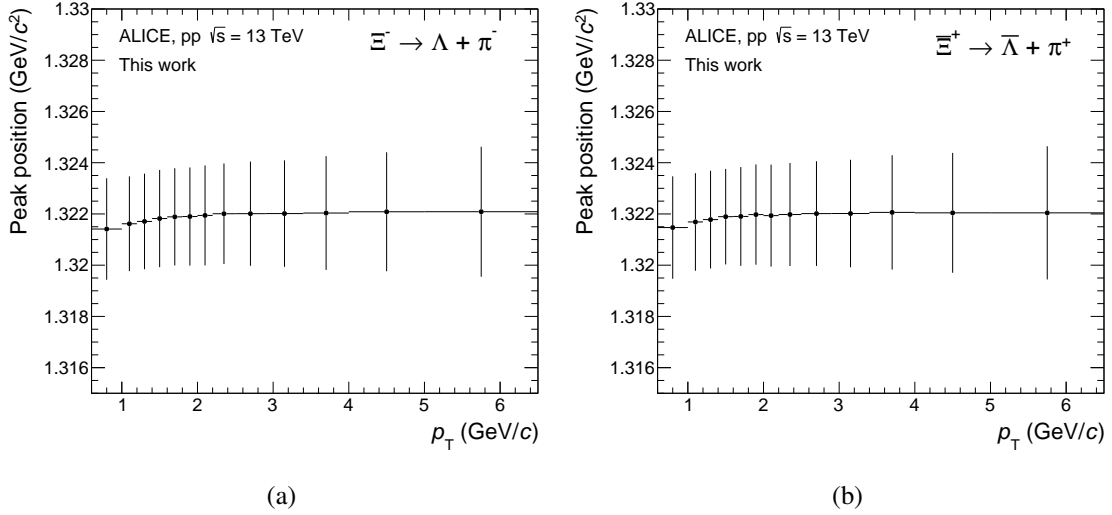


Fig. 6.19 Peak positions retrieved from the signal extraction procedure for Ξ^- (a), and Ξ^+ (b) as a function of p_T . The error bars correspond to the peak widths.

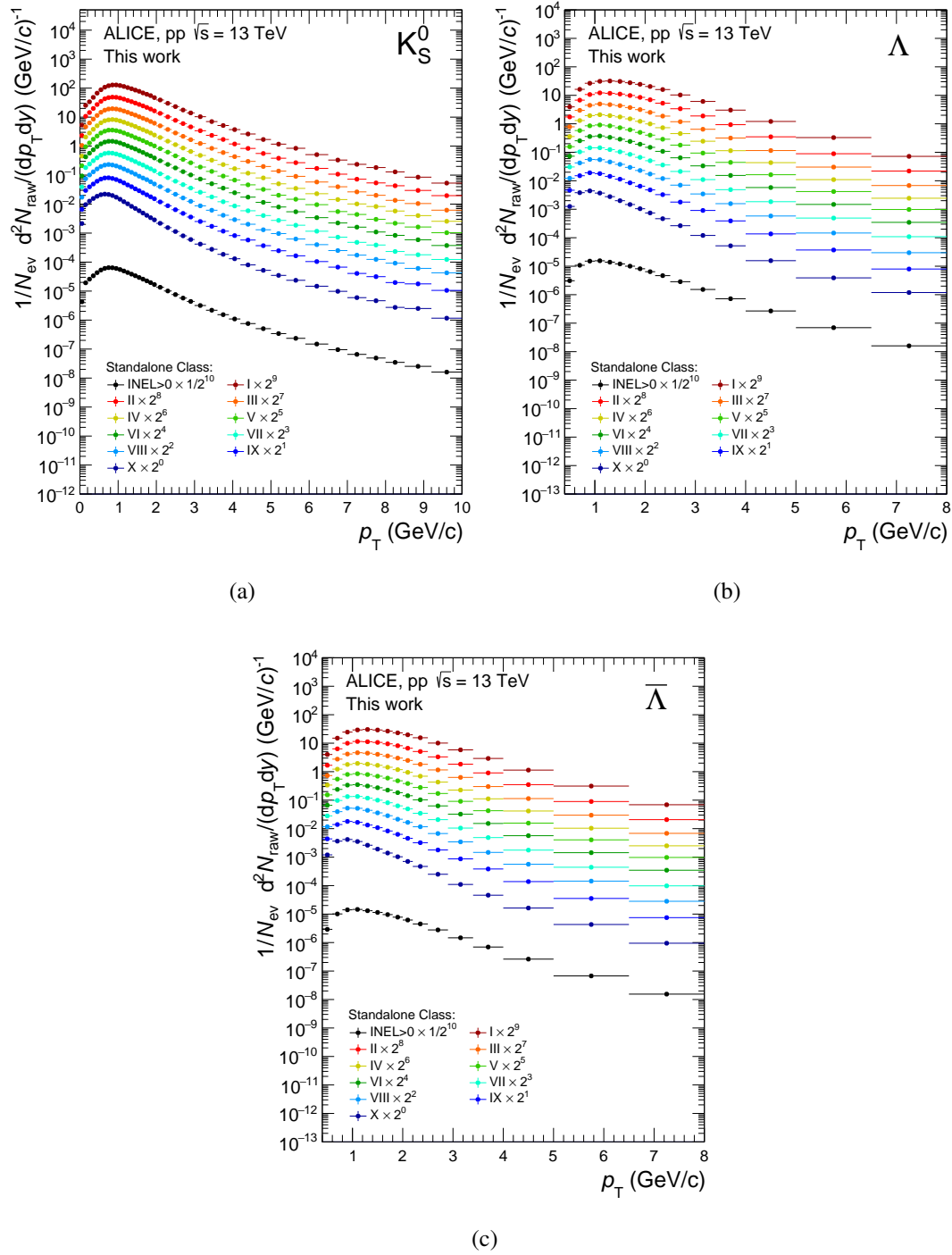


Fig. 6.20 Raw p_T spectra for K_S^0 (a), Λ (b), $\bar{\Lambda}$ (c) normalised to the number of events in the Standalone class.

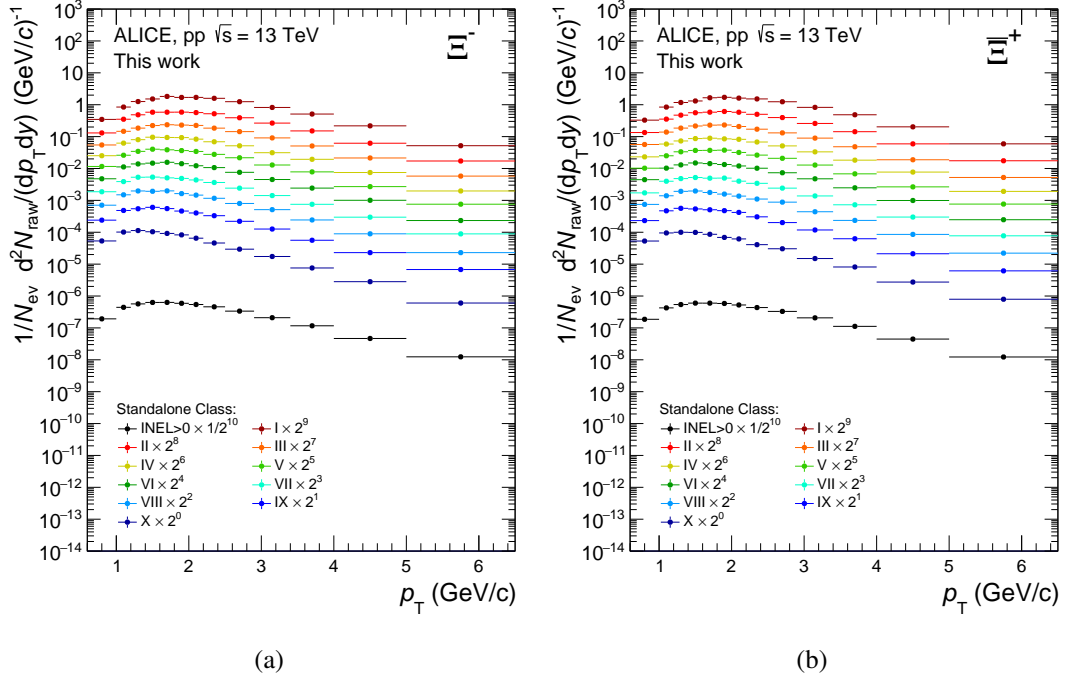


Fig. 6.21 Raw p_T spectra for Ξ^- (a), Ξ^+ (b) normalised to the number of events in the Standalone class.

6.6.2 Contamination from secondary particles

The contamination from secondary K_S^0 , Λ , and Ξ originating from interactions of primary particles and the detector materials is found to be negligible. Only the yields of Λ and $\bar{\Lambda}$ are found to be affected by a significant contamination from secondary particles from the decay of charged and neutral Ξ . The feed-down (FD) contribution to the Λ spectra coming from Ξ^- and Ξ^0 decays is computed in raw counts:

$$\Lambda_{\text{primary}}^{\text{raw}}(p_{T_i}) = \Lambda_{\text{measured}}^{\text{raw}}(p_{T_i}) - \sum_j F_{ij} \int_{p_{T_j}} \frac{dN}{dp_T}(\Xi^-) \quad (6.1)$$

where $\frac{dN}{dp_T}(\Xi^-)$ corresponds to the Levy-Tsallis fit to the measured Ξ^- spectra computed in the corresponding percentile selection. The F_{ij} is the feed-down (FD) matrix, which is defined as:

$$F_{ij} = \frac{N_{\text{reco}}(\Lambda)_{\text{from } \Xi \text{ bin } j}^{\text{in bin } i}}{N_{\text{gen}}(\Xi)_{\Xi \text{ bin } j}} \quad (6.2)$$

The same method is used to compute the feed-down contribution to the $\bar{\Lambda}$ spectra from Ξ^+ and Ξ^0 . The FD matrix represents the fraction of reconstructed Λ (or $\bar{\Lambda}$) produced in the p_T

bin- i from the decay of a Ξ particle (charged or neutral) generated in the p_T bin- j . While the denominator of the matrix is always filled with charged Ξ , the numerator can be filled following two prescriptions:

- **MC Ratio:** the numerator is filled with Λ from decays of both charged and neutral Ξ . The ratio of Ξ^- / Ξ^0 in the Monte Carlo generator is used to compute the Feed-Down matrix element. This method allows to subtract also the neutral Ξ contribution to the Λ , since no direct measurement is available for the Ξ^0 .
- **Double Charged Ξ :** the numerator is filled with Λ from decays of only charged Ξ . The charged Ξ feed-down contribution obtained is then multiplied by a factor two, assuming equal abundance of charged and neutral Ξ .

The feed-down matrix is computed using the full MB sample of events, and is displayed in Fig. 6.22 for Λ (a) and $\bar{\Lambda}$ (b). The fraction of feed-down Λ ($\bar{\Lambda}$) is then removed from the measured raw Λ ($\bar{\Lambda}$) counts in each p_T bin. The fraction of secondary Λ^{raw} and $\bar{\Lambda}^{\text{raw}}$ is shown in Fig. 6.23 for all MB events, using the two different methods described above, while the contribution in each percentile class is shown in Fig. 6.24.

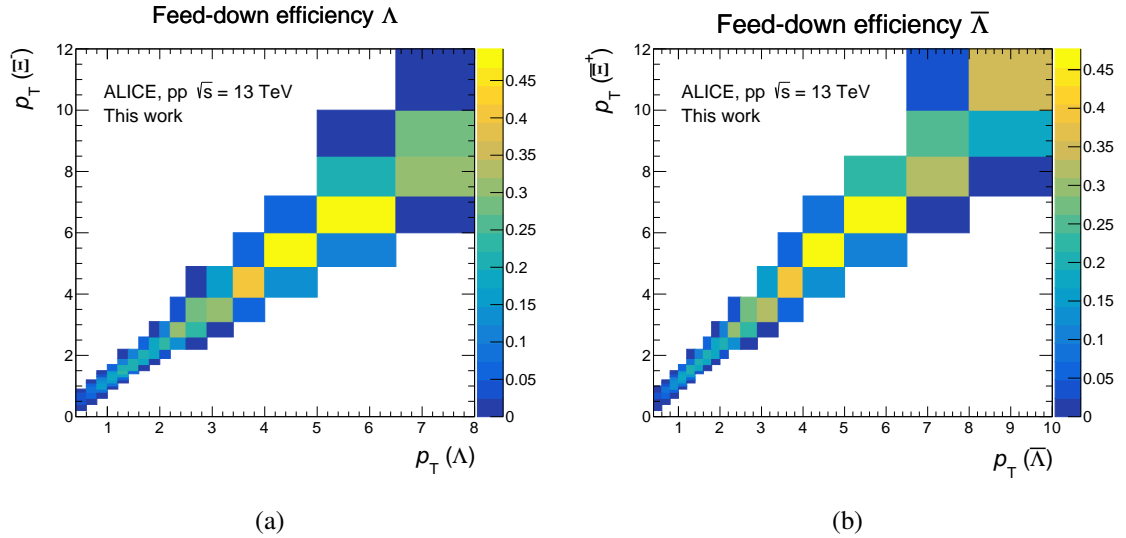


Fig. 6.22 Feed-down efficiency for Λ (a) and $\bar{\Lambda}$ (b) spectra obtained in the MB sample using the “MC Ratio” method.

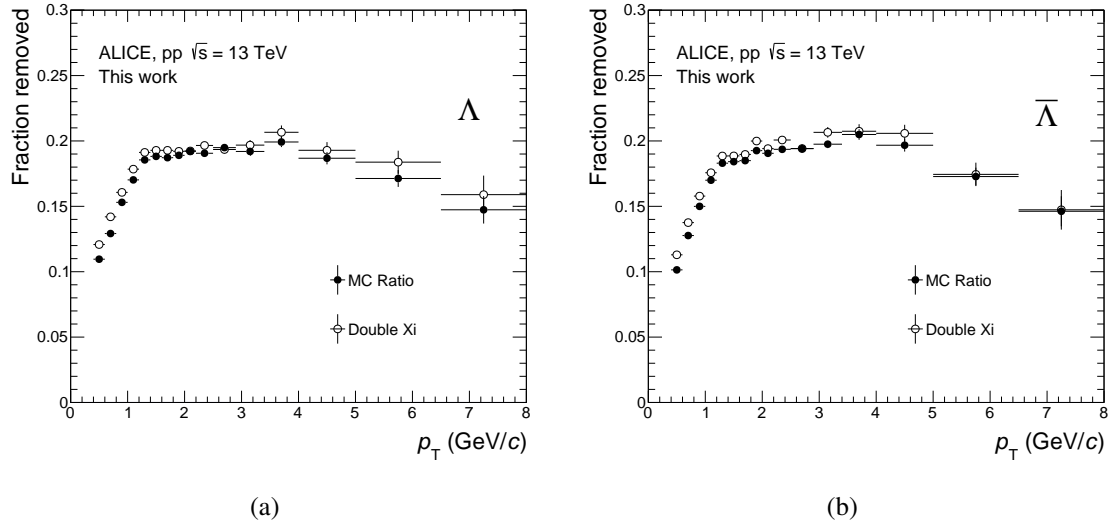


Fig. 6.23 Feed-down fraction removed in the Λ (a) and $\bar{\Lambda}$ (b) spectra obtained in the MB sample using the two different methods described in the text.

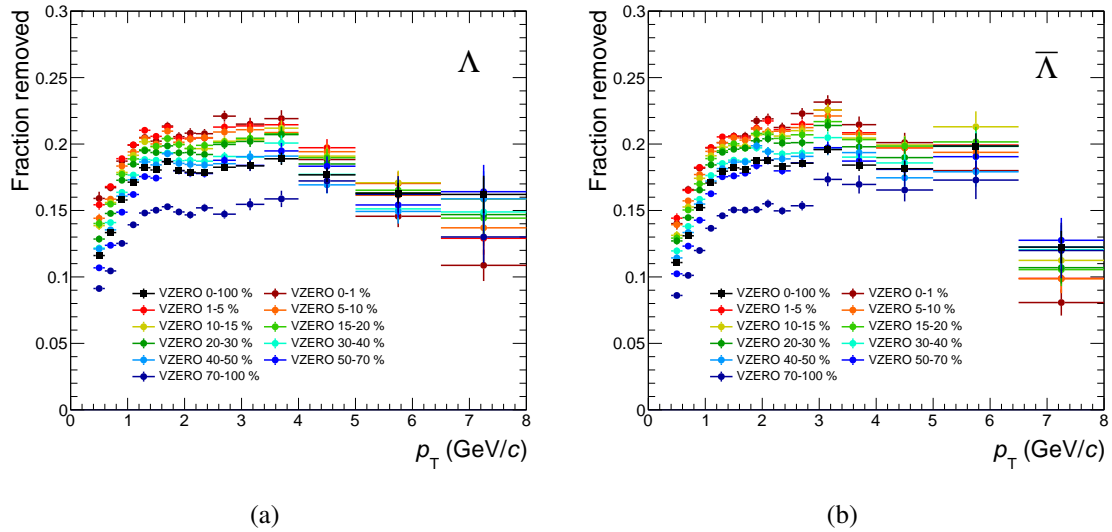


Fig. 6.24 Feed-down fraction removed in the Λ and $\bar{\Lambda}$ spectra obtained as a function of VZERO multiplicity using the “MC Ratio” method.

6.6.3 Efficiency \times acceptance correction

The efficiency \times acceptance correction reflects the capability of the detector to reconstruct a given particle using a specific decay channel. To compute this correction, the analysis is repeated on the simulated samples anchored to the data with the same selections discussed above. Moreover, in the MC analysis V^0 and cascade candidates as well as their daughters are further checked to match a true primary/secondary particle of the same type. The correction factor is computed considering the ratio of the reconstructed primary particles and the generated corresponding primaries in each p_T interval:

$$\varepsilon = \varepsilon_{\text{reco}} \times \text{acc.} \times B.R. = \frac{N_{\text{reconstructed primary}}(p_T)}{N_{\text{generated primary}}(p_T)} \quad (6.3)$$

Since we are using a different MC production for each data-taking period, the efficiency \times acceptance correction is computed separately for each sample and then averaged using a weighted mean procedure:

$$\bar{\varepsilon} = \frac{\sum_{k=1}^3 \varepsilon_i \cdot N_i^{\text{data}}}{\sum_{k=1}^3 N_i^{\text{data}}} \quad (6.4)$$

with N_i^{data} equal to the number of events for each dataset in the real data samples. The error associated with the efficiency is propagated from eq. 6.4 as:

$$\sigma_{\bar{\varepsilon}} = \frac{1}{\sum_{k=1}^3 N_i^{\text{data}}} \cdot \sqrt{\sum_{k=1}^3 (N_i^{\text{data}} \sigma_{\varepsilon_i})^2} \quad (6.5)$$

This weighted procedure is applied to all the efficiencies considered in the following. The weighted efficiencies for K_S^0 , Λ , $\bar{\Lambda}$, Ξ^- and $\bar{\Xi}^+$ are shown in Fig. 6.25. Since this analysis is performed in percentile classes, the efficiency dependence on the event class selection is studied in Fig. 6.26 for K_S^0 , Λ and Ξ^- in 3 VZEROM selections: 0-10%, 30-40% and 70-100%. No dependence on the percentile selection is observed within the uncertainties. Therefore, the efficiency \times acceptance correction used for this analysis is computed using the full MB sample. However, a safety systematic uncertainty of 2% is added to the p_T spectra to account for the differences between efficiencies obtained in different percentile classes, since the uncertainties are sometimes large.

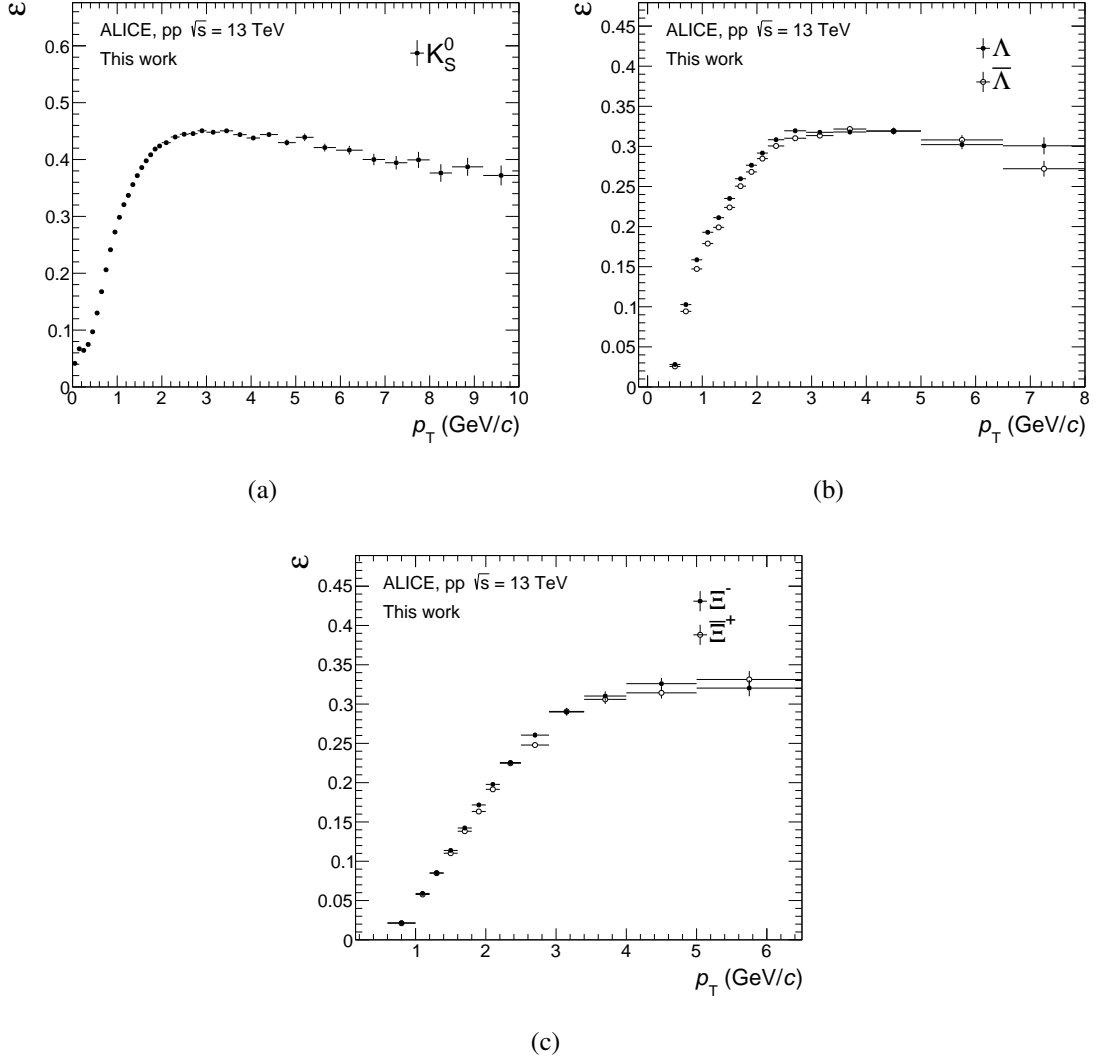


Fig. 6.25 Efficiency of K_S^0 (a), Λ ($\bar{\Lambda}$) (b), Ξ^- (Ξ^+) (c), as a function of p_T used in this analysis.

Correction of anti-proton absorption cross-section in Monte Carlo

The MC samples used in this analysis are generated with the PYTHIA8 event generator using GEANT4 for data collected in 2017 and 2018 and with PYTHIA6 using GEANT3 for 2015 data. It has been observed that the description of the absorption cross-section in GEANT3 is not optimal. In particular, the ratios of anti-particle over particle are found to become significantly larger than one at low p_T . For this reason, we applied an “offline” correction for the anti-particles, considering the ratio of the p_T -differential absorption cross sections for anti-protons in GEANT4 w.r.t. the GEANT3. To apply this correction on the anti-particle

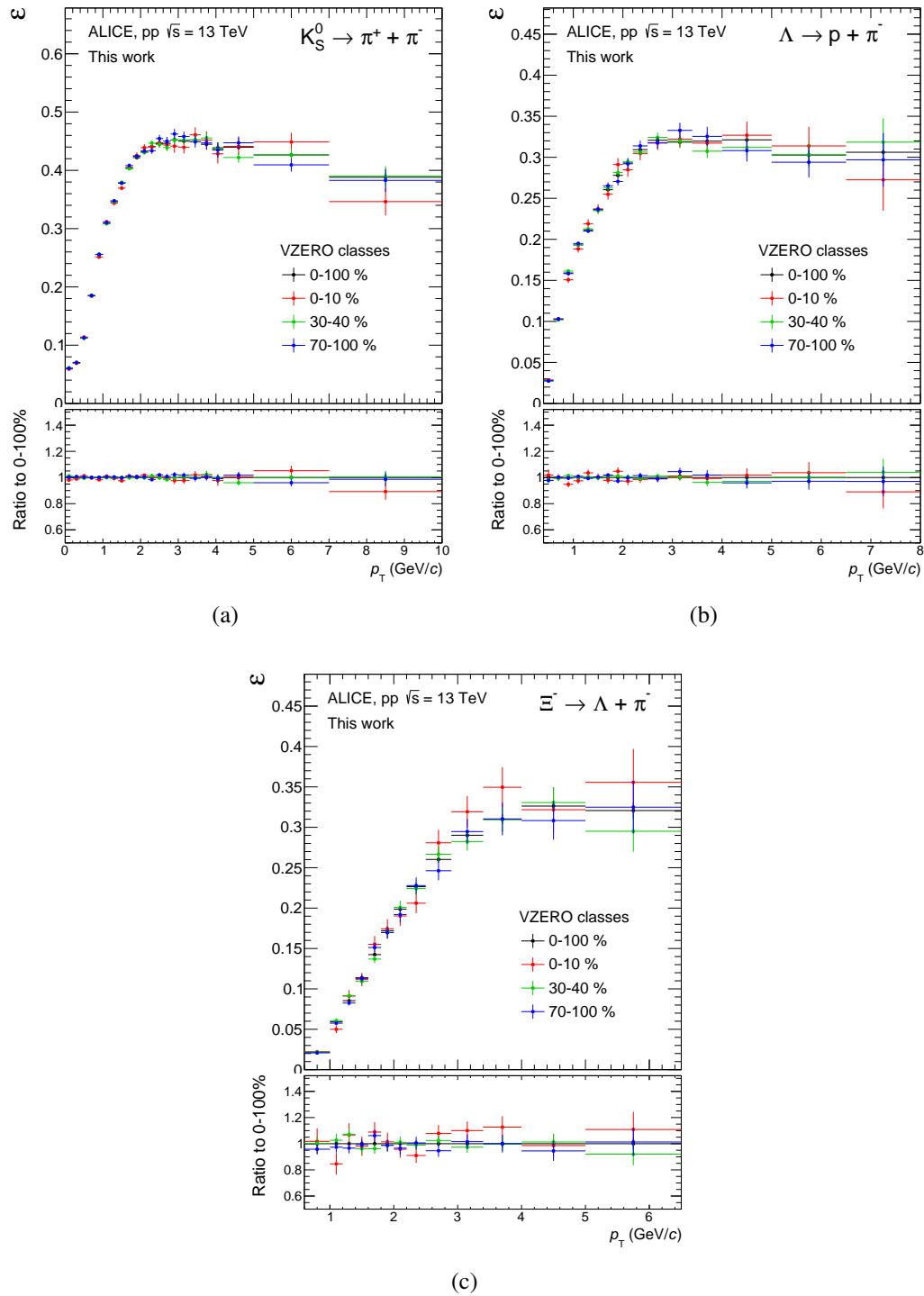


Fig. 6.26 Efficiency of K_S^0 (a), Λ (b), Ξ^- (c), as a function of p_T in 3 VZEROM percentile classes compared to the MB one, used in this analysis.

spectra, the average transverse momentum of the anti-proton daughter was computed in the p_T -bin used to measure the strange particle mother. This correction is applied only to the efficiency computed using the MC anchored to 2015 data, the effect on the total weighted efficiency is shown in Fig. 6.27.

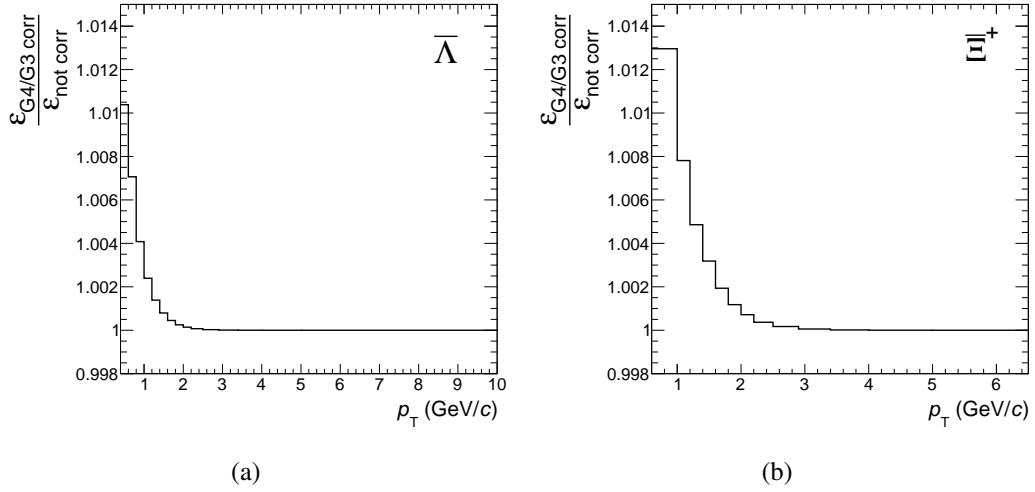


Fig. 6.27 Ratios of efficiency \times acceptance corrections with and without the GEANT4/GEANT3 correction for anti-particles $\bar{\Lambda}$ (a) and $\bar{\Xi}^+$ (b).

6.6.4 Influence of Monte Carlo p_T shape on the efficiency

To reduce the impact of statistical fluctuations, in particular for cascades, we choose large p_T bins in the softest part of the spectra. If the input transverse-momentum distributions of generated particles are substantially different from the real ones, we could introduce a bias to the final corrected spectra. To account for this effect, the measured spectra were first fitted using a Levy-Tsallis function and then re-generated following the fitted shapes with a high granularity, while for MC-generated particles, the transverse-momentum distributions were considered with the same high granularity. Then, an iterative procedure was applied, consisting of the following steps:

- 1) the ratios of the fitted shapes obtained from the data over the Monte Carlo input p_T distributions with high granularity are computed;
- 2) the ratios obtained in the previous point are used in the next iteration to re-weight the reconstructed and generate spectra to calculate efficiencies;
- 3) new corrected efficiencies are obtained by re-binning the p_T spectra obtained at point 2) in the same p_T bins used for the analysis;

- 4) the correction factors, i.e. the ratios of the new efficiencies with respect to the old ones, are applied to the measured spectra.

At every new iteration the corrected spectra from the previous point are used. The comparison between the re-generated spectra shapes and the MC inputs from the three simulations anchored to real data are shown in Fig. 6.28 for the Standalone selection. Figure 6.29 shows the correction factors together with the ratio of the corrected spectra over the new MC input p_T shape at every iteration for the Standalone class. The residual correction becomes negligible after iteration 3. The correction factors applied for all the other selection classes can be found in Appendix A.

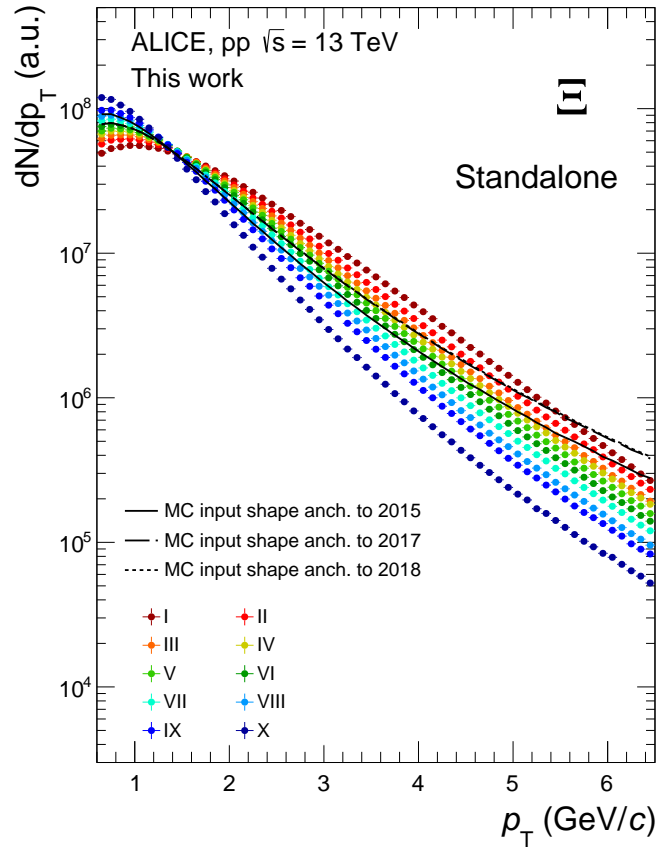
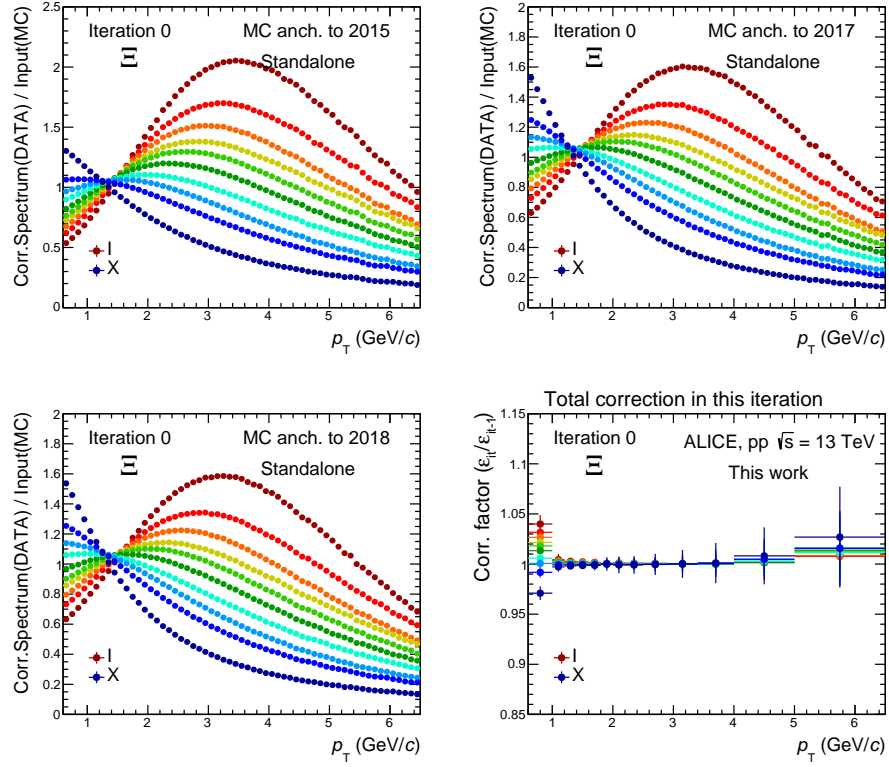
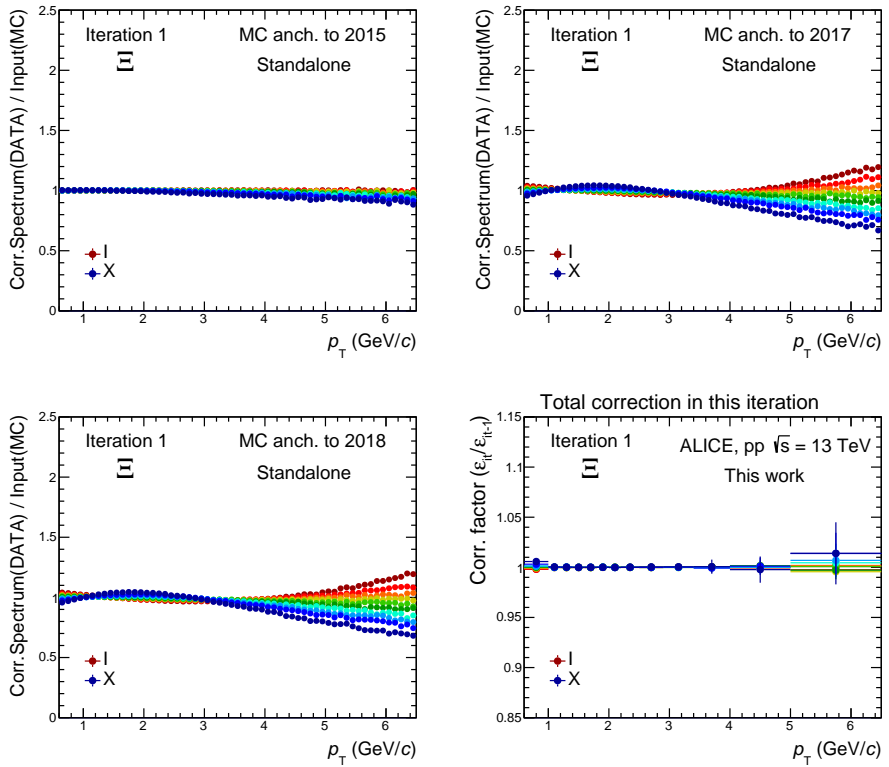


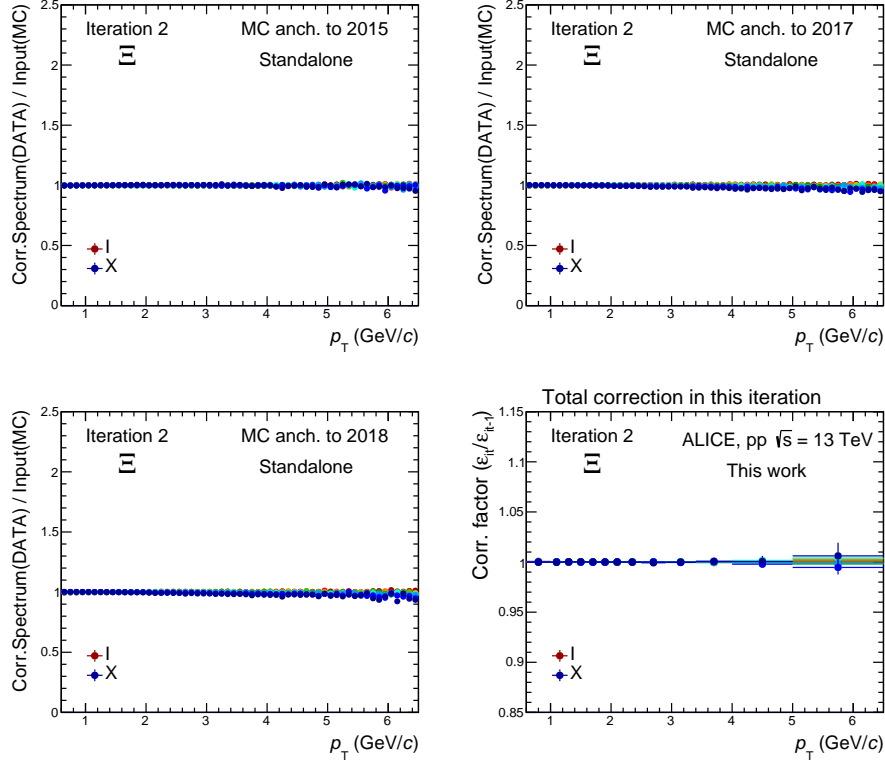
Fig. 6.28 Comparison of measured p_T shapes re-generated starting from Levy-Tsallis fits with the Monte Carlo p_T input distributions for $\Xi^- + \Xi^+$ in the Standalone event class.



(a) Iteration 0



(b) Iteration 1



(c) Iteration 2

Fig. 6.29 Results from the iterative procedure relative to $\Xi^- + \Xi^+$ spectra in the Standalone event class. See text for more details. The bottom-right panels show the correction factors obtained at each iteration. The remaining panels show the ratio of the corrected spectra over the new MC input p_T shape for the three MC simulations.

6.6.5 Normalisation corrections

The corrected spectra at this stage are normalised to the accepted $\text{INEL} > 0$ events, which pass the conditions described in Sect. 6.3. However, in order to achieve a proper normalisation of the spectra, one needs to apply a set of normalisation corrections, accounting for the fraction of event loss (ϵ_{event}) and signal loss (ϵ_{part}) with the event selection:

$$\frac{1}{N_{\text{events}}^{\text{true INEL} > 0}} \cdot \frac{dN_{\text{part}}^{\text{true INEL} > 0}}{dp_T}(p_T) = \frac{1}{N_{\text{events}}^{\text{accepted INEL} > 0}} \cdot \frac{dN_{\text{part}}^{\text{accepted INEL} > 0}}{dp_T}(p_T) \times \frac{\epsilon_{\text{event}}}{\epsilon_{\text{part}}(p_T)} \quad (6.6)$$

These factors are determined from the Monte Carlo simulations and depend on the percentile selection. The ϵ_{evt} factor accounts for the event count loss, i.e. the ratio between the number of events selected after all conditions described in Sect. 6.3 and the number of events with

a “true” production vertex located within $|z_{\text{vtx}}^{\text{true}}| < 10$ cm and at least one charged primary particle produced in $|\eta| < 1$ ($N_{\text{gen}}^{\text{prim}} \geq 1$):

$$\epsilon_{\text{evt}} = \frac{N_{\text{event}}^{\text{accepted INEL}>0}}{N_{\text{event}}^{\text{true INEL}>0}} . \quad (6.7)$$

This factor is not particle-dependent and embeds vertex reconstruction and event selection efficiencies. The event loss correction factors are summarised in Table 6.5 for all event classes used in this analysis.

Class	Correction					
	INEL>0	Standalone	High Multiplicity	Low Multiplicity	High ZN	Low ZN
I	0.9	1	1	1	1	1
II		1	1	1	1	1
III		1	1	1	1	1
IV		1	1	1	1	1
V		1	1	0.99	0.98	
VI		1	1	0.99		
VII		0.99	1	0.98		
VIII		0.98				
IX		0.96				
X		0.80				

Table 6.5 Event loss corrections.

The ϵ_{part} correction is particle and p_T dependent and considers the signal loss fraction due to the event selection. It is calculated as the ratio between the particle spectra at the generated level after the event selection and the generated particle spectra from true INEL>0 events:

$$\epsilon_{\text{part}} = \frac{\frac{dN_{\text{part}}^{\text{Gen}}}{dp_T}(\text{accepted INEL}>0)}{\frac{dN_{\text{part}}^{\text{Gen}}}{dp_T}(\text{true INEL}>0)} . \quad (6.8)$$

In Fig. 6.30, the signal loss correction factors computed for all particle species for the Standalone event class are shown. The correction factors for the other event classes are reported in Appendix A.

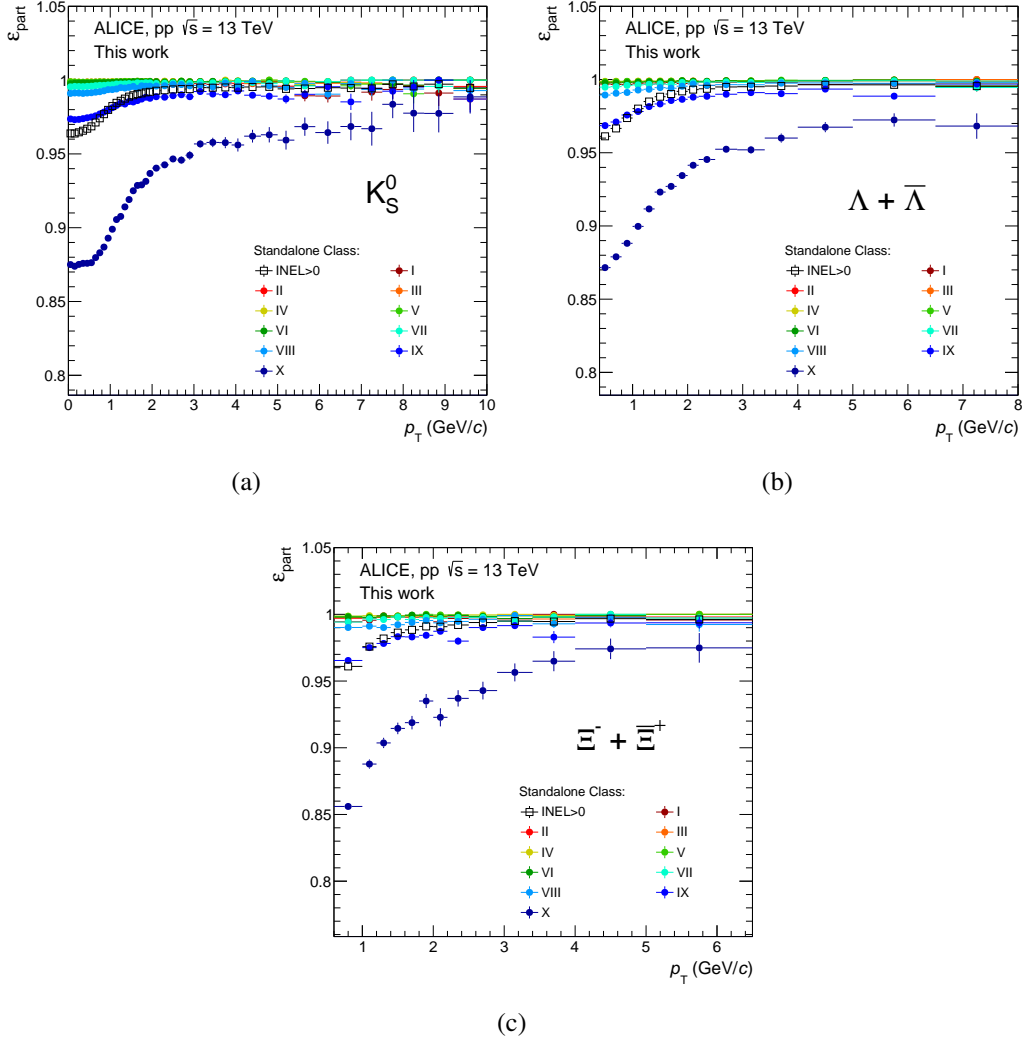


Fig. 6.30 Signal loss correction factors for K_S^0 (a), $\Lambda + \bar{\Lambda}$ (b), $\Xi^- + \bar{\Xi}^+$ (c) in the Standalone Class selection.

6.7 Systematic uncertainties

Several sources of systematic uncertainties affecting the measured p_T spectra are considered, and a detailed description of the treatment of these uncertainties is provided in this Section. The main systematic contribution to the measurements of the strange hadron spectra is related to track and topological selections. Uncertainties on the signal extraction procedure, efficiency, feed-down, material budget and hadronic interactions are also considered. The main contributions for three representative p_T values are summarised in Table 6.9 and displayed in Fig. 6.31 for the $\text{INEL} > 0$ sample. In measuring the very forward energy, the

main systematic contribution was estimated by comparing the ZDC response among the different datasets (periods) after the calibration procedure.

6.7.1 Uncertainties on strange hadron spectra

To evaluate the systematic uncertainty associated with a given selection, the analysis is repeated by varying that specific variable within defined ranges. The results are then compared to the ones obtained with the standard set of cuts described in Sec. 6.6. The stability of the acceptance and efficiency corrections was verified by varying all track and topological selection criteria within ranges, which led to a maximum variation of $\pm 10\%$ in the raw signal yield. The set of cut variations applied to K_S^0 , Λ ($\bar{\Lambda}$) and Ξ^- ($\bar{\Xi}^+$) are reported in Table 6.6, 6.7 and 6.8 respectively. Only variations not compatible with statistical fluctuations are considered, following the prescription in Ref. [136] with a 1σ threshold. According to this prescription, the uncertainty on the difference between two correlated quantities (x_{def} , x_{var}) with absolute uncertainties (σ_{def} , σ_{var}) is given by:

$$\Delta = x_{\text{var}} - x_{\text{def}}, \quad \sigma_{\Delta} = \sqrt{|\sigma_{\text{var}}^2 - \sigma_{\text{def}}^2|}$$

The Barlow variable B can be defined as follows:

$$B = \frac{\Delta}{\sigma_{\Delta}} \quad (6.9)$$

Assuming that x_{def} and x_{var} are normally distributed, B follows a Gaussian distribution with mean equal to zero and variance equal to one. The maximum deviations for each cut variable, which passes the condition $|B| > 1$, are added to the total systematic uncertainty calculation. The resulting uncertainty from topological and track selection variations (except the TPC dE/dx) are summarised in Table 6.9 for K_S^0 , $\Lambda + \bar{\Lambda}$ and $\Xi^- + \bar{\Xi}^+$.

The uncertainty related to the TPC energy loss selection was evaluated by varying the dE/dx requirement between 4 and 7σ . This selection is particularly important to reduce the combinatorial background in the strange baryon invariant mass distribution. Therefore, this uncertainty accounts for systematic contributions from this effect. The uncertainty was found to be at most 1% for all particle species.

The contribution from the competing V^0 decay rejection was studied by removing entirely this condition for Λ and $\bar{\Lambda}$ and by varying the mass window down to $3 \text{ MeV}/c^2$ and up to $5.5 \text{ MeV}/c^2$ for K_S^0 . It resulted in a deviation on the p_T spectra of at most 3% for

Cut (K_S^0)	Value			
	very loose	loose	tight	very tight
V0 Radius (cm)	> 0.3	>0.4	>0.6	>0.7
DCA V0 Neg/Pos track to PV (cm)	> 0.050	>0.055	>0.070	>0.080
DCA V0 daughters (σ)	< 1.5	<1.25	<0.75	<0.5
V0 cos(PA)	> 0.95	>0.96	>0.98	>0.99
Least number of TPC clusters			≥ 75	≥ 80
TPC CR/Findable			≥ 0.95	

Table 6.6 Variation of selections applied to K_S^0 candidates.

Cut ($\Lambda, \bar{\Lambda}$)	Value			
	very loose	loose	tight	very tight
V0 Radius (cm)	> 0.3	>0.4	>0.6	>0.7
DCA V0 Neg/Pos track to PV (cm)	> 0.050	>0.055	>0.070	>0.080
DCA V0 daughters (σ)	< 1.5	<1.25	<0.75	<0.5
V0 cos(PA)	> 0.993	>0.994	>0.996	>0.997
Least number of TPC clusters			≥ 75	≥ 80
TPC CR/Findable			≥ 0.95	

Table 6.7 Variation of selections applied to Λ and $\bar{\Lambda}$ candidates.

Cut ($\Xi^-, \bar{\Xi}^+$)	Value			
	very loose	loose	tight	very tight
V0 Radius (cm)	> 1.0	>1.1	>2.5	>5.0
Cascade Radius (cm)	> 0.4	>0.5	>0.8	>1.0
DCA V0 meson to PV (cm)	> 0.02	>0.03	>0.15	>0.30
DCA V0 baryon to PV (cm)		>0.02	>0.09	>0.11
DCA bach to PV (cm)		>0.03	>0.10	>0.17
DCA V0 to PV (cm)		>0.05	>0.1	>0.15
DCA V0 daughters (σ)	< 2.0	<1.8	<1.2	<1.0
DCA Casc daughters (cm)	< 2.0	<1.8	<1.2	<1.0
V0 cos(PA)	> 0.95	>0.96	>0.98	>0.99
Cascade cos(PA)	> 0.95	>0.96	>0.98	>0.99
V0 mass window (GeV/c^2)	± 0.01	± 0.009	± 0.007	± 0.006
Least number of TPC clusters			≥ 75	≥ 80

Table 6.8 Selections applied to Ξ^- and $\bar{\Xi}^+$ candidates.

$\Lambda + \bar{\Lambda}$ and 1% for K_S^0 .

The systematic contribution related to the selection on the proper lifetime of the candidate was computed by varying the requirements between 2.5 and 5 $c\tau$ for strange baryons and between 5 and 15 $c\tau$ for K_S^0 . The statistically significant deviations were found to be at most 3% for $\Lambda + \bar{\Lambda}$ and negligible ($< 1\%$) for K_S^0 and $\Xi^- + \bar{\Xi}^+$.

The stability of the signal extraction method was checked by varying the widths used to define the signal and background regions in terms of the number of σ of the invariant mass distributions as defined in Sec. 6.6.1. Moreover, the raw counts are extracted using a fitting procedure for the background contribution and compared to the standard ones computed using a bin counting technique. An uncertainty ranging between 0.2% and 2% depending on p_T is found for V^0 s and cascades.

The Λ and $\bar{\Lambda}$ p_T spectra are also affected by an uncertainty coming from the feed-down correction, which accounts for the description of the Ξ^\pm/Ξ^0 ratio in the MC. The latter was considered by calculating the feed-down fraction assuming $\Xi^\pm/\Xi^0 = 1$ or using the ratio provided by the Monte Carlo. The feed-down contribution to the systematic uncertainties was at most 1%.

A systematic uncertainty to the (anti-)proton absorption cross section in MC samples was also considered, as estimated from the uncertainty on the inelastic cross section and the detector thickness in units of hadronic interaction length. This uncertainty does not apply to K_S^0 and is found to account for $< 1\%$ for strange baryons.

The contribution from the out-of-bunch pile-up rejection was evaluated by changing the matching scheme of V^0 and cascade daughters using the ITS and TOF detectors. For this purpose, the following configurations were considered: matching of at least one decay track with the ITS (TOF) detector below (above) 2 GeV/ c of the reconstructed (multi-)strange hadron, ITS matching of at least one decay track in the full p_T range. Half of the maximum variation between these configurations and the standard selection was taken as a systematic contribution, which was found to increase with transverse momentum up to 3% for all particle species.

Pile-up collisions occurring within the same bunch crossing are removed by rejecting events with multiple vertices reconstructed in the SPD (see Sect. 6.3). The effect of

residual contamination from in-bunch pile-up events was estimated in Ref. [137] by varying the pile-up rejection criteria. In this analysis, we use the same systematic contributions.

The imperfect reproduction of the detector material budget in the MC simulation used to compute the reconstruction efficiencies is also taken into account as a possible source of systematic uncertainty. To assess this uncertainty, the strange hadron efficiencies are computed using a MC with a different dependence of the material budget on the radial distance from the interaction point. The relative semi-difference between the efficiency obtained with the variation and the default one is considered as a systematic uncertainty.

Hadron p_T (GeV/c)	K_S^0			$\Lambda + \bar{\Lambda}$			$\Xi^- + \bar{\Xi}^+$		
	≈ 0.5	≈ 4.8	≈ 9.0	≈ 1.0	≈ 3.5	≈ 7.0	≈ 1.3	≈ 2.8	≈ 4.7
Signal extraction	0.5	0.5	2.2	0.3	0.7	1.2	negl.	0.6	0.6
Topological and track	1.7	2.4	2.3	3.0	3.0	4.3	3.3	1.1	2.0
TPC dE/dx	0.1	0.1	negl.	0.3	0.1	0.6	0.3	0.1	negl.
Competing V0	0.1	0.4	negl.	1.1	0.3	negl.	n.a.	n.a.	n.a.
Proper lifetime	0.1	negl.	negl.	2.9	2.6	negl.	0.7	0.2	0.6
Material Budget	1.1	0.5	0.5	1.4	0.8	0.8	2.9	1.5	0.6
In-bunch (IB) pileup	1.6	2.5	2.5	2.0	2.9	2.9	2.0	2.0	2.9
OOB pileup	0.2	0.8	2.6	0.6	2.1	2.9	0.4	1.0	2.5
\bar{p} abs. cross sect.	n.a.	n.a.	n.a.	0.2	0.2	0.2	0.3	0.4	0.4
Feed-down	n.a.	n.a.	n.a.	1.0	1.0	1.0	n.a.	n.a.	n.a.

Table 6.9 Main sources of systematic uncertainties (expressed in %) of the p_T differential yields, reported for low, intermediate and high p_T . These values are calculated for the INEL>0 data sample. Results in other classes are further affected by an uncertainty originating from the multiplicity dependence of the efficiency (2%) and, in the case of the Λ , of the feed-down contributions (2%).

6.7.2 Systematics on p_T integrated yields

The p_T integrated yields (dN/dy) of strange hadrons are computed from the data in the measured ranges and using extrapolations to the unmeasured regions. In particular, a Levi-Tsallis parametrisation is used to describe the measured p_T shape and to extrapolate the spectra down to $p_T = 0$. The systematic uncertainty on the extrapolated yield is calculated by fitting the highest and lowest spectra obtained by shifting all data points within $\pm 1\sigma_{p_T}$, where σ_{p_T} represents the systematic uncertainty of the p_T dependent yield.

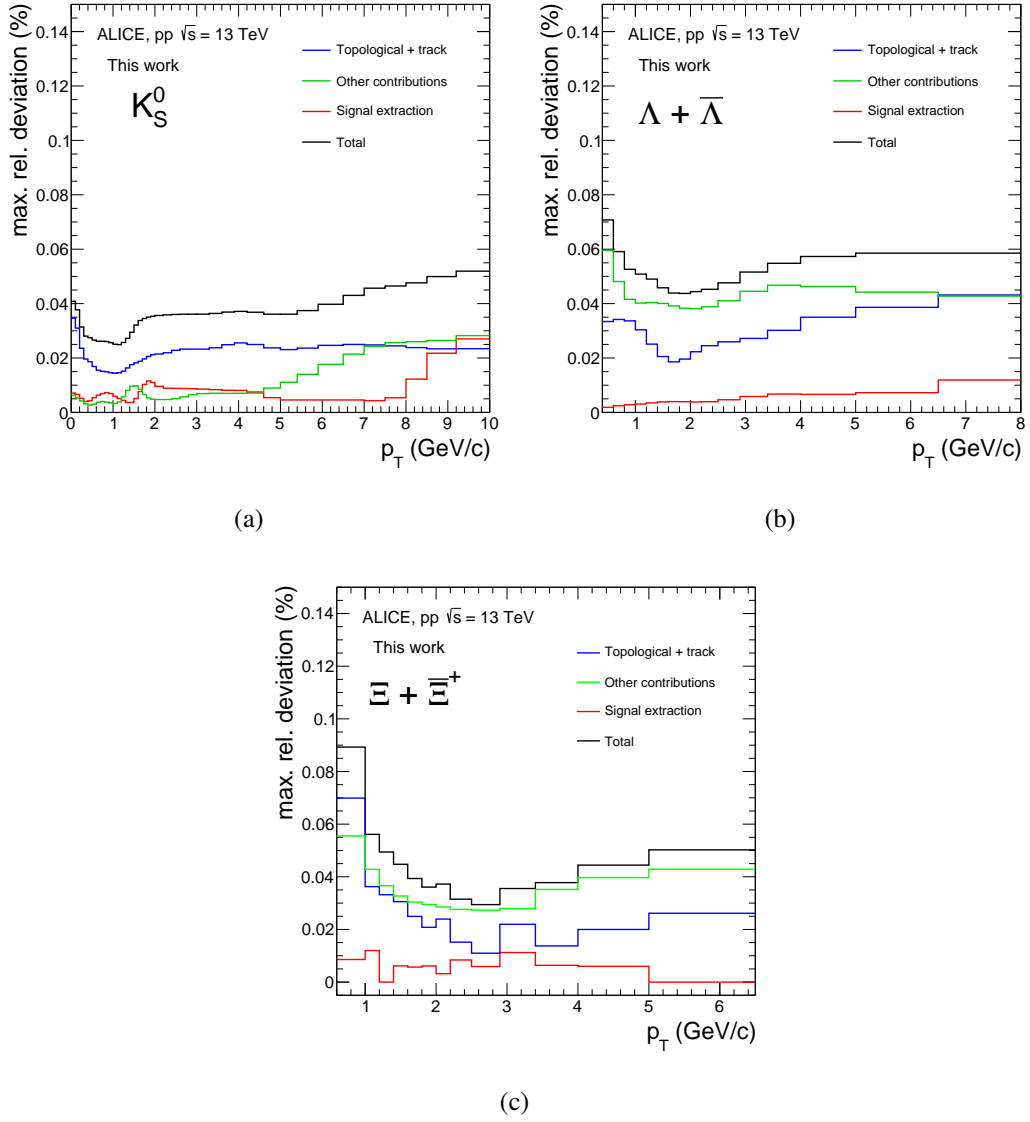


Fig. 6.31 Summary of the systematic uncertainties on the p_T spectra of K_S^0 (a), $\Lambda + \bar{\Lambda}$ (b) and $\Xi^- + \bar{\Xi}^+$ (c) in the INEL>0 data sample.

This procedure is followed assuming the sources of systematic uncertainties are correlated across p_T . Another source of systematic uncertainty of the integrated yields is associated with the choice of the fit function used to describe the measured p_T shape. This is calculated by repeating the fit of the spectra using five alternative functions (Blast-Wave, Boltzmann, Bose-Einstein, m_T -exponential, Fermi-Dirac) instead of the Levy-Tsallis, considered as a reference. The fit ranges used for the different parametrisations were “tuned” to get the best χ^2/ndf . The final systematic uncertainty on the yield is assigned by considering the maximum deviations obtained for each spectrum. This contribution is not applied to the K_S^0 spectra, since we can measure the yields down to $p_T = 0$. An example of fit to the $\Lambda + \bar{\Lambda}$ and $\Xi^- + \bar{\Xi}^+$ spectra with different functional forms is shown in Fig. 6.32 for the Standalone class.

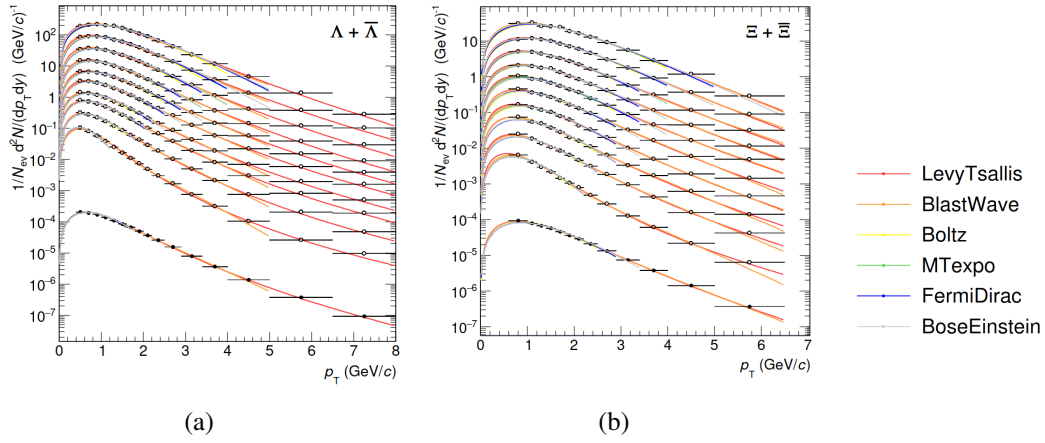


Fig. 6.32 Results from the fitting procedure of the spectra of $\Lambda + \bar{\Lambda}$ and $\Xi^- + \bar{\Xi}^+$ using different functional forms for the Standalone class.

6.7.3 Multiplicity and energy uncorrelated uncertainties

Most of the sources of systematic uncertainties considered in this analysis are fully correlated across the percentile selections since they determine a yield variation, which does not depend on the specific class. In this analysis, to illustrate the evolution of the production of strange hadrons in the multi-differential classes and reduce the systematics on the final results, we consider the yield ratios to the average MB value, measured in the inclusive INEL > 0 pp sample:

$$h/\langle h \rangle_{\text{INEL}>0}$$

where h is the p_T integrated yield (dN/dy) of strange hadrons. In the following, we will refer to this fraction as self-normalised yields. The full analysis chain, up to the extraction of integrated yields, is repeated by varying the selections described in Sec. 6.7.1, and the results are then compared to those obtained with the default set of cuts. This procedure is repeated for all the selection classes defined in this analysis and compared to the results using the MB sample. In order to determine the fraction of uncertainty which is uncorrelated across percentile selections, the ratio R_{var} is computed:

$$R_{\text{var}} = \left(\frac{h_{\text{sel}}}{\langle h \rangle_{\text{INEL}>0}} \right)^{\text{var}} / \left(\frac{h_{\text{sel}}}{\langle h \rangle_{\text{INEL}>0}} \right)^{\text{def}} = \frac{(h^{\text{var}}/h^{\text{def}})_{\text{sel}}}{\langle h^{\text{var}}/h^{\text{def}} \rangle_{\text{INEL}>0}} \quad (6.10)$$

The error associated with the ratio R_{var} accounts for the correlation between the default yield and the one obtained with a systematic variation and for the correlation between the yield in a percentile class and the MB one. If a source of uncertainty is fully correlated across selections in multiplicity and effective energy, $R_{\text{var}} = 1$. The deviation of R_{var} from unity gives the relative uncertainty uncorrelated across percentile selections:

$$\sigma_{\text{uncorr}} = |R_{\text{var}} - 1| \cdot \frac{h_{\text{sel}}}{\langle h \rangle_{\text{INEL}>0}} \quad (6.11)$$

A similar approach can be applied to estimate the uncorrelated uncertainty on the choice of the fit function for the extrapolation procedure. The fraction of the yields obtained using an alternative function over the default one, Levy-Tsallis (LT), in a given selection is compared to the inclusive MB one:

$$R_{\text{var}}^{\text{extr}} = \left(\frac{h_{\text{sel}}}{\langle h \rangle_{\text{INEL}>0}} \right)^{\text{var-func}} / \left(\frac{h_{\text{sel}}}{\langle h \rangle_{\text{INEL}>0}} \right)^{\text{LT}} = \frac{(h^{\text{var-func}}/h^{\text{LT}})_{\text{sel}}}{\langle h^{\text{var-func}}/h^{\text{LT}} \rangle_{\text{INEL}>0}} \quad (6.12)$$

Once again, the extrapolation contribution is not applied to the K_S^0 yields since we are able to measure the spectra down to $p_T = 0$. A summary of the systematic contributions uncorrelated across percentile selections for the Standalone class is reported in Fig. 6.33 for K_S^0 (a), $\Lambda + \bar{\Lambda}$ (b) and $\Xi^- + \bar{\Xi}^+$ (c). The results obtained for the other differential classes are reported in Appendix A.

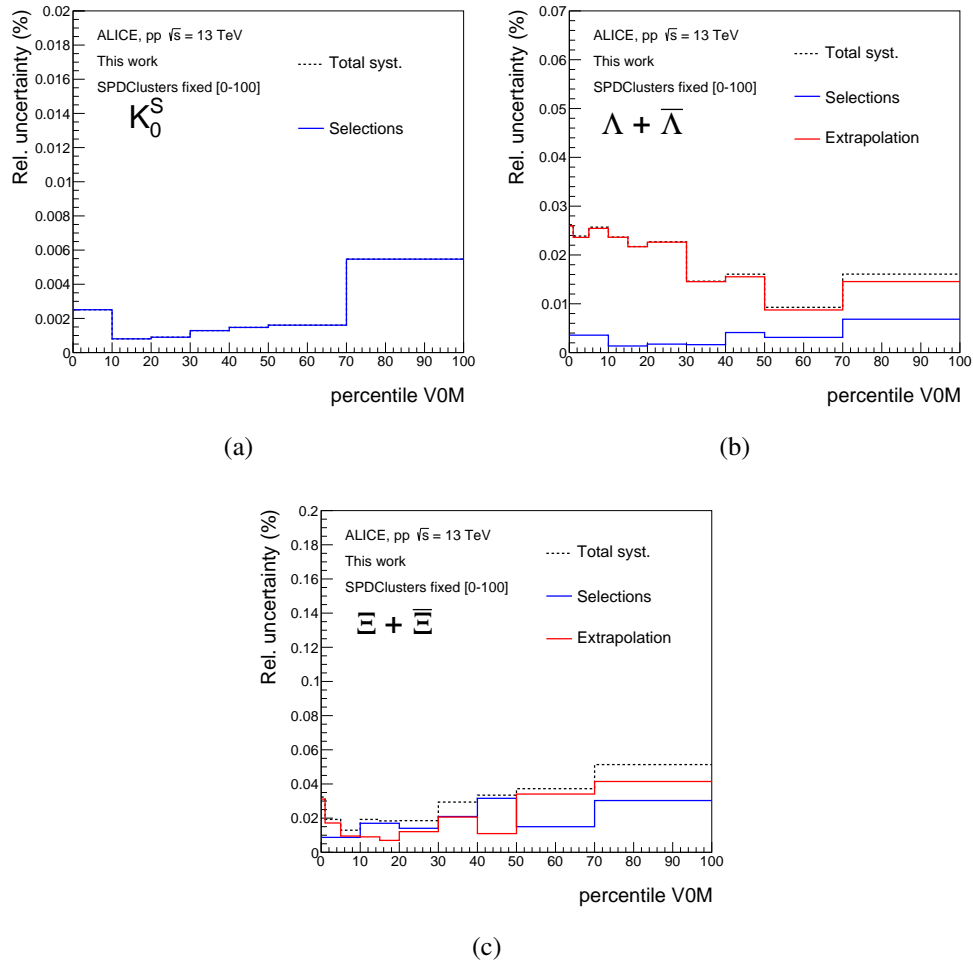


Fig. 6.33 Summary of the uncorrelated systematic uncertainties on the integrated yields for K_S^0 (a), $\Lambda + \bar{\Lambda}$ (b) and $\Xi^- + \bar{\Xi}^+$ (c) studied in the Standalone class selection. The contribution from the variation of selections and extrapolations is reported in blue and red, respectively. The total contribution is reported in black.

6.7.4 Systematic uncertainty on the very forward energy measurement

The systematic uncertainty associated with the average $\langle ZN \rangle$ value was studied after the calibration by comparing the energy measured in the three data-taking periods. The measurement was repeated in different double-differential classes defined using SPDClusters and VZERO estimators. The error associated with the $\langle ZN \rangle$ value was defined as the largest difference of each period with respect to the mean value, which is found to be at the level of 3%. In Fig. 6.34, the comparison for the three periods of the $\langle ZN \rangle$ energy is shown for double differential SPDClusters + VZERO selections. SPDClusters percentile selections are reported in the x-axis, while VZERO is varied from top (VZERO 70-100%) to bottom (0-10%).

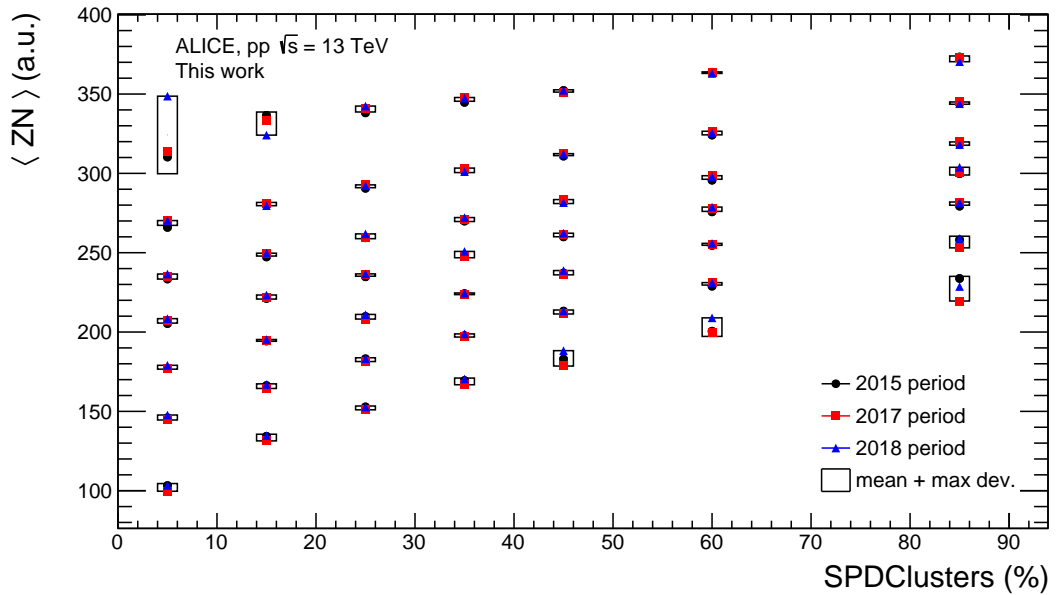


Fig. 6.34 Comparison for different periods of the $\langle ZN \rangle$ for double differential SPDClusters + VZERO selections. SPDClusters percentile selections are reported in the x-axis, while VZERO is varied from top (VZERO 70-100%) to bottom (0-10%).

Chapter 7

Results and discussion

This chapter presents the results on the production of strange mesons K_S^0 , strange baryons $\Lambda + \bar{\Lambda}$, and multi-strange baryons $\Xi^- + \bar{\Xi}^+$ in pp collisions at $\sqrt{s} = 13$ TeV. In the following, we will refer to the sum of particles and anti-particles as Λ and Ξ , respectively. For the first time, we explore the correlation of strangeness production with the event multiplicity and the energy produced in the very forward rapidity region, a proxy for the effective energy. The results are compared to the predictions of the PYTHIA8 event generator with different tunes, namely with and without colour ropes in the model. Some of the results discussed in this chapter were approved by the ALICE Collaboration and were presented at several international conferences [10].

7.1 Transverse momentum spectra of strange hadrons

The K_S^0 , Λ and Ξ raw p_T -dependent yields, extracted in all the multi-differential classes, are corrected for the efficiencies and normalisation corrections discussed in Chapter 6. The fully-corrected p_T -spectra for all particle species are displayed in Fig. 7.1 for the Standalone class selection. As already observed by previous ALICE publications [137–139], the spectra become harder as the multiplicity increases. However, it is important to consider that, as discussed in Sect. 6.5.1, the Standalone event class not only selects events with increasing midrapidity multiplicity but also with decreasing forward energy detected by the ZDCs (see Fig. 6.6). In fact, the correlation between these two observables must be taken into account when comparing the spectra in different event classes. Further insights into the nature of the collisions selected with the multi-differential classes used in this work can be obtained by studying the hadrons p_T -spectra in these selections. Figure 7.2 shows the p_T -spectra of Ξ baryons in the High Multiplicity (a) and High ZN (b) event classes. As displayed in Fig. 7.2 (a), at fixed midrapidity multiplicity, a selection based on different forward energy deposits

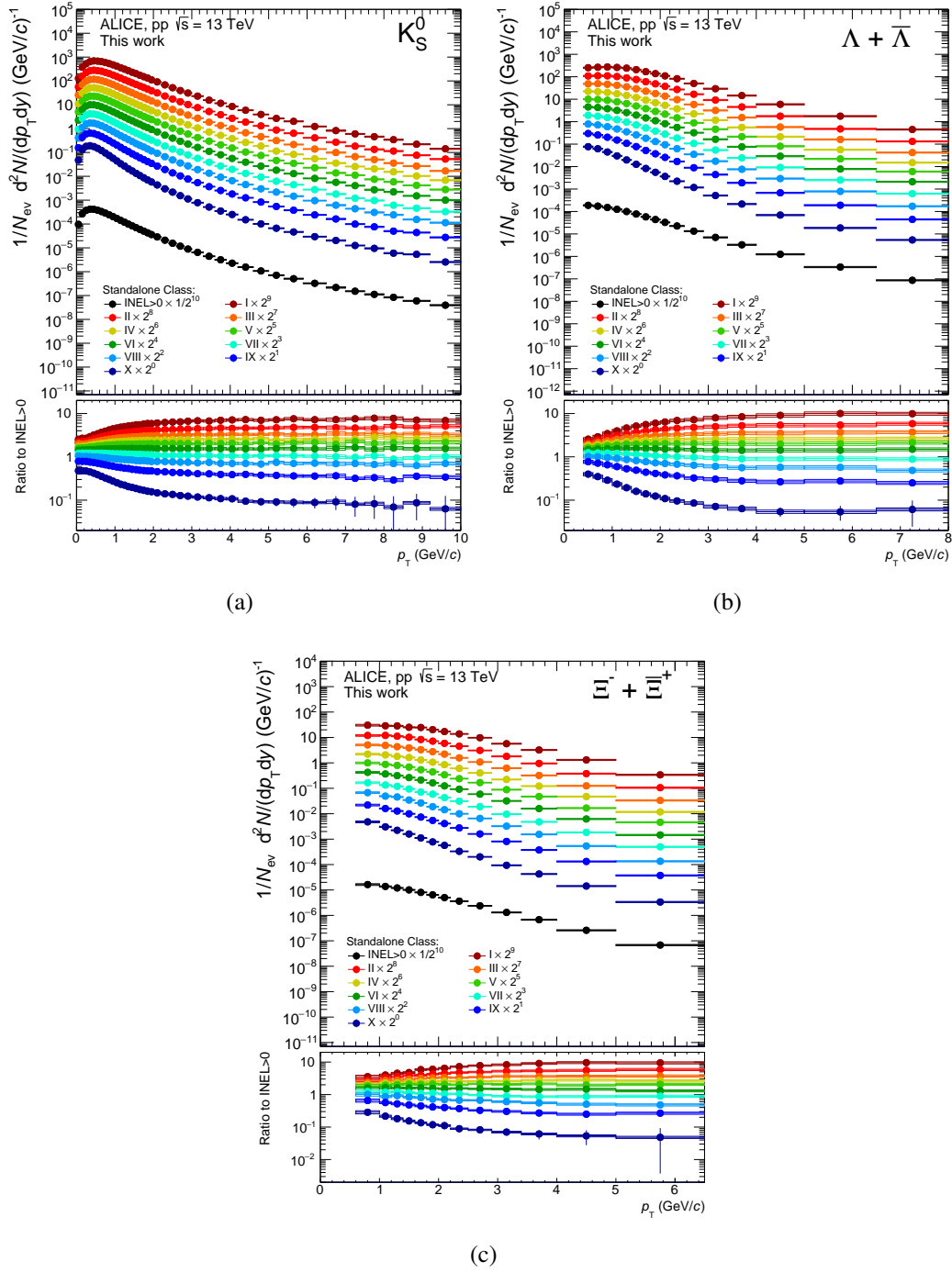


Fig. 7.1 Transverse momentum distribution of K_S^0 (a), Λ (b), and Ξ (c) in pp collisions at $\sqrt{s} = 13$ TeV in the Standalone selection (VZERO classes). Statistical and total systematic uncertainties are shown by error bars and boxes, respectively. In the bottom panels ratios of the spectra to INEL > 0 are shown. The spectra are scaled by different factors to improve the visibility.

results in different Ξ yields but similar p_T -shapes.

This is visible when looking at the ratio of the distributions with respect to the central class spectrum, shown in the bottom panel. On the other hand, at fixed energy detected by the ZN, Fig. 7.2 (b), the spectra become harder as the multiplicity increases. This behaviour suggests that the observed hardening of the Ξ spectra in the Standalone class is strongly correlated with the multiplicity produced at midrapidity. Moreover, this may indicate that once the activity at forward rapidity is fixed, at increasing midrapidity multiplicity, strangeness production is driven by harder processes.

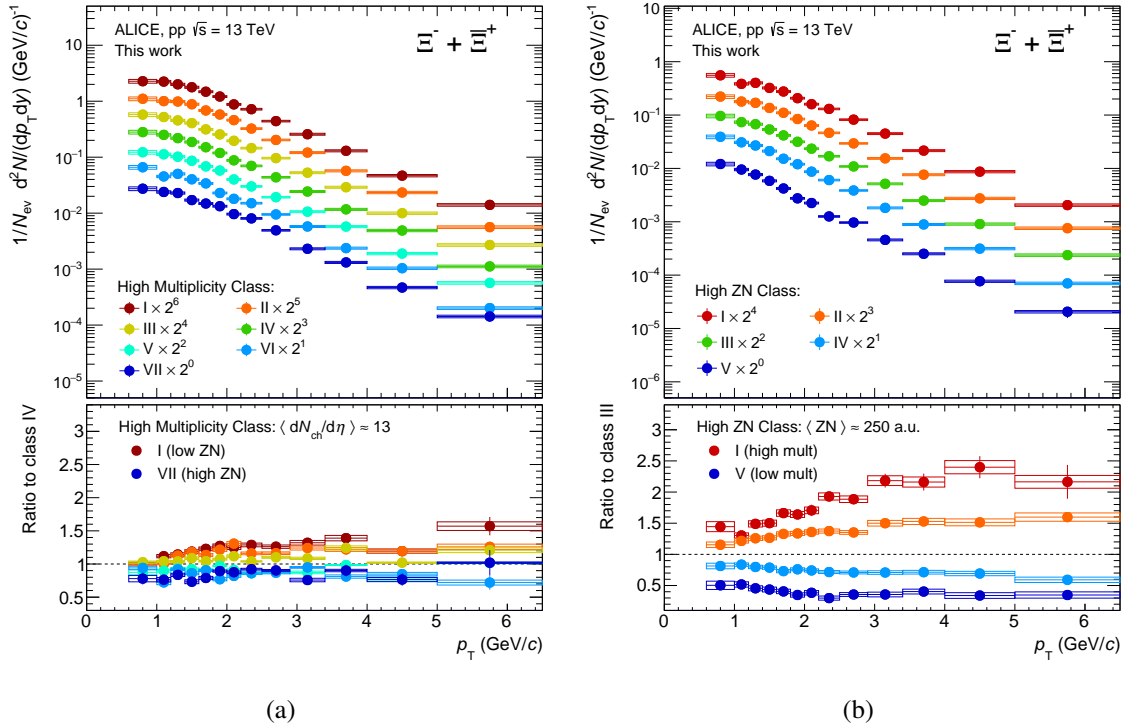


Fig. 7.2 Transverse momentum distribution of Ξ in pp collisions at $\sqrt{s} = 13$ TeV in the High Multiplicity (a) and High ZN (b) selections (SPDClusters+VZEROM classes). The bottom panels show ratios of the two most extreme selections in the event class to the central one. The spectra are scaled by different factors to improve the visibility.

Figures 7.3 and 7.4 display the p_T -spectra of Λ and K_S^0 respectively in the same selections. Figure 7.3 (a) shows that, at fixed midrapidity multiplicity, as the leading energy decreases, different Λ yields and slightly different p_T -shapes are obtained. On the other hand, looking at Fig. 7.3 (b), at fixed energy detected by the ZN, the spectra become harder as the multiplicity increases, as observed for the Ξ baryon. Finally, also for the K_S^0 meson, at fixed midrapidity multiplicity, the yields and p_T -shapes are similar for different forward energy deposits, as

shown in Fig. 7.4 (a), and, at fixed ZN energy, the spectra become harder as the multiplicity increases, as shown in Fig. 7.4 (b).

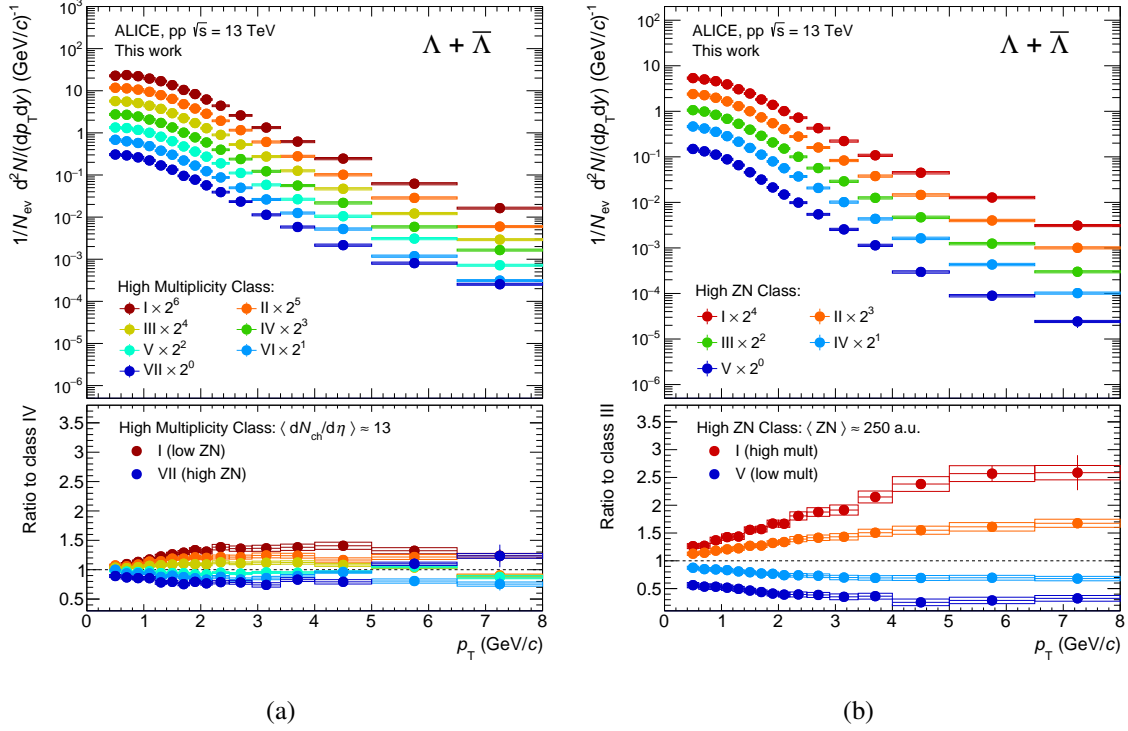


Fig. 7.3 Transverse momentum distribution of Λ in pp collisions at $\sqrt{s} = 13$ TeV in the High Multiplicity (a) and High ZN (b) selections (SPDClusters+VZEROM classes). The bottom panels show ratios of the two most extreme selections in the event class to the central one. The spectra are scaled by different factors to improve the visibility.

In summary, the average transverse momentum of strange hadrons appears to be correlated with the charged particle multiplicity, e.g. fixing the activity at forward rapidity, the spectra become harder as the multiplicity increases. Indeed, the charged-particle multiplicity produced at midrapidity is a good proxy for final state local effects, such as jet fragmentation. The results in Fig. 7.2, 7.3 and 7.4 are reported for the High Multiplicity and High ZN classes, however similar conclusions can be drawn by looking at the Low Multiplicity and Low ZN selections, which are reported in Appendix B.

7.2 Self-normalised hadron yield ratios

The p_T -integrated yields of K_S^0 , Λ and Ξ are extracted from the p_T -spectra, using extrapolations for the unmeasured regions. The spectra are fitted using a Lévy-Tsallis parametriza-

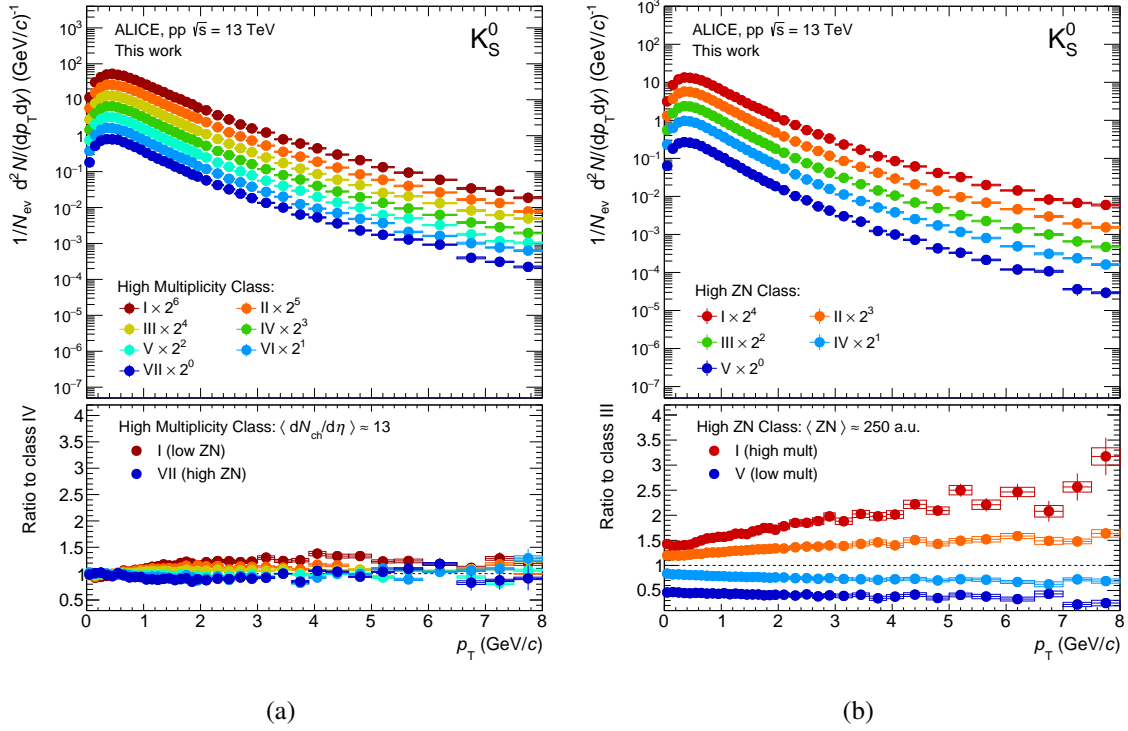


Fig. 7.4 Transverse momentum distribution of K_S^0 in pp collisions at $\sqrt{s} = 13$ TeV in the High Multiplicity (a) and High ZN (b) selections (SPDClusters+VZEROM classes). The bottom panels show ratios of the two most extreme selections in the event class to the central one. The spectra are scaled by different factors to improve the visibility.

tion [140], which best describes the individual spectra for all particles over the full p_T range. The Lévy-Tsallis function is defined as:

$$\frac{d^2N}{dydp_T} = \frac{(n-1)(n-2)}{nT[nT + m_0(n-2)]} \times \frac{dN}{dy} \times p_T \times \left(1 + \frac{m_T - m_0}{nT}\right)^{-n}, \quad (7.1)$$

where m_0 is the particle mass, $m_T = \sqrt{m_0^2 + p_T^2}$ is the transverse mass, and dN/dy is the particle yield per rapidity unit. The variables T , n , and dN/dy are free fit parameters. The Lévy-Tsallis function includes an exponential component, which describes the softer part of the spectra, and a power-law dependence for the high- p_T tail. To illustrate the evolution of strange hadron production with the multiplicity and the leading energy, we consider the yield ratios to the charged-particle multiplicity divided by the value measured in the inclusive $\text{INEL} > 0$ pp sample:

$$\frac{\langle h \rangle / \langle h \rangle_{\text{INEL} > 0}}{\langle n_{\text{ch}} \rangle / \langle n_{\text{ch}} \rangle_{\text{INEL} > 0}}, \quad (7.2)$$

where h represents the particle yield per rapidity unit (dN/dy). In the following, we will refer to the quantity in Eq. 7.2 as “self-normalised yield ratios”. The yield per charged particle (h/n_{ch}) is a good proxy for the ratio of strange to non-strange hadron yields (h/π) since the bulk of charged particles produced in a pp collision event is mainly composed by pions, followed by a smaller contribution from kaons, protons and other primary charged particles. In this work, the self-normalised yield ratios are studied as a function of the charged-particle multiplicity and the ZN energy, self-normalised to their minimum-bias INEL > 0 value. This is particularly important when considering the forward energy measurement since no absolute energy calibration is available for the ZDCs in pp collisions, as discussed in Sect. 4.2.2.

7.2.1 Standalone analysis

Strangeness enhancement in pp collisions commonly refers to the increase of strange hadron yields to pions with the charged-particle multiplicity produced in the event. This effect is displayed in the left panel of Fig. 7.5 for the Standalone event class, where the self-normalised yield ratios of K_S^0 , Λ , and Ξ are shown as a function of the charged-particle multiplicity. The enhancement is larger for Ξ multi-strange baryons than for Λ and K_S^0 strange hadrons, showing a hierarchy with the particle strangeness content. The Λ baryon and K_S^0 meson ratios are compatible within uncertainties, except for the low multiplicity region. As discussed in Sect. 6.5, the particle production at midrapidity is anti-correlated with the energy produced at forward rapidities (leading energy), i.e. the higher the activity measured at midrapidity, the smaller the forward energy deposited in the Zero Degree Calorimeters [88], as displayed in Fig. 6.6. To explore the correlation of strangeness production with the leading energy, the self-normalised yield ratios are shown also as a function of the ZN signal in the right panel of Fig. 7.5. In particular, the strange hadron production per charged particle is found to increase at decreasing forward energy detected in the ZN. This observation can be interpreted as a positive correlation of strangeness production with the effective energy, given:

$$E_{\text{eff}} \simeq \sqrt{s} - E_{\text{ZDC}} \quad .$$

In the following sections, the results of the multi-differential analysis are shown, performed to disentangle the dependence of strange hadron production on the multiplicity and the leading energy. In particular, Sect. 7.2.2 discusses the dependence of strangeness production with the multiplicity once the forward energy is fixed, and in Sect. 7.2.3, the correlation of strangeness production with the leading energy is explored once the activity at midrapidity is fixed.

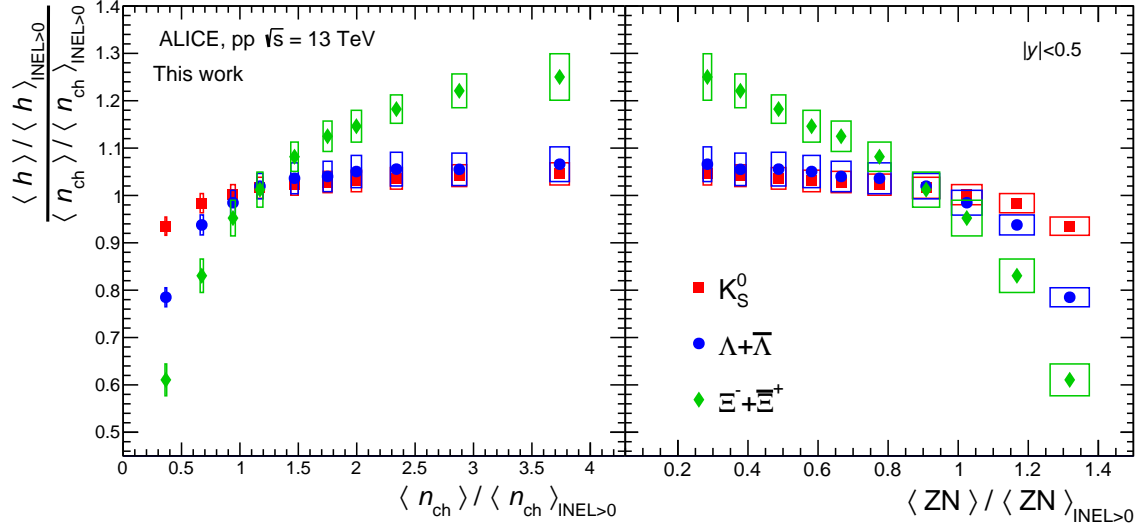


Fig. 7.5 Self-normalised yield ratios of K_S^0 , Λ , and Ξ in pp collisions at $\sqrt{s} = 13$ TeV in the Standalone selection (VZEROM classes). The ratios are shown as a function of the charged-particle multiplicity (left) and ZN energy (right) self-normalised to the minimum-bias INEL > 0 value. Statistical and total systematic uncertainties are shown by error bars and boxes, respectively.

7.2.2 Strangeness production at fixed leading energy

In order to further investigate the dependence of strange hadron production on the particle multiplicity produced at midrapidity, the self-normalised yield ratios of K_S^0 , Λ and Ξ are studied in events with fixed forward energy measured in the ZN. For this purpose, the High ZN and Low ZN event classes, defined in Sect. 6.5.1, are considered. The strange hadron production per charged particle for all particle species is displayed in Fig. 7.6 in these selections as a function of the charged-particle multiplicity (left) and the ZN energy (right). The Standalone selection is also shown for comparison (black diamond markers). The left panels of Fig. 7.6 show that, in both event classes, the self-normalised yield ratios of Λ and Ξ are found to decrease with increasing midrapidity multiplicity. Therefore, once the leading energy is fixed, the strange baryon enhancement with multiplicity is no longer observed. Instead, the Λ and Ξ yield ratios show a mild anti-correlation with particle production at midrapidity. This decreasing trend could be explained by introducing a simple energy conservation argument: at fixed effective energy, as the charged particle multiplicity increases, the remaining energy available for the production of strange hadrons decreases, therefore, their production is suppressed. Alternatively, the observed anti-correlation could be interpreted considering that events with similar effective energy may be characterised by different topologies in terms of hard scattering processes, associated to the production of jets.

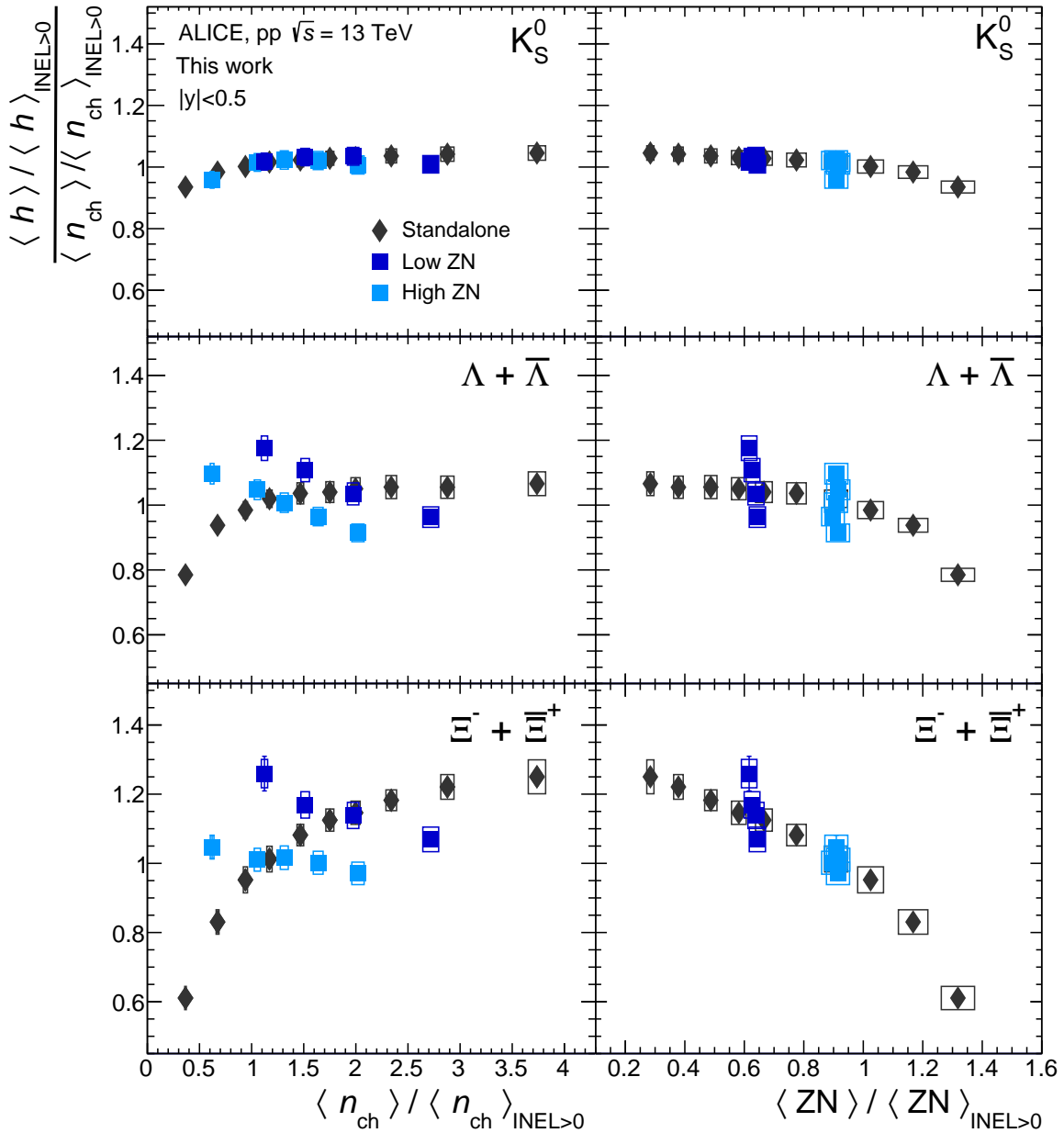


Fig. 7.6 Self-normalised yield ratios of K_S^0 , Λ , and Ξ in pp collisions at $\sqrt{s} = 13$ TeV in the High ZN and Low ZN selection (VZEROM+SPDClusters classes). The ratios are shown as a function of the charged-particle multiplicity (left) and ZN energy (right) self-normalised to the minimum-bias INEL > 0 value. Statistical and total systematic uncertainties are shown by error bars and boxes, respectively.

Indeed, the strange hadron p_T -spectra measured in the High ZN and Low ZN classes, discussed in Sect. 7.1, show that once the energy in the neutron calorimeter is fixed, the transverse momentum distributions become harder as the multiplicity increases. The presence of jets at midrapidity may result in a large local production of charged particles, while no significant increase in strange hadron yields. In fact, recent ALICE results, which were presented in Sect. 2.2.1, show that strange hadron production associated to hard (in-jet) processes shows a mild-to-no increase with multiplicity [62]. These considerations may explain the observed anti-correlation of the self-normalised yield ratios with the particle multiplicity. It is worth noting that the Λ and Ξ self-normalised yield ratios for the High ZN class are found to be systematically lower than for the Low ZN class at similar multiplicity values. This implies that at fixed multiplicity, a larger production of Λ and Ξ baryons per charged particle is observed in events with smaller values of leading energy. This observation will be further discussed in the next section, Sect. 7.2.3. Finally, the K_S^0 meson shows a mild increase with the midrapidity multiplicity once the ZN energy is fixed, which is found to be compatible with the results of the Standalone analysis. These results suggest that the production of strange mesons is less correlated with the leading energy with respect to strange baryons.

7.2.3 Strangeness production at fixed midrapidity multiplicity

To further investigate the dependence of strange hadron production on the leading energy, the self-normalised yield ratios of K_S^0 , Λ and Ξ are studied in events with fixed midrapidity multiplicity and different energy deposited in the ZN. For this purpose, the High Multiplicity and Low Multiplicity event classes, defined in Sect. 6.5.1, are considered. The results obtained with these selections for all particle species are displayed in Fig. 7.7. The left panels show the ratios as a function of the charged-particle multiplicity and the right panels as a function of the ZN energy. The Standalone selection is also displayed for comparison (black diamond markers) for all particle species. In both event classes, the self-normalised yield ratios of Λ and Ξ are found to increase at fixed midrapidity multiplicity with decreasing energy deposited in the neutron calorimeters. For Ξ baryons, the scaling with the ZN energy is observed to be compatible, within uncertainties, among all event classes. In contrast, for Λ baryons, the dependence on the forward energy is not universal to all selections. In fact, the Λ ratios in the High Multiplicity class are found to be systematically lower than the Low Multiplicity class at similar values of ZN energy. This observation implies that, at fixed leading energy, a smaller production of Λ baryons per charged particle is observed in events with larger values of multiplicity, which is in agreement with the results discussed in Sect. 7.2.2. In addition, it is worth noting that, once the multiplicity is fixed, the increase of

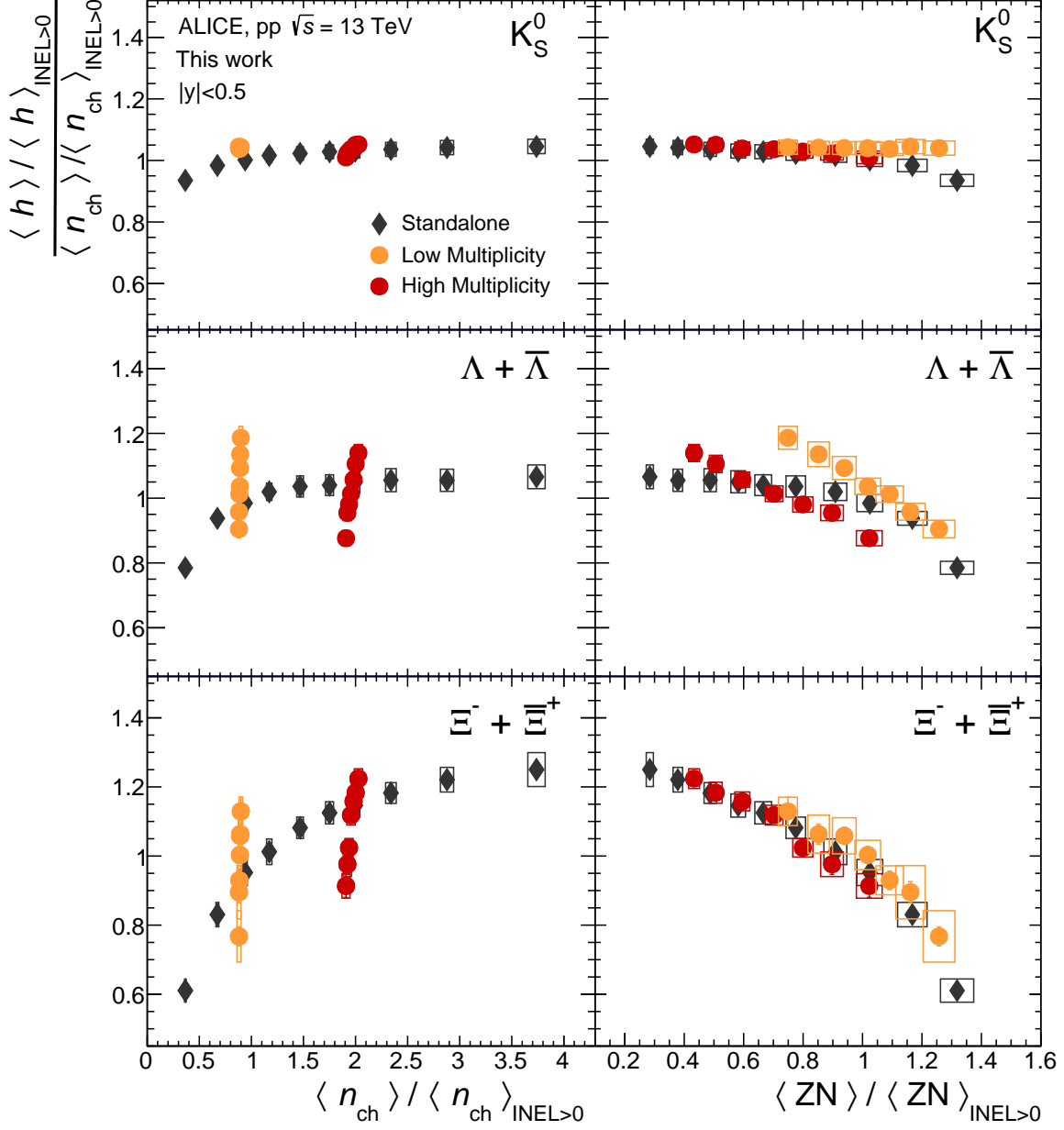


Fig. 7.7 Self-normalised yield ratios of K_S^0 , Λ , and Ξ in pp collisions at $\sqrt{s} = 13$ TeV in the High Multiplicity and Low Multiplicity selection (VZEROM+SPDClusters classes). The ratios are shown as a function of the charged-particle multiplicity (left) and ZN energy (right) self-normalised to the minimum-bias INEL > 0 value. Statistical and total systematic uncertainties are shown by error bars and boxes, respectively.

Λ production per charged particle at decreasing leading energy reaches higher values with respect to the Standalone analysis trend. The K_S^0 meson, on the other hand, shows very mild-to-no dependence on the ZN energy once the midrapidity activity is fixed.

Comparing the results for the different particle species provides interesting inputs on the correlation of strange hadron production with the leading energy once the charged particle multiplicity is fixed. At fixed midrapidity multiplicity, the production of strange baryons per charged particle increases at decreasing leading energy, while the K_S^0 meson shows very mild-to-no dependence on the ZN energy. The larger effect observed for Λ with respect to K_S^0 suggests a stronger correlation of strange baryon production with the leading energy with respect to mesons, given the two hadrons have the same strangeness content. This observation is further supported by comparing the results of Λ to Ξ yields, which show a compatible relative increase at fixed multiplicity. However, it is worth noting that while Ξ points follow a universal trend with the ZN energy, the Λ points show a residual anti-correlation with the multiplicity selection at similar values of leading energy, reminiscent of the observation discussed in the previous section (Sect. 7.2.2).

7.3 Phenomenological models

The results presented in Sect. 7.2.1, 7.2.3 and 7.2.2 are compared to the predictions of the PYTHIA8 phenomenological model with the standard Monash tune and with colour ropes. In particular, the description of the non-perturbative hadronisation process in PYTHIA8 Monash is based on string fragmentation, in particular on the Lund String hadronisation Model [74]. In this model, a massless relativistic string is used to model the QCD field between coloured objects, and when the string breaks, a new $q\bar{q}$ pair forms through quantum mechanical tunnelling. In this context, an additional mechanism can be included so that overlapping strings are allowed to interact with each other, forming colour ropes, which result in a higher effective string tension. Further details on these models were provided in Chapter 2 Sect. 2.2.2. The two event generators are embedded into the ALICE framework, which provides an interface for the generation of the events. The analysis is performed at the generator level, i.e. using only the kinematic information of the generated particles, without simulating their passage through the ALICE detector and reconstructing each event as it is done for the real collisions. The generated sample consists of 2×10^9 pp collision events at $\sqrt{s} = 13$ TeV simulated with the PYTHIA8 Monash generator and 2×10^9 with PYTHIA8 colour ropes. The analysis procedure reproduces the one used for the data, starting from the generator level information. Using a full simulation sample, i.e. including the simulation

of the detector response, we checked that the correlation between the simulated percentile estimators (VZEROM and SPDClusters) and the simulated ZN energy were in agreement with reconstructed ones. In fact, the full simulation sample of 3×10^6 events generated with the PYTHIA8 Monash tune was not sufficient to perform a multi-differential analysis, but allowed us to validate the analysis procedure using generator level information.

7.3.1 Multiplicity and leading energy correlation in the models

The self-normalised ZN signal as a function of the self-normalised charged-particle multiplicity measured at midrapidity is compared in Fig. 7.8 with the two phenomenological models. Both models are able to describe the overall decreasing trend of the Standalone points. A good agreement between data and MC is observed in the low multiplicity and high ZN energy region, while at low leading energies the agreement is worse. In particular, both models are found to underestimate the ZN energy up to 40%. Moreover, the two models can qualitatively describe the behaviour of the data points in the multi-differential classes.

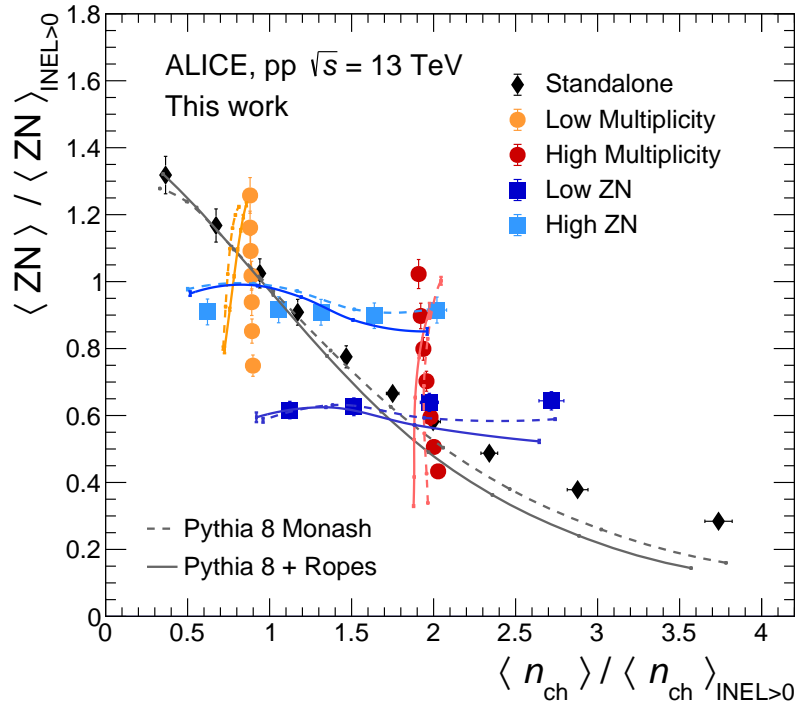


Fig. 7.8 Self-normalised ZN signal as a function of the self-normalised charged-particle multiplicity measured at midrapidity compared with model predictions. The PYTHIA8 Monash tune and with colour ropes are shown as a dashed and full line, respectively.

The High Multiplicity and Low Multiplicity event classes (red and orange lines) select simulated collisions with fixed multiplicity, slightly underestimating the multiplicity values with respect to the data points, and different leading energy in the ZN acceptance, covering an energy range similar to the data. The High ZN and Low ZN event classes (blue and azure lines) select simulated collisions with leading energy values varying within $\pm 10\%$ and different midrapidity multiplicity, covering a range of values similar to the data points. In general, the agreement between data and MC is found to be slightly better for the PYTHIA8 Monash tune. However, one can observe that including colour ropes in the model does not have a big impact on the description of the correlation between the multiplicity and the leading energy.

7.3.2 Correlation with the number of Multi-Parton Interactions (MPI)

According to the PYTHIA8 event generator, a high-activity at midrapidity in pp collisions can originate either from several semi-hard parton-parton interactions occurring within the same pp collision (MPI) or by multi-jet final states (hard processes). Understanding the interplay between these two mechanisms is crucial to shed light on the underlying processes at play in the different event classes reported in Fig. 7.8. Studying the correlation between the effective energy and the number of MPI can provide important insights into the interpretation of the results on strange hadron production reported in Fig. 7.7 and 7.6. In fact, the string hadronisation processes implemented in PYTHIA8 (Lund String Model with and without colour ropes) are strongly influenced by the number of multi-parton interactions in the collision. The correlation between the very forward energy and the number of MPI in PYTHIA8 was first studied in Ref. [88]. Those results showed that the average leading energy decreases with an increasing number of MPI, resembling the observed dependence on the charged-particle multiplicity in Fig. 7.8. It is known, in fact, that the activity at midrapidity increases with the number of multi-parton interactions in the pp collision. In this thesis, we further explore this correlation in Figure 7.9, which shows the average number of MPI as a function of the midrapidity multiplicity (left) and of the leading energy in the ZN acceptance (right) in the different multi-differential classes introduced in this work. These results are obtained with a PYTHIA8 Monash event generator, but consistent results were obtained using the same generator including colour ropes. In the Standalone selection, the average number of MPI is found to increase with the midrapidity multiplicity and decrease with the leading energy, in agreement with the results in Ref. [88]. In the High Multiplicity and Low Multiplicity event classes, the average number of MPI increases at fixed midrapidity multiplicity with decreasing leading energies. This behaviour is reminiscent of the results obtained in Fig. 7.7, where the production of strange baryons per charged particle is found

to increase at fixed multiplicity. On the other hand, once the leading energy is fixed (High ZN and Low ZN classes), the average number of MPI does not change significantly with the midrapidity multiplicity, exhibiting a rather flat trend in the left panel of Fig. 7.9.

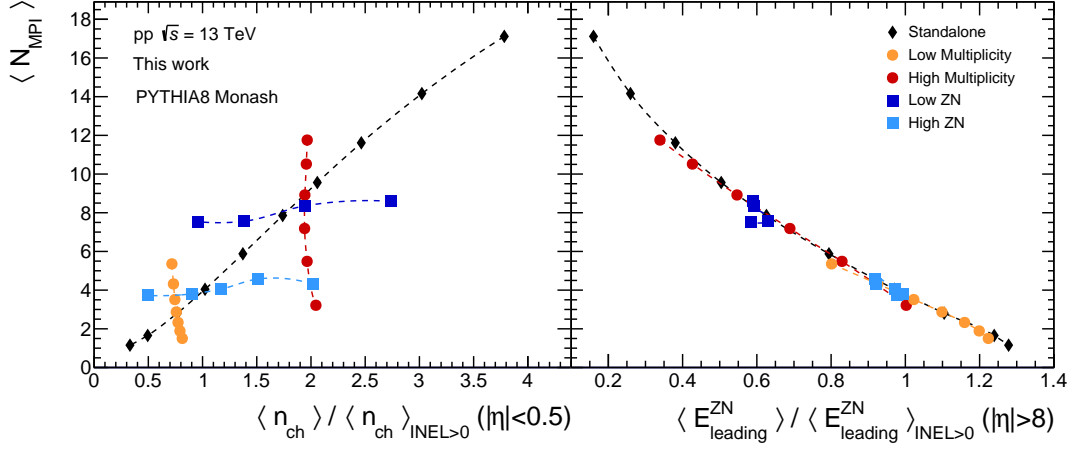


Fig. 7.9 Average number of MPI as a function of the midrapidity multiplicity (left) and of the leading energy in the ZN acceptance (right) in the different multi-differential classes introduced in this work.

It is worth noting that the average number of MPI shows a universal dependence with the leading energy, i.e. common for all differential selections. Indeed, the effective energy available for particle production at midrapidity is expected to be strongly correlated with the number of parton-parton collisions that occurred in the event. These results show that the leading energy is a powerful observable to probe the dependence of particle production on the number of MPI. In addition, it is worth to study the correlation of the p_T of the hard parton scattering process with the local charged particle multiplicity and the leading energy. In particular, the presence of jets in the final state can be studied considering the average transverse momentum of charged pions, which constitute the bulk of particle production in pp collisions. In order to study the “hardness” of the collision events in the different differential classes, Fig. 7.10 shows the average transverse momentum of charged pions as a function of the midrapidity multiplicity (left) and of the leading energy in the ZN acceptance (right). In PYTHIA, hard-jet final states in pp collisions can produce a high activity at midrapidity. In fact, in the Standalone event class, the $\langle p_T^\pi \rangle_{|\eta| < 0.5}$ is found to increase with the midrapidity multiplicity, as expected from previous publications [137–139]. Given the correlation of midrapidity multiplicity with the leading energy, in the right panel of Fig. 7.10 one can also observe that the average transverse momentum is anti-correlated with the forward energy. This suggests that events with a small energy deposit in the ZN calorimeters (high effective energy) are characterised by harder event topologies.

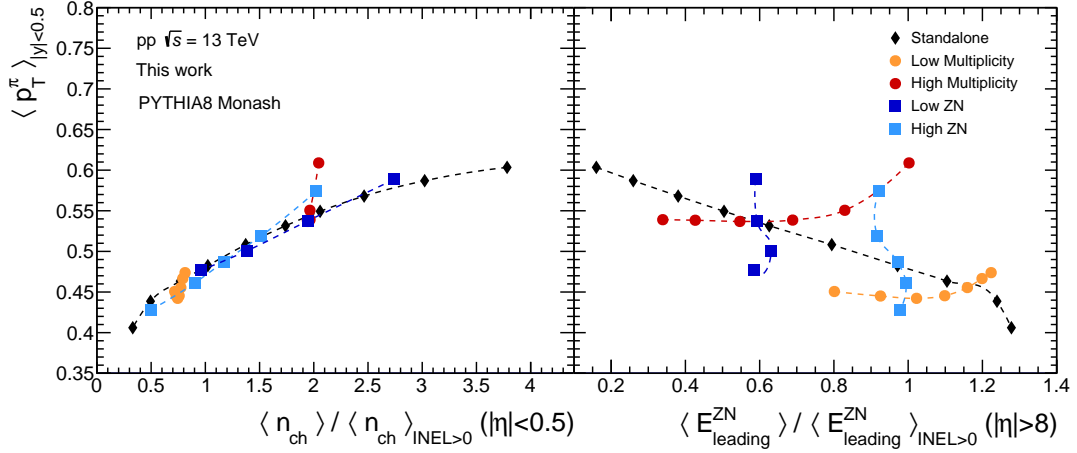


Fig. 7.10 Average transverse momentum of charged pions as a function of the midrapidity multiplicity (left) and of the leading energy in the ZN acceptance (right) in the different multi-differential classes introduced in this work.

Once the leading energy is fixed (High ZN and Low ZN classes), the $\langle p_T^\pi \rangle_{|y|<0.5}$ is found to increase with the midrapidity multiplicity, following a universal dependence for all event classes. On the other hand, at fixed midrapidity multiplicity, in the High Multiplicity and Low Multiplicity event classes, the $\langle p_T^\pi \rangle_{|y|<0.5}$ shows only a very mild increase with increasing leading energies. This rising trend can be explained considering the strong correlation observed between the effective energy and the number of MPI. In fact, in events with fixed midrapidity multiplicity, at increasing leading energies, the number of parton-parton interactions decreases, as shown in the right panel of Fig. 7.9. In order to produce on average the same charged particle multiplicity, events with large leading energies and a small number of MPI may be characterised by hard-jet processes at midrapidity. In contrast, events with a large number of MPI, for low leading energies, may result in isotropic topologies. These considerations could explain the slight mean p_T increase with the leading energy in the right panel of Fig. 7.10. These results suggest that the two event observables considered in this analysis, the midrapidity multiplicity and the leading energy, may be sensitive to very different phases of the pp collision events. Once the activity at midrapidity is fixed, the leading energy proves to be strongly correlated to the number of MPI that occurred in the initial phases of the collision. On the other hand, once the leading energy is fixed, the charged particle multiplicity proves to be sensitive to local effects, such as multi-jet final states at midrapidity. In conclusion, according to the PYTHIA8 event generator, the definition of the multi-differential classes introduced in this work allows to disentangle initial state effects, connected to global properties of the event, such as the effective energy and the number of MPI, from final state effects, related to local phenomena, such as hard-jet fragmentation.

7.3.3 Comparison of the strange self-normalised yield ratios to model predictions

The self-normalised yield ratios of K_S^0 , Λ and Ξ in the Standalone event class are compared in Fig. 7.11 to the PYTHIA8 Monash generator (dashed line) and to PYTHIA8 colour ropes (full line). The Monash tune does not reproduce the strangeness enhancement observed in the data, showing a flat trend as a function of the particle multiplicity and the leading energy for all particle species. Including colour ropes in the model strongly improves the agreement with the data points for the Ξ baryon. However, the model is found to overestimate the production of Λ baryons per charged particle at high multiplicity. In this model, the enhancement observed for the Ξ and Λ baryons is found to be rather compatible, while no enhancement is foreseen for the K_S^0 meson, underestimating the increasing trend observed in the data. These results suggest that the Lund String hadronisation Model [74],

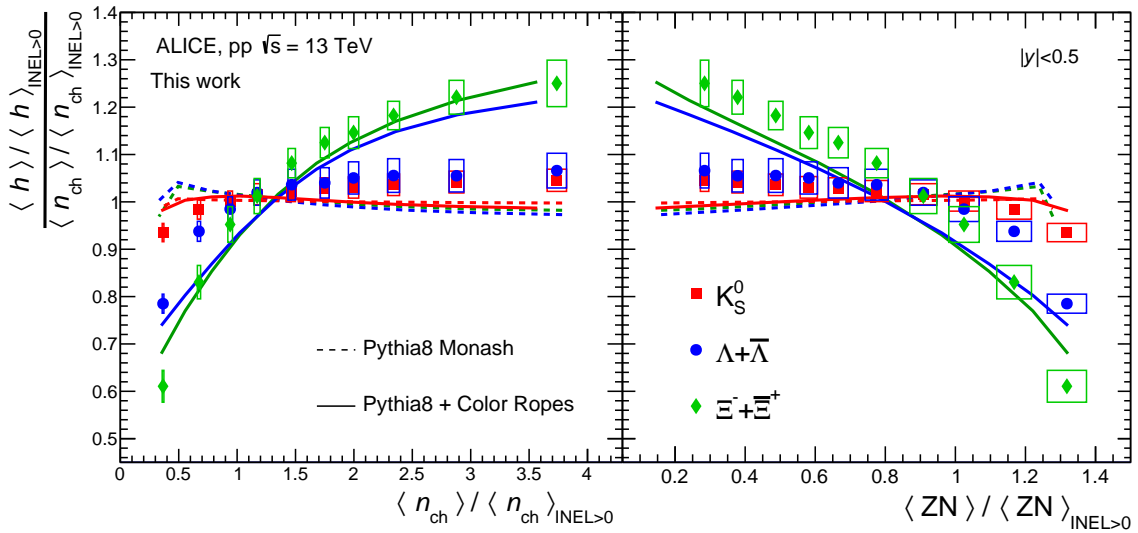


Fig. 7.11 Self-normalised yield ratios of K_S^0 , Λ , and Ξ in pp collisions at $\sqrt{s} = 13$ TeV in the Standalone selection (VZEROM classes). The PYTHIA8 Monash generator and with colour ropes are shown with a dashed and full lines respectively.

implemented in the PYTHIA8 Monash generator, is not able to reproduce the strangeness enhancement with multiplicity observed in pp collisions, as already discussed in previous publications [137–139]. Including the colour ropes mechanism in the hadronisation process results in an enhanced production of strange baryons with respect to strange mesons. This leads to similar Λ and Ξ production per charged particle at high multiplicity and no enhancement for K_S^0 mesons, failing to reproduce the hierarchy with the strangeness content observed in the data. It is important to note that, even if the PYTHIA8 colour ropes model

does an excellent job in reproducing the Ξ enhancement in the Standalone event class, it is known that PYTHIA does not perfectly reproduce the p_T -spectra shape of strange hadrons [141].

Figure 7.12 shows the self-normalised yield ratios for the K_S^0 meson in all the multi-differential event classes introduced in this work, compared to the PYTHIA8 Monash generator (dashed line) and to PYTHIA8 colour ropes (full line). The two models predict a very similar behaviour for the K_S^0 meson, suggesting that including colour ropes in the hadronisation process does not have a big impact on the production of strange mesons. At fixed midrapidity multiplicity (top left and right panels), the two models predict very small dynamics with the leading energy, similarly to what is observed in the data points. At fixed leading energy (bottom left and right panels), both models predict a very mild decrease of the K_S^0 yield per charged particle with the charged multiplicity. This behaviour does not agree with the data points, which show an increase with the multiplicity in the Low ZN and High ZN classes, compatible with the Standalone selections.

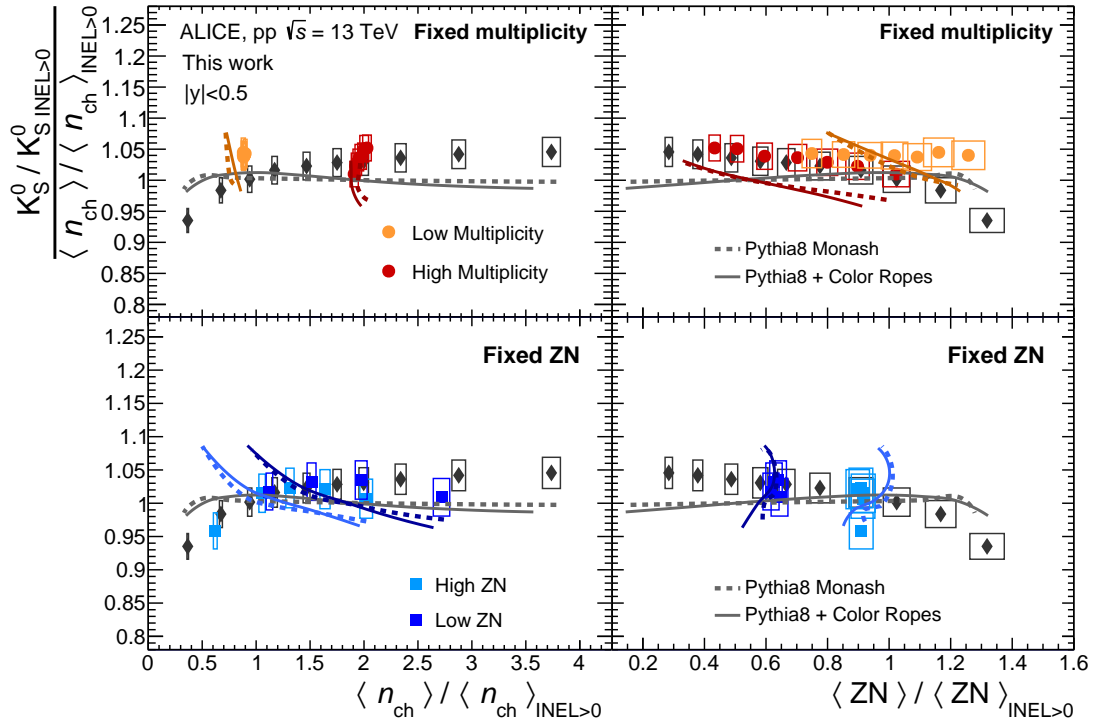


Fig. 7.12 Self-normalised yield ratios of K_S^0 in pp collisions at $\sqrt{s} = 13$ TeV in the Standalone, High Multiplicity, Low Multiplicity, High ZN and Low ZN selections compared to PYTHIA Monash and PYTHIA colour ropes results. The classes at fixed multiplicity are displayed in the top panels, and the classes at fixed leading energy are displayed in the bottom panels. The PYTHIA8 Monash generator without and with colour ropes are shown with dashed and full lines, respectively.

Figure 7.13 shows the model comparison to the self-normalised yield ratios for the Λ baryon in all event classes. At fixed midrapidity multiplicity (top left and right panels), the two models predict an increase of Λ production per charged particle with decreasing leading energy. It is worth noting that the Pythia8 Monash tune does not reproduce the strange hadron enhancement in the Standalone event selections. However, once the multiplicity is fixed, an increase is observed at decreasing leading energy. The data points for the Low ZN and High ZN classes are compared to the model predictions in the bottom left and right panels. At fixed leading energy, the PYTHIA8 Monash generator predicts a decrease of the Λ yield per charged particle with the multiplicity, similarly to what is observed in the data points, but struggling to reproduce the real data values quantitatively. The model including colour ropes, predicts small-to-no dynamics with the multiplicity once the leading energy is fixed.

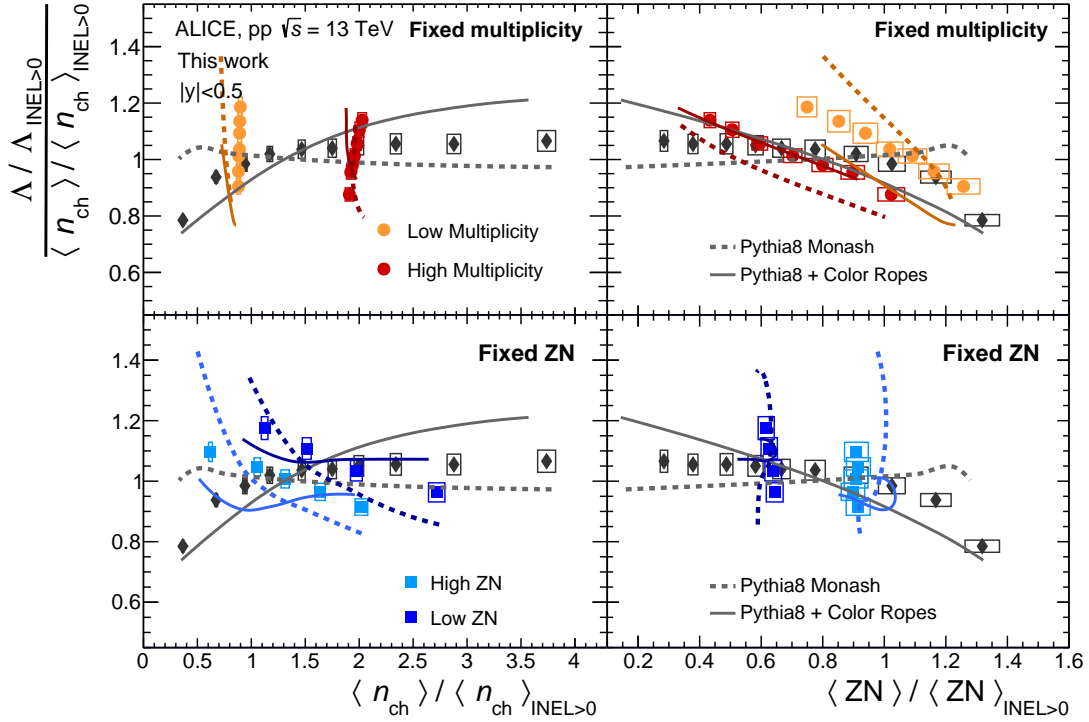


Fig. 7.13 Self-normalised yield ratios of Λ in pp collisions at $\sqrt{s} = 13$ TeV in the Standalone, High Multiplicity, Low Multiplicity, High ZN and Low ZN selections compared to PYTHIA Monash and PYTHIA colour ropes results. The classes at fixed multiplicity are displayed in the top panels, and the classes at fixed leading energy are displayed in the bottom panels. The PYTHIA8 Monash generator without and with colour ropes are shown with dashed and full lines, respectively.

Finally, Fig. 7.14 shows the model comparison to the self-normalised yield ratios for the Ξ baryon in all event classes. In this case, the PYTHIA8 event generator including colour ropes, does an excellent job in reproducing the data points in the Standalone selection, as discussed above. At fixed midrapidity multiplicity (top left and right panels), PYTHIA8 with colour ropes qualitatively describes the increase of Ξ production per charged particle with decreasing leading energy, also reproducing the universal trend observed in the data points with the ZN energy. However, the model struggles to reproduce the real data values quantitatively. The PYTHIA8 Monash event generator fails to reproduce the strangeness enhancement in the Standalone event selection. However, once the multiplicity is fixed, an increase is observed at decreasing leading energy.

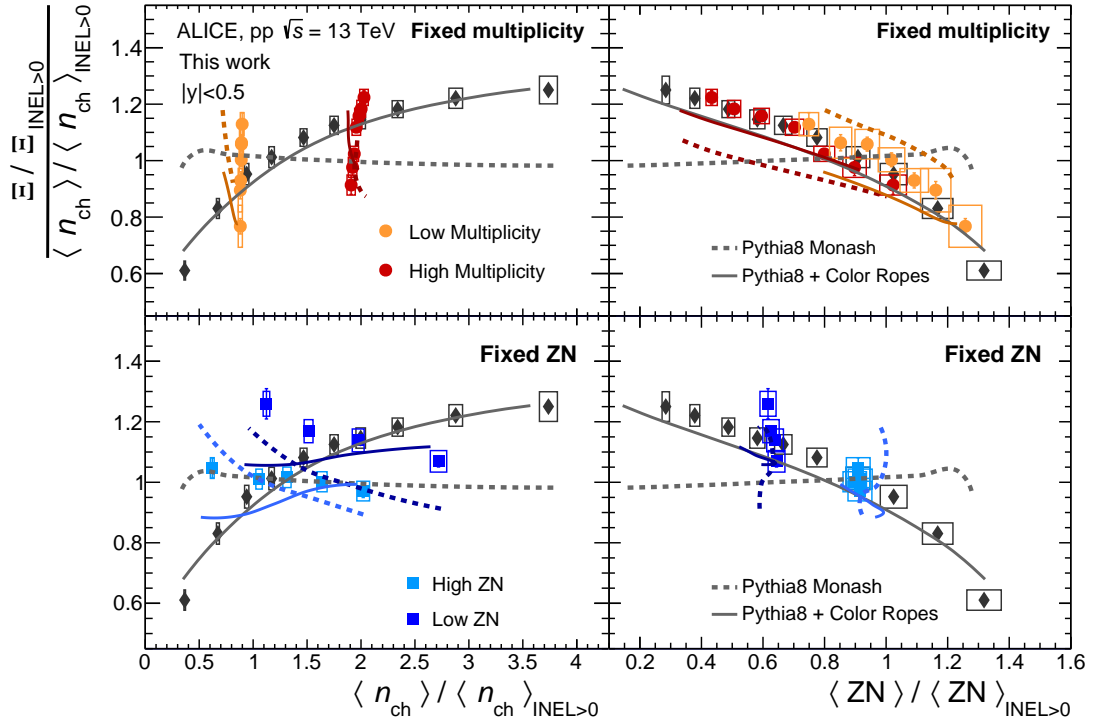


Fig. 7.14 Self-normalised yield ratios of Ξ in pp collisions at $\sqrt{s} = 13$ TeV in the Standalone, High Multiplicity, Low Multiplicity, High ZN and Low ZN selections compared to PYTHIA Monash and PYTHIA colour ropes results. The classes at fixed multiplicity are displayed in the top panels, and the classes at fixed leading energy are displayed in the bottom panels. The PYTHIA8 Monash generator without and with colour ropes are shown with dashed and full lines, respectively.

At fixed forward energy (bottom left and right panels), the PYTHIA8 Monash generator predicts a decrease of the Ξ yield per charged particle with the multiplicity, similarly to what is observed in the data points, but failing to reproduce the real data values quantitatively. The

model including colour ropes, predicts a very small increase with the multiplicity once the leading energy is fixed.

In summary, interesting insights on the dependence of strange hadron production on the multiplicity and the leading energy can be obtained by comparing the data points to the predictions of phenomenological models. The PYTHIA8 Monash tune, is not able to reproduce the strangeness enhancement with multiplicity observed in pp collisions in Standalone selections. The strange baryon yields are significantly increased including the rope formation mechanism in the model, compared to the baseline Monash prediction based on Lund string hadronisation. The magnitude of the enhancement is directly related to the string density before hadronisation sets in, which can produce an increased effective string tension. The number of multiple parton-parton interactions occurred in the pp collision exert a significant influence on the string density, namely as the number of MPI increases, so does the number of colour strings, resulting in a more intricate interplay during hadronisation.

The predictions of the PYTHIA8 generator including colour ropes for the Standalone scaling of Ξ baryon yields per charged particle with the event multiplicity are in agreement with the data. However, the model overestimates the increasing trend for Λ baryons, overshooting the data points at high multiplicity, and generally underestimates the dependence observed for K_S^0 mesons.

Once the activity at midrapidity is fixed, both models predict an increase of strange baryon yields per charged particle with decreasing leading energy. Given the anti-correlation between the forward energy and the number of MPI, this finding indicates that also at fixed midrapidity multiplicity an increase in strange baryon production is expected at increasing number of MPI, regardless of the hadronisation mechanism at play. On the other hand, no dynamics is foreseen in both models for strange K_S^0 mesons.

The largely different predictions for Λ and K_S^0 hadrons obtained including the rope formation mechanism in the model suggest that the interplay between MPI and colour ropes hadronisation may have a stronger impact on the enhancement of (strange) baryons, rather than on the enhancement of strangeness itself. This interpretation is further supported by comparing the results of Λ and Ξ baryons, which show similar predictions in the model, however characterised by a different strangeness content. To predict an enhancement of strange baryon yields in PYTHIA the interplay between the Multiple Parton Interactions (MPI) and the hadronisation mechanism is essential, i.e. with MPI increasing the string

density and the rope formation mechanism effectively enhancing the string tension. However, we are still far from a complete understanding of strange hadron production in pp collisions. While the interaction between MPI and rope hadronization mechanisms provides valuable insights on strange baryon production, discrepancies are observed in the data between different strangeness content baryons, for instance Λ and Ξ .

Chapter 8

First results on Ω production with Run 3 data

In this chapter, we present the first Run 3 results on the production of Ω multi-strange baryons in pp collisions at $\sqrt{s} = 13.6$ TeV and $\sqrt{s} = 900$ GeV, the highest and lowest collision energies reached so far at the LHC. This analysis marks a significant achievement for ALICE. As discussed in Chapter 4, the upgraded ALICE experiment in Run 3, with most of the detectors operating in continuous readout mode and with the new O^2 processing system, deeply changed the data acquisition and processing paradigm with respect to Run 1 and 2. Therefore, the methodology developed in this thesis lays the groundwork for future strangeness analyses in ALICE using Run 3 data. The large statistics of pp collisions at $\sqrt{s} = 13.6$ TeV already collected by ALICE in Run 3, provides the unique opportunity to study the production of Ω multi-strange baryons with higher statistical precision and unprecedented multiplicity differential sensitivity with respect to previous results. Moreover, the sample of pp collisions at $\sqrt{s} = 900$ GeV collected during the so-called Pilot Beam allows to extend the study of strange hadron production to the Ω baryons at this collision energy, reaching the lowest multiplicity region explored at the LHC and complementing the results of lighter hadrons obtained in Run 1. Therefore, the results presented in this chapter constitute the first step towards future studies on strangeness production in pp collisions at the LHC with Run 3 data.

8.1 Analysis details

As discussed in Chapter 4, the ALICE experiment in Run 3 is recording Pb–Pb collisions at an interaction rate of up to 50 kHz, with most of the detectors operating in continuous

readout mode. By design, the experiment can be operated at an interaction rate of up to 4 MHz in pp collisions, giving similar particle rates to Pb–Pb collisions at 50 kHz. However, an interaction rate of 500 kHz is mainly used in Run 3 to limit the pile-up of collisions within the ITS readout time. This nominal interaction rate corresponds to an instantaneous luminosity of about $6 \times 10^{30} \text{ s}^{-1} \text{ cm}^{-2}$, larger by a factor of five with respect to the typical values used for ALICE in Run 1 and 2. With this increase, combined with the new readout capabilities, ALICE is expecting to collect a data sample with an integrated luminosity of $\approx 200 \text{ pb}^{-1}$, corresponding to about 14×10^{12} inelastic collisions, larger by three orders of magnitude with respect to the minimum bias sample collected in Run 2. About 10^{-3} of these collision events will be selected, after calibration and reconstruction, based on particle multiplicity and of rare signal candidates, exploiting specific software triggers [123]. The first collisions delivered by the LHC after the Long Shutdown 2 (LS2) were collected in November 2021 during the so-called Pilot Run of pp collisions at $\sqrt{s} = 900 \text{ GeV}$. A second Pilot Beam of pp collisions at $\sqrt{s} = 900 \text{ GeV}$ was delivered in May and June 2022, followed by the first Run 3 pp runs at $\sqrt{s} = 13.6 \text{ TeV}$ and 500 kHz interaction rate. Since 2022, about 20 pb^{-1} of pp collisions at $\sqrt{s} = 13.6 \text{ TeV}$ were collected with the ALICE experiment. Among these events, a total of 1 pb^{-1} of raw data were stored to tape, corresponding to about $80 \times 10^9 \text{ MB}$ pp collisions at $\sqrt{s} = 13.6 \text{ TeV}$, while the rest was skimmed based on the mentioned software triggers. With this large MB data sample, a study of Ω production versus multiplicity in pp collisions can be extended to reach unprecedented multiplicity differential precisions. Moreover, the sample of pp collisions at $\sqrt{s} = 900 \text{ GeV}$ collected during the Pilot Beam is larger by a factor of 300 with respect to the Run 1 sample at the same collision energy. This increased statistics allows to extend the study of strange hadron production at this collision energy for the first time to the Ω baryons.

8.1.1 Data and Monte Carlo samples

The data used for this analysis was collected in 2022 during the LHC pp runs at $\sqrt{s} = 13.6 \text{ TeV}$ and $\sqrt{s} = 900 \text{ GeV}$. The selected 13.6 TeV dataset contains 13 runs for a total of 80×10^9 events, while the 900 GeV dataset contains 34 runs for a total of 86×10^6 events. Different Monte Carlo (MC) simulations are used to compute the reconstruction efficiency of Ω candidates and to calculate the correction factors applied to the p_T spectra. The MC samples used for this work are simulated with the PYTHIA8 event generator, based on GEANT4 to describe the propagation of particles through the detector material. The simulations are anchored to the real data samples, reproducing the configuration of the detector during the data acquisition. The format of the simulated samples also reproduces the one of the data, being composed of several continuous data streams. The

reconstruction efficiency of Ω baryons is calculated using dedicated MC samples of 2×10^6 events, one for 13.6 TeV and one for 900 GeV, simulated generating pp collisions and saving events with at least one Ω^- or $\bar{\Omega}^+$ particle once every 4 generated minimum-bias collisions. This method is referred to as the “gap-trigger” method and was specifically developed in the context of this work. This is used to increase the statistics of the simulated dataset for the specific physics channel of interest without introducing biases while requiring the presence of specific particles in the sample. In fact, in Run 3, due to the continuous readout, simply injecting strange particles in the event sample may result in ambiguous particle-collision associations during the reconstruction of the simulated events. For normalisation corrections, General Purpose Monte Carlo samples are used, with 2×10^7 events for the sample anchored to 13.6 TeV data, and 1×10^7 to the 900 GeV data.

8.1.2 Event selection and multiplicity percentile

A minimum bias (MB) event trigger is used in this analysis. This requires coincident signals in the FT0A and FT0C detectors to be synchronous with the bunch crossing time defined by the LHC clock. In order to keep the conditions of the detectors as uniform as possible and reject background collisions, the coordinate of the primary vertex along the beam axis is required to be within 10 cm from the nominal interaction point. The final results are reported for the INEL>0 event class, defined by requiring at least one reconstructed primary charged particle within the pseudorapidity interval $|\eta| < 1$. Approximately 90% of the reconstructed events pass these selections. The selected events are then divided into several percentile classes, defined from the distribution of the sum of the signal amplitudes measured with the FT0A and FT0C (FT0M amplitude). The following percentile classes are used:

- 13.6 TeV analysis: [0–1]%, [1–5]%, [5–10]%, [10–15]%, [15–20]%, [20–30]%, [30–40]%, [40–50]%, [50–70]%, [70–100]% ;
- 900 GeV analysis: [0–30]%, [30–100]% .

8.1.3 Signal extraction

The Ω baryon candidates are identified through their decay into charged kaons and Λ baryons, which then decay into a proton and a pion:

$$\Omega^- \rightarrow \Lambda + K^- \rightarrow p + \pi^- + K^- \quad (8.1)$$

$$\bar{\Omega}^+ \rightarrow \bar{\Lambda} + K^+ \rightarrow \bar{p} + \pi^+ + K^+ \quad (8.2)$$

with branching ratio $\text{B.R.} = (67.8 \pm 0.7)\%$ [13]. A set of geometrical and kinematic selections are applied to the reconstructed Ω candidates, as already discussed in Sect. 6.6. The specific kinematic and topological cuts used in this analysis are listed in Table 8.1 for the 13.6 TeV and 900 GeV analysis. These selections were chosen after a dedicated study on the Run 3 data sample in order to optimise the purity of the Ω sample, maximising the signal. The definition of the topological and kinematic variables in Table 8.1 was discussed in Sect. 6.6. Therefore, we refer to that section for a detailed description.

Ω	
Topological selections	Cut 13.6 TeV (900 GeV)
V^0 decay radius	$> 1.2 \text{ cm}$
Cascade decay radius	$> 0.5 \text{ cm}$
DCA meson daughter to primary vertex	$> 0.03 (0.0) \text{ cm}$
DCA baryon daughter to primary vertex	$> 0.03 (0.0) \text{ cm}$
DCA bachelor to primary vertex	$> 0.04 \text{ cm}$
DCA V^0 to PV	$> 0.04 (0.0) \text{ cm}$
DCA between daughter tracks of the V^0	$< 0.4 (1.0) \text{ cm}$
DCA between bachelor and V^0	$< 0.8 (1.0) \text{ cm}$
DCAxy between bachelor and baryon	$> 0.015 \text{ cm}$
cascade $\cos(\text{PA})$	$> 0.99 (0.95)$
$V^0 \cos(\text{PA})$	$> 0.97 (0.99)$
Other selections	Cut 13.6 TeV (900 GeV)
Rapidity Interval $ y $	< 0.5
Daughter Track Pseudorapidity Interval $ \eta $	< 0.8
$ m_{\pi p} - m_{\Lambda} $	$< 7.5(20.0) \text{ MeV}/c^2$
$ m_{\pi \Lambda} - m_{\Xi} $	$> 10 \text{ MeV}/c^2$
Proper Lifetime (mL/p)	$< 3c\tau$
Number of TPC crossed pad rows	> 50
dE/dx measured in the TPC (real data only)	$< 4\sigma (3.5\sigma \text{ for } K^{\pm})$
Primary Selection (MC Only)	Is physical primary
MC Association (MC Only)	PDG code

Table 8.1 Selections applied to identify Ω among the reconstructed cascade candidates.

The $\Omega^- + \bar{\Omega}^+$ signal extraction is performed starting from the invariant mass distributions of their decay daughters in different p_T bins. The distributions for the 13.6 TeV analysis are first fitted with a sum of two Gaussian functions, used to describe the signal shape, and a second degree polynomial used to describe the background. The Gaussian fit to the invariant mass spectrum reflects the resolution of the detector: since it receives contributions from different sources, in this case it is better modelled by two Gaussian functions rather than one. For the 900 GeV analysis, a single Gaussian function is used for the signal, and a first degree polynomial is used to describe the background. The polynomial fit is performed in a region which excludes the signal peak (i.e. $1.63 < m_\Omega < 1.655 \text{ GeV}/c^2$ and $1.689 < m_\Omega < 1.71 \text{ GeV}/c^2$), while the fit with the (two-)Gaussian function is performed in the peak region (i.e. $1.65 < m_\Omega < 1.69 \text{ GeV}/c^2$). The parameters obtained in this first fitting procedure are used as input parameters for the total fit, which is performed in the full invariant mass range: $[1.63 - 1.71] \text{ GeV}/c^2$. In particular, for the 13.6 TeV analysis, the average mean value $\mu = \frac{1}{2}(\mu_1 + \mu_2)$ and the average width $\sigma = \frac{1}{2}(\sigma_1 + \sigma_2)$ of the two Gaussian functions are used. Fig. 8.1 shows the invariant mass distributions of $\Omega^- + \bar{\Omega}^+$ candidates in six p_T intervals for the inclusive minimum bias INEL > 0 sample in pp collisions at $\sqrt{s} = 13.6 \text{ TeV}$. The total fit function is shown in blue, the Gaussian functions in red and magenta, and the background function as a black dotted line. The same distributions for the 900 GeV analysis are shown in Fig. 8.2. The signal (S) is given by the difference between the sum of the bin contents of the invariant mass distribution (S+B) and the integral of the background function (B) in the invariant mass region $\mu - 4.2\sigma < m_\Omega < \mu + 4.2\sigma$. A dedicated study was performed to define the region used for the signal extraction ($\mu \pm 4.2\sigma$), where the raw yield was calculated with increasingly wider regions centred around the mean value μ . The raw yield was found to saturate starting from 4.2σ , allowing the inclusion of more than the 99.5% of the signal obtained with the wider selections. The raw spectra ($1/N_{\text{ev}} d^2N_{\text{raw}}/(dy dp_T)$) of $\Omega^- + \bar{\Omega}^+$ are shown in Fig. 8.3 as a function of p_T for the different FT0M multiplicity classes for the 13.6 TeV (a) and 900 GeV (b) analyses.

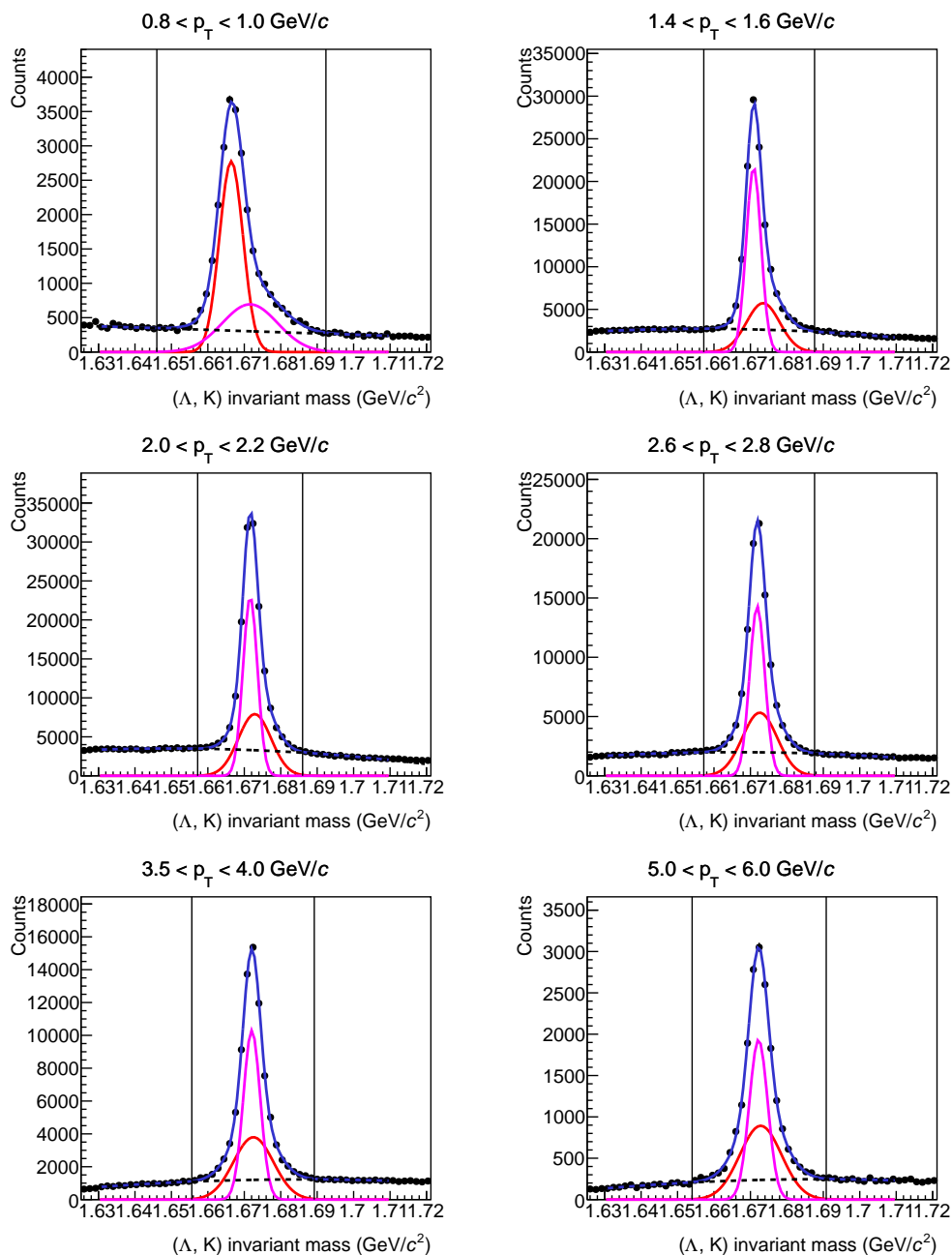


Fig. 8.1 Invariant mass distributions of $\Omega^- + \bar{\Omega}^+$ candidates in pp collisions at 13.6 TeV in the inclusive minimum bias INEL > 0 sample. Different plots refer to different p_T intervals, as indicated in the titles of the plots. The total fit function is shown in blue, the Gaussian functions in red and magenta, and the second degree polynomial as a black dotted line. The two vertical lines represent the outer limits of the invariant mass region from which the signal is extracted.

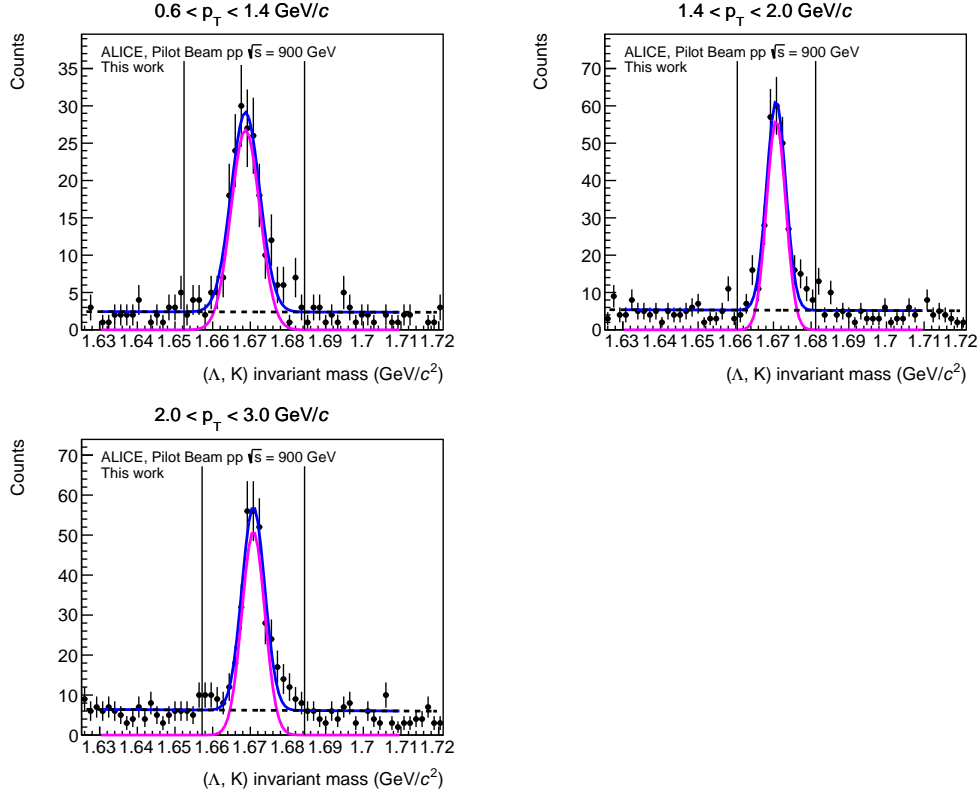


Fig. 8.2 Invariant mass distributions of $\Omega^- + \bar{\Omega}^+$ candidates in pp collisions at 900 GeV in the inclusive minimum bias INEL > 0 sample. Different plots refer to different p_T intervals, as indicated in the titles of the plots. The total fit function is shown in blue, the Gaussian function in magenta, and the first degree polynomial as a black dotted line. The two vertical lines represent the outer limits of the invariant mass region from which the signal is extracted.

8.1.4 Efficiency and normalisation corrections

As discussed in Sect. 6.6.3, the raw spectra must be corrected for the efficiency \times acceptance correction, which reflects the capability of the detector to reconstruct a given particle using a specific decay channel. Moreover, to achieve the correct spectra normalisation, the yields must be corrected for event and signal loss corrections, as discussed in Sect. 6.6.5. To compute the efficiency \times acceptance correction, the analysis is repeated on the simulated samples anchored to the data with the same selections discussed above. Moreover, in the MC analysis Ω candidates are further checked to match a true primary particle of the same type. The correction factor is computed considering the ratio of the reconstructed primary particles and the generated corresponding primaries in each p_T interval, as reported in Eq. 6.3. The efficiency \times acceptance correction used for this analysis is computed using the inclusive INEL > 0 sample and is shown in Fig. 8.4 for the 13.6 TeV and 900 GeV analyses.

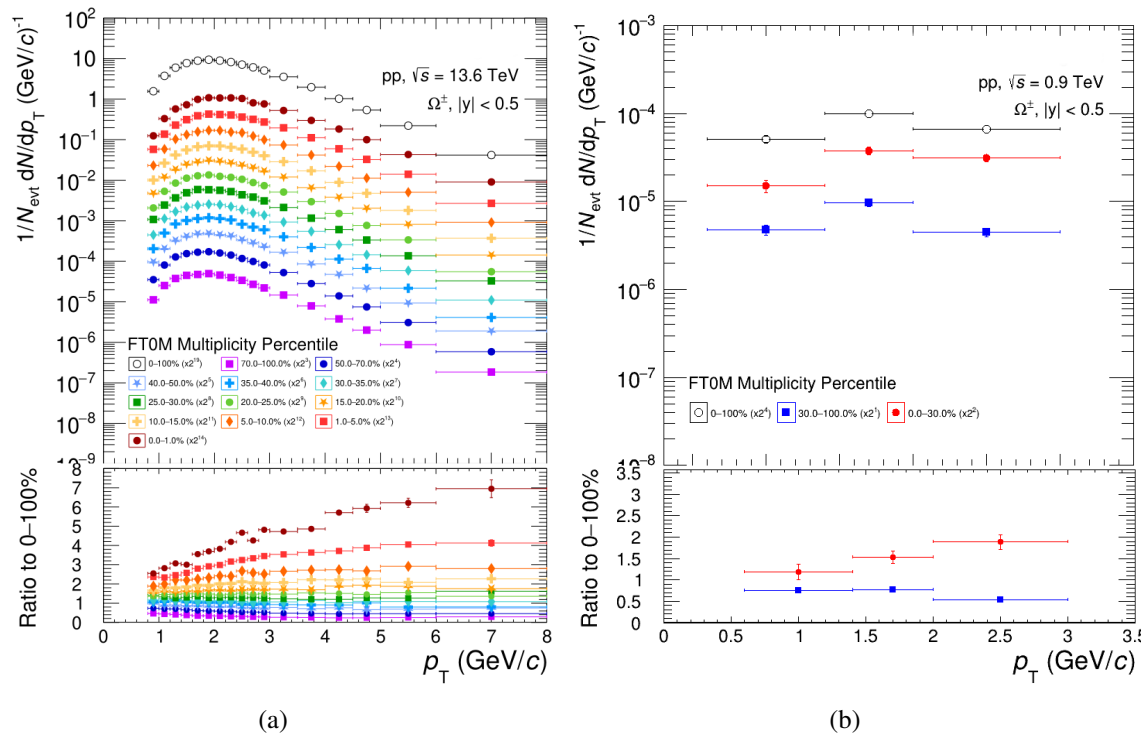


Fig. 8.3 Raw yields of $\Omega^- + \bar{\Omega}^+$ for the 13.6 TeV (a) and 900 GeV (b) analyses. The bottom panels show the ratios between the values obtained in the different FT0M multiplicity classes and those obtained in the inclusive INEL > 0 selection.

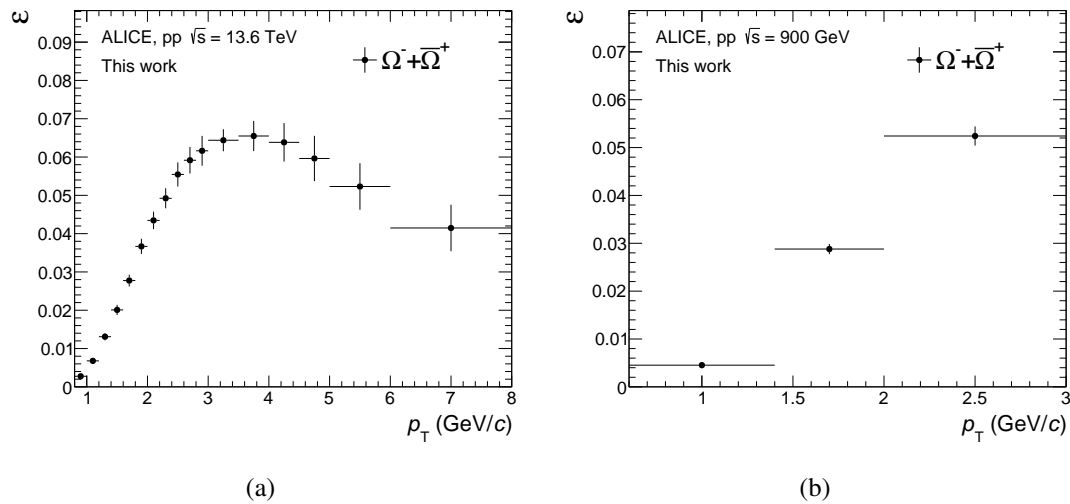


Fig. 8.4 Efficiency \times acceptance of $\Omega^- + \bar{\Omega}^+$ as a function of p_T for the 13.6 TeV (a) and 900 GeV (b) analyses.

As discussed in Sect 6.6.5, the corrected spectra at this stage are normalised to the accepted $\text{INEL} > 0$ events, which pass the conditions described in Sect. 8.1.2. In order to achieve a proper normalisation of the spectra, one needs to apply a set of normalisation corrections, accounting for the fraction of event loss (ϵ_{event}), event splitting (ϵ_{split}), and signal loss (ϵ_{part}) with the event selection:

$$\frac{1}{N_{\text{events}}^{\text{true}}} \cdot \frac{dN_{\text{part}}^{\text{true}}}{dp_T}(p_T) = \frac{1}{N_{\text{events}}^{\text{accepted}}} \cdot \frac{dN_{\text{part}}^{\text{accepted}}}{dp_T}(p_T) \times \frac{\epsilon_{\text{event}}}{\epsilon_{\text{part}}(p_T) \cdot \epsilon_{\text{split}}} \quad (8.3)$$

These factors are determined from the Monte Carlo simulations and are calculated as discussed in Sect 6.6.5, with few differences for Run 3 data. As discussed in the previous chapters, in Run 3, the ALICE detector works in continuous readout. Therefore, the data are not delimited by physics triggers but are composed of several constant data streams. In the reconstruction, collision events are built starting from the time-space information from several detectors. A Primary Vertex is built with reconstructed tracks within specific time and space windows. Of course, this procedure is not immune to ambiguous track-collision association, with tracks that, due to different time resolution, may be wrongly assigned within their time windows, resulting in the possibility that one collision event is reconstructed more than once (“event splitting”). In summary, in Run 3, three normalisation effects must be studied with a Monte Carlo production to correct the final spectra: the fraction of generated events which are not reconstructed (“event loss”), the fraction of generated events which are reconstructed more than once (“event splitting”), and the fraction of generated particles which are not reconstructed (“signal loss”). A sketch of these effects is displayed in Fig. 8.5.

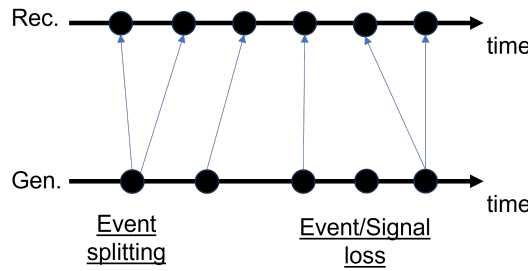


Fig. 8.5 Sketch of the event loss, signal loss and event splitting effects.

The event splitting factor is multiplicity dependent and is defined as:

$$\epsilon_{\text{split}} = \frac{N_{\text{gen}}(\geq 1 \text{ reco})}{N_{\text{reco}}} \quad , \quad (8.4)$$

where $N_{\text{gen}}(\geq 1 \text{ reco})$ is the number of true INEL > 0 events and with a “true” production vertex located within $|z_{\text{vtx}}^{\text{true}}| < 10$ cm and with at least one reconstructed associated event, while N_{reco} is the total number of reconstructed events which pass the event selection. The events loss factor is defined as:

$$\epsilon_{\text{evt}} = \frac{N_{\text{gen}}(\geq 1 \text{ reco})}{N_{\text{gen}}} , \quad (8.5)$$

where N_{gen} is the total number of generated true INEL > 0 events and with a “true” production vertex located within $|z_{\text{vtx}}^{\text{true}}| < 10$ cm.

A combined event correction factor can be calculated as:

$$\text{Event Factor} = \frac{\epsilon_{\text{evt}}}{\epsilon_{\text{split}}} = \frac{N_{\text{reco}}}{N_{\text{gen}}} . \quad (8.6)$$

Finally, the signal loss (ϵ_{part}) correction is calculated as reported in Eq. 6.8, as the ratio between the particle spectra at the generated level after the event selection and the generated particle spectra from true INEL >0 events with $|z_{\text{vtx}}^{\text{true}}| < 10$ cm. The event factor and signal loss factors for both centre-of-mass energies are displayed in Fig. 8.6 and 8.7, respectively.

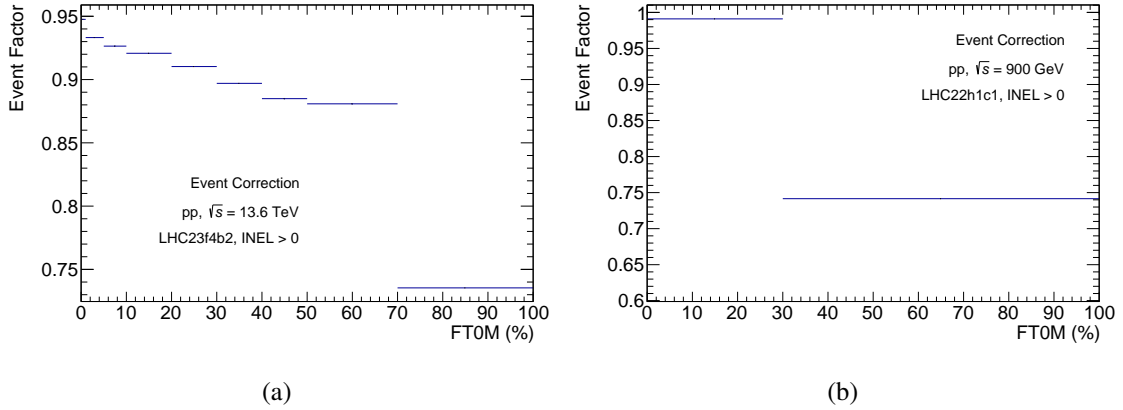


Fig. 8.6 Event factor for the 13.6 TeV (a) and for the 900 GeV (b) analysis.

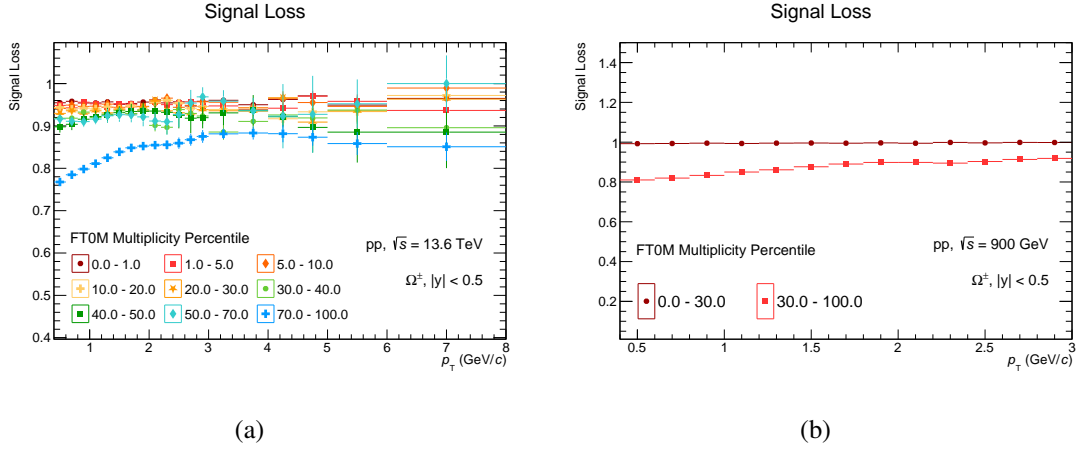


Fig. 8.7 Signal loss correction for the 13.6 TeV (a) and for the 900 GeV (b) analysis.

8.1.5 Systematic uncertainties

To evaluate the systematic uncertainty associated with a given selection, the full analysis is repeated varying that specific variable within defined ranges. The results are then compared to the ones obtained with the standard set of cuts reported in Table 8.1. The strategy used in this analysis is the multi-trial approach, where all selection cuts are generated randomly with a uniform probability distribution within the limits listed in Table 8.2. The number of different sets of cuts (trials) used for this analysis to compute the systematics is 500. The deviation of the efficiency-corrected $\Omega^- + \bar{\Omega}^+$ yields obtained with default selections over the ones obtained with varied cuts in each p_T bin is considered:

$$x = 1 - \frac{Y^{\text{varied}}(p_T)}{Y^{\text{default}}(p_T)} \quad . \quad (8.7)$$

Only variations not compatible with statistical fluctuations are accepted, following the prescription in Ref. [136] with a 1σ threshold. More details on this prescription can be found in Sect. 6.7.1. The distributions of the variable in Eq. 8.7 are fitted with a Gaussian function, and the standard deviation is considered as the systematic contribution. An example of this distribution for three p_T bins for the 13.6 TeV analysis is shown in Fig. 8.8. The multi-trial approach includes topological and track quality selections, TPC energy loss selection, competing cascade decay rejection and the cut on the proper lifetime of the candidate.

In addition, the stability of the signal extraction method was checked by varying the range of the background fit to the invariant mass spectra. In this analysis, the width of the signal extraction was optimised, as described in Sect. 8.1.3, by calculating the raw yields

with increasingly wider regions in terms of $n\sigma$ centred around the mean value μ . This is done until a raw signal saturation is reached, which is found to start at 4.2σ . Therefore, the systematic uncertainty associated to the extraction of the signal is considered to be negligible.

Cut	Value	
	loose	tight
V0 Radius	> 1.1	> 1.3
Cascade Radius	> 0.4	> 0.6
V0 CosPA	> 0.96	> 0.99
Cascade CosPA	> 0.97	> 0.995
DCA Bach To PV (cm)	> 0.03	> 0.1
DCA Pos/Neg To PV (cm)	> 0.02	> 0.1
DCA Cascade Daughters (cm)	< 1.5	< 0.7
DCA V0 Daughters (cm)	< 1.0	< 0.3
DCA V0 To PV (cm)	> 0.03	> 0.1
NTPC crossed rows (dau tracks)	> 40	> 80
V0 Mass Window (GeV/c^2)	± 0.01	± 0.006
TPC dEdx (σ)	< 5	< 3
Proper Lifetime ($c\tau$)	< 7	< 4
Comp. Rejection (GeV/c^2)	> 0.016	> 0.008

Table 8.2 The selections applied to $\Omega^- + \bar{\Omega}^+$ candidates are varied simultaneously within the limits reported in this table.

The contribution from the out-of-bunch pile-up rejection was evaluated by changing the matching scheme of Ω daughters using the ITS and TOF detectors. In particular, at least one decay track of the strange hadron was required to match either the TOF detector or the ITS (> 2 ITS hits) in the full p_T range. The variation between this configuration and no selection (default) is considered as a systematic uncertainty.

The imperfect reproduction of the detector material budget in the MC simulation is also taken into account as a possible source of systematic uncertainty. In particular, this uncertainty was inherited from the Run 2 analysis, which was discussed in Sect. 6.7.1. This

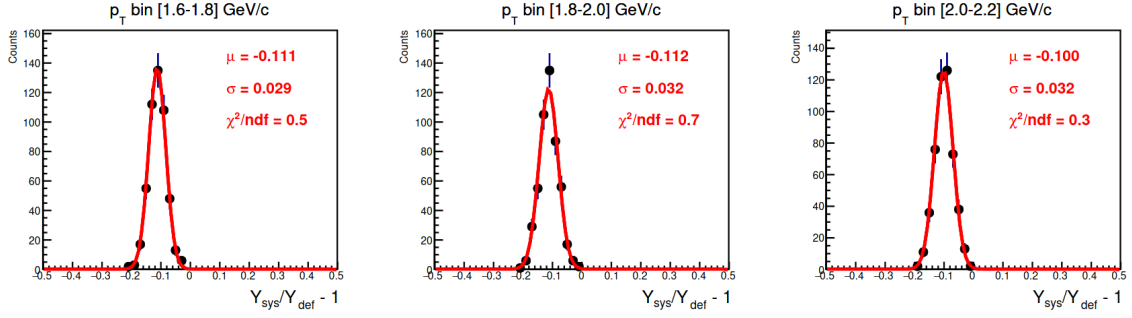


Fig. 8.8 Distributions of the deviation of the efficiency-corrected $\Omega^- + \bar{\Omega}^+$ yields obtained with default selections over the ones obtained with varied cuts in three p_T bins. The distributions, populated with 500 trials, are fitted with a Gaussian function, and the standard deviation is considered as a systematic uncertainty.

is a conservative approach, as the detector material budget in the ALICE2 upgraded detector is expected to be lower than in Run 2, mainly due to the upgrade of the ITS. A dedicated study will be performed in the future to better evaluate this contribution in Run 3.

All systematic uncertainties are calculated using the inclusive INEL > 0 data sample, as these contributions are not expected to depend on the multiplicity selection. An additional contribution is applied to the spectra calculated in multiplicity classes to account for the possible multiplicity dependence of the efficiency \times acceptance correction ($\sim 2\%$). The summary of all contributions to the total systematic uncertainty applied to the p_T spectra is reported in Table 8.3. The systematic uncertainty calculated for the 13.6 TeV data sample was also applied to the 900 GeV analysis.

Systematics on the integrated yields

The p_T integrated yields (dN/dy) of Ω baryons are computed from the data in the measured ranges and using extrapolations to the unmeasured regions. In particular, a Levi-Tsallis parametrisation is used to describe the measured p_T shape and to extrapolate the spectra down to $p_T = 0$. The systematic uncertainty on the extrapolated yield is calculated in order to account for the fraction of uncertainty uncorrelated with p_T . In particular, for the selections listed in Table 8.1, the deviation of integrated yields (dN/dy) obtained with each set of cut variations (trial) with respect to the default selections was computed. In this case, all integrated yields are obtained without extrapolation. The distribution of the 500 deviations obtained is shown in Fig. 8.9. This was fitted using a Gaussian function and the

Hadron p_T (GeV/c)	Ω		
	≈ 1.0	≈ 3.5	≈ 7.0
Multi-trial	6.5	3.4	5.1
Signal extraction	1.1	0.6	0.9
Material Budget	4.0	1.5	1.5
Pileup	negl.	negl.	0.1

Table 8.3 Main sources of systematic uncertainties (expressed in %) of the p_T differential yields, reported for low, intermediate and high p_T . The multi-trial approach includes topological and track quality selections, TPC energy loss selection, competing cascade decay rejection and the cut on the proper lifetime of the candidate. These values are calculated for the INEL>0 data sample, results in other classes are further affected by an uncertainty originating from the multiplicity dependence of the efficiency (2%).

standard deviation is used as p_T uncorrelated contribution. The remaining contributions

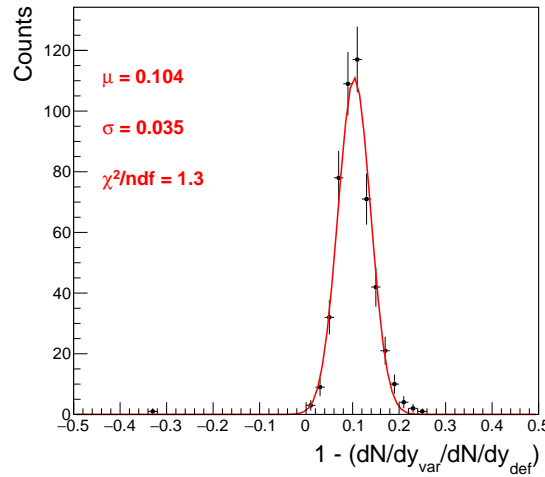


Fig. 8.9 Distribution of relative deviation of integrated yields using multi-trials with respect to the ones using the default selections. The distribution is fitted with a Gaussian function.

are considered correlated across p_T , and the systematic uncertainty on the p_T -integrated yield is obtained by fitting the highest and lowest spectra obtained by shifting all data points within $\pm 1\sigma_{p_T}$, where σ_{p_T} represents the p_T -correlated systematic uncertainty. Finally, an extrapolation uncertainty is applied to the integrated yield, extracted by varying the fit function used for the extrapolation. This is calculated by repeating the fit of the spectra using five alternative functions (Blast-Wave, Boltzmann, Bose-Einstein, m_T -exponential, Fermi-Dirac) instead of the Lévy-Tsallis, considered as a reference. The fit ranges used for the different parametrisations were “tuned” to get the best χ^2/ndf . The relative systematic

uncertainty associated with the choice of the fit function, given by the relative half-difference between the maximum and the minimum extrapolated yield, is shown in Fig. 8.10 for the 13.6 TeV analysis for all multiplicity classes. For the 900 GeV analysis, only the $\text{INEL} > 0$ yield is computed. In this case, the systematic contribution on extrapolation is found to be $\sim 6\%$.

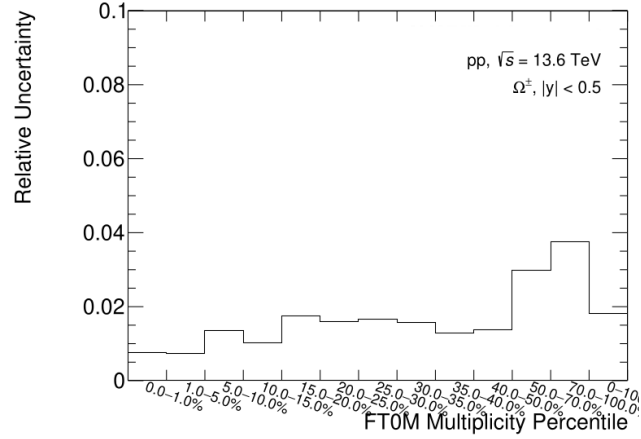


Fig. 8.10 Relative systematic uncertainty associated with the choice of the fit function. The uncertainty is given by the half-difference between the maximum extrapolated yield and the minimum extrapolated yield obtained with different fit functions.

8.2 Results

The $\Omega^- + \bar{\Omega}^+$ fully-corrected p_T -spectra in $|y| < 0.5$ for FT0M percentile classes are displayed in Fig. 8.11 for 13.6 TeV and in Fig. 8.12 for 900 GeV. The bottom panels show the ratio to the minimum bias ($\text{INEL} > 0$) p_T distribution. The p_T spectra for pp collisions at $\sqrt{s} = 13.6$ TeV are normalised to the minimum bias ($\text{INEL} > 0$) integrated yields, showing the p_T spectral shape in the different multiplicity classes. This is done to re-absorb possible inefficiencies in the normalisation of the spectra, which is not trivial with the new ALICE Run 3 data format and is still under study. The p_T spectra for both collision energies become harder as the multiplicity increases. In particular, this is the first multiplicity differential study on Ω production performed in pp collisions at $\sqrt{s} = 900$ GeV, confirming that the hardening of the spectra with increasing multiplicity is already observed at the lowest centre-of-mass energy studied at the LHC. In Fig. 8.13 the $\text{INEL} > 0$ Ω spectra in pp collisions at $\sqrt{s} = 900$ GeV are compared to the predictions of the PYTHIA8 Monash tune, PYTHIA8 color ropes and EPOS-LHC event generators. All models fail to qualitatively describe the data points. The large MB data sample collected to this day by ALICE in Run 3, which was

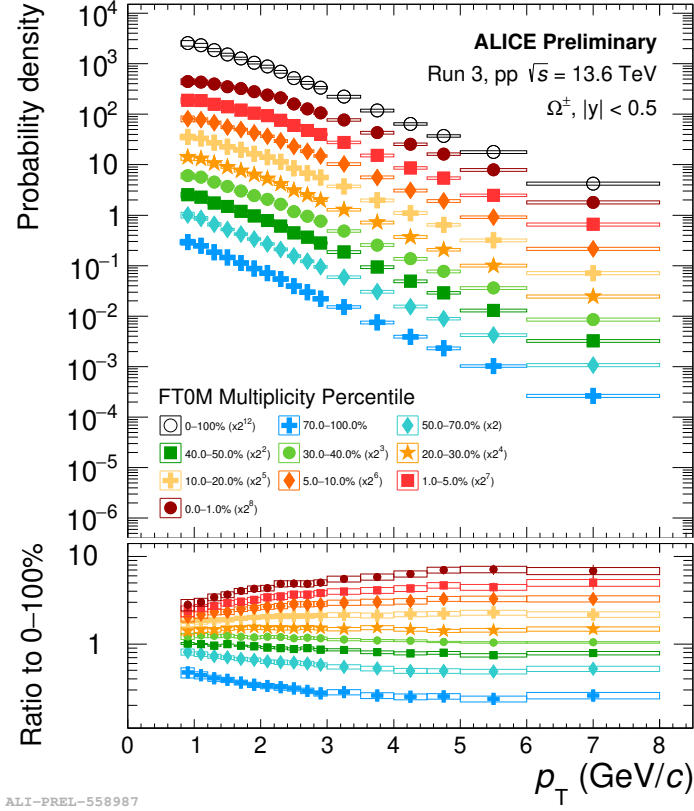


Fig. 8.11 Transverse momentum distribution of Ω in pp collisions at $\sqrt{s} = 13.6$ TeV for multiplicity classes selected using the FT0 detector. Statistical and total systematic uncertainties are shown by error bars and boxes, respectively. In the bottom panels, ratios of multiplicity dependent spectra to INEL > 0 are shown. The spectra are scaled by different factors to improve the visibility.

used in this analysis, already allows us to strongly improve the precision of this measurement with respect to previous ALICE publications [138, 137]. This is shown in Fig. 8.14, where the statistical uncertainty on the Ω INEL > 0 spectrum in pp collisions at $\sqrt{s} = 13.6$ TeV is compared to the one of the previous ALICE measurement at $\sqrt{s} = 13$ TeV [137]. With this analysis we are able to improve the statistical uncertainty up to a factor 20 in the low p_T region and up to a factor 10 in the high p_T region. Moving forward, we expect to further improve the quality of this measurement by optimising the data reconstruction quality, which is still developing in the early stage of Run 3. The p_T -integrated yields of $\Omega^- + \bar{\Omega}^+$ are extracted, as discussed in Sect. 7.2, from the data in the measured ranges and using extrapolations to the unmeasured regions with a Lévy-Tsallis parametrization [140]. The ratio of resulting integrated $\Omega^- + \bar{\Omega}^+$ yields to pions are shown in Fig. 8.15 as a function of the charged pions multiplicity for different FT0M percentile classes at 13.6 TeV and for the inclusive INEL > 0 sample at 900 GeV. For reference, ALICE results on Ω production in pp

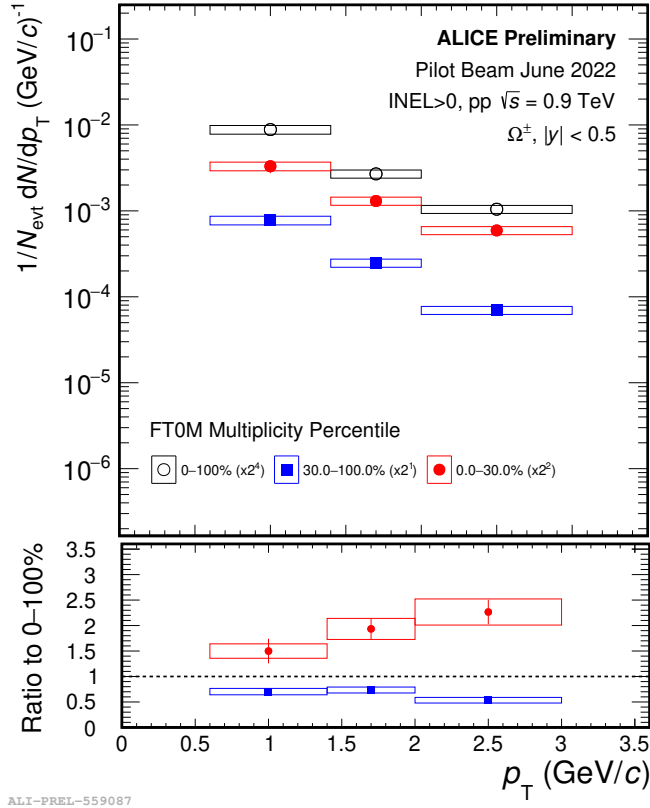
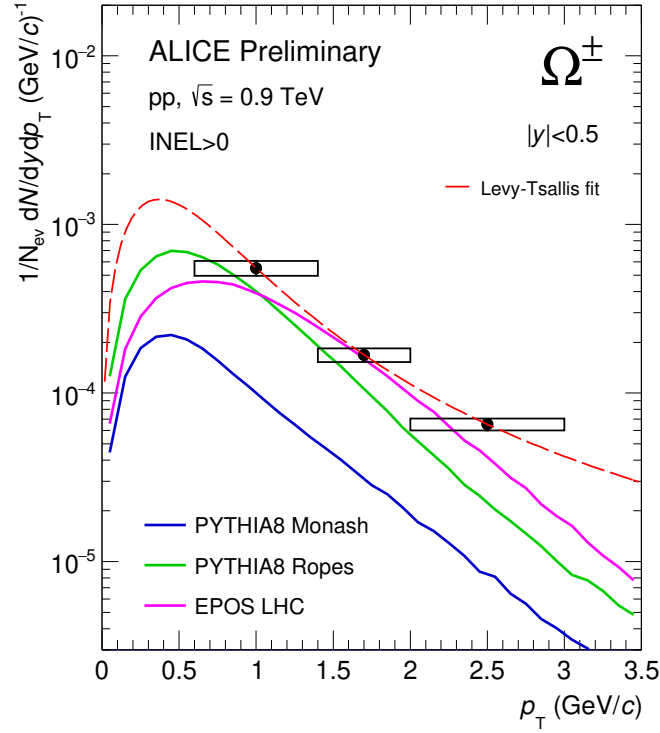


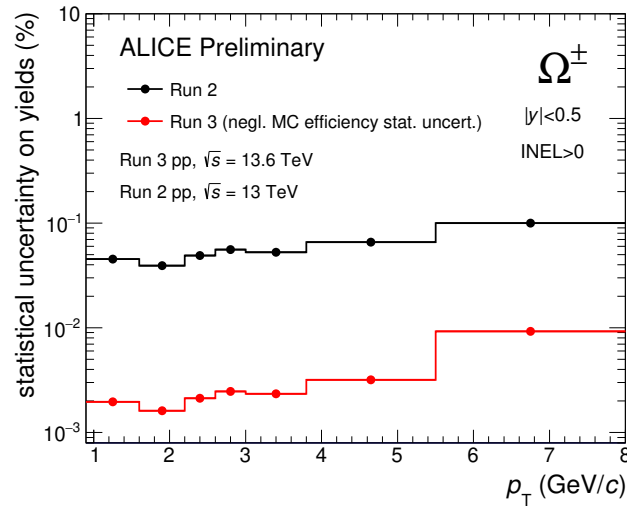
Fig. 8.12 Transverse momentum distribution of Ω in pp collisions at $\sqrt{s} = 900$ GeV for multiplicity classes selected using the FT0 detector. Statistical and total systematic uncertainties are shown by error bars and boxes, respectively. In the bottom panels, ratios of multiplicity dependent spectra to INEL > 0 are shown. The spectra are scaled by different factors to improve the visibility.

collisions at $\sqrt{s} = 7$ TeV [138] are also shown. The increase of Ω/π ratio with multiplicity is studied with an unprecedented differential precision and is found to be in agreement with the previous ALICE measurement at $\sqrt{s} = 7$ TeV. The multiplicity of charged pions is used as a proxy for the charged particle multiplicity, as the pions are the most abundant charged particles produced in pp collisions. Despite the initial expectations, the values reached in the highest multiplicity class do not exceed the ones reached in pp collisions at $\sqrt{s} = 7$ TeV. In fact, the FT0M estimator is found to be less efficient in selecting high multiplicity events than the previous V0M used in Run 1 and 2. Moving forward, we are working on the possibility of combining the FT0M and FV0A detectors in order to improve the efficiency in selecting high multiplicity events in Run 3.



ALI-PREL-558500

Fig. 8.13 Transverse momentum distribution of Ω in pp collisions at $\sqrt{s} = 900$ GeV for the inclusive $\text{INEL} > 0$ compared to the PYTHIA8 Monash tune, PYTHIA8 color ropes and EPOS-LHC event generators.



ALI-PREL-558268

Fig. 8.14 Statistical uncertainty reached in Run 2 [137] compared to the one reached with this analysis in Run 3 neglecting MC efficiency errors.

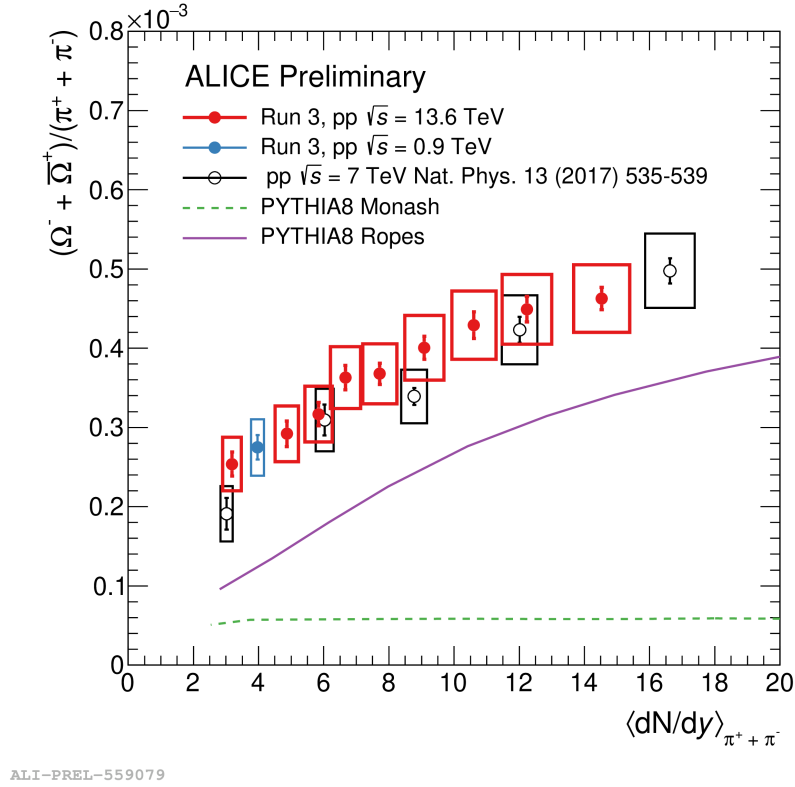


Fig. 8.15 Ω/π ratio measured in Run 3 in pp collisions at $\sqrt{s} = 13.6$ and 0.9 TeV, compared to Run 1 measurement at $\sqrt{s} = 7$ TeV [138].

8.3 Perspectives

The results shown in this chapter were obtained by exploiting the full MB pp data sample collected in 2022 Run 3 runs and stored to tape. As mentioned, the huge amount of data collected in Run 3 cannot be fully stored, therefore, a selection to retain the events of interest is performed on the basis of specific software triggers. In fact, since the Run 3 data taking applies a continuous readout mode, the event selection is not based on hardware triggers, but it is performed at the software level, by applying selections exploiting the full reconstruction of each event. In order to cope with the available computing resources, the fraction of selected events should be of the order of 10^{-3} [123]. Several software triggers (or filters) have been discussed within the ALICE collaboration, with the purpose of studying rare probes with high precision. In the context of this thesis, the following dedicated filters for multi-differential studies on strangeness production were developed:

- Events with at least one Ω^\pm baryon.

Considering an integrated luminosity of about 200 pb^{-1} , a sample of about 1×10^9 Ω^\pm baryons will be selected. Such a sample will allow us to extend the study of Ω

production as a function of the charged particle multiplicity produced at midrapidity up to values of multiplicity of about 100, comparable to those reached in semi-central Pb–Pb collisions. These studies will reveal if the Ω/π ratio in high-multiplicity pp collisions reaches the thermal limit observed in Pb–Pb collisions or if it increases above these values. With respect to the results presented in this thesis, the precision of the measurement will be further improved.

- Events with two or more Ξ^\pm baryons.

This sample of events will be useful to study exotic states decaying into two Ξ baryons as well as to perform correlation studies.

- Events with one high- p_T charged hadron and at least one Ξ^\pm baryon candidate.

These events will be crucial to extend the studies on strange hadron production in- and out-of-jets, which were discussed in Sect. 2.2.1.

- Events with a Ξ^\pm baryon candidate with large decay radius.

This sample will allow us to improve the current knowledge of the Ξ -nucleon elastic cross section, which is based on low-statistics measurements performed at low transverse momentum ($p_T < 1$ GeV/ c) [142]. To measure the elastic cross-section as a function of the scattering angle θ , the momentum of the Ξ must be determined before and after the scattering event occurs. The momentum after the scattering process can be determined from the topological reconstruction of Ξ candidates, whereas the momentum before the scattering event can be directly measured by tracking the Ξ with the innermost ITS layers, thanks to a novel reconstruction technique called strangeness tracking [143].

In the initial stages of this work, Run 2 pp collisions data were analyzed to compute expected rejection factors, i.e. the fraction of events with a specific signal of interest over the total number of events, which served as a baseline for further development. This step was crucial to evaluate if the selectivity of the triggers was within the limits defined to cope with the available computing resources. The software triggers were then implemented in the new analysis framework O^2 , and first validated using Monte Carlo simulations and then using the first pp collisions collected in Run 3. The filters are currently being used in production to skim the pp collision data. The samples of events selected with the software triggers will allow us to push the precision of strangeness production studies in Run 3 to a new level, opening the possibility to perform several multi-differential studies of strangeness production in high energy pp collisions. In this context, an analysis of particle production as a function of the very forward energy detected by the Zero Degree Calorimeters in pp collisions will

be possible in Run 3. To preserve the ZDC from radiation damage, given their crucial role in Pb–Pb collisions, the detectors are switched off during most of the pp data taking. In addition, at large crossing angles of the beams, such as the ones typically delivered by the LHC, neutral particles produced in the interaction point (IP) may hit collimators or other elements of the beam pipe between the IP and the calorimeters, which would cause signal losses in the ZDC. However, during specific data-taking periods, the LHC provides a beam optics with a reduced crossing angle, which allows the ZDC to be operated in pp collisions. In 2022, ALICE collected pp data samples including the ZDC, which can be used for physics analysis.

Conclusions

This thesis presented a comprehensive study of the production of K_S^0 strange mesons, Λ ($\bar{\Lambda}$) strange baryons, and Ξ^- ($\bar{\Xi}^+$) multi-strange baryons in pp collisions at $\sqrt{s} = 13$ TeV measured with the ALICE detector at the LHC. A novel approach is exploited, introducing, for the first time, the concept of effective energy in the study of strangeness production in hadronic collisions at the LHC.

In the past, strangeness enhancement in pp collisions was extensively studied as a function of the charged-particle multiplicity, which reflects the final hadronic state produced in the interaction. This thesis characterised for the first time the production of strange hadrons at midrapidity not only as a function of the local particle multiplicity, but also as a function of the energy detected in ALICE forward calorimeters (ZDC). Strangeness enhancement is observed also at decreasing ZDC energy, which implies a positive correlation of strange hadron production with the effective energy. In addition, this work complements previous studies on strange hadron production at midrapidity, by disentangling the correlation between the local charged-multiplicity and the ZDC energy through a multi-differential technique. In particular, the pp collision sample was analysed by fixing the forward energy measured in the ZDC and varying the charged-particle multiplicity, and viceversa.

Studying the transverse momentum spectra of K_S^0 , $\Lambda + \bar{\Lambda}$, and $\Xi^- + \bar{\Xi}^+$ at fixed leading energy and at fixed multiplicity shows that the average p_T of strange hadrons is strongly correlated with the activity at midrapidity. Namely, fixing the forward energy in the ZN, the spectra become harder as the multiplicity increases, suggesting that for increasing midrapidity activity strangeness production is driven by harder processes. In addition, no major dependence of the spectral shapes on the leading energy is observed at fixed multiplicity.

To illustrate the evolution of strange hadron production, we considered the yield ratios to the charged-particle multiplicity, which is a good proxy for the ratio of strange hadron yields to pions. Once the energy measured at forward rapidity is fixed, the Λ and Ξ enhancement with multiplicity is no longer observed. Instead, the strange baryon yield ratios show an anti-correlation with particle production at midrapidity. This effect is not observed for K_S^0

mesons, which maintain a mild positive correlation with the charged-particle multiplicity, also at fixed leading energy. One way to explain the observed anti-correlation for strange baryons is by introducing a simple energy conservation argument: at fixed effective energy, as the charged particle multiplicity increases, the residual energy available for the creation of strange hadrons decreases, and their production is suppressed. Another possible explanation is that, once the activity at forward rapidity is fixed, as the multiplicity increases strange hadron production is dominated by harder processes at midrapidity. The presence of jets at central rapidity may result in a large local production of charged particles with no significant increase in the strange hadron yields, as was recently observed by the ALICE Collaboration in Ref. [63].

At fixed midrapidity multiplicity, the production of Λ and Ξ strange baryons per charged particle is enhanced at increasing effective energy (anti-correlated with the ZN energy). This effect is not observed for K_S^0 mesons, which display a very mild-to-no dependence on the ZN energy.

The largely different results obtained in this multi-differential analysis for Λ and K_S^0 hadrons suggest that the production of strange baryons and mesons in pp collisions is driven by different mechanisms. The enhancement of strange baryons appears to be strongly correlated with the effective energy, suggesting that the conditions in the initial phase of the collision influence the hadronisation mechanism for strange baryons. On the other hand, the hadronisation of strange quarks into K_S^0 mesons does not seem to be strongly influenced by the initial state of the collision. It is worth noting that the results presented in this thesis also show substantial differences between baryons with different strangeness content (Λ and Ξ). In general, the Ξ yield ratios show a larger enhancement with multiplicity than the Λ yield ratio, as presented in this thesis and in previous ALICE results [137].

Further insights on the relation of strange hadron production with the multiplicity and the effective energy were obtained by comparing the data points to the predictions of phenomenological models. In particular, the simulations considered in this work are based on two tunes of the PYTHIA8 event generator: the Monash tune and the one including the colour rope hadronisation mechanism. In general, the effective energy is observed to be strongly correlated with the number of Multi-Parton Interactions (MPI) in PYTHIA. The comparison with phenomenological models suggests that the interplay between the MPI and the rope hadronisation mechanism is essential to reproduce the observed enhancement of strange baryons. In fact, the PYTHIA8 Monash tune alone, based on the Lund String hadronisation model, fails to reproduce the observed enhancement of strange baryons with multiplicity. No dynamics in terms of multiplicity and effective energy is foreseen in both models for the production of K_S^0 mesons. This implies that the PYTHIA8 generator with

colour rope hadronisation produces an enhancement of (strange) baryons, rather than of strangeness itself.

Future analyses of strange hadron production will benefit from the large Run 3 statistics and the specific software triggers developed in the context of this work. To further push our understanding of the origin of strangeness enhancement in pp collisions, Run 3 will allow to improve the precision of the current measurements in the strange sector and open new possibilities for multi-differential studies. In this context, this thesis presented the first Run 3 results on the production of Ω multi-strange baryons in pp collisions at $\sqrt{s} = 13.6$ TeV and $\sqrt{s} = 900$ GeV, the highest and lowest collision energies reached so far at the LHC. The Ω/π enhancement with multiplicity in pp collisions at $\sqrt{s} = 13.6$ TeV is found to be consistent with previous results obtained by ALICE in Run 1 and 2, reaching a higher statistical precision (by a factor 10–20) and an unprecedented multiplicity differential sensitivity. Moreover, the first measurement of Ω production in pp collisions at $\sqrt{s} = 900$ GeV is presented, complementing the results of lighter strange hadrons obtained in Run 1 at the same collision energy. The Ω/π ratio at $\sqrt{s} = 900$ GeV is found to be consistent with the results obtained at higher energies, showing that universal evolution of strangeness enhancement with multiplicity across collision systems and energies is already at play at lowest centre-of-mass energy reached at the LHC.

References

- [1] M. Basile et al. The energy dependence of charged particle multiplicity in pp interactions. *Phys. Lett. B*, 95:311, 1980.
- [2] M. Basile et al. Evidence of the same multiparticle production mechanism in p-p collisions as in e^+e^- annihilation. *Phys. Lett. B*, 92:367, 1980.
- [3] M. Basile et al. The “leading”-particle effect in hadron physics. *Nuovo Cim.*, 66A(2), 1981.
- [4] M. Basile et al. The method of removing the leading protons in the study of high-energy pp reactions, compared with the standard analysis. *Nuovo Cim. Lett.*, 31:273, 1981.
- [5] M. Basile et al. Charged-particle multiplicities in pp interactions and comparison with e^+e^- data. *Nuovo Cim. A*, 65:414, 1981.
- [6] M. Basile et al. The transverse-momentum distributions of particles produced in pp reactions and comparison with e^+e^- . *Lett. Nuovo Cimento*, 32:321, 1981.
- [7] M. Basile et al. The inclusive momentum distribution in (pp) reactions, compared with low-energy (e^+e^-) data in the range $(\sqrt{s})_{e^+e^-} = (3.0 \div 7.8) GeV$. *Nuovo Cim. A*, 67:244, 1982.
- [8] M. Basile et al. The leading effect explains the forward-backward multiplicity correlations in hadronic interactions. *Lett. Nuovo Cim.*, 38:359, 1983.
- [9] M. Basile et al. Scaling in the charged-particle multiplicity distributions at the ISR and comparison with (e^+e^-) data. *Nuovo Cim. A*, 79:1, 1984.
- [10] F. Ercolessi. New insights into strangeness production in pp collisions with ALICE at the LHC. *PoS, ICHEP2022*:458, 2022.
- [11] F. Ercolessi. Investigating the origin of strangeness enhancement in small systems through multi-differential analyses. *EPJ Web Conf.*, 259:11006, 2022.
- [12] G. Dissertori et al. Quantum Chromodynamics: High Energy Experiments and Theory. *Oxford University Press*, 2003.
- [13] Particle Data Group et al. Review of Particle Physics. *Progress of Theoretical and Experimental Physics*, 2022(8):083C01, 2022.

- [14] C. Ratti and R. Bellwied. *The Deconfinement Transition of QCD: Theory Meets Experiment*, volume 981 of *Lecture Notes in Physics*. 6 2021.
- [15] M. Baldo et al. Neutron stars and the transition to color superconducting quark matter. *Phys. Lett. B* 562, pages 153–160, 2003.
- [16] J. Letessier and J. Rafelski. *Hadrons and Quark-Gluon Plasma*. Cambridge Monographs on Particle Physics, Nuclear Physics and Cosmology. Cambridge University Press, 2023.
- [17] G. Odyniec. The RHIC Beam Energy Scan program in STAR and what’s next. *Journal of Physics: Conference Series*, 455(1):012037, 2013.
- [18] R. K. Ellis, W. J. Stirling, and B. R. Webber. *Fundamentals of QCD*, pages 1–21. Cambridge Monographs on Particle Physics, Nuclear Physics and Cosmology. Cambridge University Press, 1996.
- [19] U. Heinz and M. Jacob. Evidence for a New State of Matter: An Assessment of the Results from the CERN Lead Beam Programme, 2000, nucl-th/0002042.
- [20] C. A. Ogilvie. Review of nuclear reactions at the AGS. *Nuclear Physics A*, 698(1-4):3–12, 2002.
- [21] M. Harrison, T. Ludlam, and S. Ozaki. RHIC project overview. *Nuclear Instruments and Methods in Physics Research Section A: Accelerators, Spectrometers, Detectors and Associated Equipment*, 499(2):235–244, 2003.
- [22] ALICE collaboration. The ALICE experiment - A journey through QCD. 2022, arXiv:2211.04384.
- [23] S. J. Sanders M. L. Miller, K. Reygers and P. Steinberg. Glauber modeling in high energy nuclear collisions. *Ann. Rev. Nucl. Part. Sci.*, 57:205–243, 2007, arXiv:nucl-ex/0701025.
- [24] E. Abbas et al. Performance of the ALICE VZERO system. *JINST*, 8:10016, 2013, arXiv:1306.3130.
- [25] B. B. Abelev et al. Performance of the ALICE Experiment at the CERN LHC. *Int. J. Mod. Phys.*, A29:1430044, 2014, arXiv:1402.4476.
- [26] C. Gale, S. Jeon, and B. Schenke. Hydrodynamic Modeling of Heavy-Ion Collisions. *International Journal of Modern Physics A*, 28(11):1340011, 2013.
- [27] The ATLAS Collaboration. Measurement of the centrality dependence of the charged particle pseudorapidity distribution in lead–lead collisions at $\sqrt{s_{NN}} = 2.76$ with the ATLAS detector. *Physics Letters B*, 710(3):363–382, 2012.
- [28] The CMS collaboration, S. Chatrchyan, V. Khachatryan, et al. Dependence on pseudorapidity and on centrality of charged hadron production in pbbp collisions at $\sqrt{s_{NN}} = 2.76$ tev. *Journal of High Energy Physics*, 2011:141, 2011.
- [29] NA50 Collaboration, M. Abreu, et al. Scaling of charged particle multiplicity in pb pb collisions at sps energies. *Physics Letters B*, 530:43–55, 2002.

- [30] I. G. Bearden and BRAHMS Collaboration. Measurement of transverse momentum spectra of Au+Au collisions at $\sqrt{s_{\text{NN}}} = 130$ gev. *Physical Review Letters*, 88:202301, 2002.
- [31] STAR Collaboration, B. Abelev, et al. Systematic measurements of identified particle spectra in pp, d+au and au+au collisions from star. *Physical Review C*, 79:034909, 2009, arXiv:0808.2041 [nucl-ex].
- [32] PHENIX Collaboration, K. Adcox, et al. Centrality dependence of charged particle multiplicity in Au - Au collisions at $\sqrt{s_{\text{NN}}} = 130$ GeV. *Physical Review Letters*, 86:3500–3505, 2001, arXiv:nucl-ex/0012008.
- [33] PHOBOS Collaboration, B. Alver, et al. Phobos results on charged particle multiplicity and pseudorapidity distributions in Au+Au, Cu+Cu, d+Au, and p+p collisions at ultra-relativistic energies. *Physical Review C*, 83:024913, 2011, arXiv:1011.1940 [nucl-ex].
- [34] F. Becattin. An Introduction to the Statistical Hadronization Model. *Contribution to: International School on Quark-Gluon Plasma and Heavy Ion Collisions: past, present, future*, 2009.
- [35] S. Wheaton, J. Cleymans, and M. Hauer. THERMUS. arXiv:1108.4588 [hep-ph].
- [36] J. Cleymans, I. Kraus, H. Oeschler, K. Redlich, and S. Wheaton. Statistical model predictions for particle ratios at $\sqrt{s_{\text{NN}}} = 5.5$ TeV. *Physical Review C*, 74:034903, 2006, arXiv:hep-ph/0604237.
- [37] G. Torrieri, S. Steinke, W. Broniowski, W. Florkowski, J. Letessier, and J. Rafelski. SHARE: Statistical hadronization with resonances. *Computer Physics Communications*, 167:229–251, 2005, arXiv:nucl-th/0404083.
- [38] G. Torrieri, S. Jeon, J. Letessier, and J. Rafelski. SHAREv2: Fluctuations and a comprehensive treatment of decay feed-down. *Computer Physics Communications*, 175:635–649, 2006, arXiv:nucl-th/0603026.
- [39] M. Petran, J. Letessier, J. Rafelski, and G. Torrieri. SHARE with CHARM. *Computer Physics Communications*, 185:2056–2079, 2014, arXiv:1310.5108 [hep-ph].
- [40] V. Vovchenko, M. I. Gorenstein, and H. Stoecker. Finite resonance widths influence the thermal-model description of hadron yields. *Physical Review C*, 98:034906, 2018, arXiv:1807.02079 [nucl-th].
- [41] V. Vovchenko and H. Stoecker. Thermal-FIST: A package for heavy-ion collisions and hadronic equation of state. *Computer Physics Communications*, 244:295–310, 2019, arXiv:1901.05249 [nucl-th].
- [42] A. Andronic, P. Braun-Munzinger, B. Friman, P. M. Lo, K. Redlich, and J. Stachel. The thermal proton yield anomaly in Pb-Pb collisions at the LHC and its resolution. *Physics Letters B*, 792:304–309, 2019, arXiv:1808.03102 [hep-ph].
- [43] D. H. Rischke, M. I. Gorenstein, H. Stoecker, and W. Greiner. Excluded volume effect for the nuclear matter equation of state. *Zeitschrift für Physik C*, 51:485–490, 1991.

- [44] ALICE Collaboration. Anisotropic flow of identified particles in Pb-Pb collisions at $\sqrt{s_{\text{NN}}} = 5.02$ TeV. *Journal of High Energy Physics*, 2018(9), 2018.
- [45] R. Fries, B. Müller, C. Nonaka, and S. A. Bass. Hadronization in heavy ion collisions: Recombination and fragmentation of partons. *Phys. Rev. Lett.*, 90:202303, 2003, arXiv:nucl-th/0301087.
- [46] ALICE Collaboration. Multiplicity dependence of light-flavor hadron production in pp collisions at $\sqrt{s} = 7$ TeV. *Phys. Rev. C*, 99:024906, Feb 2019.
- [47] The CMS collaboration. Multiplicity and transverse momentum dependence of two- and four-particle correlations in ppb and pbpb collisions. *Physics Letters B*, 724(4):213–240, 2013.
- [48] The CMS collaboration. Observation of long-range, near-side angular correlations in proton-proton collisions at the LHC. *J. High Energ. Phys.*, 724(91), 2010.
- [49] ALICE Collaboration. Investigations of Anisotropic Flow Using Multiparticle Azimuthal Correlations in pp , p -Pb, Xe-Xe, and Pb-Pb Collisions at the LHC. *Phys. Rev. Lett.*, 123:142301, Oct 2019.
- [50] P. Koch, B. Müller, and J. Rafelski. Strangeness in relativistic heavy ion collisions. *Physics Reports*, 142(4):167–262, 1986.
- [51] NA35 Collaboration. Neutral strange particle production in sulphur-sulphur and proton-sulphur collisions at 200 GeV/nucleon. *Zeitschrift für Physik C Particles and Fields* 48, pages 191–200, 1990.
- [52] E. et al. Andersen. Strangeness enhancement at mid-rapidity in Pb–Pb collisions at 158 A GeV/c. *Physics Letters B*, 449:401–406, 1999.
- [53] F. Antinori et al. Enhancement of hyperon production at central rapidity in 158 A GeV/c Pb-Pb collisions. *J. Phys. G*, 32:427–442, 2006, nucl-ex/0601021.
- [54] F. Antinori et al. Strangeness enhancements at central rapidity in 40 A GeV/c Pb-Pb collisions. *Journal of Physics G: Nuclear and Particle Physics*, 37:045105, 2010, arXiv:1001.1884.
- [55] C. Alt et al. Ω^- and $\bar{\Omega}^+$ production in central Pb + Pb collisions at 40 and 158A GeV. *Phys. Rev. Lett.*, 94:192301, 2005, nucl-ex/0409004.
- [56] C. Alt et al. Energy dependence of Λ and Ξ production in central Pb + Pb collisions at 20A, 30A, 40A, 80A, and 158A GeV measured at the CERN Super Proton Synchrotron. *Phys. Rev. C*, 78:034918, 2008, arXiv:0804.3770.
- [57] T. Anticic et al. System-size dependence of Λ and Ξ production in nucleus-nucleus collisions at 40A and 158A GeV measured at the CERN Super Proton Synchrotron. *Phys. Rev. C*, 80:034906, 2009, arXiv:0906.0469.
- [58] J. Adams, C. Adler, and et al. Multistrange baryon production in Au-Au collisions at $\sqrt{s_{\text{NN}}} = 130$ GeV. *Phys. Rev. Lett.*, 92:182301, 2004, nucl-ex/0307024.

- [59] J. Adams, C. Adler, and et al. Identified particle distributions in pp and Au+Au collisions at $\sqrt{s_{\text{NN}}} = 200$ GeV. *Phys. Rev. Lett.*, 92:112301, 2004, nucl-ex/0310004.
- [60] B. I. Abelev, M. Aggarwal, and et al. Enhanced strange baryon production in Au+Au collisions compared to p + p at $\sqrt{s_{\text{NN}}} = 200$ GeV. *Phys. Rev. C*, 77:044908, 2008, 0705.2511.
- [61] B. B. Abelev and et al. Multi-strange baryon production at mid-rapidity in Pb-Pb collisions at $\sqrt{s_{\text{NN}}} = 2.76$ TeV. *Phys. Lett. B*, 728:216–227, 2014, 1307.5543. [Erratum: *Phys. Lett. B* 734, 409 (2014)].
- [62] The ALICE Collaboration. Production of Λ and K_S^0 in jets in p-Pb collisions at $\sqrt{s_{\text{NN}}} = 5.02$ TeV and pp collisions at $\sqrt{s} = 7$ TeV. *Physics Letters B*, 827:136984, 2022.
- [63] C. De Martin. Understanding the production mechanisms of particles with strangeness in pp collisions with the ALICE experiment at the LHC, 2022. PhD Thesis. Presented 24 Feb 2023.
- [64] R. Singh, R. Bala, and S.S. Sambyal. Centrality and transverse sphericity dependent study of charged-particle production in Xe-Xe collisions at $\sqrt{s_{\text{NN}}} = 5.44$ TeV using PYTHIA8 Angantyr and AMPT models. *Ukrainian Journal of Physics*, 67(11):765, jan 2023.
- [65] T. Sjöstrand and et al. An Introduction to PYTHIA 8.2. *Computational Physics Communications*, 191:159–177, 2015, arXiv:1410.3012.
- [66] M. Bahr and et al. Herwig++ Physics and Manual. *European Physical Journal C*, 58:639–707, 2008, arXiv:0803.0883.
- [67] J. Bellm and et al. Herwig 7.0/Herwig++ 3.0 release note. *European Physical Journal C*, 76:196, 2016, arXiv:1512.01178.
- [68] T. Pierog, I. Karpenko, J. M. Katzy, E. Yatsenko, and K. Werner. EPOS LHC: Test of collective hadronization with data measured at the CERN Large Hadron Collider. *Physical Review C*, 92:034906, 2015, arXiv:1306.0121.
- [69] Y. Kanakubo, Y. Tachibana, and T. Hirano. Unified description of hadron yield ratios from dynamical core-corona initialization. *Physical Review C*, 101:024912, 2020, arXiv:1910.10556.
- [70] Y. Kanakubo, Y. Tachibana, and T. Hirano. Interplay between core and corona components in high-energy nuclear collisions. *Physical Review C*, 105:024905, 2022, arXiv:2108.07943.
- [71] S. Wheaton and J. Cleymans. THERMUS: A Thermal model package for ROOT. *Comput. Phys. Commun.*, 180:84–106, 2009, arXiv:0407174.
- [72] V. Vislavicius and A. Kalweit. Multiplicity dependence of light flavour hadron production at LHC energies in the strangeness canonical suppression picture, 2019, arXiv:1610.03001.

- [73] C. Bierlich and J. R. Christiansen. Effects of color reconnection on hadron flavor observables. *Physical Review D*, 92:094010, 2015, arXiv:1507.02091.
- [74] B. Andersson. *The Lund model*. Cambridge University Press, July 2005.
- [75] ALICE Collaboration. Multiplicity dependence of π , K, and p production in pp collisions at $\sqrt{s} = 13$ TeV. *Eur. Phys. J. C*, 80:693, 2020, arXiv:2003.02394(2020).
- [76] C. Bierlich, G. Gustafson, L. Lönnblad, and H. Shah. The Angantyr model for heavy-ion collisions in PYTHIA8. *Journal of High Energy Physics*, 10:134, 2018, arXiv:1806.10820.
- [77] O. Biebel, P. Nason, and B. R. Webber. Jet fragmentation in e^+e^- annihilation, 2001, hep-ph/0109282.
- [78] A. Akindinov et al. Multiplicity studies and effective energy in ALICE at the LHC. *The European Physical Journal C*, 50(2):341–352, 2007.
- [79] M. Basile et al. Experimental proof that leading protons are not correlated. *Nuovo Cimento*, 73A(329), 1983.
- [80] A. Zichichi. Totally unexpected results from the ISR. *Il Nuovo Saggiatore*, 27(N3-4):48–56, 2011.
- [81] A. Zichichi. Multiparticle hadronic systems produced in high-energy pp interactions, and comparison with e^+e^- , 1981. Proceedings of the EPS International Conference on “High-Energy Physics”, Lisbon, Portugal, 9-15 July 1981 (EPS, Geneva, 1982), 1133.
- [82] M. Basile et al. The leading effect explains the forward-backward multiplicity correlations in hadronic interactions. *Lett. Nuovo Cim.*, 38(359), 1983.
- [83] B. B. Back and PHOBOS Collaboration. Comparison of the Total Charged-Particle Multiplicity in High-Energy Heavy Ion Collisions with $e+e^-$ and pp/pbar-p Data, 2003, nucl-ex/0301017.
- [84] U.C. Davis J. Klay. Phd. thesis. traverse mass and rapidity spectra of pions and protons from au+au collisions at the alternating gradient synchrotron., 2001.
- [85] S. V. Afanasiev et al. Energy dependence of pion and kaon production in central Pb+Pb collisions. *Phys. Rev. C*, 66:054902, 2002.
- [86] F. Noferini. The effective energy in QCD. Proceedings at 60 Year of Subnuclear Physics in Bologna. *Bologna University Press (editor Luisa Cifarelli)*, page 85, 2019.
- [87] L. Cifarelli et al. An interesting result in pp collisions at 7 TeV. *Proceedings of the International Symposium 30 October - 2 November 2011 Scripta Varia 119*, 2011.
- [88] The ALICE Collaboration. Study of very forward energy and its correlation with particle production at midrapidity in pp and p-pb collisions at the LHC. *Journal of High Energy Physics*, 2022(86), 2022.

- [89] O. S. Brüning et al. *LHC Design Report*. CERN Yellow Reports: Monographs. CERN, Geneva, 2004.
- [90] E. Lopienska. The CERN accelerator complex, layout in 2022. Complexe des accélérateurs du CERN en janvier 2022. 2022. General Photo.
- [91] M. Vretenar et al. *Linac4 design report*, volume 6 of *CERN Yellow Reports: Monographs*. CERN, Geneva, 2020.
- [92] The Proton Synchrotron Booster, <https://cds.cern.ch/record/1997372>. 2012.
- [93] E. Regenstreif. *The CERN Proton Synchrotron*. CERN Yellow Reports: Monographs. CERN, Geneva, 1962. French version published as CERN 61-09.
- [94] The Super Proton Synchrotron, <https://cds.cern.ch/record/1997188>. 2012.
- [95] *CMS Physics: Technical Design Report Volume 1: Detector Performance and Software*. Technical design report. CMS. CERN, Geneva, 2006. There is an error on cover due to a technical problem for some items.
- [96] Technical Design Report for the Phase-II Upgrade of the ATLAS TDAQ System. Technical report, CERN, Geneva, 2017.
- [97] LHCb TDR Computing Technical Design Report CERN-LHCC-2005-019. 6 2005.
- [98] The ALICE Collaboration. The ALICE experiment at the CERN LHC. *Journal of Instrumentation*, 3(08):S08002, aug 2008.
- [99] Performance of the ALICE experiment at the CERN LHC. *International Journal of Modern Physics A*, 29(24):1430044, sep 2014.
- [100] *ALICE Inner Tracking System (ITS): Technical Design Report*. Technical design report. ALICE. CERN, Geneva, 1999.
- [101] ALICE Collaboration. Upgrade of the ALICE Time Projection Chamber. Technical report, 2013.
- [102] ALICE Collaboration. The ALICE TPC, a large 3-dimensional tracking device with fast readout for ultra-high multiplicity events. *Nuclear Instruments and Methods in Physics Research Section A: Accelerators, Spectrometers, Detectors and Associated Equipment*, 622(1):316–367, 2010.
- [103] The ALICE collaboration. Performance of the ALICE VZERO system. *Journal of Instrumentation*, 8(10):P10016–P10016, 2013.
- [104] R. Albrecht and et al. Limits on the Production of Direct Photons in 200A GeV 32S+Au Collisions. *Phys. Rev. Lett.*, 76:3506, 1996.
- [105] T. Anticic and et al. System-size and centrality dependence of charged kaon and pion production in nucleus-nucleus collisions at 40A GeV and 158A GeV beam energy. *Phys. Rev. C*, 86:054903, 2012.

- [106] M. C. Abreu and et al. (NA50 Collaboration). Anomalous suppression in Pb-Pb interactions at 158 GeV/c per nucleon. *Phys. Lett. B*, 410:327, 1997.
- [107] ALICE Zero-Degree Calorimeter (ZDC): Technical Design Report CERN-LHCC-99-005, ALICE-TDR-3. Technical report, CERN, Geneva, 1999.
- [108] P. Cortese and for the ALICE Collaboration. Performance of the ALICE Zero Degree Calorimeters and upgrade strategy. *Journal of Physics: Conference Series*, 1162(1):012006, 2019.
- [109] The ALICE collaboration. Neutron emission from electromagnetic dissociation of Pb nuclei at $\sqrt{s_{NN}} = 2.76$ TeV measured with the ALICE ZDC. *EPJ Web of Conferences*, 70:00073, 2014.
- [110] ALICE Collaboration. ALICE: Physics Performance Report, Volume II. *J. Phys. G: Nucl. Part. Phys.*, 32:1295–2040, 2006.
- [111] K. Bos et al. *LHC computing Grid: Technical Design Report. Version 1.06 (20 Jun 2005)* <https://cds.cern.ch/record/840543>. Technical design report. LCG. CERN, Geneva, 2005.
- [112] S. Bagnasco, L. Betev, P. Buncic, F. Carminati, C. Cirstoiu, C. Grigoras, A. Hayrapetyan, A. Harutyunyan, A. J. Peters, and P. Saiz. AliEn: ALICE environment on the GRID. *Journal of Physics: Conference Series*, 119(6):062012, 2008.
- [113] P. Cortese et al. *ALICE computing: Technical Design Report*. Technical design report. ALICE. CERN, Geneva, 2005. Submitted on 15 Jun 2005.
- [114] F. Bruyant et al. R. Brun. *GEANT 3: user's guide Geant 3.10, Geant 3.11; rev. version*. CERN, Geneva, 1987.
- [115] S. Agostinelli et al. Geant4 a simulation toolkit. *Nuclear Instruments and Methods in Physics Research Section A: Accelerators, Spectrometers, Detectors and Associated Equipment*, 506(3):250–303, 2003.
- [116] A. Ferrari, P. R. Sala, A. Fassò, and J. Ranft. *FLUKA: A multi-particle transport code (program version 2005)*. CERN Yellow Reports: Monographs. CERN, Geneva, 2005.
- [117] AliPhysics: the ALICE software repository, <https://github.com/alishw/AliPhysics>.
- [118] ALICE Collaboration. Performance of the ALICE experiment at the CERN LHC. *International Journal of Modern Physics A*, 29(24):1430044, 2014.
- [119] P. Billoir. Progressive track recognition with a Kalman-like fitting procedure. *Computer Physics Communications*, 57(1):390–394, 1989.
- [120] The ALICE Collaboration. Upgrade of the ALICE Experiment: Letter of Intent. Technical report, CERN, Geneva, 2014.
- [121] A. Maevskaya. ALICE FIT data processing and performance during LHC Run 3. *Phys. At. Nucl.*, 84(4):579–584, 2021, 2012.02760.

- [122] P. Buncic, M. Krzewicki, and P. Vande Vyvre. Technical Design Report for the Upgrade of the Online-Offline Computing System. Technical report, 2015.
- [123] The ALICE Collaboration. Future high-energy pp programme with ALICE <https://cds.cern.ch/record/2724925>. 2020.
- [124] A. Anton et al. ALICE Run 3 Analysis Framework. *EPJ Web Conf.*, 251:03063, 2021.
- [125] Apache Arrow, a cross-language development platform for in-memory analytics, <https://arrow.apache.org/>.
- [126] S. Gorbunov D. Rohr, M. O. Schmidt, and R. Shahoyan. Track Reconstruction in the ALICE TPC using GPUs for LHC Run 3, 2018, 1811.11481.
- [127] O. M. Schmidt D. Rohr, S. Gorbunov and R. Shahoyan. Gpu-Based Online Track Reconstruction for the Alice Tpc in Run 3 With Continuous Read-Out. *EPJ Web of Conferences*, 214:01050, 2019.
- [128] G. Dellacasa et al. ALICE technical design report of the time-of-flight system (TOF). 2 2000.
- [129] P. Cortese et al. ALICE: Addendum to the technical design report of the time of flight system (TOF). 4 2002.
- [130] P. Konopka and B. von Haller. The ALICE O2 data quality control system. *EPJ Web Conf.*, 245:01027, 2020.
- [131] The ALICE Collaboration. Determination of the event collision time with the ALICE detector at the LHC. *The European Physical Journal Plus*, 132(2), 2017.
- [132] S. Acharya et al. J/ψ elliptic and triangular flow in Pb – Pb collisions at $\sqrt{s_{NN}} = 5.02$ TeV. *JHEP*, 10:141, 2020, 2005.14518.
- [133] ALICE Collaboration. Pseudorapidity densities of charged particles with transverse momentum thresholds in pp collisions at $\sqrt{s} = 5.02$ and 13 tev, 2022, 2211.15364.
- [134] A. Dobrin. Event shape engineering with alice. *Nuclear Physics A*, 904-905:455c–458c, 2013. The Quark Matter 2012.
- [135] R. L. Workman and Others. Review of Particle Physics. *PTEP*, 2022:083C01, 2022.
- [136] R. Barlow. Systematic Errors: facts and fictions, 2002, hep-ex/0207026.
- [137] The ALICE Collaboration. Multiplicity dependence of (multi-)strange hadron production in proton-proton collisions at $\sqrt{s} = 13$ TeV. *The European Physical Journal C*, 80(2), 2020.
- [138] ALICE Collaboration. Enhanced production of multi-strange hadrons in high-multiplicity proton-proton collisions. *Nature Phys.*, 13:535–539, 2017, 1606.07424.
- [139] ALICE Collaboration. Multiplicity dependence of light-flavor hadron production in pp collisions at $\sqrt{s} = 7$ TeV. *Phys. Rev. C*, 99:024906, 2019.

- [140] J. Cleymans. The Tsallis Distribution for p-p collisions at the LHC. *Journal of Physics Conference Series*, 455:2049–, 08 2013.
- [141] C. Loizides and A. Morsch. Apparent strangeness enhancement from multiplicity selection in high energy proton-proton collisions, 2021, 2109.05181.
- [142] J.K. Ahn and S. Aoki et al. Measurement of the Ξ -p Scattering Cross Sections at Low Energy. *Physics Letters B*, 633(2-3):214–218, feb 2006.
- [143] D. D. Chinellato and. Charm and multi-charm baryon measurements via strangeness tracking with the upgraded ALICE detector. *EPJ Web of Conferences*, 259:09004, 2022.

Appendix A

Details on the analysis strategy

A.1 ZDC energy as an event-by-event estimator

In the early stages of this analysis, the ZDC energy was first considered at the event-by-event level to build a percentile estimator, starting from the distribution of the sum of the energy deposited in the ZN and ZP calorimeters:

$$\text{ZDC Energy Sum} = \text{ZNA} + \text{ZNC} + \text{ZPA} + \text{ZPC} \quad . \quad (\text{A.1})$$

The distribution of the variable in Eq. A.1 for the 2015 dataset is shown in Fig. A.1. In order to obtain a ZDC percentile estimator, we considered the fraction of entries in each bin of this distribution over the total number of events. This fraction is then summed recursively in order to produce a cumulative distribution, as shown in Fig. A.2 (a), from which it is possible to associate the ZDC energy deposit in each event to a value in percentiles. The distribution of ZDC percentiles for the full 2015 dataset is visible in Fig A.2 (b), showing a homogeneous distribution over the total events, as expected. In the final analysis, the extraction of the ZDC percentile was done separately run-by-run. The definition of this estimator is built such that a low ZDC percentile value corresponds to a high effective energy and charged-particle multiplicity, therefore, in the final results, it will be referred to as “ $(\sqrt{s} - \text{ZDC})$ percentile”. The first preliminary results of this work were obtained using a combination of the $(\sqrt{s} - \text{ZDC})$ and VZEROM percentile estimators, expected to be sensitive to the effective energy and multiplicity respectively. The former was used to select events with fixed leading energy, requiring the percentile to fall within the ranges [0–30]% and [70–100]%, and selecting different multiplicity classes through the VZEROM estimator. The latter was used to select events with fixed multiplicity, requiring the percentile to fall within the same ranges ([0–30]% and [70–100]%), and selecting different effective energy classes through

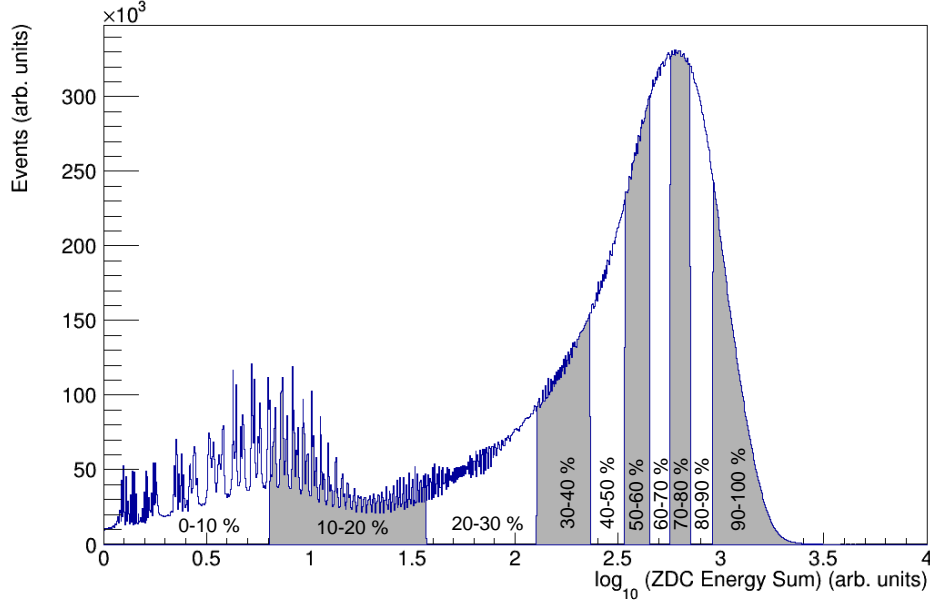


Fig. A.1 Distribution of the *ZDC Energy Sum* variable for the 2015 dataset. The events are grouped in percentile classes which reflect the fraction of events in each region over the total number. The pseudo-peaks visible in the region marked as 0-20 %, are fluctuations on the small energy deposit in the ZDC, which are almost empty in that range (pedestal effect).

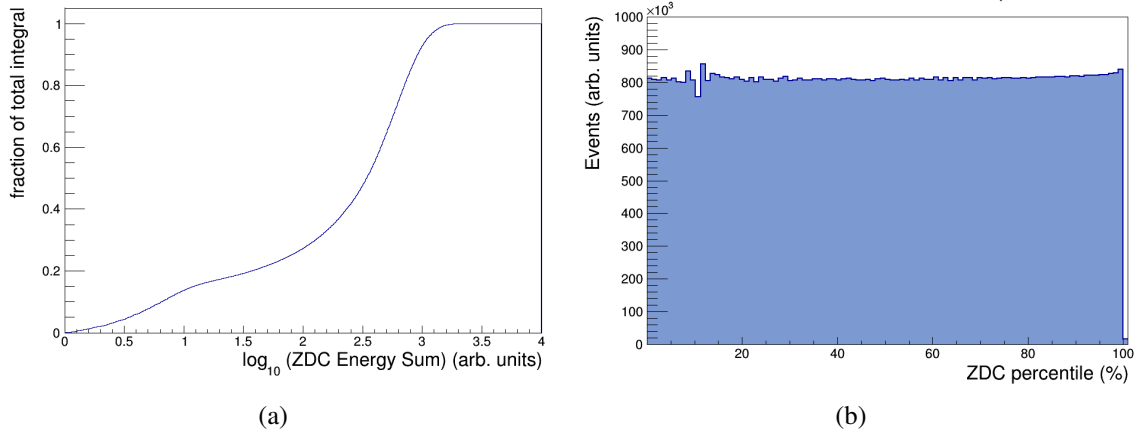


Fig. A.2 (a) Cumulative distribution of the fraction of events in each bin of the distribution in Fig. A.1 over the total number of entries. (b) ZDC percentile distribution for all events.

the $(\sqrt{s} - \text{ZDC})$ estimator. The results obtained with this analysis strategy were approved by the ALICE Collaboration and presented at international conferences [11]. The key outcome of this study will be briefly discussed here. Combining two event estimators based on information collected at forward rapidity (VZEROM and ZDC), was found to strongly

reduce the discriminatory power in terms of midrapidity multiplicity and effective energy. In particular, the ZDC energy measured event-by-event was found to be strongly correlated with the VZEROM signal amplitude, suggesting that the two estimators may be sensitive to the same physics. Starting from these results, further studies were performed, testing the combination of several estimators based on different detector information, at central and forward rapidity. The outcome of these studies showed that using VZEROM and SPDClusters combined was the most efficient way to select events at fixed midrapidity multiplicity and fixed ZDC energy. The forward energy measured in the ZDC was found to be much more effective as an average observable, property of the event class, compared to an event-by-event estimator.

A.2 Raw p_T spectra in all event classes

The raw yields for the High Multiplicity, Low Multiplicity, High ZN, Low ZN event classes are displayed in Fig. A.3, A.4 and A.3 for V^0 s and in Fig. A.6 and A.7 for cascades. These spectra are still subject to all the inefficiencies and the acceptance limitations of the detector.

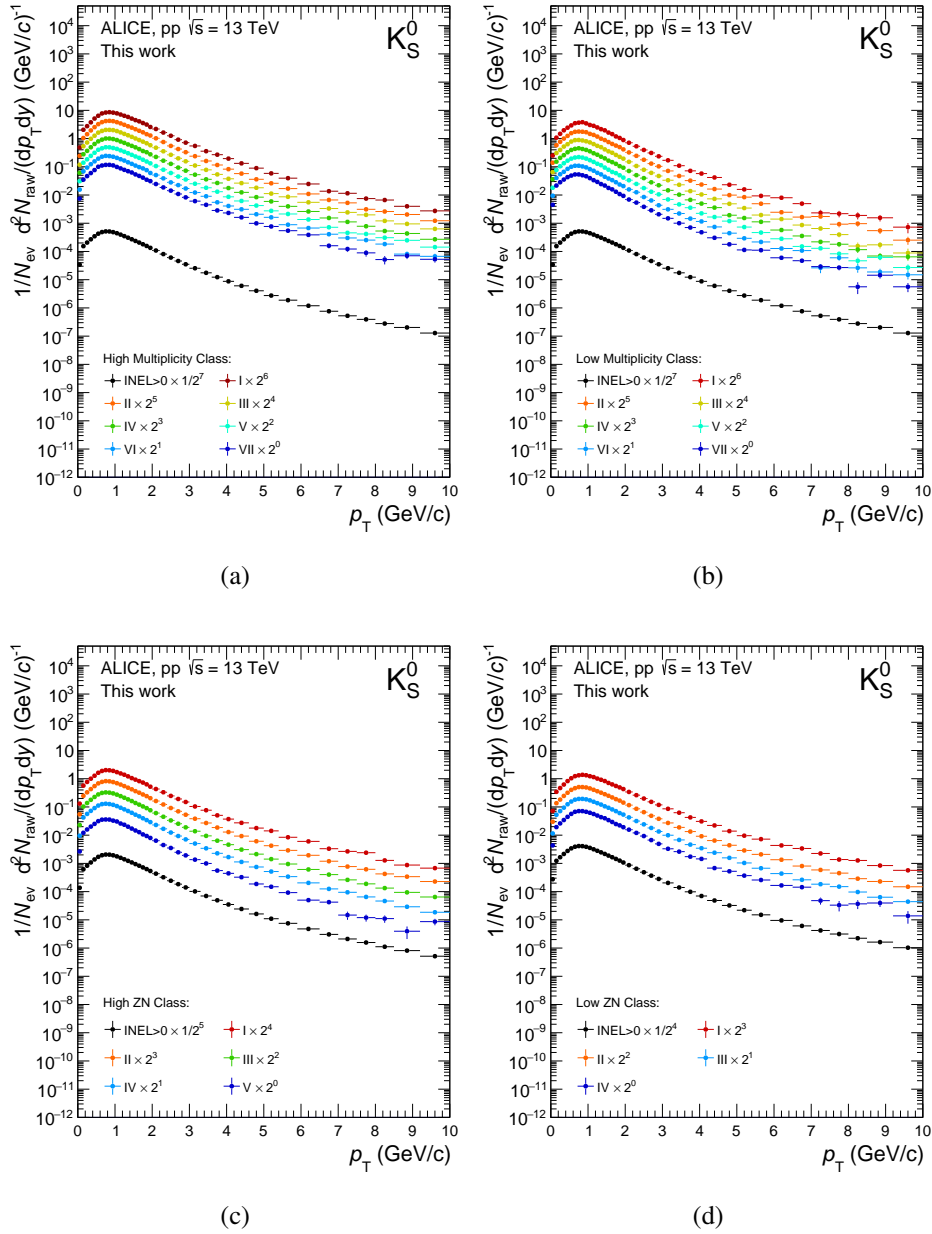


Fig. A.3 Raw p_T spectra for K_S^0 normalised by the number of events in the High Multiplicity (a), Low Multiplicity (b), High ZN (c), Low ZN (d) event classes.

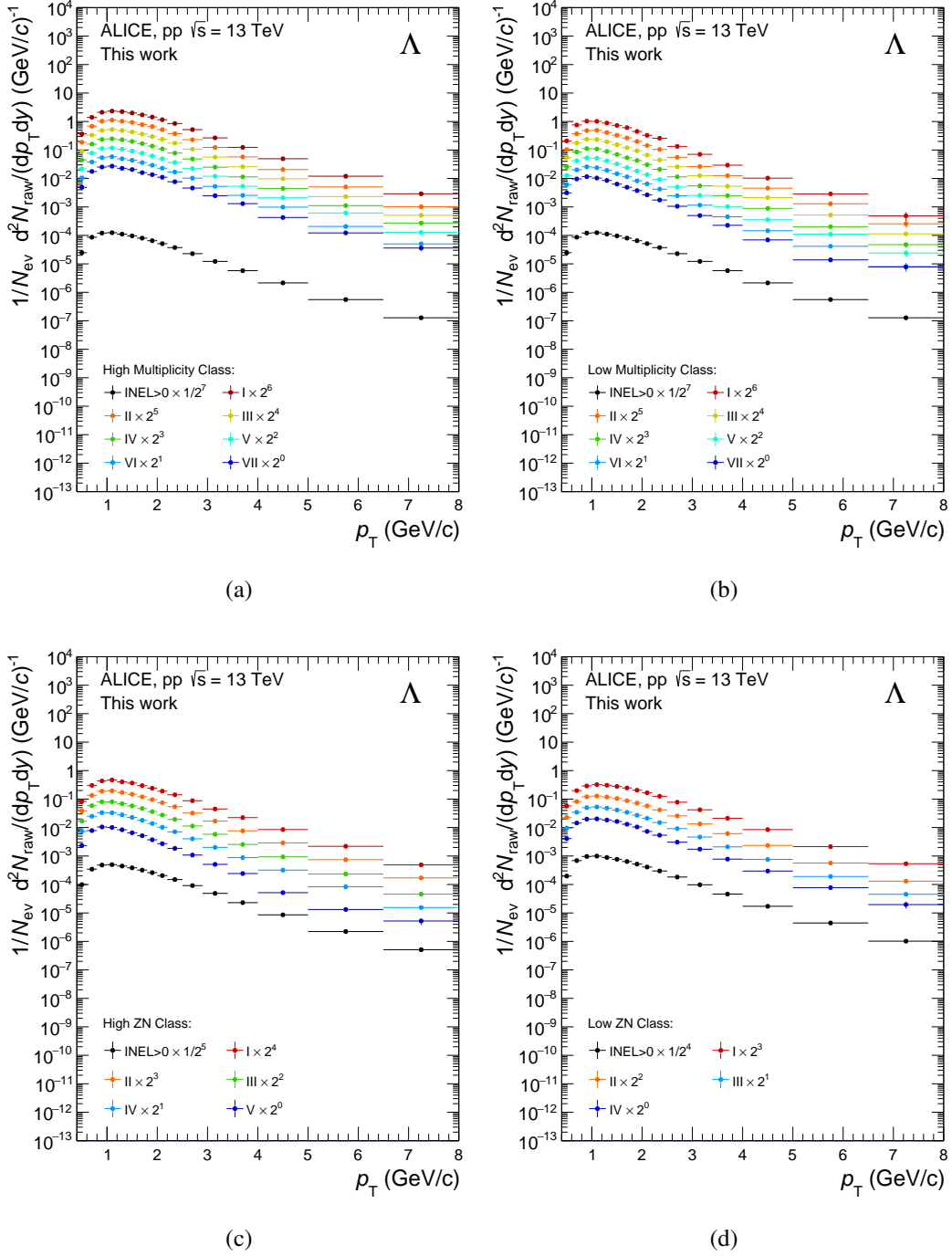


Fig. A.4 Raw p_T spectra for Λ normalised by the number of events in the High Multiplicity (a), Low Multiplicity (b), High ZN (c), Low ZN (d) event classes.

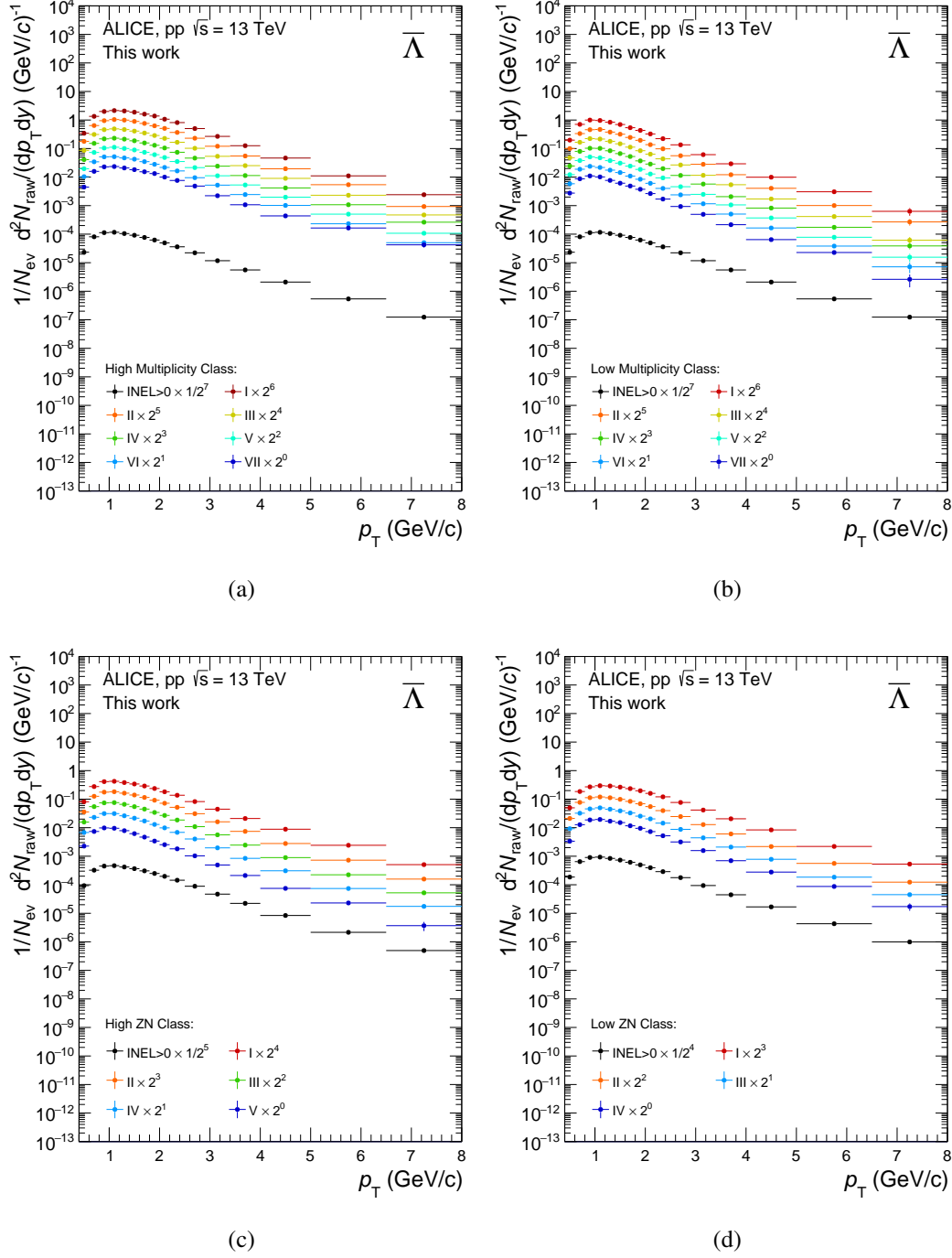


Fig. A.5 Raw p_T spectra for $\bar{\Lambda}$ normalised by the number of events in the High Multiplicity (a), Low Multiplicity (b), High ZN (c), Low ZN (d) event classes.

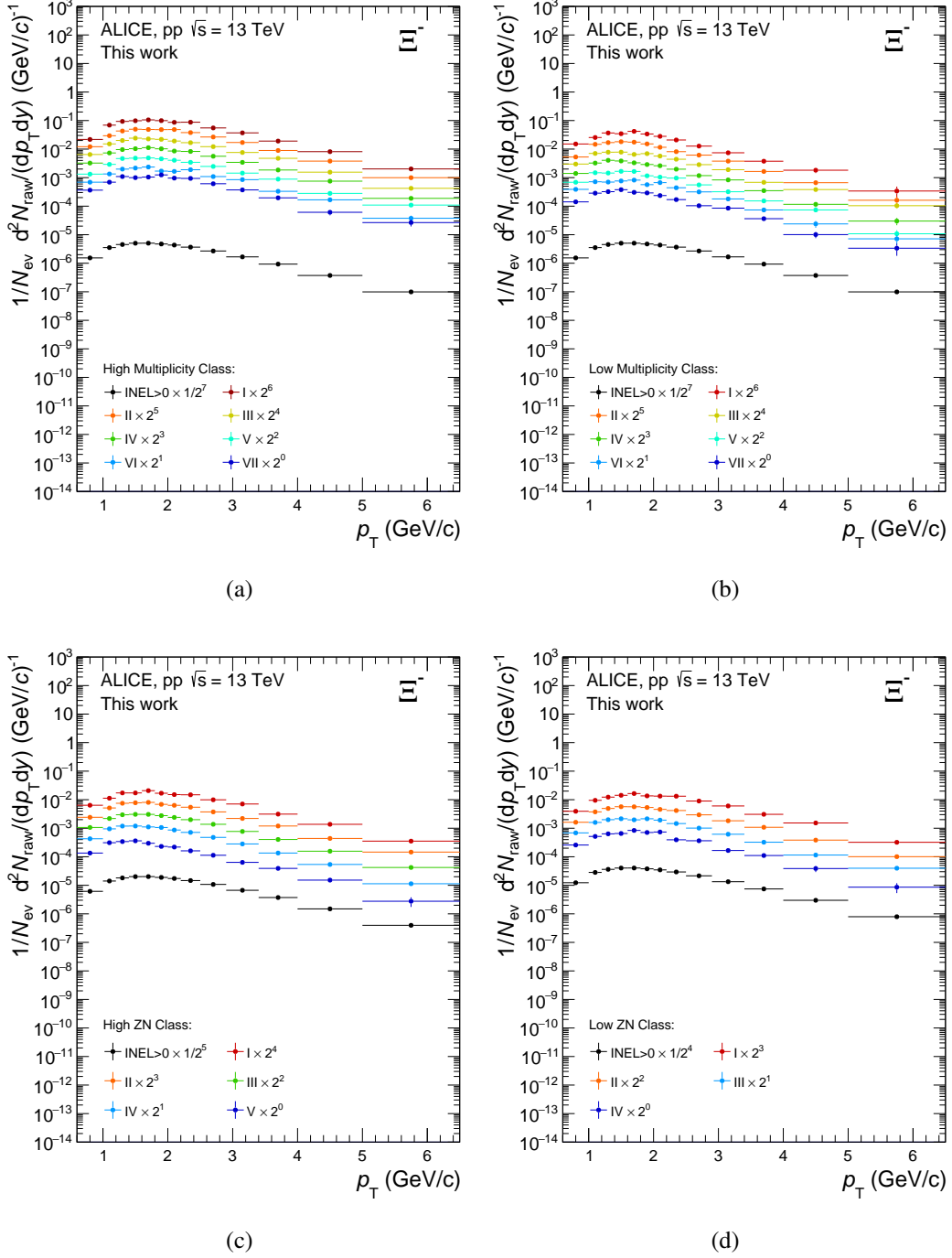


Fig. A.6 Raw p_T spectra for Ξ^- normalised by the number of events in the High Multiplicity (a), Low Multiplicity (b), High ZN (c), Low ZN (d) event classes.

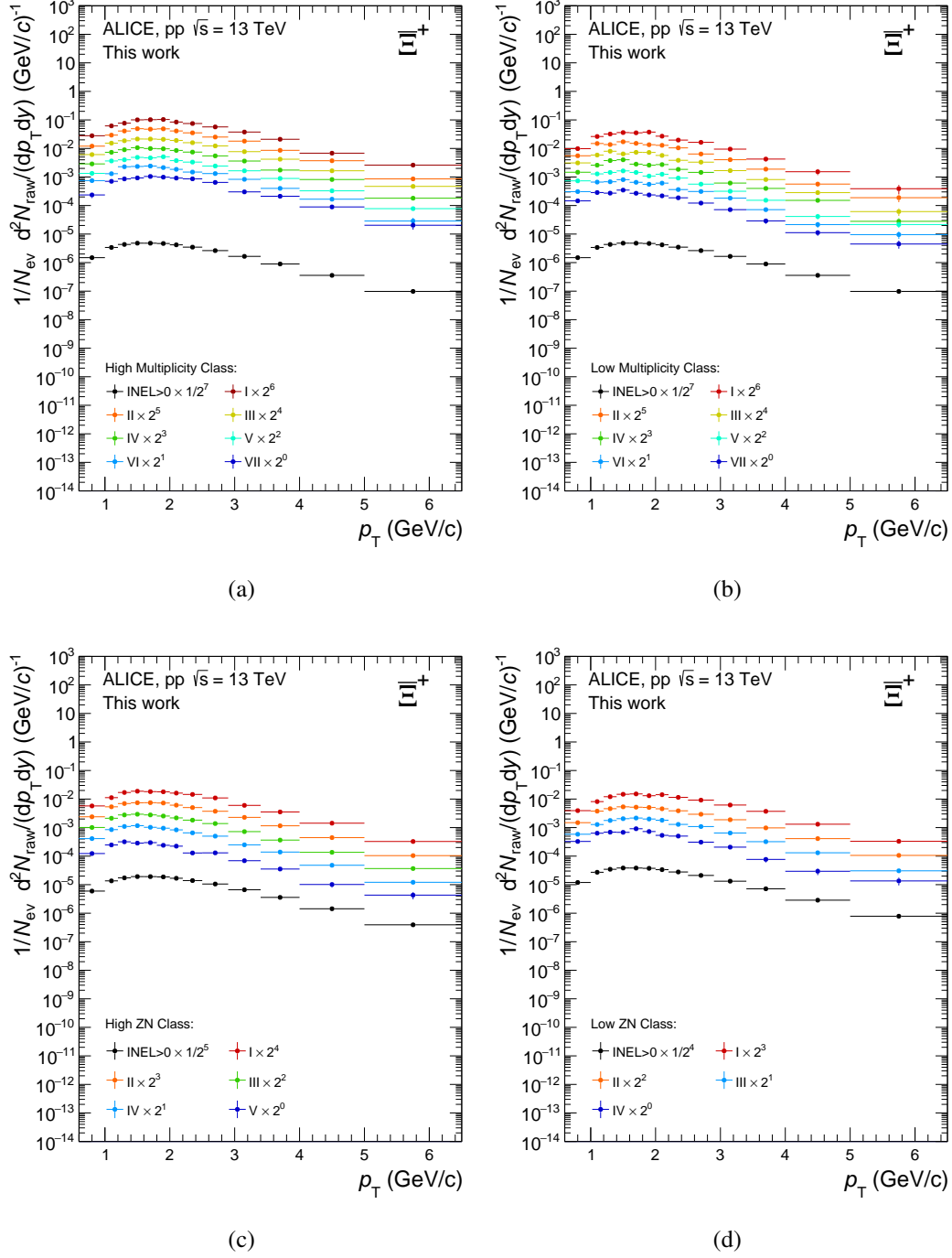
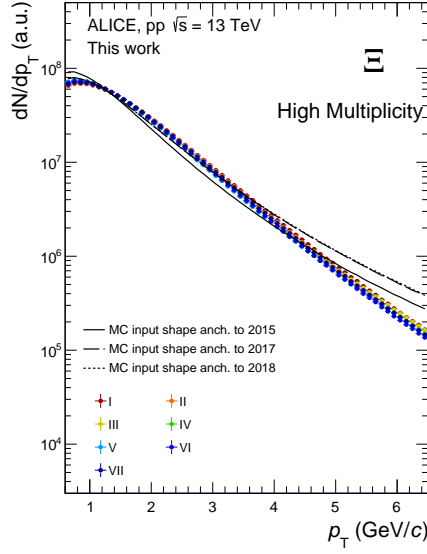


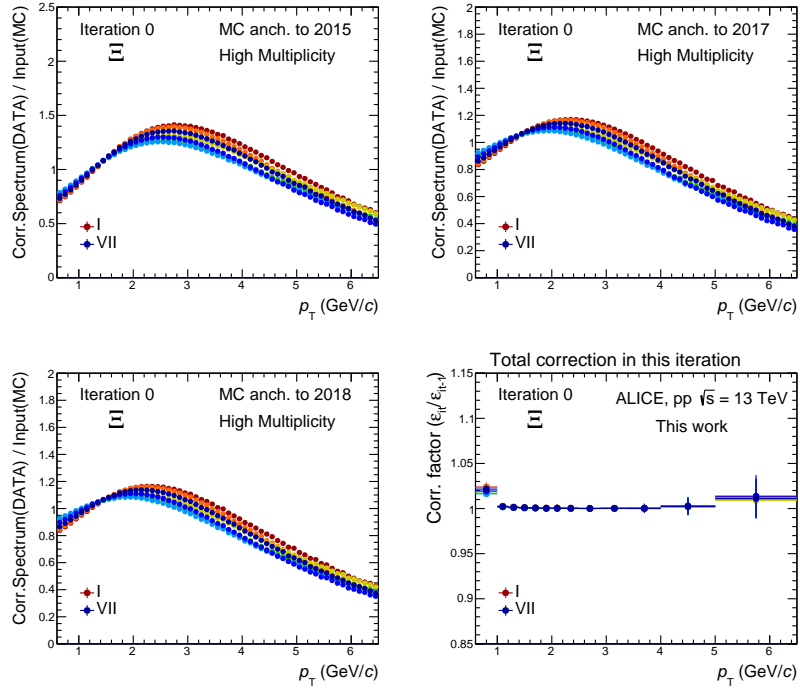
Fig. A.7 Raw p_T spectra for $\bar{\Xi}^+$ normalised by the number of events in the High Multiplicity (a), Low Multiplicity (b), High ZN (c), Low ZN (d) event classes.

A.3 MC p_T shape correction in all event classes

The input MC p_T shape correction factors, discussed in Sect. 6.6.4, are shown in Fig. A.8, A.9, A.10, A.11 for $\Xi^- + \bar{\Xi}^+$ for all event classes.



(a)



(b)

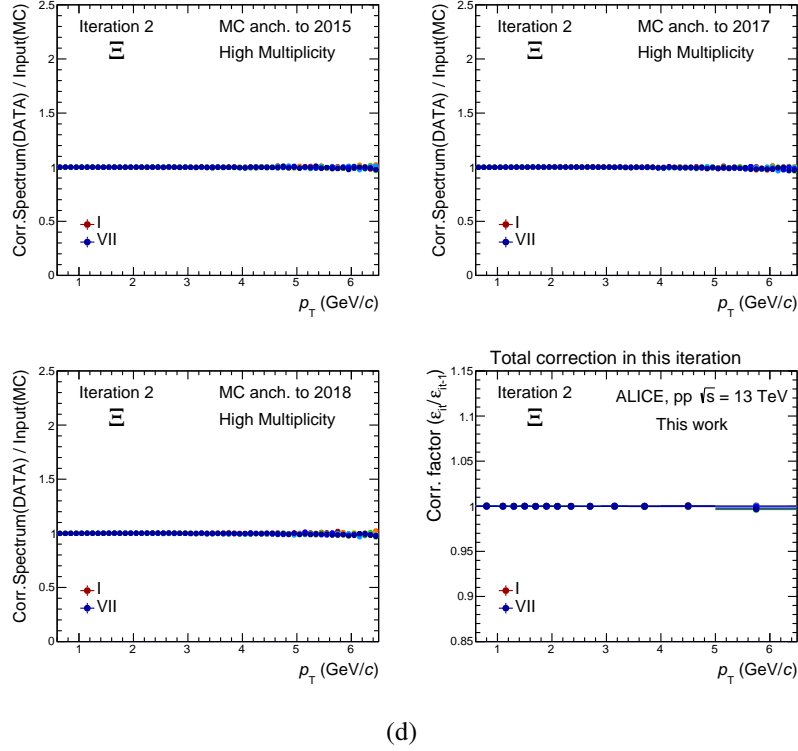
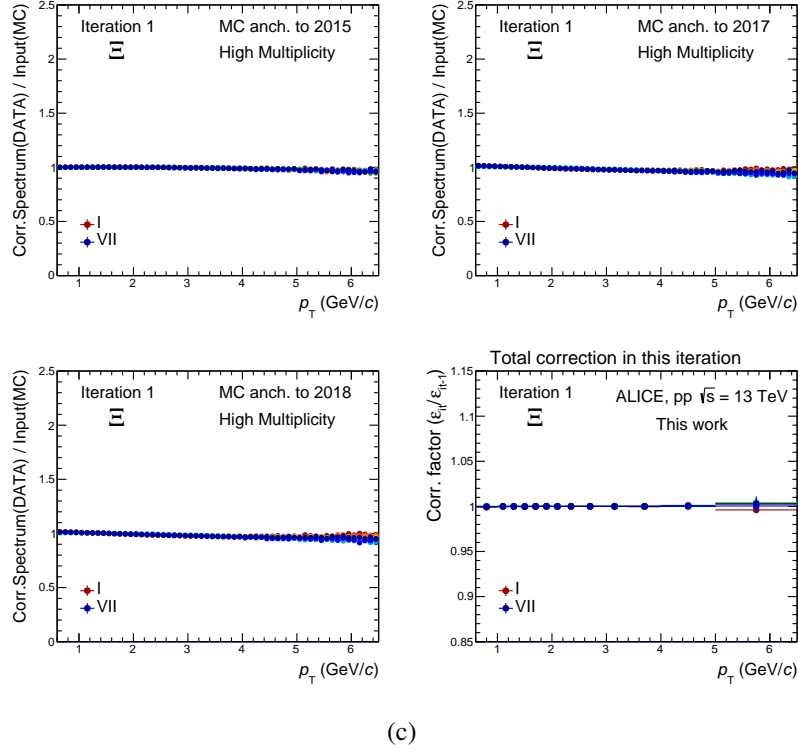
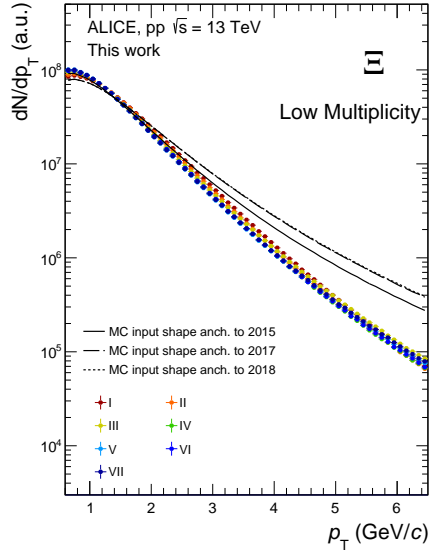
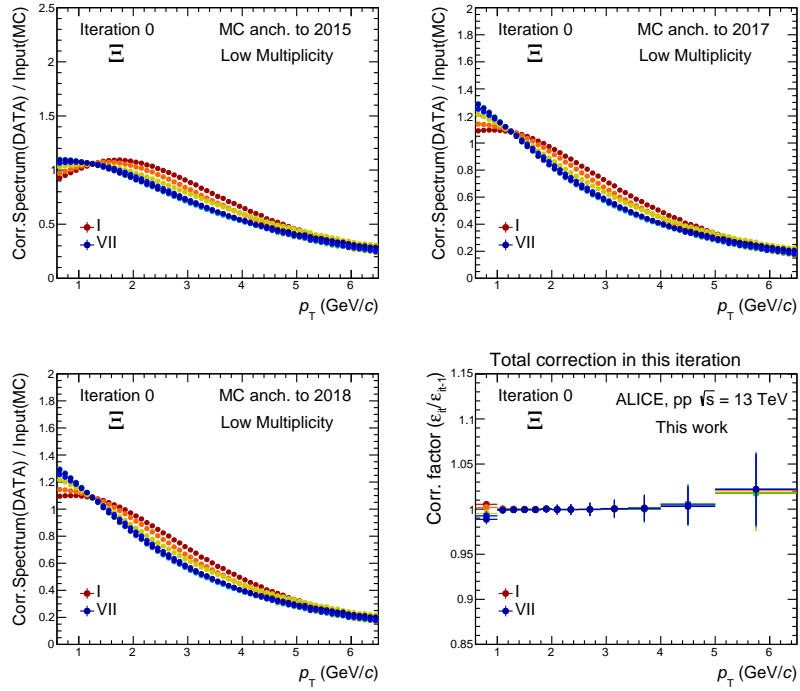


Fig. A.8 (a) Comparison of measured p_T shapes re-generated starting from Levy-Tsallis fits with the Monte Carlo p_T input distributions for $\Xi^- + \bar{\Xi}^+$ in the High Multiplicity event class. (b), (c), (d) Results from the iterative procedure relative to $\Xi^- + \bar{\Xi}^+$ spectra, see text for more details.



(a)



(b)

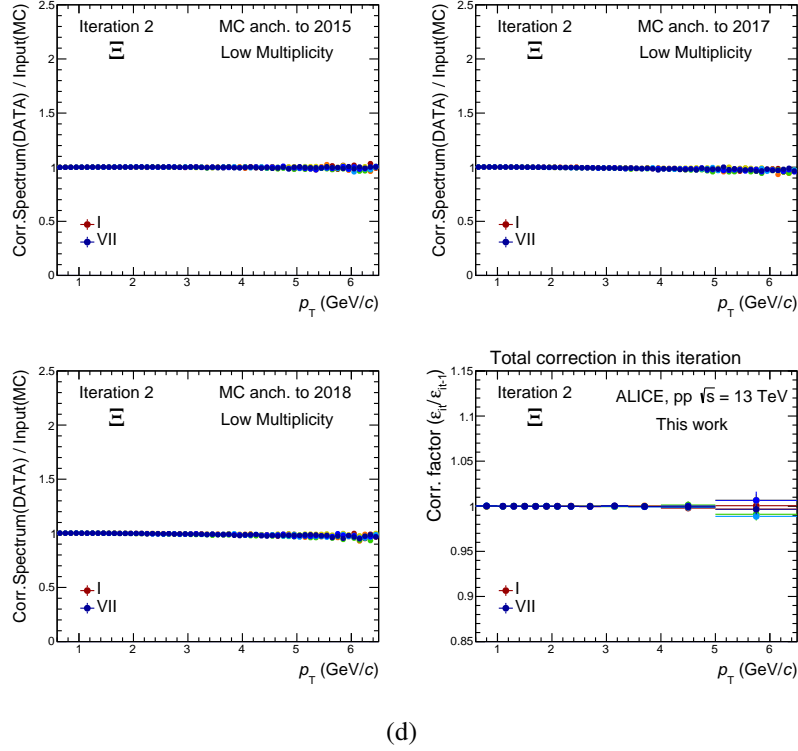
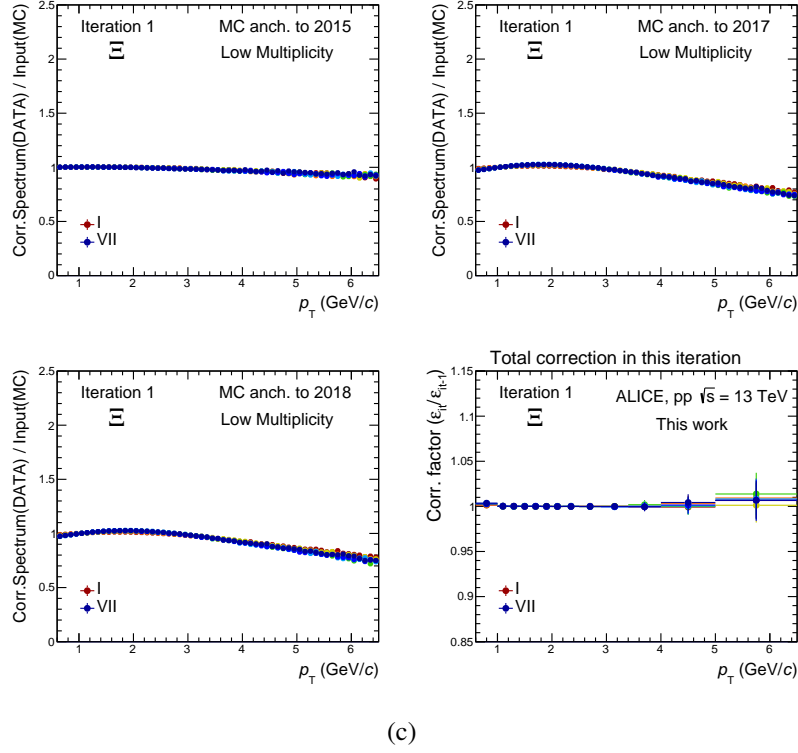
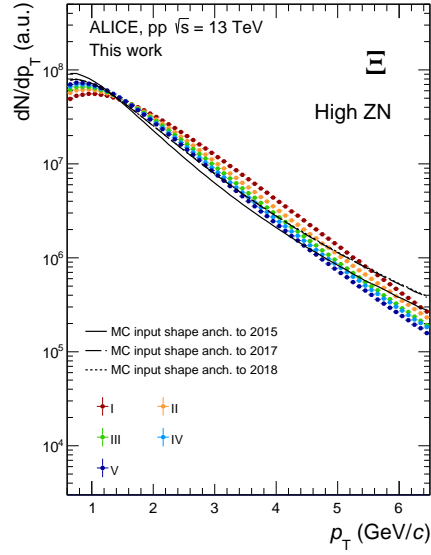
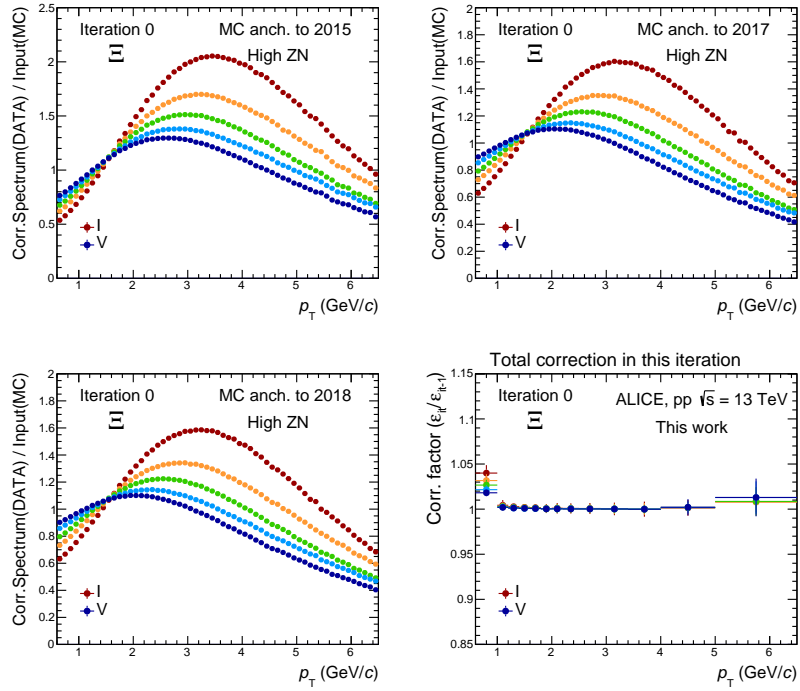


Fig. A.9 (a) Comparison of measured p_T shapes re-generated starting from Levy-Tsallis fits with the Monte Carlo p_T input distributions for $\Xi^- + \Xi^+$ in the Low Multiplicity event class. (b), (c), (d) Results from the iterative procedure relative to $\Xi^- + \Xi^+$ spectra, see text for more details.



(a)



(b)

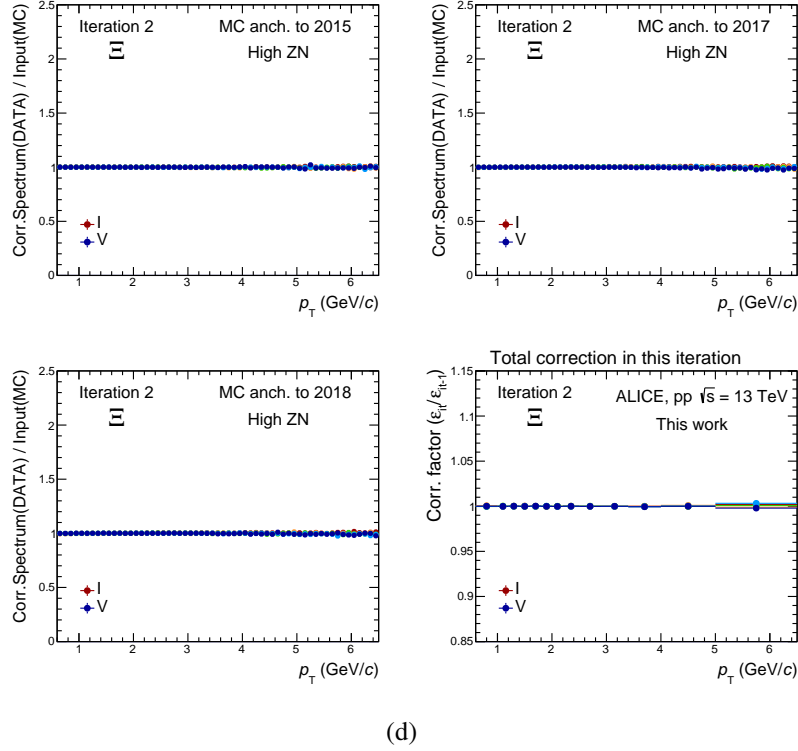
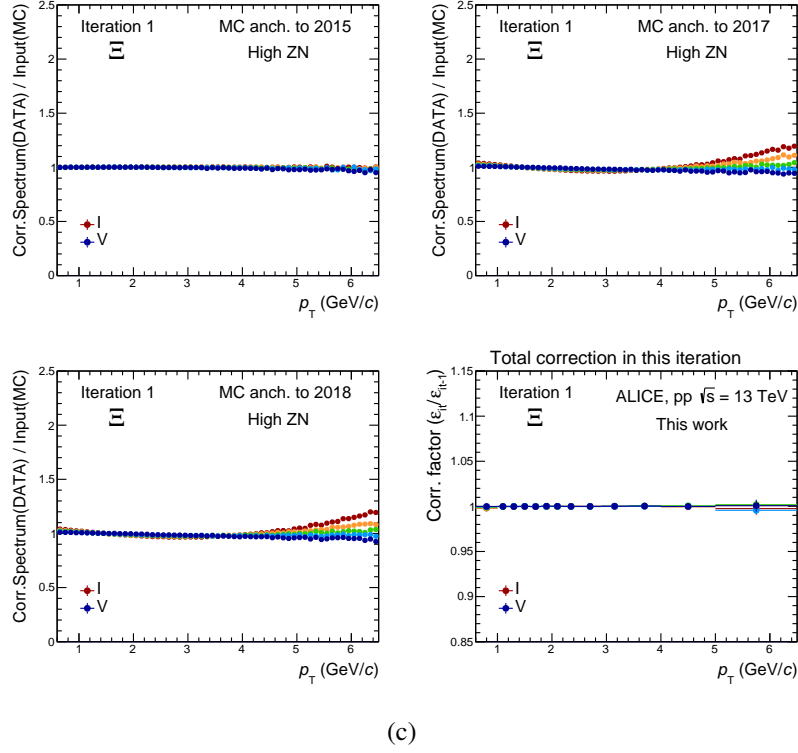
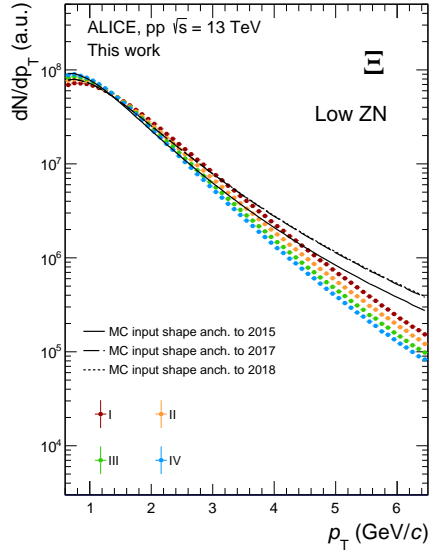
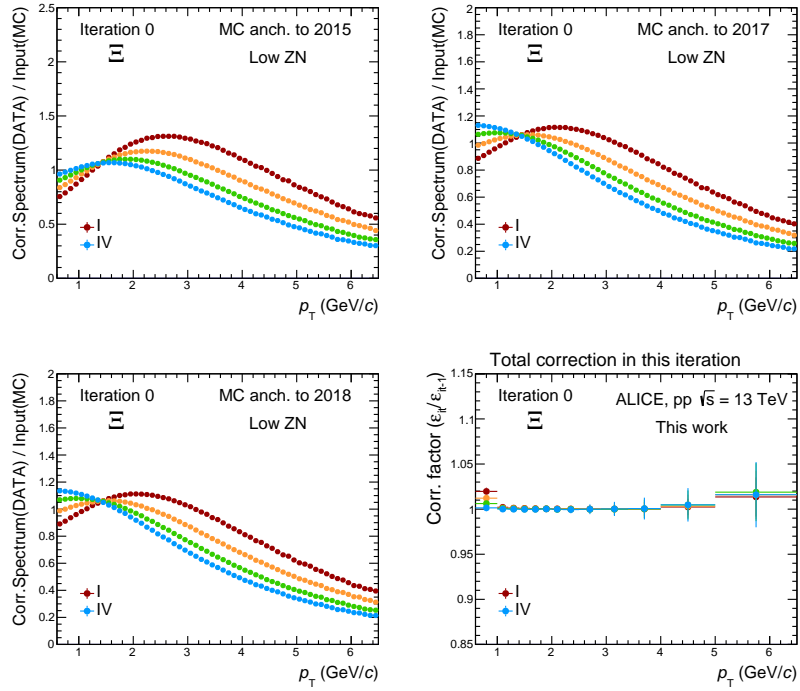


Fig. A.10 (a) Comparison of measured p_T shapes re-generated starting from Levy-Tsallis fits with the Monte Carlo p_T input distributions for $\Xi^- + \bar{\Xi}^+$ in the High ZN event class. (b), (c), (d) Results from the iterative procedure relative to $\Xi^- + \bar{\Xi}^+$ spectra, see text for more details.



(a)



(b)

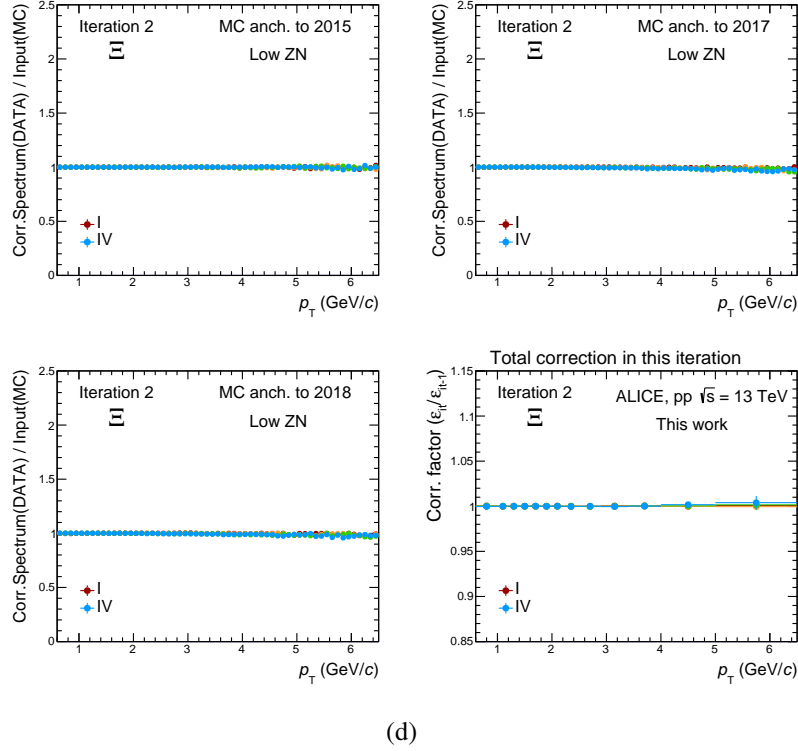
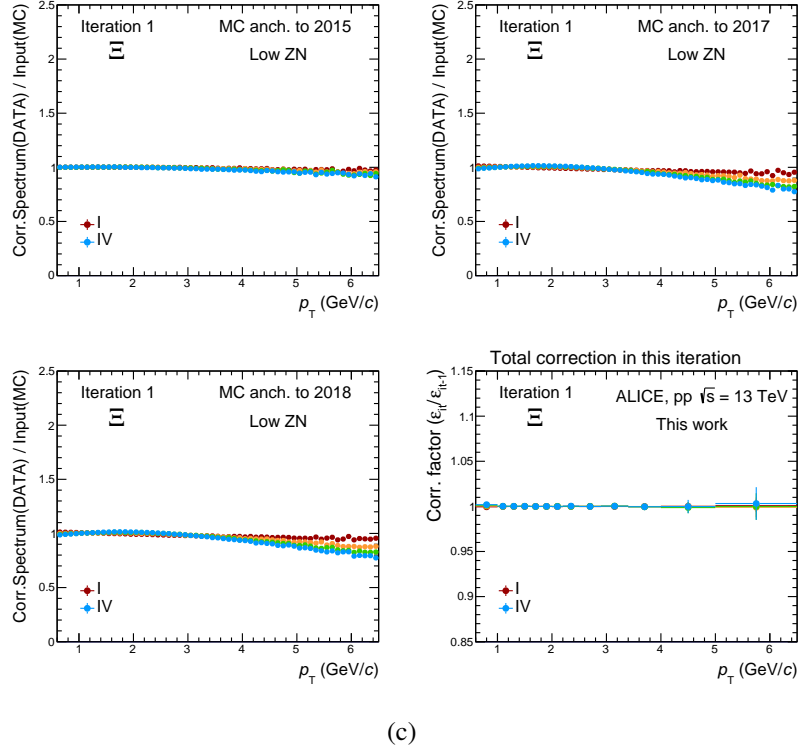


Fig. A.11 (a) Comparison of measured p_T shapes re-generated starting from Levy-Tsallis fits with the Monte Carlo p_T input distributions for $\Xi^- + \bar{\Xi}^+$ in the Low ZN event class. (b), (c), (d) Results from the iterative procedure relative to $\Xi^- + \bar{\Xi}^+$ spectra, see text for more details.

A.4 Signal loss corrections in all event classes

The signal loss correction factors, discussed in Sect. 6.6.5, are shown in Fig. A.12, A.13, A.14, A.11 for K_S^0 , Λ and Ξ , respectively, for all event classes.

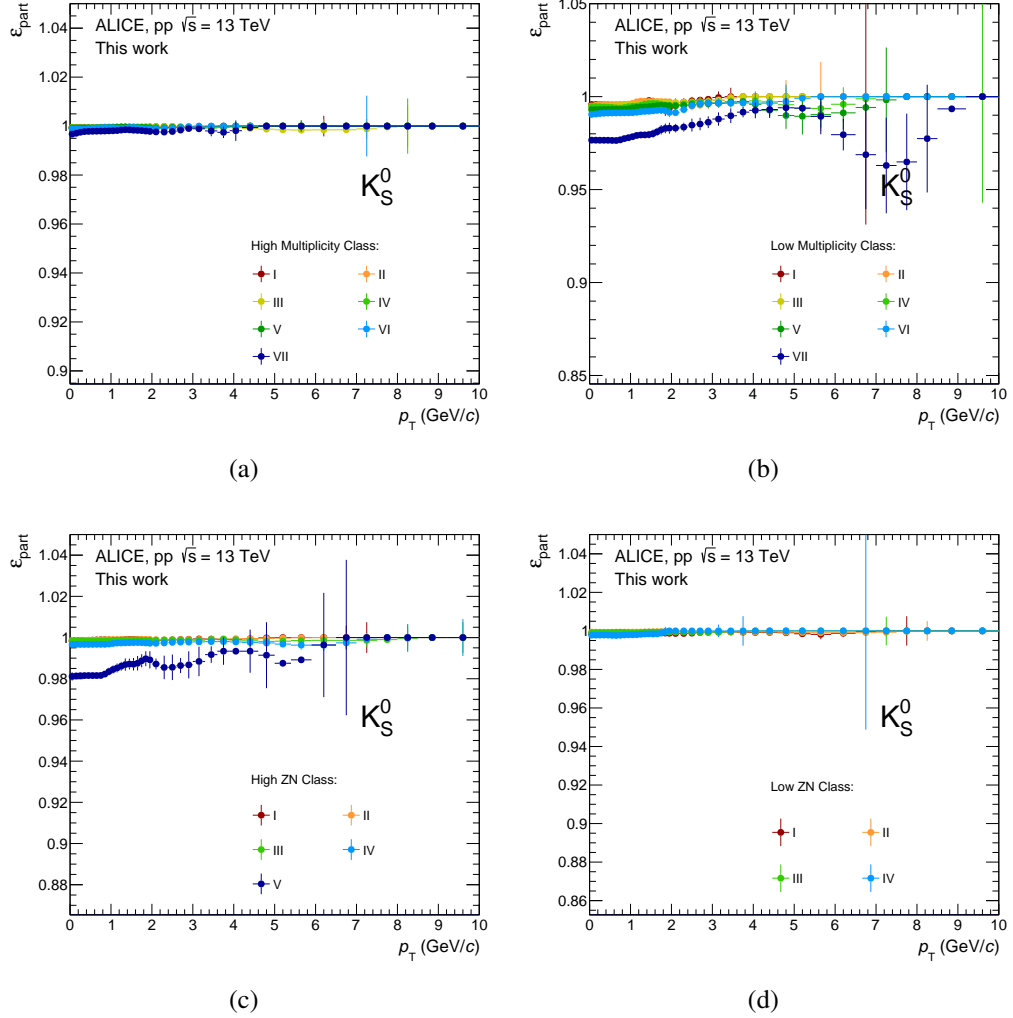


Fig. A.12 Signal loss correction factors for K_S^0 in the High Multiplicity (a), Low Multiplicity (b), High ZN (c) and Low ZN (d) Class selection.

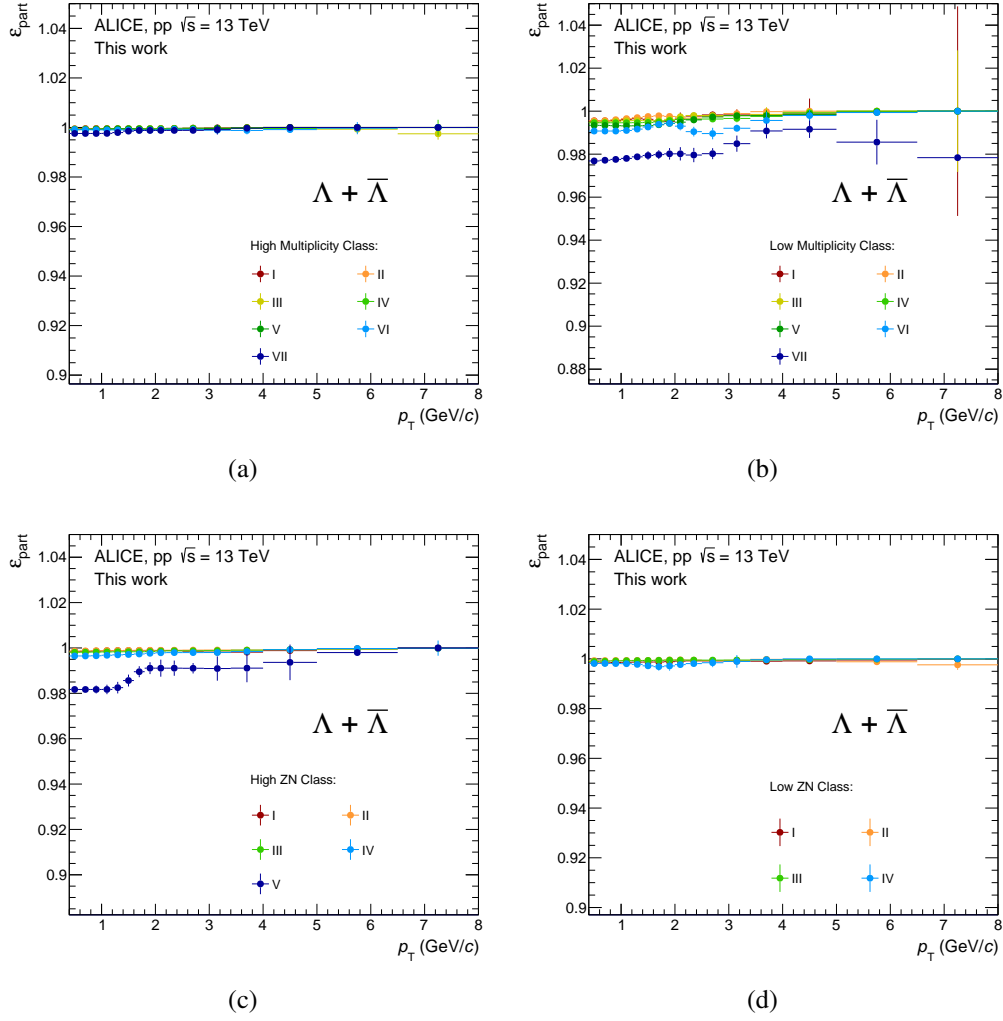


Fig. A.13 Signal loss correction factors for Λ in the High Multiplicity (a), Low Multiplicity (b), High ZN (c) and Low ZN (d) Class selection.

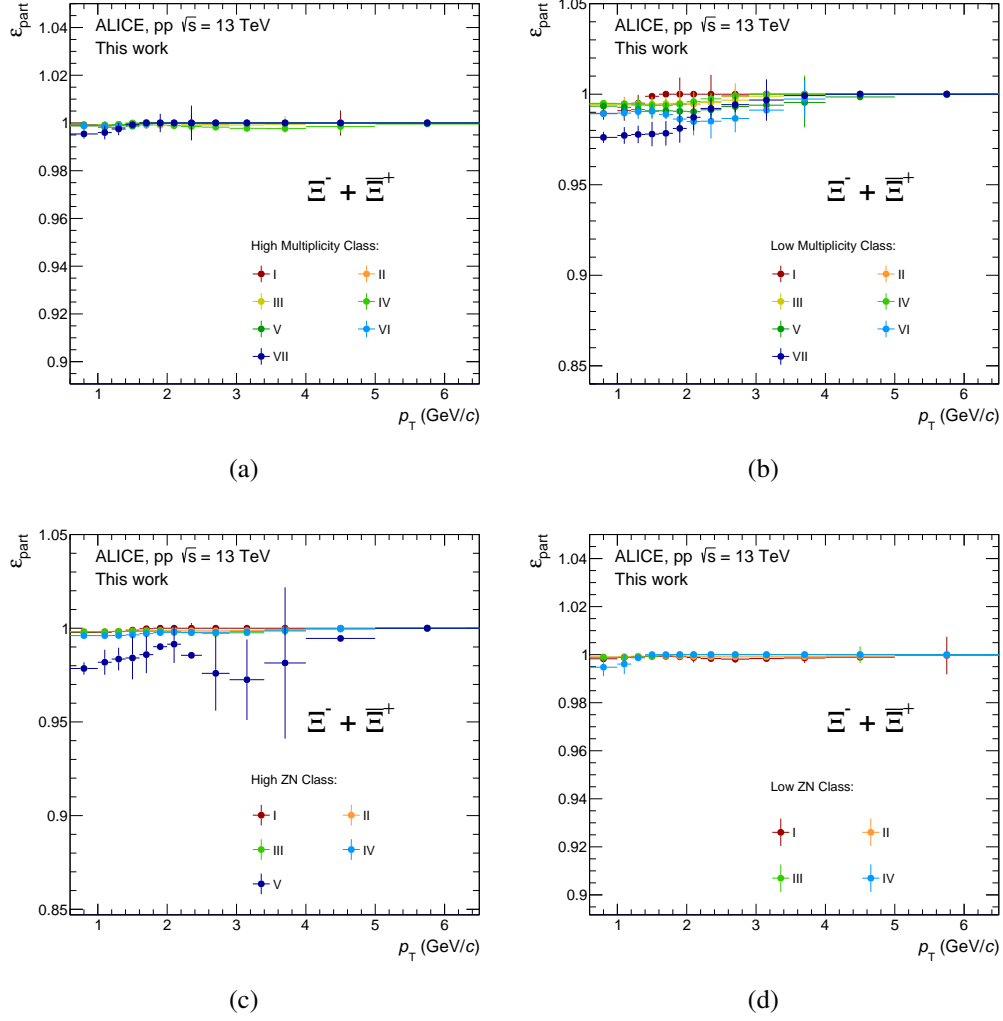


Fig. A.14 Signal loss correction factors for Ξ in the High Multiplicity (a), Low Multiplicity (b), High ZN (c) and Low ZN (d) Class selection.

A.5 Uncorrelated systematics in all event classes

A summary of the systematic contributions uncorrelated across percentile selections for the High Multiplicity, Low Multiplicity, High ZN and Low ZN classes is reported in Fig. A.15, A.16 and A.17 for K_S^0 , $\Lambda + \bar{\Lambda}$ and $\Xi^- + \bar{\Xi}^+$, respectively.

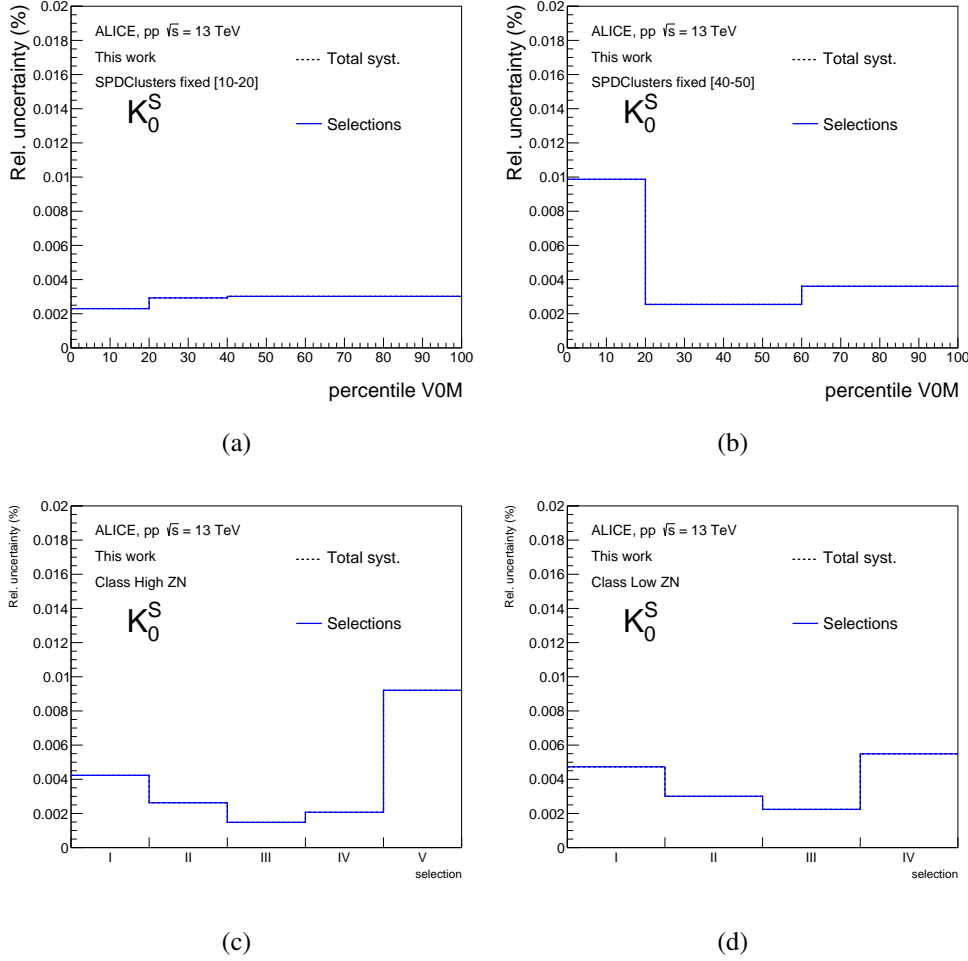


Fig. A.15 Summary of the uncorrelated systematic uncertainties on the integrated yields for K_S^0 studied in the High Multiplicity (a), Low Multiplicity (b), High ZN (c) and Low ZN (d) selections. The contribution from the variation of selections and extrapolations is reported in blue and red, respectively. The total contribution is reported in black.

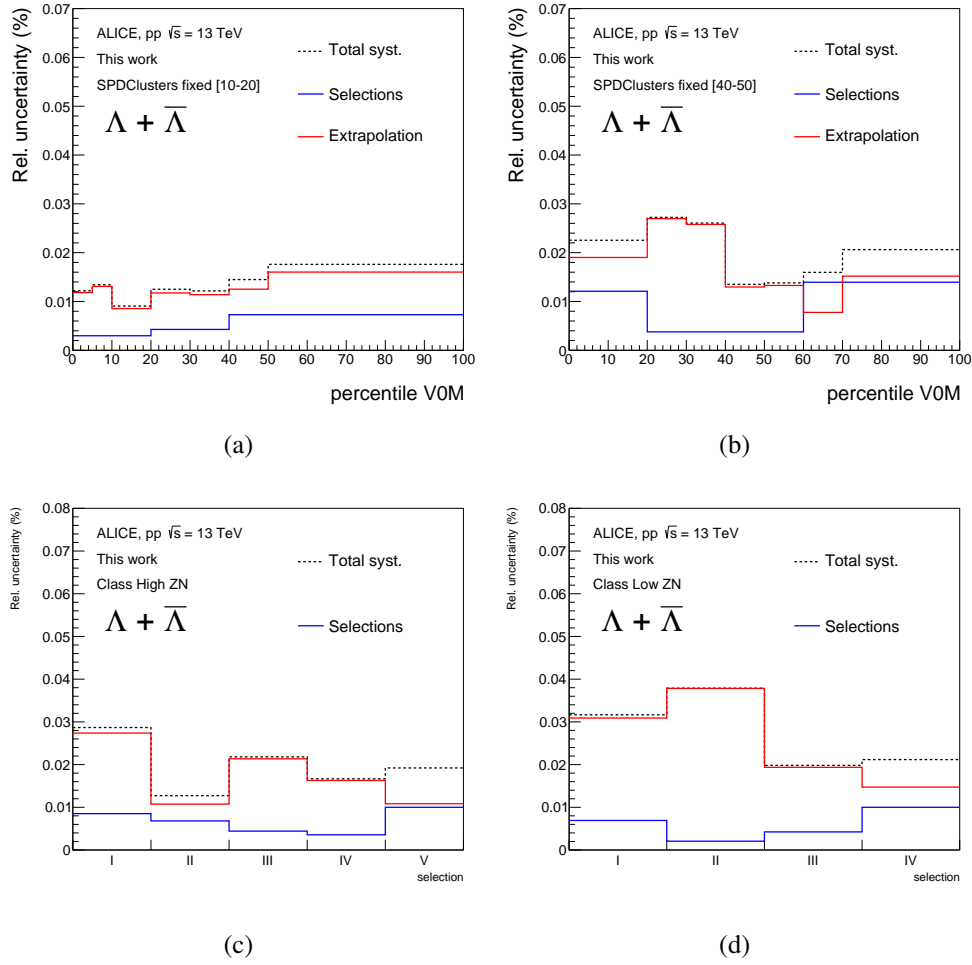


Fig. A.16 Summary of the uncorrelated systematic uncertainties on the integrated yields for $\Lambda + \bar{\Lambda}$ studied in the High Multiplicity (a), Low Multiplicity (b), High ZN (c) and Low ZN (d) selections. The contribution from the variation of selections and extrapolations is reported in blue and red, respectively. The total contribution is reported in black.

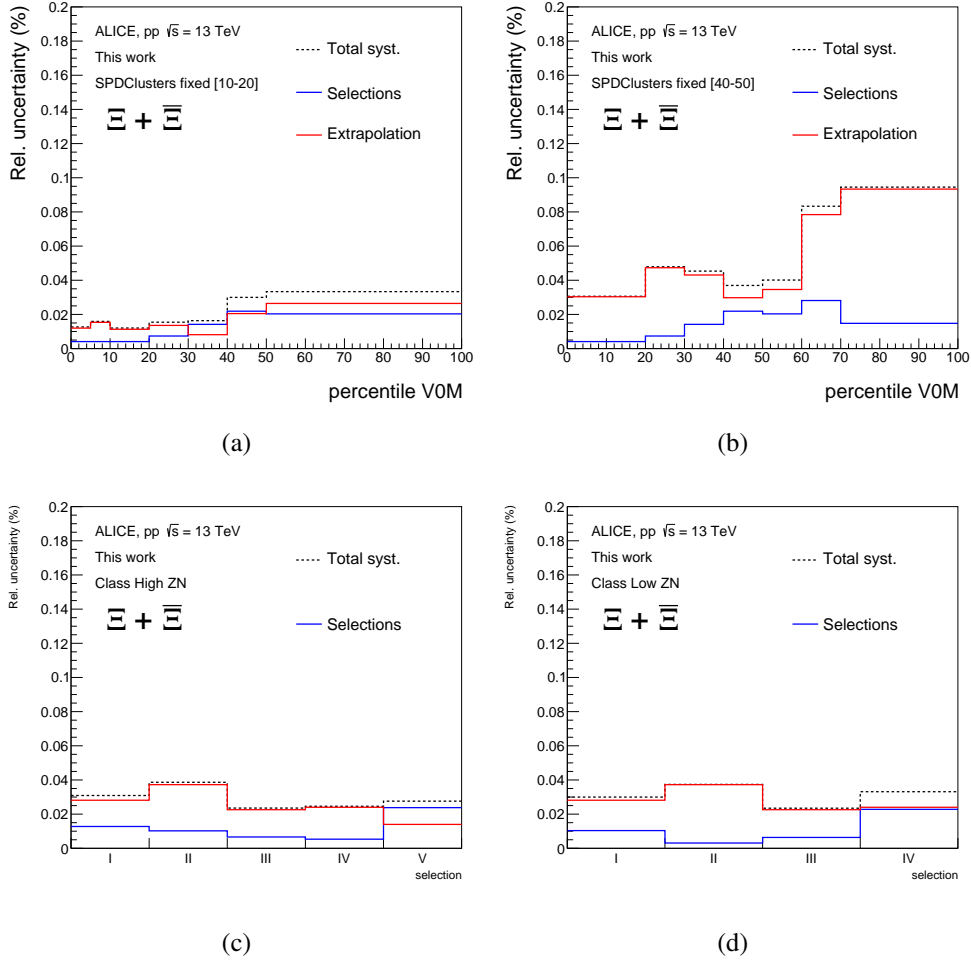


Fig. A.17 Summary of the uncorrelated systematic uncertainties on the integrated yields for $\Xi^- + \Xi^+$ studied in the High Multiplicity (a), Low Multiplicity (b), High ZN (c) and Low ZN (d) selections. The contribution from the variation of selections and extrapolations is reported in blue and red, respectively. The total contribution is reported in black.

Appendix B

Transverse momentum spectra of strange hadrons

Figures B.1, B.2 and B.3 show the p_T —spectra of Ξ baryons, Λ baryons, and K_S^0 mesons, respectively, in the Low Multiplicity (a) and Low ZN (b) event classes.

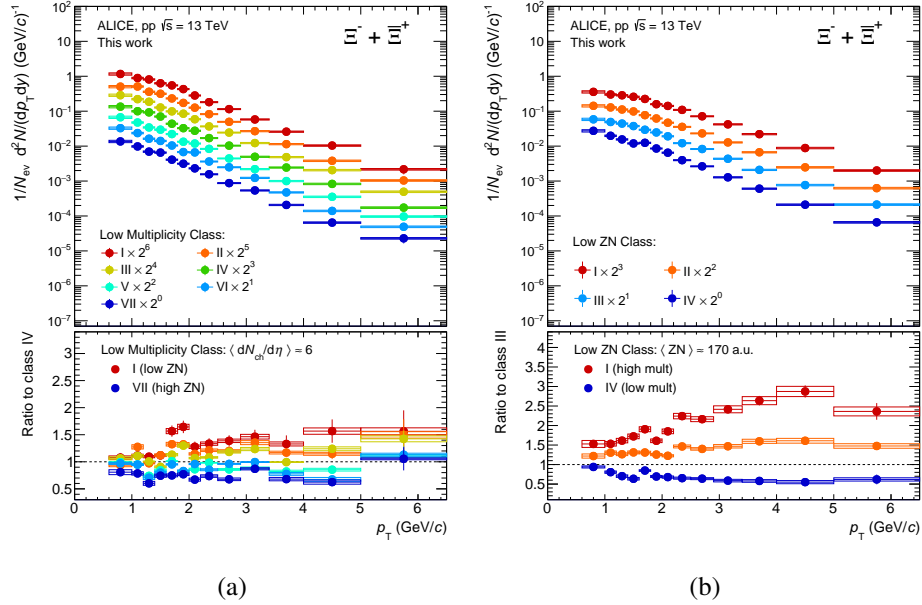


Fig. B.1 Transverse momentum distribution of Ξ in pp collisions at $\sqrt{s} = 13$ TeV in the Low Multiplicity (a) and Low ZN (b) selections (SPDClusters+VZEROM classes). The bottom panels show ratios of the two most extreme selections in the event class to the central one. The spectra are scaled by different factors to improve the visibility.

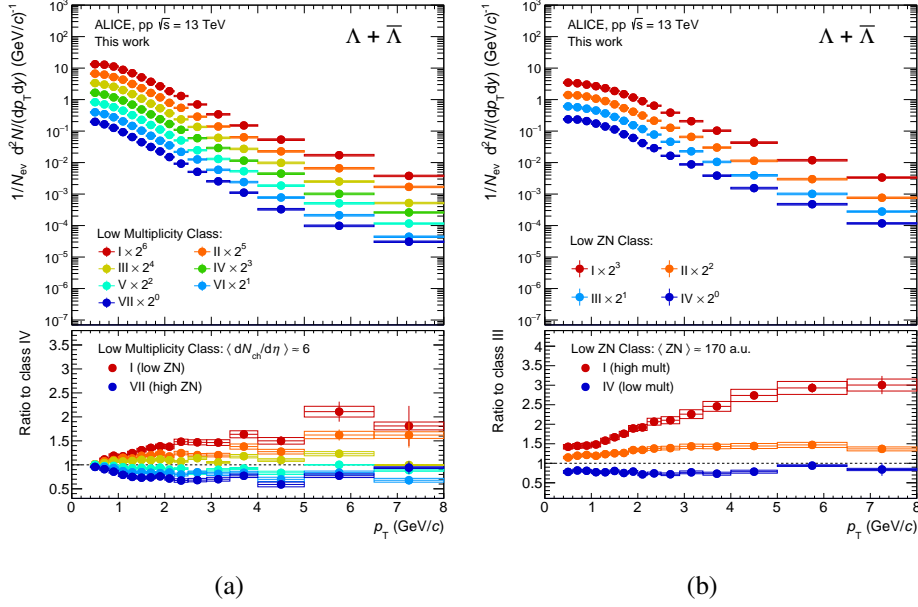


Fig. B.2 Transverse momentum distribution of Λ in pp collisions at $\sqrt{s} = 13$ TeV in the Low Multiplicity (a) and Low ZN (b) selections (SPDClusters+VZEROM classes). The bottom panels show ratios of the two most extreme selections in the event class to the central one. The spectra are scaled by different factors to improve the visibility.

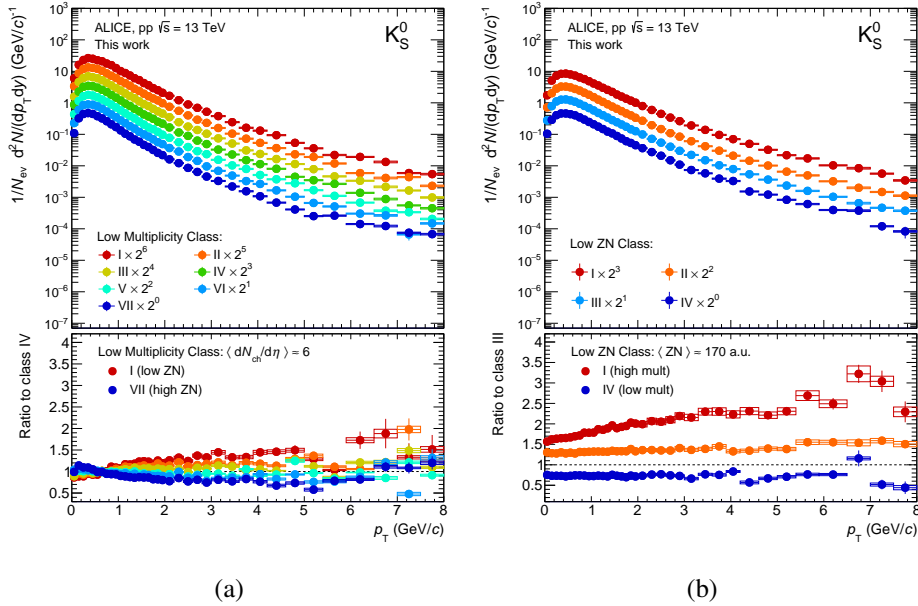


Fig. B.3 Transverse momentum distribution of K_S^0 in pp collisions at $\sqrt{s} = 13$ TeV in the Low Multiplicity (a) and Low ZN (b) selections (SPDClusters+VZEROM classes). The bottom panels show ratios of the two most extreme selections in the event class to the central one. The spectra are scaled by different factors to improve the visibility.